Benemérita Universidad Autónoma de Puebla
Instituto de Física "Luis Rivera Terrazas"

Design and modeling of piezoelectromagnetic metamaterials

Thesis presented by

Anatolii Konovalenko

to obtain the Degree of

Doctor of Philosophy
in
Materials Science

Directed by
Dr. Felipe Pérez Rodríguez

Puebla, México
September 2017

Acknowledgments

This research was carried out with the financial support of CONACYT (Consejo Nacional de Ciencia y Tecnología), VIEP-BUAP (Vicerrectoría de Investigación y Estudios de Posgrado de la Benemérita Universidad Autónoma de Puebla), PRODEP network “Magnetophotonic materials”, and the resources of IFUAP and Advanced Materials Group.

Agradecimientos

Este trabajo se ha realizado con apoyo financiero del CONACYT (Consejo Nacional de Ciencia y Tecnología), VIEP-BUAP (Vicerrectoría de Investigación y Estudios de Posgrado de la Benemérita Universidad Autónoma de Puebla), la red PRODEP “Materiales magnetofotónicos” y con los recursos del Instituto de Física y del Cuerpo Académico de Materiales Avanzados.

ABSTRACT

This dissertation introduces a novel theory of piezoelectromagnetic crystal homogenization which provides the basis to characterize media with *nonlocal* piezoelectric and piezomagnetic properties, normally described by material tensors. The introduced formalism extends the conventional homogenization theory which can not predict the dispersion of certain resonant structures of the electromagnetoelastic medium beyond the long wavelength limit. Specifically, the existence of the negative refraction index for photonic crystals and negative dynamic mass density and bulk modulus for phononic crystals can not be predicted by classical formalisms.

The new theory is able to describe accurately the physical parameters of the homogenized electromagnetoelastic medium, even for wavelengths comparable with the characteristic period of the crystal lattice. The results of the novel theory application to the photonic and phononic crystals show a very good correspondence with those of other homogenization theories with the assumption of weak piezoelectric and piezomagnetic effects.

Furthermore, a metamaterial transformation of the nonlocal response of the homogenized piezoelectromagnetic medium is proposed. The developed theory of the metamaterial response was applied to well-known metamaterials (2D system of metallic wires, split-ring resonators) and for introducing a new symmetric window resonators metamaterials with enhanced properties. The experimental study of the window resonators proved the correctness of the new formalism predictions. An important advantage of the proposed homogenization theory is that it allows to calculate reflectivity and transmission coefficients for finite-size samples in the nonlocal regime.

RESUMEN

Esta tesis introduce una novedosa teoría de homogeneización de cristales piezoelectromagnéticos que proporciona la base para caracterizar medios con propiedades piezoeléctricas y piezomagnéticas *no locales* que normalmente se describen con tensores materiales. El formalismo introducido extiende la teoría convencional que no puede predecir la dispersión de ciertas estructuras resonantes del medio electromagnetoelástico más allá del límite de longitud de onda larga. Específicamente, la existencia del índice de refracción negativo para los cristales fotónicos, y la densidad de masa dinámica y el módulo de bulto negativos para los cristales fonónicos no puede predecirse con formalismos clásicos.

La nueva teoría es capaz de describir con precisión los parámetros físicos del medio electromagnetoelástico homogeneizado, incluso para longitudes de onda comparables con el periodo característico de la red cristalina. Los resultados de la aplicación de la nueva teoría a cristales fotónicos y fonónicos muestran una muy buena correspondencia con los resultados de las teorías de homogeneización publicadas con la suposición de efectos piezoeléctricos y piezomagnéticos débiles.

Además, se propone una transformación metamaterial de la respuesta no local del medio piezoeléctricomagnético homogeneizado. La teoría desarrollada de la respuesta metamaterial se aplicó a metamateriales bien conocidos (sistema 2D de alambres metálicos, resonadores de anillos abiertos) y para introducir un metamaterial nuevo basado en resonadores tipo ventana con propiedades mejoradas. El estudio experimental de los resonadores de ventana comprobó la exactitud de las predicciones del formalismo propuesto. Una ventaja importante de la teoria de homogeneización propuesta consiste en que permite calcular coeficientes de reflectividad y transmisión para muestras de tamaño finito en el régimen no local.

Contents

List of Figures

Chapter 1

Introduction

Since ancient times, the humans have utilized the natural materials such as metals, wood, or ceramics to satisfy everyday needs. The modern industry dictates the novel level of the physical properties of these materials. For example, certain technological processes require improved mechanical strength, enhanced stability at low and high temperatures, chemical resistance in aggressive environment, enhanced lifetime, decreased weight etc. The obvious way to solve this problem is to combine the materials with dissimilar physical properties into the composite, in other words, to synthesize complex structures inheriting native parameters of the original elements. Additionally, these complex structures could acquire unique mechanical, electrical, magnetic, and optical properties. One of the most significant innovations in materials science is the introduction of the so-called metamaterials. Such materials possess novel physical behavior that could not be found in nature. As an example, the metamaterials exhibit extraordinary properties such as the negative refraction index. This effect introduces a new class of mechanisms for controlling the propagation of the electromagnetic and acoustic waves.

1.1 Electromagnetic metamaterials

The prefix “meta-” comes from the Greek word $\mu\epsilon\tau\alpha$ and means “to go beyond”. The direct translation gives an idea that a metamaterial should be a material with unusual properties, which are very different from that found in nature.

Although V.M. Agranovich and V.L. Ginzburg in 1966 reported the repercussions of negative permittivity, negative permeability, and negative group velocity during

(a) Victor Georgievich Veselago, Moscow Institute of Physics and Technology.

(b) Sir John Brian Pendry, Imperial College London.

Figure 1.1: Pioneers in metamaterials - Victor Veselago and John Pendry.

their study of crystals, the scientific work [1] by Victor Georgievich Veselago, published in 1967, is considered the starting point of metamaterials research. Despite no such materials were known at the time of the paper publication, V. Veselago predicted wave phenomena occurring in the case of the simultaneously negative electrical permittivity and magnetic permeability. The exhaustive definition of a metamaterial was given later in [2]: "*..Metamaterials are defined as macroscopic composites having a man-made, three dimensional, periodic cellular architecture designed to produce an optimized combination, not available in nature, of two or more responses to a specific excitation*".

In order to achieve non-usual physical properties, the electromagnetic metamaterials are assumed to be metal-dielectric periodic structures. A high dielectric contrast in such systems together with specific inclusion geometry results in a metamaterial effects appearance. Works of John Pendry about the control of the effective negative permittivity in thin wire systems ([3], [4]) together with artificial magnetism creation using the specific resonators configuration [5] opened a new era in materials science.

Nowadays, metallic inclusions of negative index metamaterials (NIMs) or left-handed metamaterials (LHMs) can have a great variety of forms [6]. The first implementation of NIMs [7] was based on the superposition of the conducting wires and split-ring resonators (SRRs) [5] to achieve the simultaneous negative permittivity and permeability

(Fig. 1.2). The structural asymmetry of the original SRRs design leads to a significant magneto-electric coupling, making their electromagnetic response bianisotropic [8]. Another class of SRRs was proposed to eliminate the bianisotropy [8] and to fabricate NIMs with broadband response [9] for any direction of propagation and any polarization [10]. In order to shift the operating frequency of metamaterials from microwave to optical range, the SRRs have been redesigned and scaled. Subsequently, new types of NIMs such as arrays of paired metallic nanorods [11], the staple-shaped nanostructure [12], arrays of ellipsoidal voids in a pair of metal sheets [13], and the nanofishnet negative-index structures with rectangular voids [14]-[15] were introduced.

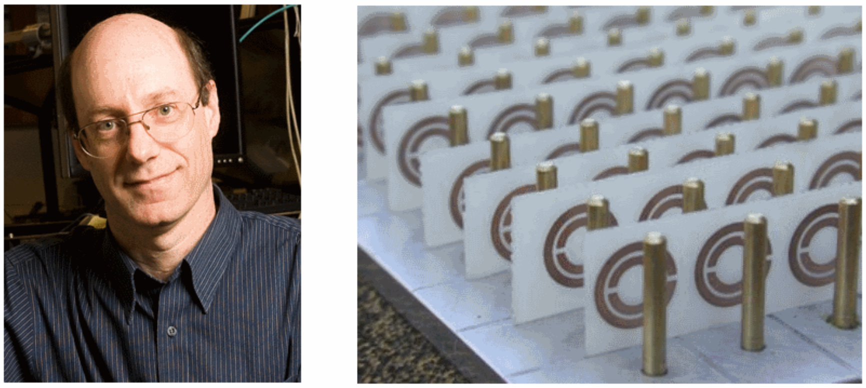

Figure 1.2: David R. Smith (UCSD, Duke University) and first ever implementation of a double-negative metamaterial, a split-ring resonators structure.

The alternative design of left-handed metamaterials (LHMs) contains metallic double-crosses inclusions inside the unit cell [16]–[18]. The double-cross metamaterial is introduced by adding a second orthogonal wire pair. The bars of the metallic crosses are responsible for the negative permittivity of the medium in certain frequency interval, whereas the negative permeability emerges because of the presence of the bar of the second cross [16], [17]. In [18], it was shown that metamaterials with double-cross structure can have a negative refractive index at the visible range and exhibit much lower losses in comparison to the nanofishnet LHMs. An interesting cross metamaterial is a periodic array of tightly conductor pairs forming Jerusalem cross [19], [20], that possesses NIM response to the linearly s-polarized incident waves [19].

NIMs can also be fabricated by using chiral structures presented in [21]–[24]. The chiral metamaterials are characterized by the absence of the inversion symmetry and may contain inclusions of following samples: metal rosettes [25], [26], metallic crosses [27]–[29], ‘U’-shaped SRRs [30], [31]), conjugated structures (gammadion resonator pairs [32], bi-layer C8 structures[33]), metal helices [34], and other complex structures (see [21], [22], [35]–[37]). These artificial structures can exhibit enhanced optical activity and circular dichroism in comparison to those observed in natural materials [22], [25], [26], [32], [33], [38]. In chiral metamaterials with strong magneto-electric coupling, the negative refraction may occur even if both permittivity and permeability are positive [22], [23].

1.2 Acoustic metamaterials

Among metamaterials, the acoustic ones are most commonly studied. Alike electromagnetic metamaterials, acoustic metamaterials can possess negative refraction of sound waves. This unusual property can be employed to make focusing and filtering of sound waves possible, which has a variety of applications. Recently, the acoustic metamaterials (or metafluids) are the object of intensive study ([39]–[49]). Such artificial materials are periodic arrays of liquid or solid isolated inclusions in a liquid or gas matrix. They behave like fluids and may have either anisotropic effective mass density [44]–[48] or negative effective dynamical parameters (mass density and/or bulk modulus) within certain frequency intervals [39], [42], [43], [49]. If the matrix is a solid host material, the phononic dispersion of the periodic structures (elastic metamaterials) may additionally exhibit narrow bands with negative effective shear modulus as well as negative dynamic mass density [50]–[54].

The use of solid components increases the number of relevant parameters and, therefore, the behavior of elastic metamaterials is rather complex [45]–[50], [55]–[57] compared with that of the metafluids. For example, as is demonstrated in ref. [49], the phononic band structure for a two-dimensional elastic metamaterial with multi-mass locally resonant inclusions exhibits a double-negative pass band where its behavior is “fluid-like”, whereas in other negative dispersion bands the phenomenon of “super-anisotropy” occurs, i.e. compressional waves and shear waves can propagate only along different directions. The anisotropy of mass density in acoustic metamaterials is well manifest in the low-frequency limit [44]–[48]. In the case of elastic metamaterials, the mass-density anisotropy has been observed at resonant frequencies only. In ref. [50], the experimental observation of strong anisotropy of mass density along two principal orientations of metamaterials, based on a soft-coated elastic core embedded in a solid matrix, has been reported. There, it was found that the local stiffness anisotropy in the coating layer is responsible for the difference of the locally resonant frequencies for the effective mass densities along two principal directions of the system and leads to the anisotropy of the mass density for the elastic metamaterial in bands close to the resonant frequencies. For such a system, the effective mass densities for the principal directions turned out to be equal to the average density in the static limit.

In a work [51], a homogenization theory, based on the plane-wave expansion (PWE) method, to calculate the effective elastic response of phononic crystals (PCs) with solid components, was put forward. It was shown how the derived expressions can also be applied to phononic crystals with liquid components.

Besides, it was demonstrated that rectangular two-dimensional lattices of water-filled holes in an elastic host matrix exhibit solid-like behavior with strongly anisotropic mass density in the low-frequency limit. These new elastic metamaterials were called metasolids. However, the experimental observation of their intriguing mass-density anisotropy in the quasi-static case has not been reported yet. Therefore, designing three-dimensional periodic structures with mass density anisotropy is an actual scientific problem with a variety of potential applications.

1.3 Overview of the existing homogenization theories

1.3.1 Electromagnetic crystal homogenization formalisms

One of the central problems of crystals study is to determine the medium dispersion. For the electromagnetic system it can be achieved if one could calculate the dielectric function which is generally speaking is dependent on the frequency ω and the wave-vector $\boldsymbol{k}$. That is, an appropriate nonlocal theoretical description should be used. Unfortunately, the classical theories can give an exhaustive response in the limited number of relatively simple cases. The reason for that is the high contrast of the physical parameters inside the unit cell (in particular, the metal-dielectric contrast in photonic crystals, the high solid-liquid shear modulus contrast in elastic structures) together with difficulties of the analytical problem solution due to boundary conditions determination ([58], [59]).

To overcome the mentioned difficulties, a homogenization approach is widely used. The core idea of the homogenization is to replace a real structure with a homogeneous medium described by effective parameters. Indeed, the fast-oscillating physical fields inside a homogenized medium should be properly described to work at high frequencies. There exist several homogenization procedures for calculating the effective parameters of photonic metamaterials (see, for example, [60]–[69]), their main difference is how to represent average electromagnetic field inside the unit cell to describe medium dispersion in correct manner.

Perhaps, the most commonly-used procedure is the effective parameter retrieval [60]. With this method, the effective permittivity $\epsilon(\omega)$ and permeability $\mu(\omega)$ (and, inclusively, parameters of the bianisotropic response [22], [38], [63]) are determined by requiring that experimental optical scattering spectra for a heterogeneous slab coincide with theoretical spectra for a homogeneous layer. However, such procedure may provide multiple solutions [21]. Besides, unlike homogeneous media, the retrieved effective parameters are sensitive to the slab thickness [70], [71] and depend on the characteristics of the substrate and top layers [63]. The application of homogenization approach to periodical media is still far from final solution due to several difficulties (see, for example, [72]–[74] and references therein).

Recently in [75], a general homogenization theory for metal-dielectric photonic crystals (PCs) based on the Fourier formalism was proposed. Unlike similar approaches [52], [76]–[83], in the work [75] the macroscopic magnetic field and electric displacement vector were redefined such that the non-magnetic inclusions in metal-dielectric periodic arrays can produce not only magnetic effects but also chiral ones. Nevertheless, the calculation of the effective tensors of the bianisotropic response, namely the permittivity, the permeability and the crossed magneto-electric tensors, is complicated due to the inversion of very large matrices [75]. To avoid these numerical difficulties, for example, in [84]–[86] an efficient recursive method to calculate the effective optical response of three-dimensional (3D) periodic metal-dielectric structures with an arbitrary form of the inclusions has been developed. This method makes use of the Haydock's recursive scheme [87] and, consequently, requires minimal computing resources to obtain well-converged results. Another useful method is the form-factor division approach (FFDA) [52], which also leads to a substantial reduction of the computation effort.

In spite of the existence of many methods for calculating effective parameters, each method has certain disadvantages even at the long wavelength limit. Hence, the development of a consistent homogenization approach has known difficulties and remains as an actual scientific problem.

1.3.2 Elastic medium homogenization theories

The description of sound propagation through a phononic crystal, composed of materials with different mass density, elastic parameters, arbitrary Bravais lattice and any inclusion shape, could be a quite complex task. To simplify the calculations needed for such a description, as in the case of electromagnetic crystals, an elastic homogenization approach is commonly used. The main idea of the homogenization approximation is similar to that of the electromagnetic case - to consider a phononic crystal as a homogeneous medium with effective parameters - effective mass density $\overset{\leftrightarrow}{\boldsymbol{\rho}}$ and effective compliance tensor $\overset{\leftrightarrow}{\boldsymbol{S}}$.

In the quasi-static limit ($\omega \to 0$), where the phononic dispersion relation is linear and, therefore, phase and group velocities coincide, the effective sound velocity can be directly calculated by using the plane wave expansion (PWE) method (see, for example, Refs. [53], [54], [88]–[93]). The effective sound velocity v_{eff} depends not only on the type of the periodic array and the geometry of the unit cell but also on the direction of propagation. According to the exact analytical formulas for the speed of transverse sound propagating in a two-dimensional arrangement of solids, derived in Ref. [53], the effective speed of transverse sound is determined by the average density $\overset{\leftrightarrow}{\boldsymbol{\rho}}$ and an effective shear modulus depending on the details of the microstructure.

On the basis of the homogenization method presented in Ref. [53], compact formulas of the effective velocities for the quasi-longitudinal, quasi-shear vertical, and shear horizontal modes were obtained in the works [88], [89]. The fact that the effective mass density in the quasi-static limit is given by the average one, $\overset{\leftrightarrow}{\boldsymbol{\rho}}$, implies that such an effective parameter depends only on the filling fraction of the components, but it is independent of their shape, as well as of their distribution inside the phononic crystal. As it has been shown in several works (see, for example, Ref. [48], [50], [94]), at sufficiently high frequencies, the effective mass density for solid phononic crystals depends not only on the filling fraction of the components but also on frequency ω of the phononic modes. Besides, the effective mass density turns out to be distinct for transverse and longitudinal phononic modes, and it may even be negative at certain frequency intervals.

Recently, a general homogenization theory [51], based on the Fourier formalism, has been proposed to calculate the effective parameters for phononic crystals having solid inclusions embedded in a solid host matrix. The theory provides explicit formulas for determining all the components of the effective mass-density and compliance tensors for any

Bravais lattice and shape of the inclusion not only in the long wavelength limit, but also at high frequencies where the effective dynamic parameters depend on both frequency ω and wave vector $\boldsymbol{k}$ and, therefore, the effective elastic response is nonlocal. The homogenized rectangular 2D PC can be called *metafluid* [95]–[98] since it behaves as a liquid, having zero effective shear modulus, but possessing an anisotropic effective mass density tensor. Besides, it was found that rectangular two-dimensional lattices of water-filled holes in an elastic host matrix exhibit solid-like behavior with strongly anisotropic mass density in the low-frequency limit.

Another useful general homogenization scheme was introduced in the work [99], where expressions for the fully dynamic effective material parameters, governing the spatially averaged fields by using the plane wave expansion method, were obtained. As it is shown there, the effective material parameters can be calculated for arbitrary frequency and wave number combinations, including but not restricted to Bloch wave branches for wave propagation in the periodic medium.

1.4 Thesis objectives

The progress in homogenization theories study lead to invention of new and more efficient metamaterials. Despite that a huge progress was made last decade, due to conceptual and numerical difficulties of existing approaches the feasible results of real structures study are often located in the long wavelength limit both for homogenized electromagnetic and elastic metamaterials. In practice, it is strongly desirable to calculate effective parameters of a designed structure far beyond the quasi-static limit with ability to predict metamaterial effects (negative permittivity and permeability for photonic crystals, negative mass density and bulk modulus for phononic structures). On the other hand, there consistent homogenization theory that could describe wave propagation in a photonic-phononic (foxonic) structures still not exist.

Taking into account the state-of-art of metamaterials science, the main objectives of this dissertation are:

- To develop a consistent electromagnetoelastic homogenization formalism to calculate nonlocal effective parameters of a coupled elastic and electromagnetic crystal that is valid far beyond the long wavelength limit.

- To apply the new theory for designing, fabricating and characterizing metamaterials in the microwave range.
- To design metasolids using the piezoelectromagnetic homogenization formalism.

According to the research objectives, the present thesis is organized as follows:

1. Theoretical description of a homogenized piezoelectromagnetic crystal (Chapter II):
    (a) Development of a theoretical formalism to calculate the effective parameters of the homogenized nonlocal piezoelectromagnetic crystal.
    (b) Demonstration of the nonlocal response transformation into a metamaterial one to describe metamaterial effects such as the negative refraction.
2. Electromagnetic metamaterials (Chapter III):
    (a) Theoretical description of the nonlocal dielectric response of a homogenized electromagnetic crystal being a particular case of the general piezoelectromagnetic formalism.
    (b) Demonstration of the metamaterial transformation of the nonlocal dielectric response.
    (c) Comparison between the purely nonlocal response and its metamaterial transformation for well-known physical systems in the microwave range.
    (d) Determination of the correct boundary conditions for the macroscopic electromagnetic field to calculate reflectivity and transmittance spectra of a finite-size metamaterial slab.
    (e) Design, modeling, and characterization of microwave metamaterials: split-ring resonators and a new structure - framed crosses.
3. Acoustic metamaterials (Chapter IV):
    (a) Derivation of homogenization formalism based on the developed nonlocal piezoelectromagnetic homogenization theory.
    (b) Transformation of the nonlocal elastic response into a metamaterial one to describe the elastic metamaterial behavior.
    (c) Design and modeling of an acoustic metamaterial with mass density anisotropy.

Chapter 2

Theoretical description of a homogenized piezoelectromagnetic crystal

This part is focused on the theoretical formalism development that could predict effective dynamic properties for a homogenized nonlocal piezoelectromagnetic crystal. Within such a formalism the explicit expressions for all material tensors of the coupled photonic-phononic structure beyond long wavelength limit will be obtained. In fact, a new class of metamaterials - piezoelectromagnetic metamaterials, can be introduced, possessing quadruple-negative behavior: negative dynamic mass density and bulk modulus together with negative permittivity and permeability.

A medium allowing the propagation of an elastic-electromagnetic wave is called piezoelectromagnetic or electromagnetoelastic[100]. The main characteristic of such a medium is the existence of the elastic-electromagnetic wave coupling mechanism inside the crystal. This mechanism is presented by the piezoelectric and piezomagnetic effects correspondingly, so it is necessary to bring up a brief description of the effects involved.

2.1 Piezoelectric effect

The piezoelectric effect is a physical phenomenon of electrical charge appearance in a crystal under applied mechanical pressure. The piezoelectricity can only occur in crystals

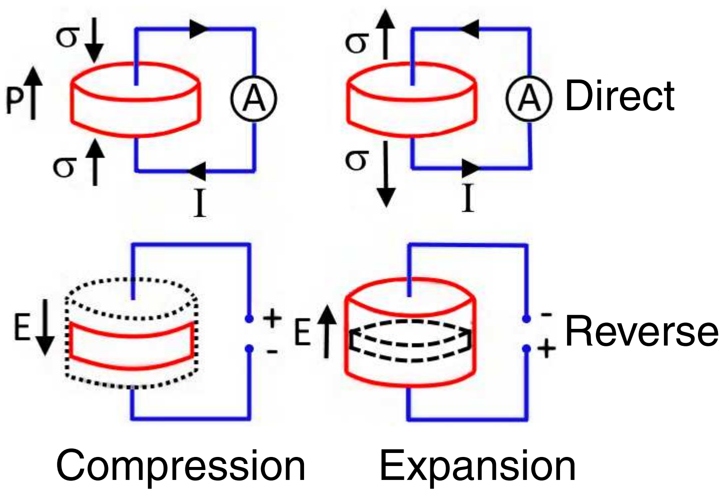

Figure 2.1: Schematic representation of piezoelectric effect.

without inversion symmetry. There exist direct and reverse piezoelectric effects (Figure 2.1):

The phenomenon of the piezoelectricity was observed in 1880 by Jacques Curie and Pierre Curie. The reverse piezoelectric effect was discovered by Gabriel Lippmann from theoretical predictions of thermodynamics in 1881 and in the same year it was demonstrated by Jacques and Pierre Curie.

Figure 2.2: Jacques Curie (1856-1941), Pierre Curie (1859-1906) Nobel Prize in Physics, 1903; Gabriel Lippmann (1845-1921), Nobel Prize in Physics, 1908.

One of the most classical examples of piezoelectricity is observed in a crystal of quartz SiO_2. To give an example of the quartz efficiency, a centimeter thick slab of quartz under pressure of 2 kN produces 12500 V.

The origin of the piezoelectric effect by using a crystal of quartz can be described

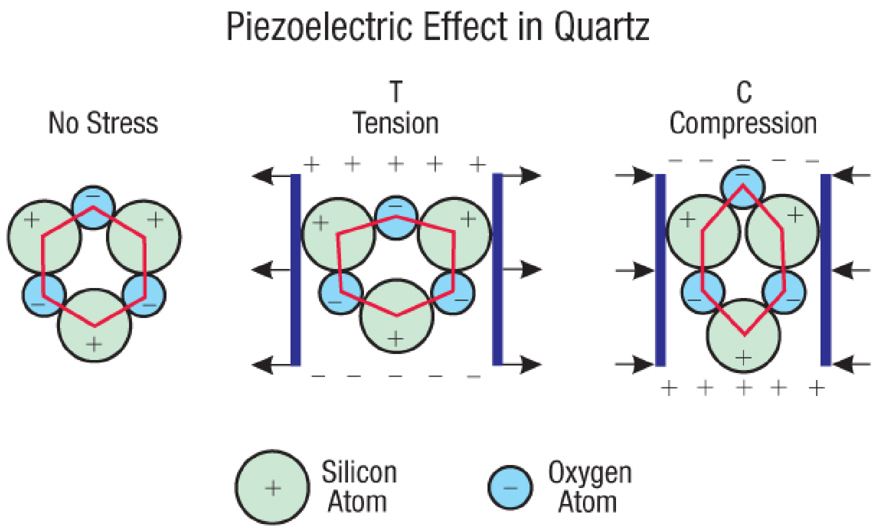

Figure 2.3: Piezoelectric effect explanation in SiO_2 quartz unit cell.

using the scheme displayed in Figure 2.3. In the absence of external mechanical pressure, a crystal remains in the unstrained state; that is, the net charge is equal to 0. Due to the application of a mechanical stress in a particular crystal direction, a relative displacement of both silicon and oxygen atoms occurs. The geometry of a deformed crystal cell no longer allows the compensation of the total charge. The latter results in the appearance of electric dipoles polarization. In other words, an external force leads to a compulsive charge separation, which results in the appearance of voltage between two points of a piezoelectric crystal. Besides, the voltage application from an external source between two opposing points in a piezoelectric crystal produces charge redistribution inside the crystal in order to reach a charge equilibrium state which is a phonon excitation process. Feeding a quartz slab with the external voltage source using frequency that is close to a resonance frequency of the slab, a very efficient mechanical oscillator can be built with quality factor $\boldsymbol{Q}$ reaching 10^6. This property of a piezoelectric quartz slab is widely used in electronics to make a very stable and efficient frequency generator.

Although the quartz plays important role in modern electronics, more efficient materials were synthesized to achieve higher values of the piezoelectric coefficients, an increase of the electromechanical coupling factor (denoted as tensor $\overset{\leftrightarrow}{\boldsymbol{k}}$) - an indicator of the efficiency of the electrical-mechanical energy conversion. Lead zirconate titanate $Pb[Zr_xTi_{1-x}]O_3$ ceramics is an example of piezoelectric materials with enhanced properties (Table 2.1).

	$\alpha-$quartz	PZT 65/35	PZT-4
Density, kg/m^3	2650	7825	7600
Lattice	Trigonal	Hexagonal	Tetragonal
C_{11}, GPa	86.74	159.4	139
C_{12}, GPa	6.99	73.85	77.8
C_{13}, GPa	11.91	70.13	74.3
C_{14}, GPa	-17.91	0	0
C_{33}, GPa	107.2	126.1	115
C_{44}, GPa	57.94	38.9	25.6
C_{66}, GPa	39.875	42.775	30.6
e_{11}, C/m^2	0.171	0	0
e_{14}, C/m^2	-0.04	0	0
e_{31}, C/m^2	0	-6.127	-5.2
e_{33}, C/m^2	0	10.71	15.1
e_{15}, C/m^2	0	8.387	12.7
ϵ_{11}/ϵ_0	4.51	639.24	728.46
ϵ_{33}/ϵ_0	4.63	253.32	634.72

Table 2.1: The elastic tensor components C_{ik}, piezoelectric stress tensor coefficients e_{ikl} and permittivity tensor components ϵ_{ik}/ϵ_0 of commonly-used piezoelectric materials - quartz [101], PZT 65/35 [102] and PZT-4 [103].

The piezoelectric effect is widely used in practice, and there is a big field for the metamaterials science. A possible investigation is the demonstration of the piezoelectric effect in the macroscopic periodic structures. Questions of the piezoelectric effect enhancement are also very important, it is necessary to develop materials with coefficients higher than those of the already known piezoelectric materials.

2.2 Piezomagnetic effect

The piezomagnetic effect consists in the magnetization appearance inside the crystal under mechanical strain [104]. In a piezomagnetic material, one may induce a spontaneous magnetic moment by applying physical stress or produce crystal deformation by applying a magnetic field (Figure 2.4). Alike the piezoelectric effect, the piezomagnetic effect is thermodynamically reversible. The magnetostriction of antiferromagnets is linear, i.e. the variations of the crystal dimensions are proportional to the intensity of the applied magnetic field.

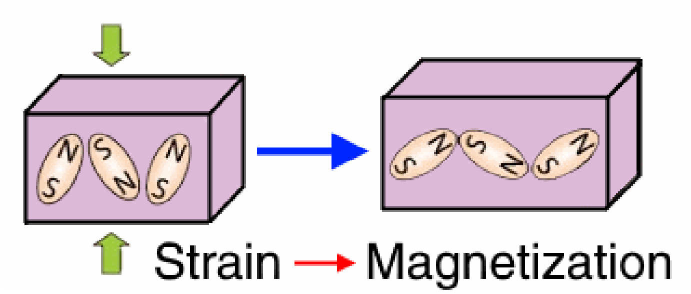

Figure 2.4: A piezomagnetic effect mechanism, the applied pressure changes the magnetic symmetry of an antiferromagnetic crystal in such a way that a weak ferromagnetism arises.

The origin of the piezomagnetic effect is the absence of certain symmetry of the crystal structure. The piezomagnetic effect was theoretically predicted by Igor E. Dzyaloshinskii (1958) [105] and experimentally (1959) observed in the fluorides of cobalt by Andrey Borovik-Romanov [106].

Figure 2.5: Discoverers of the piezomagnetic effect - I. Dzialoshinskii and A. Borovik-Romanov.

The piezomagnetic effect is experimentally observed in antiferromagnetic crystals of MnF_2, CoF_2, and α-Fe_2O_3 [106], [107].

By itself, the piezomagnetic effect is rather weak; a brief description of typical

Material	d_{33}, nm/A
Nickel	3
Alfenol	7
Terfenol-D	15
Metglas 2605CO	70-88
Metglas 2605SC	300-400

Table 2.2: Piezoelectric tensor component d_{33} for available piezomagnetic materials [108].

piezomagnetic materials is given in Table 2.2. Hence, the demonstration and measurement of the piezomagnetic effect in artificial macro-structures is an actual scientific problem.

2.3 Electromagnetoelastic crystal homogenization formalism

The most obvious way to create a piezoelectromagnetic crystal is to take a piezoelectromagnetic crystal is to use piezoelectric and piezomagnetic materials [109]. This approach is quite common, however, an important characteristic of metamaterials is that their physical properties can be very different from the constituents since they mainly come from the structure. In this section a homogenization theory for calculating the effective parameters of homogenized piezoelectromagnetic crystals will be developed.

The real behavior of a coupled piezoelectromagnetic crystal is rather complex, and the material tensors that determine the relation between fields can depen on other physical functions as, for example, temperature [100]. In the present thesis, the constitutive equations for an electromagnetoelastic crystal considering the linear response regime will be written.

2.3.1 Initial point of the piezoelectromagnetic system description

The constitutive equations of a coupled magnetic-electrical-mechanical crystal description are given expressions [110]:

$$\begin{aligned} \sigma_{ij} &= C_{ijkl}u_{kl} - e_{kij}E_k - d_{kij}H_k \\ D_i &= e_{ikl}u_{kl} + \epsilon_{ik}E_k + \alpha_{ik}H_k \\ B_i &= d_{ikl}u_{kl} + \alpha^T_{ik}E_k + \mu_{ik}H_k, \end{aligned} \tag{2.3.1}$$

where σ_{ij} is the stress tensor, u_{kl} is the displacement tensor, E_k and H_k are the components of the electric and magnetic fields, e_{kij} is the piezoelectric tensor, d_{kij} is the piezomagnetic tensor, ϵ_{ik} is the permittivity tensor, μ_{ik} is the permeability tensor, α_{ik} is the crossed magnetoelectric tensor.

The system of equations (2.3.1) can serve as a starting point in developing a new theoretical formalism. Nevertheless, the initial form of material equations is not applicable directly. The reason is that physical phenomena occurring in a piezoelectromagnetic system are being described in terms of a 4-rank stiffness tensor $\overset{\leftrightarrow}{C}_{ijkl}$ together with 3-rank tensors of piezoelectric $\overset{\leftrightarrow}{e}_{ikl}$ and piezomagnetic $\overset{\leftrightarrow}{d}_{ikl}$ coefficients respectively. In order to develop the homogenization method it will be convenient to write the system of equations in a matrix form and to carry out tensors contraction using their symmetry properties.

2.3.2 Tensors contraction using the symmetry properties

For the stiffness tensor C_{ijkl} the number of components is equal to 81, the indexes i, j, k, l are integers with values $1, 2, 3$. However, it is possible to reduce the rank of the stiffness tensor C_{ijkl} using symmetry properties:

$$C_{ijkl} = C_{klij} = C_{jikl} = C_{ijlk}. \tag{2.3.2}$$

Let us write the summation over indexes kl of the term $\mathrm{C}_{ijkl}\ u_{kl}$ in (2.3.1) as:

$$\begin{aligned} C_{ijkl}u_{kl} &= C_{ij11}u_{11} + C_{ij12}u_{12} + C_{ij13}u_{13} \\ &+ C_{ij21}u_{21} + C_{ij22}u_{22} + C_{ij23}u_{23} \\ &+ C_{ij31}u_{31} + C_{ij32}u_{32} + C_{ij33}u_{33}. \end{aligned} \tag{2.3.3}$$

The symmetric displacement tensor u_{kl} can be expressed as:

$$u_{kl} = \frac{1}{2}\left(\nabla_k u_l + \nabla_l u_k\right). \tag{2.3.4}$$

Substituting previous expression into (2.3.3) gives:

$$\begin{aligned} C_{ijkl}u_{kl} &= \frac{1}{2}C_{ij11}(\nabla_1 u_1 + \nabla_1 u_1) + \frac{1}{2}C_{ij12}(\nabla_1 u_2 + \nabla_2 u_1) + \frac{1}{2}C_{ij13}(\nabla_1 u_3 + \nabla_3 u_1) \\ &+ \frac{1}{2}C_{ij21}(\nabla_2 u_1 + \nabla_1 u_2) + \frac{1}{2}C_{ij22}(\nabla_2 u_2 + \nabla_2 u_2) + \frac{1}{2}C_{ij23}(\nabla_2 u_3 + \nabla_3 u_2) \\ &+ \frac{1}{2}C_{ij31}(\nabla_3 u_1 + \nabla_1 u_3) + \frac{1}{2}C_{ij32}(\nabla_3 u_2 + \nabla_2 u_3) + \frac{1}{2}C_{ij33}(\nabla_3 u_3 + \nabla_3 u_3). \end{aligned} \tag{2.3.5}$$

Hence,

$$\begin{aligned} C_{ijkl}u_{kl} &= C_{ij11}\nabla_1 u_1 + \frac{1}{2}C_{ij12}(\nabla_1 u_2 + \nabla_2 u_1) + \frac{1}{2}C_{ij13}(\nabla_1 u_3 + \nabla_3 u_1) \\ &+ \frac{1}{2}C_{ij21}(\nabla_2 u_1 + \nabla_1 u_2) + C_{ij22}\nabla_2 u_2 + \frac{1}{2}C_{ij23}(\nabla_2 u_3 + \nabla_3 u_2) \\ &+ \frac{1}{2}C_{ij31}(\nabla_3 u_1 + \nabla_1 u_3) + \frac{1}{2}C_{ij32}(\nabla_3 u_2 + \nabla_2 u_3) + C_{ij33}\nabla_3 u_3. \end{aligned} \tag{2.3.6}$$

Indexes pairs ij can be replaced using the Voigt scheme:

Double index, ij	11	22	33	23, 32	31, 13	12, 21
Replaced by i'	1	2	3	4	5	6

Replacing ij pair with i', and kl with k' in expression (2.3.6) to obtain:

$$\begin{aligned} C_{i'k'}\nabla_k u_l = \; & C_{i'1}\nabla_1 u_1 + \frac{1}{2}C_{i'6}(\nabla_1 u_2 + \nabla_2 u_1) + \frac{1}{2}C_{i'5}(\nabla_1 u_3 + \nabla_3 u_1) \\ + \; & \frac{1}{2}C_{i'6}(\nabla_2 u_1 + \nabla_1 u_2) + C_{i'2}\nabla_2 u_2 + \frac{1}{2}C_{i'4}(\nabla_2 u_3 + \nabla_3 u_2) \\ + \; & \frac{1}{2}C_{i'5}(\nabla_3 u_1 + \nabla_1 u_3) + \frac{1}{2}C_{i'4}(\nabla_3 u_2 + \nabla_2 u_3) + C_{i'3}\nabla_3 u_3. \end{aligned} \tag{2.3.7}$$

Grouping terms to finally state:

$$\begin{aligned} C_{i'k'}\nabla_k u_l &= C_{i'1}\nabla_1 u_1 + C_{i'2}\nabla_2 u_2 + C_{i'3}\nabla_3 u_3 \\ &+ C_{i'4}(\nabla_3 u_2 + \nabla_2 u_3) \\ &+ C_{i'5}(\nabla_3 u_1 + \nabla_1 u_3) \\ &+ C_{i'6}(\nabla_1 u_2 + \nabla_2 u_1). \end{aligned} \tag{2.3.8}$$

A more convenient form of the resulting expression is given by the following equation:

$$C_{i'k'}\nabla_k u_l = \begin{pmatrix} C_{11} & C_{12} & C_{13} & C_{14} & C_{15} & C_{16} \\ C_{21} & C_{22} & C_{23} & C_{24} & C_{25} & C_{26} \\ C_{31} & C_{32} & C_{33} & C_{34} & C_{35} & C_{36} \\ C_{41} & C_{42} & C_{43} & C_{44} & C_{45} & C_{46} \\ C_{51} & C_{52} & C_{53} & C_{54} & C_{55} & C_{56} \\ C_{61} & C_{62} & C_{63} & C_{64} & C_{65} & C_{66} \end{pmatrix} \begin{pmatrix} \nabla_1 u_1 \\ \nabla_2 u_2 \\ \nabla_3 u_3 \\ \nabla_3 u_2 + \nabla_2 u_3 \\ \nabla_3 u_1 + \nabla_1 u_3 \\ \nabla_2 u_1 + \nabla_1 u_2 \end{pmatrix} \tag{2.3.9}$$

Now the stiffness tensor C is a 2-rank tensor having 36 components. However, only 21 of them are independent (all the elements on and above the main diagonal). Furthermore, applying specific crystal symmetry rules the number of independent components is even less (see Appendix A.1):

Triclinic	Monoclinic	Orthorhombic	Tetragonal	Trigonal	Hexagonal	Cubic	Isotropic
21	13	9	7,6	7,6	5	3	2

Turning back to expression (2.3.9), it is possible to split the second matrix as a product of two matrices - derivatives matrix and a matrix of displacements:

$$C_{i'k'}\nabla_k u_l = \begin{pmatrix} C_{11} & C_{12} & C_{13} & C_{14} & C_{15} & C_{16} \\ C_{21} & C_{22} & C_{23} & C_{24} & C_{25} & C_{26} \\ C_{31} & C_{32} & C_{33} & C_{34} & C_{35} & C_{36} \\ C_{41} & C_{42} & C_{43} & C_{44} & C_{45} & C_{46} \\ C_{51} & C_{52} & C_{53} & C_{54} & C_{55} & C_{56} \\ C_{61} & C_{62} & C_{63} & C_{64} & C_{65} & C_{66} \end{pmatrix} \begin{pmatrix} \nabla_1 & 0 & 0 \\ 0 & \nabla_2 & 0 \\ 0 & 0 & \nabla_3 \\ 0 & \nabla_3 & \nabla_2 \\ \nabla_3 & 0 & \nabla_1 \\ \nabla_2 & \nabla_1 & 0 \end{pmatrix} \begin{pmatrix} u_1 \\ u_2 \\ u_3 \end{pmatrix} \tag{2.3.10}$$

Now let us proceed to the contraction of piezoelectric tensor, explicitly substituting the k index ($k = 1, 2, 3$) in (2.3.1) to get

$$e_{kij}E_k = e_{1ij}E_1 + e_{2ij}E_2 + e_{3ij}E_3. \tag{2.3.11}$$

Making the index replacement $ij \to i^{'}$ and employing Voigt notation,

$$e_{kij}E_k \to e^T_{i'k}E_k. \tag{2.3.12}$$

Consequently,

$$e^T_{i'k}E_k = e^T_{i'1}E_1 + e^T_{i'2}E_2 + e^T_{i'3}E_3. \tag{2.3.13}$$

Matrix $e_{ki'}$ (3×6) has the form:

$$e_{ki'} = \begin{pmatrix} e_{11} & e_{12} & e_{13} & e_{14} & e_{15} & e_{16} \\ e_{21} & e_{22} & e_{23} & e_{24} & e_{25} & e_{26} \\ e_{31} & e_{32} & e_{33} & e_{34} & e_{35} & e_{36} \end{pmatrix} \tag{2.3.14}$$

Finally, one can transform $e_{kij}E_k$ as

$$e_{kij}E_k \to e^T_{i'k}E_k = \begin{pmatrix} e_{11} & e_{21} & e_{31} \\ e_{12} & e_{22} & e_{32} \\ e_{13} & e_{23} & e_{33} \\ e_{14} & e_{24} & e_{34} \\ e_{15} & e_{25} & e_{35} \\ e_{16} & e_{26} & e_{36} \end{pmatrix} \begin{pmatrix} E_1 \\ E_2 \\ E_3 \end{pmatrix} \tag{2.3.15}$$

Similarly, the contraction of the piezomagnetic tensor d_{kij} in (2.3.1) can be rewritten as

$$d_{kij}H_k \to d^T_{i'k}H_k = \begin{pmatrix} d_{11} & d_{21} & d_{31} \\ d_{12} & d_{22} & d_{32} \\ d_{13} & d_{23} & d_{33} \\ d_{14} & d_{24} & d_{34} \\ d_{15} & d_{25} & d_{35} \\ d_{16} & d_{26} & d_{36} \end{pmatrix} \begin{pmatrix} H_1 \\ H_2 \\ H_3 \end{pmatrix} \tag{2.3.16}$$

The tensor products $e_{ikl}u_{kl}$ and $d_{ikl}u_{kl}$ can also be contracted by using the described procedure of reducing the tensor rank. Let us express $e_{ikl}u_{kl}$ in the form

$$\begin{aligned} e_{ikl}u_{kl} &= e_{i11}u_{11} + e_{i12}u_{12} + e_{i13}u_{13} \\ &+ e_{i21}u_{21} + e_{i22}u_{22} + e_{i23}u_{23} \\ &+ e_{i31}u_{31} + e_{i32}u_{32} + e_{i33}u_{33}. \end{aligned} \tag{2.3.17}$$

Expressing explicitly the symmetric displacement tensor as a half sum of displacement derivatives (2.3.4), one can obtain

$$\begin{aligned} e_{ikl}\nabla_k u_l &= \frac{1}{2}e_{i11}(\nabla_1 u_1 + \nabla_1 u_1) + \frac{1}{2}e_{i12}(\nabla_1 u_2 + \nabla_2 u_1) + \frac{1}{2}e_{i13}(\nabla_1 u_3 + \nabla_3 u_1) \\ &+ \frac{1}{2}e_{i21}(\nabla_2 u_1 + \nabla_1 u_2) + \frac{1}{2}e_{i22}(\nabla_2 u_2 + \nabla_2 u_2) + \frac{1}{2}e_{i23}(\nabla_2 u_3 + \nabla_3 u_2) \\ &+ \frac{1}{2}e_{i31}(\nabla_3 u_1 + \nabla_1 u_3) + \frac{1}{2}e_{i32}(\nabla_3 u_2 + \nabla_2 u_3) + \frac{1}{2}e_{i33}(\nabla_3 u_3 + \nabla_3 u_3). \end{aligned} \tag{2.3.18}$$

Hence,

$$\begin{aligned} e_{ikl}\nabla_k u_l &= e_{i11}\cdot\nabla_1 u_1 + \frac{1}{2}e_{i12}(\nabla_1 u_2 + \nabla_2 u_1) + \frac{1}{2}e_{i13}(\nabla_1 u_3 + \nabla_3 u_1) \\ &+ \frac{1}{2}e_{i21}(\nabla_2 u_1 + \nabla_1 u_2) + e_{i22}\nabla_2 u_2 + \frac{1}{2}e_{i23}(\nabla_2 u_3 + \nabla_3 u_2) \\ &+ \frac{1}{2}e_{i31}(\nabla_3 u_1 + \nabla_1 u_3) + \frac{1}{2}e_{i32}(\nabla_3 u_2 + \nabla_2 u_3) + e_{i33}\nabla_3 u_3. \end{aligned} \tag{2.3.19}$$

Replacing indexes $kl \to k'$ and using Voigt notation, it follows

$$\begin{aligned} e_{ik'}\nabla_k u_l &= e_{i1}\cdot\nabla_1 u_1 + \frac{1}{2}e_{i6}(\nabla_1 u_2 + \nabla_2 u_1) + \frac{1}{2}e_{i5}(\nabla_1 u_3 + \nabla_3 u_1) \\ &+ \frac{1}{2}e_{i6}(\nabla_2 u_1 + \nabla_1 u_2) + e_{i2}\nabla_2 u_2 + \frac{1}{2}e_{i4}(\nabla_2 u_3 + \nabla_3 u_2) \\ &+ \frac{1}{2}e_{i5}(\nabla_3 u_1 + \nabla_1 u_3) + \frac{1}{2}e_{i4}(\nabla_3 u_2 + \nabla_2 u_3) + e_{i3}\nabla_3 u_3. \end{aligned} \tag{2.3.20}$$

Grouping common terms to obtain:

$$\begin{aligned} e_{ik'}\nabla_k u_l &= e_{i1}\nabla_1 u_1 + e_{i2}\nabla_2 u_2 + e_{i3}\nabla_3 u_3 \\ &+ e_{i4}(\nabla_2 u_3 + \nabla_3 u_2) \\ &+ e_{i5}(\nabla_1 u_3 + \nabla_3 u_1) \\ &+ e_{i6}(\nabla_1 u_2 + \nabla_2 u_1). \end{aligned} \tag{2.3.21}$$

The latter result can be written in matrix form as

$$e_{ik'}\nabla_k u_l = \begin{pmatrix} e_{11} & e_{12} & e_{13} & e_{14} & e_{15} & e_{16} \\ e_{21} & e_{22} & e_{23} & e_{24} & e_{25} & e_{26} \\ e_{31} & e_{32} & e_{33} & e_{34} & e_{35} & e_{36} \end{pmatrix} \begin{pmatrix} \nabla_1 u_1 \\ \nabla_2 u_2 \\ \nabla_3 u_3 \\ \nabla_3 u_2 + \nabla_2 u_3 \\ \nabla_3 u_1 + \nabla_1 u_3 \\ \nabla_2 u_1 + \nabla_1 u_2 \end{pmatrix} \tag{2.3.22}$$

The number of independent components of the piezoelectric tensor depends on the crystal symmetry (see Appendix A.2). The expression (2.3.22) can be modified by splitting the second matrix as a product of a derivatives matrix and a displacement column as follows

$$e_{ikl}u_{kl} \rightarrow e_{ik'}\nabla_k u_l = \begin{pmatrix} e_{11} & e_{12} & e_{13} & e_{14} & e_{15} & e_{16} \\ e_{21} & e_{22} & e_{23} & e_{24} & e_{25} & e_{26} \\ e_{31} & e_{32} & e_{33} & e_{34} & e_{35} & e_{36} \end{pmatrix} \begin{pmatrix} \nabla_1 & 0 & 0 \\ 0 & \nabla_2 & 0 \\ 0 & 0 & \nabla_3 \\ 0 & \nabla_3 & \nabla_2 \\ \nabla_3 & 0 & \nabla_1 \\ \nabla_2 & \nabla_1 & 0 \end{pmatrix} \begin{pmatrix} u_1 \\ u_2 \\ u_3 \end{pmatrix} \tag{2.3.23}$$

Similarly, an expression for the tensor product $d_{ikl}u_{kl}$ obtained:

$$d_{ikl}u_{kl} \rightarrow d_{ik'}\nabla_k u_l = \begin{pmatrix} d_{11} & d_{12} & d_{13} & d_{14} & d_{15} & d_{16} \\ d_{21} & d_{22} & d_{23} & d_{24} & d_{25} & d_{26} \\ d_{31} & d_{32} & d_{33} & d_{34} & d_{35} & d_{36} \end{pmatrix} \begin{pmatrix} \nabla_1 & 0 & 0 \\ 0 & \nabla_2 & 0 \\ 0 & 0 & \nabla_3 \\ 0 & \nabla_3 & \nabla_2 \\ \nabla_3 & 0 & \nabla_1 \\ \nabla_2 & \nabla_1 & 0 \end{pmatrix} \begin{pmatrix} u_1 \\ u_2 \\ u_3 \end{pmatrix} \tag{2.3.24}$$

2.3.3 Complete set of piezoelectromagnetic equations

Let us write the Newton law:

$$(\nabla_{3\times 6})_{ij}\sigma_j = -\omega^2 \rho u_i, \tag{2.3.25}$$

where ω is the frequency of the time-varying stress σ_j and displacement u_i.

The general expression of Hooke‘s law is given by

$$\sigma_i = C_{ij}((\nabla_{3\times 6})^T)_{jk}u_k - e^T_{ik}E_k - d^T_{ik}H_k. \tag{2.3.26}$$

Multiplying both sides of previous expression by the compliance matrix to get

$$S_{ji}\sigma_i = ((\nabla_{3\times 6})^T)_{jk}u_k - S_{ji}e^T_{ik}E_k - S_{ji}d^T_{ik}H_k. \tag{2.3.27}$$

It is convenient to write Hooke‘s law in the following form

$$(\nabla_{3\times 6})^T_{jk}u_k = S_{ji}\sigma_i + S_{ji}e^T_{ik}E_k + S_{ji}d^T_{ik}H_k. \tag{2.3.28}$$

Thus, the equations that describe the elastic behavior of a piezoelectromagnetic medium can be written as

$$\begin{cases} (\nabla_{3\times 6})_{ij}\sigma_j & = & -\,\omega^2 \rho u_i, \\ (\nabla_{3\times 6})^T_{jk}u_k & = & S_{ji}\sigma_i + S_{ji}e^T_{ik}E_k + S_{ji}d^T_{ik}H_k. \end{cases} \tag{2.3.29}$$

The electromagnetic waves propagation inside a passive medium is described by Maxwell equations (Faraday and Ampere laws correspondingly):

$$\begin{cases} (\nabla\times \overset{\leftrightarrow}{I})_{ij}E_j & = & & i\omega B_i, \\ (\nabla\times \overset{\leftrightarrow}{I})_{ij}H_j & = & - & i\omega D_i. \end{cases} \tag{2.3.30}$$

The expressions for B$_i$ and D$_i$ should be added in the form

$$\begin{array}{rclclcl} B_i & = & d_{ij}(\nabla_{3\times 6})^T_{jk}u_k & + & \delta_{ik}E_k & + & \mu_{ik}H_k, \\ D_i & = & e_{ij}(\nabla_{3\times 6})^T_{jk}u_k & + & \epsilon_{ik}E_k & + & \gamma_{ik}H_k. \end{array} \tag{2.3.31}$$

Hereafter, instead of α_{ik}, α^T_{ik} tensors in (2.3.1), the γ_{ik} and δ_{ik} tensors will be used. The reason for that is to avoid confusion with the thermoelectric coefficient α. Furthermore, the usage of the γ_{ik} and δ_{ik} tensors allows us to describe the electromagnetic equations in terms of a bianisotropic response that is described in the generalized form as:

$$\begin{aligned} \boldsymbol{D} &= \overset{\leftrightarrow}{\boldsymbol{\epsilon}}\, \boldsymbol{E} + \overset{\leftrightarrow}{\boldsymbol{\gamma}}\, \boldsymbol{H}, \\ \boldsymbol{B} &= \overset{\leftrightarrow}{\boldsymbol{\delta}}\, \boldsymbol{E} + \overset{\leftrightarrow}{\boldsymbol{\mu}}\, \boldsymbol{H}. \end{aligned} \tag{2.3.32}$$

Employing the expression for $(\nabla_{3\times6})^T_{jk}u_k$ given by the second equation of the system (2.3.29), it is possible to group tensors, as:

$$
\begin{array}{rcccccc}
B_i & = & d_{ij}\left(S_{ji}\sigma_i + S_{ji}e^T_{ik}E_k + S_{ji}d^T_{ik}H_k\right) & + & \delta_{ik}E_k & + & \mu_{ik}H_k = \\
& = & d_{ij}S_{ji}\sigma_i & + & \underbrace{\left(\delta_{ik} + d_{ij}S_{ji}e^T_{ik}\right)}_{\delta^{'}_{ik}}E_k & + & \underbrace{\left(\mu_{ik} + d_{ij}S_{ji}d^T_{ik}\right)}_{\mu^{'}_{ik}}H_k, \\
D_i & = & e_{ij}\left(S_{ji}\sigma_i + S_{ji}e^T_{ik}E_k + S_{ji}d^T_{ik}H_k\right) & + & \epsilon_{ik}E_k & + & \gamma_{ik}H_k = \\
& = & e_{ij}S_{ji}\sigma_i & + & \underbrace{\left(\epsilon_{ik} + e_{ij}S_{ji}e^T_{ik}\right)}_{\epsilon^{'}_{ik}}E_k & + & \underbrace{\left(\gamma_{ik} + e_{ij}S_{ji}d^T_{ik}\right)}_{\gamma^{'}_{ik}}H_k.
\end{array}
\tag{2.3.33}
$$

The material tensors $\epsilon'_{ik}, \gamma'_{ik}, \delta'_{ik}, \mu'_{ik}$ (3×3) are expressed as follows:

$$
\begin{array}{ll}
\epsilon'_{ik} = \epsilon_{ik} + e_{ij}S_{ji}e^T_{ik}, & \gamma'_{ik} = \gamma_{ik} + e_{ij}S_{ji}d^T_{ik}, \\
\delta'_{ik} = \delta_{ik} + d_{ij}S_{ji}e^T_{ik}, & \mu'_{ik} = \mu_{ik} + d_{ij}S_{ji}d^T_{ik}.
\end{array}
\tag{2.3.34}
$$

Using the expressions (2.3.29) together with (2.3.30) and (2.3.33), to get the full set of material equations for a piezoelectromagnetic system:

$$
\begin{cases}
(\nabla_{3\times6})_{ij}\sigma_j & = & -\omega^2\rho u_i \\
(\nabla_{3\times6})^T_{jk}u_k & = & S_{ji}\sigma_i + S_{ji}e^T_{ik}E_k + S_{ji}d^T_{ik}H_k \\
(\nabla\times \overset{\leftrightarrow}{I})_{ij}E_j & = & i\omega\left(d_{ij}S_{ji}\sigma_i + \delta^{'}_{ik}E_k + \mu^{'}_{ik}H_k\right) \\
(\nabla\times \overset{\leftrightarrow}{I})_{ij}H_j & = & -i\omega\left(e_{ij}S_{ji}\sigma_i + \epsilon^{'}_{ik}E_k + \gamma^{'}_{ik}H_k\right)
\end{cases}
\tag{2.3.35}
$$

Here, matrix $\nabla_{3\times6}$ has the form:

$$
\nabla_{3\times6} = \begin{pmatrix}
\nabla_x & 0 & 0 & 0 & \nabla_z & \nabla_y \\
0 & \nabla_y & 0 & \nabla_z & 0 & \nabla_x \\
0 & 0 & \nabla_z & \nabla_y & \nabla_x & 0
\end{pmatrix},
\tag{2.3.36}
$$

the $\nabla\times \overset{\leftrightarrow}{I}$ operation is given by

$$
\begin{aligned}
\nabla\times \overset{\leftrightarrow}{I} &= \begin{vmatrix}
\vec{i} & \vec{j} & \vec{k} \\
\nabla_x & \nabla_y & \nabla_z \\
e_xe_x & e_ye_y & e_ze_z
\end{vmatrix} = \vec{i}(\nabla_ye_ze_z - \nabla_ze_ye_y) + \vec{j}(\nabla_ze_xe_x - \nabla_xe_ze_z) + \vec{k}(\nabla_xe_ye_y - \nabla_ye_xe_x) = \\
&= \begin{pmatrix}
0 & -\nabla_z & \nabla_y \\
\nabla_z & 0 & -\nabla_x \\
-\nabla_y & \nabla_z & 0
\end{pmatrix} = \nabla^{rot}_{3\times3}.
\end{aligned}
\tag{2.3.37}
$$

2.3.4 Equations for an infinite nonlocal periodic composite

Within a periodic composite, its physical properties periodically dependent on coordinate $\boldsymbol{r}$. In order to write the material equations for an infinite periodic crystal, it is possible to follow the pattern of the system of equations (2.3.35):

$$\overline{\overline{\boldsymbol{\nabla}}}\,\boldsymbol{v}(\boldsymbol{r}) = \overline{\overline{\boldsymbol{X}}}\,\boldsymbol{v}(\boldsymbol{r}), \tag{2.3.38}$$

with $\overline{\overline{\boldsymbol{\nabla}}}$ matrix containing the derivatives operators and $\overline{\overline{\boldsymbol{X}}}$ is standing for tensors on the right hand side of equations.

In order to proceed with the description of system of equations in matrix form (2.3.38), it is necessary to define the vector-column $\boldsymbol{v}(\boldsymbol{r})$ first. All physical fields involved in the electromagnetoelastic effect - the displacement $\boldsymbol{u}_{(3\times1)}$, the stress $\boldsymbol{\sigma}_{(6\times1)}$, and the components of electric $\boldsymbol{E}_{(3\times1)}$ and magnetic $\boldsymbol{H}_{(3\times1)}$ fields are included in the vector-column $\boldsymbol{v}(\boldsymbol{r})$:

$$\boldsymbol{v}(\boldsymbol{r}) = \begin{pmatrix} \boldsymbol{u}_{3\times1}(\boldsymbol{r}) \\ \boldsymbol{\sigma}_{6\times1}(\boldsymbol{r}) \\ \boldsymbol{E}_{3\times1}(\boldsymbol{r}) \\ \boldsymbol{H}_{3\times1}(\boldsymbol{r}) \end{pmatrix} \tag{2.3.39}$$

With the vector column $\boldsymbol{v}(\boldsymbol{r})$ given by well-defined fields, it is possible to write down the material equations (2.3.35) in the form of the expression (2.3.38):

$$\begin{pmatrix} 0_{3\times3} & \nabla_{3\times6} & 0_{3\times3} & 0_{3\times3} \\ (\nabla_{3\times6})^T & 0_{6\times6} & 0_{6\times3} & 0_{6\times3} \\ 0_{3\times3} & 0_{3\times6} & 0_{3\times3} & \nabla^{rot}_{3\times3} \\ 0_{3\times3} & 0_{3\times6} & -\nabla^{rot}_{3\times3} & 0_{3\times3} \end{pmatrix} \begin{pmatrix} \boldsymbol{u} \\ \boldsymbol{\sigma} \\ \boldsymbol{E} \\ \boldsymbol{H} \end{pmatrix} = \begin{pmatrix} -\omega^2 \overset{\leftrightarrow}{\rho} & 0_{3\times6} & 0_{3\times3} & 0_{3\times3} \\ 0_{6\times3} & \overset{\leftrightarrow}{S} & \overset{\leftrightarrow}{S}\overset{\leftrightarrow}{e}^T & \overset{\leftrightarrow}{S}\overset{\leftrightarrow}{d}^T \\ 0_{3\times3} & -i\omega\, \overset{\leftrightarrow}{e}\overset{\leftrightarrow}{S} & -i\omega\, \overset{\leftrightarrow}{\epsilon}' & -i\omega\, \overset{\leftrightarrow}{\gamma}' \\ 0_{3\times3} & -i\omega\, \overset{\leftrightarrow}{d}\overset{\leftrightarrow}{S} & -i\omega\, \overset{\leftrightarrow}{\delta}' & -i\omega\, \overset{\leftrightarrow}{\mu}' \end{pmatrix} \begin{pmatrix} \boldsymbol{u} \\ \boldsymbol{\sigma} \\ \boldsymbol{E} \\ \boldsymbol{H} \end{pmatrix} \tag{2.3.40}$$

However, one can still represent matrix $\overline{\overline{\boldsymbol{X}}}$ as a product of two matrices - a frequency matrix $\overline{\overline{\boldsymbol{\Omega}}}$ multiplied by the periodic matrix $\overline{\overline{\boldsymbol{A}}}(\boldsymbol{r})$:

$$\begin{pmatrix} 0_{3\times3} & \nabla_{3\times6} & 0_{3\times3} & 0_{3\times3} \\ (\nabla_{3\times6})^T & 0_{6\times6} & 0_{6\times3} & 0_{6\times3} \\ 0_{3\times3} & 0_{3\times6} & 0_{3\times3} & \nabla^{rot}_{3\times3} \\ 0_{3\times3} & 0_{3\times6} & -\nabla^{rot}_{3\times3} & 0_{3\times3} \end{pmatrix} \begin{pmatrix} \boldsymbol{u} \\ \boldsymbol{\sigma} \\ \boldsymbol{E} \\ \boldsymbol{H} \end{pmatrix} = \begin{pmatrix} -\omega^2 \overset{\leftrightarrow}{I}_3 & 0_{3\times6} & 0_{3\times3} & 0_{3\times3} \\ 0_{6\times3} & \overset{\leftrightarrow}{I}_6 & 0_{6\times3} & 0_{6\times3} \\ 0_{3\times3} & 0_{3\times6} & -i\omega\, \overset{\leftrightarrow}{I}_3 & 0_{3\times3} \\ 0_{3\times3} & 0_{3\times6} & 0_{3\times3} & -i\omega\, \overset{\leftrightarrow}{I}_3 \end{pmatrix} \begin{pmatrix} \rho\, \overset{\leftrightarrow}{I}_3 & 0_{3\times6} & 0_{3\times3} & 0_{3\times3} \\ 0_{6\times3} & \overset{\leftrightarrow}{S} & \overset{\leftrightarrow}{S}\overset{\leftrightarrow}{e}^T & \overset{\leftrightarrow}{S}\overset{\leftrightarrow}{d}^T \\ 0_{3\times3} & \overset{\leftrightarrow}{e}\overset{\leftrightarrow}{S} & \overset{\leftrightarrow}{\epsilon}' & \overset{\leftrightarrow}{\gamma}' \\ 0_{3\times3} & \overset{\leftrightarrow}{d}\overset{\leftrightarrow}{S} & \overset{\leftrightarrow}{\delta}' & \overset{\leftrightarrow}{\mu}' \end{pmatrix} \begin{pmatrix} \boldsymbol{u} \\ \boldsymbol{\sigma} \\ \boldsymbol{E} \\ \boldsymbol{H} \end{pmatrix} \tag{2.3.41}$$

The refined form of the generalized equations set (2.3.38) is:

$$\overline{\overline{\boldsymbol{\nabla}}}\boldsymbol{v}(\boldsymbol{r}) = \overline{\overline{\boldsymbol{\Omega}\boldsymbol{A}}}(\boldsymbol{r})\boldsymbol{v}(\boldsymbol{r}), \tag{2.3.42}$$

where the derivatives matrix $\overline{\overline{\boldsymbol{\nabla}}}$ is given by

$$\overline{\overline{\boldsymbol{\nabla}}} = \begin{pmatrix} 0_{3\times3} & \nabla_{3\times6} & 0_{3\times3} & 0_{3\times3} \\ (\nabla_{3\times6})^T & 0_{6\times6} & 0_{6\times3} & 0_{6\times3} \\ 0_{3\times3} & 0_{3\times6} & 0_{3\times3} & \nabla^{rot}_{3\times3} \\ 0_{3\times3} & 0_{3\times6} & -\nabla^{rot}_{3\times3} & 0_{3\times3}, \end{pmatrix} \tag{2.3.43}$$

and the frequency matrix $\overline{\overline{\boldsymbol{\Omega}}}$ has the form

$$\overline{\overline{\boldsymbol{\Omega}}} = \begin{pmatrix} -\omega^2 \overset{\leftrightarrow}{I}_3 & 0_{3\times6} & 0_{3\times3} & 0_{3\times3} \\ 0_{6\times3} & \overset{\leftrightarrow}{I}_6 & 0_{6\times3} & 0_{6\times3} \\ 0_{3\times3} & 0_{3\times6} & -i\omega \overset{\leftrightarrow}{I}_3 & 0_{3\times3} \\ 0_{3\times3} & 0_{3\times6} & 0_{3\times3} & -i\omega \overset{\leftrightarrow}{I}_3 \end{pmatrix} \tag{2.3.44}$$

The periodic matrix $\overline{\overline{\boldsymbol{A}}}(\boldsymbol{r})$ in (2.3.42) contains coordinate-dependent coefficients describing the heterogeneity of the piezoelectromagnetic crystal:

$$\overline{\overline{\boldsymbol{A}}}(\boldsymbol{r}) = \begin{pmatrix} \overset{\leftrightarrow}{\rho}(\boldsymbol{r}) & 0_{3\times6} & 0_{3\times3} & 0_{3\times3} \\ 0_{6\times3} & \overset{\leftrightarrow}{S}(\boldsymbol{r}) & \overset{\leftrightarrow}{S}(\boldsymbol{r})\cdot \overset{\leftrightarrow}{e}^T(\boldsymbol{r}) & \overset{\leftrightarrow}{S}(\boldsymbol{r})\cdot \overset{\leftrightarrow}{d}^T(\boldsymbol{r}) \\ 0_{3\times3} & \overset{\leftrightarrow}{e}(\boldsymbol{r})\cdot \overset{\leftrightarrow}{S}(\boldsymbol{r}) & \overset{\leftrightarrow}{\epsilon}'(\boldsymbol{r}) & \overset{\leftrightarrow}{\gamma}'(\boldsymbol{r}) \\ 0_{3\times3} & \overset{\leftrightarrow}{d}(\boldsymbol{r})\cdot \overset{\leftrightarrow}{S}(\boldsymbol{r}) & \overset{\leftrightarrow}{\delta}'(\boldsymbol{r}) & \overset{\leftrightarrow}{\mu}'(\boldsymbol{r}) \end{pmatrix} \tag{2.3.45}$$

2.3.5 Fourier formalism application

The system of equations describing an infinite periodic piezoelectromagnetic composite is given by (2.3.42). It should be emphasized that matrix of material parameters, $\overline{\overline{\boldsymbol{A}}}(\boldsymbol{r})$, contains coordinate-dependent components; the main goal of the developed formalism is to find an *effective* matrix $\overline{\overline{\boldsymbol{A}}}_{\text{eff}}$ for the homogenized piezoelectromagnetic crystal.

Because of crystal periodicity, matrix $\overline{\overline{\boldsymbol{A}}}(\boldsymbol{r})$ (2.3.45) can be expanded into Fourier series:

$$\overline{\overline{\boldsymbol{A}}}(\boldsymbol{r}) = \sum_{\boldsymbol{G}} \overline{\overline{\boldsymbol{A}}}(\boldsymbol{G}) e^{i\boldsymbol{G}\boldsymbol{r}}. \tag{2.3.46}$$

The vector-column $\boldsymbol{v}(\boldsymbol{r})$ can be expressed as a Bloch function:

$$\boldsymbol{v}(\boldsymbol{r}) = e^{i\boldsymbol{kr}} \sum_{\boldsymbol{G}} \boldsymbol{v}(\boldsymbol{G}) e^{i\boldsymbol{Gr}}. \tag{2.3.47}$$

Here, series can be split into a slow oscillating part with the reciprocal lattice vector $\boldsymbol{G} = 0$ and the terms of the oscillating harmonics ($\boldsymbol{G} \neq 0$):

$$\begin{aligned} \boldsymbol{v}(\boldsymbol{r}) =& e^{i\boldsymbol{kr}} \sum_{\boldsymbol{G}} \boldsymbol{v}(\boldsymbol{G}) e^{i\boldsymbol{Gr}} = e^{i\boldsymbol{kr}} \left(\boldsymbol{v}(\boldsymbol{G}=0) e^{i \cdot 0 \cdot \boldsymbol{r}} + \sum_{\boldsymbol{G}\neq 0} \boldsymbol{v}(\boldsymbol{G}) e^{i\boldsymbol{Gr}} \right) = \\ =& \boldsymbol{v}(\boldsymbol{G}=0) e^{i\boldsymbol{kr}} + e^{i\boldsymbol{kr}} \sum_{\boldsymbol{G}\neq 0} \boldsymbol{v}(\boldsymbol{G}) e^{i\boldsymbol{Gr}}. \end{aligned} \tag{2.3.48}$$

It is convenient to introduce the macroscopic components with $\boldsymbol{G} = 0$:

$$\begin{aligned} \boldsymbol{V}_0 &= \boldsymbol{v}(\boldsymbol{G}=0), \\ \boldsymbol{A}_0 &= \boldsymbol{A}(\boldsymbol{G}=0). \end{aligned} \tag{2.3.49}$$

The macroscopic piezoelectromagnetic field in the crystal can be defined by using the definition (2.3.47) and the newly introduced $\boldsymbol{V}_0$ amplitude:

$$\boldsymbol{V}(\boldsymbol{r}) = e^{i\boldsymbol{kr}} \boldsymbol{V}_0. \tag{2.3.50}$$

As now the expressions for $\overline{\overline{\boldsymbol{A}}}(\boldsymbol{r})$ (2.3.46) and $\boldsymbol{v}(\boldsymbol{r})$ (2.3.48) are described in terms of $\boldsymbol{G}$-components, it is possible to return to (2.3.42) and substitute therein this values. One gets

$$\overline{\overline{\boldsymbol{\nabla}}} \left(e^{i\boldsymbol{kr}} \sum_{\boldsymbol{G}} \boldsymbol{v}(\boldsymbol{G}) e^{i\boldsymbol{Gr}} \right) = \overline{\overline{\boldsymbol{\Omega}}} \left(\sum_{\boldsymbol{G'}} \overline{\overline{\boldsymbol{A}}}(\boldsymbol{G'}) e^{i\boldsymbol{G'r}} \right) \left(e^{i\boldsymbol{kr}} \sum_{\boldsymbol{G''}} \boldsymbol{v}(\boldsymbol{G''}) e^{i\boldsymbol{G''r}} \right). \tag{2.3.51}$$

Grouping exponentials on the right hand side of the equation:

$$\overline{\overline{\boldsymbol{\nabla}}} \left(e^{i\boldsymbol{kr}} \sum_{\boldsymbol{G}} \boldsymbol{v}(\boldsymbol{G}) e^{i\boldsymbol{Gr}} \right) = e^{i\boldsymbol{kr}} \overline{\overline{\boldsymbol{\Omega}}} \sum_{\boldsymbol{G'}} \sum_{\boldsymbol{G''}} \overline{\overline{\boldsymbol{A}}}(\boldsymbol{G'}) \boldsymbol{v}(\boldsymbol{G''}) e^{i(\boldsymbol{G'}+\boldsymbol{G''})\boldsymbol{r}}. \tag{2.3.52}$$

Now let us define the next replacement of indexes:

$$\begin{aligned} \boldsymbol{G} &= \boldsymbol{G'} + \boldsymbol{G''}, \\ \boldsymbol{G'} &= \boldsymbol{G'} + \boldsymbol{G''}. \end{aligned} \tag{2.3.53}$$

Introducing this replacements in the right hand side of previous equations,

$$\overline{\overline{\boldsymbol{\nabla}}} \left(e^{i\boldsymbol{kr}} \sum_{\boldsymbol{G}} \boldsymbol{v}(\boldsymbol{G}) e^{i\boldsymbol{Gr}} \right) = e^{i\boldsymbol{kr}} \overline{\overline{\boldsymbol{\Omega}}} \sum_{\boldsymbol{G''}} \sum_{\boldsymbol{G}-\boldsymbol{G''}} \overline{\overline{\boldsymbol{A}}}(\boldsymbol{G}-\boldsymbol{G''}) \boldsymbol{v}(\boldsymbol{G''}) e^{i\boldsymbol{Gr}}. \tag{2.3.54}$$

Both $\boldsymbol{G}$ and $\boldsymbol{G''}$ tend to infinity, so summation over $\boldsymbol{G}-\boldsymbol{G''}$ can be replaced as just a summation over $\boldsymbol{G}$:

$$\overline{\overline{\boldsymbol{\nabla}}}\left(e^{i\boldsymbol{kr}}\sum_{\boldsymbol{G}}\boldsymbol{v}(\boldsymbol{G})e^{i\boldsymbol{Gr}}\right)=e^{i\boldsymbol{kr}}\overline{\overline{\boldsymbol{\Omega}}}\sum_{\boldsymbol{G}}\sum_{\boldsymbol{G''}}\overline{\overline{\boldsymbol{A}}}(\boldsymbol{G}-\boldsymbol{G''})\boldsymbol{v}(\boldsymbol{G''})e^{i\boldsymbol{Gr}}. \tag{2.3.55}$$

From the inspection of the right part of this expression, it is can be found

$$\overline{\overline{\boldsymbol{\nabla}}}\left(e^{i\boldsymbol{kr}}\sum_{\boldsymbol{G}}\boldsymbol{v}(\boldsymbol{G})e^{i\boldsymbol{Gr}}\right)=e^{i\boldsymbol{kr}}\overline{\overline{\boldsymbol{\Omega}}}\sum_{\boldsymbol{G}}\underbrace{\sum_{\boldsymbol{G''}}\overline{\overline{\boldsymbol{A}}}(\boldsymbol{G}-\boldsymbol{G''})\boldsymbol{v}(\boldsymbol{G''})}_{\boldsymbol{w}(\boldsymbol{G})}e^{i\boldsymbol{Gr}}. \tag{2.3.56}$$

Explicitly, $\boldsymbol{w}(\boldsymbol{G})$ is:

$$\boldsymbol{w}(\boldsymbol{G})=\sum_{\boldsymbol{G''}}\overline{\overline{\boldsymbol{A}}}(\boldsymbol{G}-\boldsymbol{G''})\boldsymbol{v}(\boldsymbol{G''}). \tag{2.3.57}$$

Let consider $\boldsymbol{G}=0$, so the result for $\boldsymbol{w}(\boldsymbol{G})$ will be:

$$\begin{aligned}\boldsymbol{w}(\boldsymbol{G}=0)=&\boldsymbol{W_0}=\sum_{\boldsymbol{G''}}\overline{\overline{\boldsymbol{A}}}(0-G^{''})\boldsymbol{v}(\boldsymbol{G''})=\sum_{\boldsymbol{G}}\overline{\overline{\boldsymbol{A}}}(-\boldsymbol{G})\boldsymbol{v}(\boldsymbol{G})=\\ =&\overline{\overline{\boldsymbol{A}}}(0)\boldsymbol{v}(0)+\sum_{\boldsymbol{G}\neq\boldsymbol{0}}\overline{\overline{\boldsymbol{A}}}(-\boldsymbol{G})\boldsymbol{v}(\boldsymbol{G}).\end{aligned} \tag{2.3.58}$$

Returning to (2.3.56), the result for the gradient operator on the left hand side

$$\begin{gathered}i\sum_{\boldsymbol{G}}e^{i(\boldsymbol{k}+\boldsymbol{G})\boldsymbol{r}}\begin{pmatrix}0_{3\times3} & \overline{\overline{\boldsymbol{K}}}_{3\times6}(\boldsymbol{k}+\boldsymbol{G}) & 0_{3\times3} & 0_{3\times3}\\ (\overline{\overline{\boldsymbol{K}}}_{3\times6}(\boldsymbol{k}+\boldsymbol{G}))^T & 0_{6\times6} & 0_{6\times3} & 0_{6\times3}\\ 0_{3\times3} & 0_{3\times6} & 0_{3\times3} & \overline{\overline{\boldsymbol{K}}}^{rot}_{3\times3}(\boldsymbol{k}+\boldsymbol{G})\\ 0_{3\times3} & 0_{3\times6} & -\overline{\overline{\boldsymbol{K}}}^{rot}_{3\times3}(\boldsymbol{k}+\boldsymbol{G}) & 0_{3\times3}\end{pmatrix}\boldsymbol{v}(\boldsymbol{G})=\\ e^{i\boldsymbol{kr}}\overline{\overline{\boldsymbol{\Omega}}}\sum_{\boldsymbol{G}}\sum_{\boldsymbol{G''}}\overline{\overline{\boldsymbol{A}}}(\boldsymbol{G}-\boldsymbol{G''})\boldsymbol{v}(\boldsymbol{G''})e^{i\boldsymbol{Gr}}.\end{gathered} \tag{2.3.59}$$

To keep compact notation, a $\overline{\overline{\boldsymbol{K}}}_{15\times15}$ tensor, containing components of wave-vector $\boldsymbol{k}$ and reciprocal lattice vectors $\boldsymbol{G}$, is introduced

$$\overline{\overline{\boldsymbol{K}}}_{15\times15}(\boldsymbol{k}+\boldsymbol{G})=\begin{pmatrix}0_{3\times3} & \overline{\overline{\boldsymbol{K}}}_{3\times6}(\boldsymbol{k}+\boldsymbol{G}) & 0_{3\times3} & 0_{3\times3}\\ (\overline{\overline{\boldsymbol{K}}}_{3\times6}(\boldsymbol{k}+\boldsymbol{G}))^T & 0_{6\times6} & 0_{6\times3} & 0_{6\times3}\\ 0_{3\times3} & 0_{3\times6} & 0_{3\times3} & \overline{\overline{\boldsymbol{K}}}^{rot}_{3\times3}(\boldsymbol{k}+\boldsymbol{G})\\ 0_{3\times3} & 0_{3\times6} & -\overline{\overline{\boldsymbol{K}}}^{rot}_{3\times3}(\boldsymbol{k}+\boldsymbol{G}) & 0_{3\times3}\end{pmatrix} \tag{2.3.60}$$

Here the $\overline{\overline{\boldsymbol{K}}}_{3\times 6}$ tensor is:

$$\overline{\overline{\boldsymbol{K}}}_{3\times 6}(\boldsymbol{k}+\boldsymbol{G}) = \begin{pmatrix} k_x+G_x & 0 & 0 & 0 & k_z+G_z & k_y+G_y \\ 0 & k_y+G_y & 0 & k_z+G_z & 0 & k_x+G_x \\ 0 & 0 & k_z+G_z & k_y+G_y & k_x+G_x & 0 \end{pmatrix} \tag{2.3.61}$$

Tensor $\overline{\overline{\boldsymbol{K}}}^{rot}_{3\times 3}(\boldsymbol{k}+\boldsymbol{G})$ is defined as follows:

$$\overline{\overline{\boldsymbol{K}}}^{rot}_{3\times 3}(\boldsymbol{k}+\boldsymbol{G}) = \begin{pmatrix} 0 & -(k_z+G_z) & (k_y+G_y) \\ (k_z+G_z) & 0 & -(k_x+G_x) \\ -(k_y+G_y) & (k_z+G_z) & 0 \end{pmatrix} \tag{2.3.62}$$

To continue the derivation of the effective matrix expression it is necessary to return to expression (2.3.59) and grouping exponentials on the right hand side of equation:

$$i\sum_{\boldsymbol{G}} e^{i(\boldsymbol{k}+\boldsymbol{G})\boldsymbol{r}}\overline{\overline{\boldsymbol{K}}}_{15\times 15}(\boldsymbol{k}+\boldsymbol{G})\boldsymbol{v}(\boldsymbol{G}) = \sum_{\boldsymbol{G}} e^{i(\boldsymbol{k}+\boldsymbol{G})\boldsymbol{r}}\cdot\overline{\overline{\boldsymbol{\Omega}}}\sum_{\boldsymbol{G''}}\overline{\overline{\boldsymbol{A}}}(\boldsymbol{G}-\boldsymbol{G''})\boldsymbol{v}(\boldsymbol{G''}). \tag{2.3.63}$$

Grouping terms, a compact expression is obtained

$$\overline{\overline{\boldsymbol{K}}}_{15\times 15}(\boldsymbol{k}+\boldsymbol{G})\boldsymbol{v}(\boldsymbol{G}) = \frac{\overline{\overline{\boldsymbol{\Omega}}}}{i}\sum_{\boldsymbol{G''}}\overline{\overline{\boldsymbol{A}}}(\boldsymbol{G}-\boldsymbol{G''})\boldsymbol{v}(\boldsymbol{G''}). \tag{2.3.64}$$

Rewriting the left part of this equation as a summation over $\boldsymbol{G''}$ and using Kronecker delta (remember that $\boldsymbol{v}(\boldsymbol{G})\to\boldsymbol{v}(\boldsymbol{G''})$):

$$\sum_{\boldsymbol{G''}}\overline{\overline{\boldsymbol{K}}}_{15\times 15}(\boldsymbol{k}+\boldsymbol{G})\boldsymbol{v}(\boldsymbol{G''})\delta_{\boldsymbol{G},\boldsymbol{G''}} = \frac{\overline{\overline{\boldsymbol{\Omega}}}}{i}\sum_{\boldsymbol{G''}}\overline{\overline{\boldsymbol{A}}}(\boldsymbol{G}-\boldsymbol{G''})\boldsymbol{v}(\boldsymbol{G''}). \tag{2.3.65}$$

Grouping all terms under summation in the left part of the expression, it follows

$$\sum_{\boldsymbol{G''}}\overline{\overline{\boldsymbol{K}}}_{15\times 15}(\boldsymbol{k}+\boldsymbol{G})\boldsymbol{v}(\boldsymbol{G''})\delta_{\boldsymbol{G},\boldsymbol{G''}} - \frac{\overline{\overline{\boldsymbol{\Omega}}}}{i}\overline{\overline{\boldsymbol{A}}}(\boldsymbol{G}-\boldsymbol{G''})\boldsymbol{v}(\boldsymbol{G''}) = 0. \tag{2.3.66}$$

For convenience, index $\boldsymbol{G''}$ is changed to $\boldsymbol{G'}$:

$$\sum_{\boldsymbol{G'}}\left[\overline{\overline{\boldsymbol{K}}}_{15\times 15}(\boldsymbol{k}+\boldsymbol{G})\delta_{\boldsymbol{G},\boldsymbol{G'}} - \frac{\overline{\overline{\boldsymbol{\Omega}}}}{i}\overline{\overline{\boldsymbol{A}}}(\boldsymbol{G}-\boldsymbol{G'})\right]\boldsymbol{v}(\boldsymbol{G'}) = 0. \tag{2.3.67}$$

2.3.6 Dynamic piezoelectromagnetic matrix expression

The expression under summation in (2.3.67) is the dynamic piezoelectromagnetic matrix:

$$\overline{\overline{\boldsymbol{D}}}(\boldsymbol{k},\boldsymbol{G},\boldsymbol{G'}) = \overline{\overline{\boldsymbol{K}}}_{15\times 15}(\boldsymbol{k}+\boldsymbol{G})\delta_{\boldsymbol{G},\boldsymbol{G'}} - \frac{\overline{\overline{\boldsymbol{\Omega}}}}{i}\overline{\overline{\boldsymbol{A}}}(\boldsymbol{G}-\boldsymbol{G'}). \tag{2.3.68}$$

Using the dynamic matrix, the expression (2.3.67) can be rewritten as:

$$\sum_{\boldsymbol{G'}} \overline{\overline{\boldsymbol{D}}}(\boldsymbol{k},\boldsymbol{G},\boldsymbol{G'})\boldsymbol{v}(\boldsymbol{G'}) = 0. \tag{2.3.69}$$

It is worth to note that, in principle, one can solve the problem of system eigenvalues directly by restricting the infinite dynamic matrix to a very large square matrix with a further diagonalization. For a sufficient number of plane waves in the Fourier expansion, the numerical solution is rather difficult.

In order to proceed, the dynamic matrix (2.3.69) can be split into the slowly varying terms (the macroscopic, one with $\boldsymbol{G}=0$) and the other terms having $\boldsymbol{G}\neq 0$:

$$\overline{\overline{\boldsymbol{D}}}(\boldsymbol{k},\boldsymbol{G},0)\boldsymbol{v}(0) + \sum_{\boldsymbol{G'}\neq 0} \overline{\overline{\boldsymbol{D}}}(\boldsymbol{k},\boldsymbol{G},\boldsymbol{G'})\boldsymbol{v}(\boldsymbol{G'}) = 0. \tag{2.3.70}$$

For $\boldsymbol{G}\neq 0$,

$$\overline{\overline{\boldsymbol{D}}}(\boldsymbol{k},\boldsymbol{G},0)\boldsymbol{V_0} + \sum_{\boldsymbol{G'}\neq 0} \overline{\overline{\boldsymbol{D}}}_s(\boldsymbol{k},\boldsymbol{G},\boldsymbol{G'})\boldsymbol{v}(\boldsymbol{G'}) = 0, \tag{2.3.71}$$

where $\overline{\overline{\boldsymbol{D}}}_s(\boldsymbol{k},\boldsymbol{G},\boldsymbol{G'})$ is a submatrix of $\overline{\overline{\boldsymbol{D}}}(\boldsymbol{k},\boldsymbol{G},\boldsymbol{G'})$ that results from eliminating the row $\boldsymbol{G}=0$ and the column $\boldsymbol{G'}=0$.

Now let us establish the relation between the macroscopic field $\boldsymbol{V}_0$ and $\boldsymbol{v}(\boldsymbol{G'})$:

$$\sum_{\boldsymbol{G'}\neq 0} \overline{\overline{\boldsymbol{D}}}_s(\boldsymbol{k},\boldsymbol{G},\boldsymbol{G'})\boldsymbol{v}(\boldsymbol{G'}) \;=\; -\overline{\overline{\boldsymbol{D}}}(\boldsymbol{k},\boldsymbol{G},0)\boldsymbol{V_0}. \tag{2.3.72}$$

Explicitly, the expression for $\boldsymbol{v}(\boldsymbol{G'})$ is:

$$\boldsymbol{v}(\boldsymbol{G'}) \;=\; -\sum_{\boldsymbol{G}\neq 0} \overline{\overline{\boldsymbol{D}}}_s^{-1}(\boldsymbol{k},\boldsymbol{G'},\boldsymbol{G})\overline{\overline{\boldsymbol{D}}}(\boldsymbol{k},\boldsymbol{G},0)\boldsymbol{V_0}. \tag{2.3.73}$$

A proved relation that links an inverse dynamic matrix $\overline{\overline{\boldsymbol{D}}}(\boldsymbol{k},\boldsymbol{G},\boldsymbol{G'})$ with the inverse sub-matrix $\overline{\overline{\boldsymbol{D}}}_s(\boldsymbol{k},\boldsymbol{G},\boldsymbol{G'})$ [111] will be used:

$$\overline{\overline{\boldsymbol{D}}}_s^{-1}(\boldsymbol{k},\boldsymbol{G'},\boldsymbol{G}) \;=\; \overline{\overline{\boldsymbol{D}}}^{-1}(\boldsymbol{k},\boldsymbol{G'},\boldsymbol{G}) - \overline{\overline{\boldsymbol{D}}}^{-1}(\boldsymbol{k},\boldsymbol{G'},0)\left(\overline{\overline{\boldsymbol{D}}}^{-1}(\boldsymbol{k},0,0)\right)^{-1}\overline{\overline{\boldsymbol{D}}}^{-1}(\boldsymbol{k},0,\boldsymbol{G}). \tag{2.3.74}$$

The relation (2.3.74) can be substituted into (2.3.73) to get:

$$\begin{aligned}\boldsymbol{v}(\boldsymbol{G'}) \;&=\; -\sum_{\boldsymbol{G}\neq 0}\left(\overline{\overline{\boldsymbol{D}}}^{-1}(\boldsymbol{k},\boldsymbol{G'},\boldsymbol{G}) - \overline{\overline{\boldsymbol{D}}}^{-1}(\boldsymbol{k},\boldsymbol{G'},0)\left(\overline{\overline{\boldsymbol{D}}}^{-1}(\boldsymbol{k},0,0)\right)^{-1} \times\right.\\ &\left.\times\;\; \overline{\overline{\boldsymbol{D}}}^{-1}(\boldsymbol{k},0,\boldsymbol{G})\right)\overline{\overline{\boldsymbol{D}}}(\boldsymbol{k},\boldsymbol{G},0)\boldsymbol{V_0}.\end{aligned} \tag{2.3.75}$$

The matrix multiplication gives the following expression for $\boldsymbol{v}(\boldsymbol{G'})$:

$$\begin{aligned}\boldsymbol{v}(\boldsymbol{G'}) \;&=\; \underbrace{-\sum_{\boldsymbol{G}\neq 0}\overline{\overline{\boldsymbol{D}}}^{-1}(\boldsymbol{k},\boldsymbol{G'},\boldsymbol{G})\overline{\overline{\boldsymbol{D}}}(k,\boldsymbol{G},0)\boldsymbol{V_0}+}_{\overline{\overline{\boldsymbol{I}}}\delta_{\boldsymbol{G'},0}\boldsymbol{V}_0}\\ &+\;\sum_{\boldsymbol{G}\neq 0}\overline{\overline{\boldsymbol{D}}}^{-1}(\boldsymbol{k},\boldsymbol{G'},0)\left(\overline{\overline{\boldsymbol{D}}}^{-1}(\boldsymbol{k},0,0)\right)^{-1}\overline{\overline{\boldsymbol{D}}}^{-1}(\boldsymbol{k},0,\boldsymbol{G})\overline{\overline{\boldsymbol{D}}}(\boldsymbol{k},\boldsymbol{G},0)\boldsymbol{V_0}.\end{aligned} \tag{2.3.76}$$

The first term on the right hand side of previous equation vanishes because $\boldsymbol{v}(\boldsymbol{G'})$ is defined only for non-zero components of the Fourier expansion; the second summation disappears giving the unity matrix. Finally, for $\boldsymbol{v}(\boldsymbol{G})$ it is possible to write:

$$\boldsymbol{v}(\boldsymbol{G}) \;=\; \overline{\overline{\boldsymbol{D}}}^{-1}(\boldsymbol{k},\boldsymbol{G},0)\left(\overline{\overline{\boldsymbol{D}}}^{-1}(\boldsymbol{k},0,0)\right)^{-1}\boldsymbol{V_0}. \tag{2.3.77}$$

Substituting the found expression for $\boldsymbol{v}(\boldsymbol{G})$ into equation (2.3.58) to get:

$$\boldsymbol{W_0} = \sum_{\boldsymbol{G}}\overline{\overline{\boldsymbol{A}}}(-\boldsymbol{G})\overline{\overline{\boldsymbol{D}}}^{-1}(\boldsymbol{k},\boldsymbol{G},0)\left(\overline{\overline{\boldsymbol{D}}}^{-1}(\boldsymbol{k},0,0)\right)^{-1}\boldsymbol{V_0}. \tag{2.3.78}$$

To proceed further the next property is used:

$$\sum_{\boldsymbol{G'}}\overline{\overline{\boldsymbol{D}}}(\boldsymbol{k},\boldsymbol{G},\boldsymbol{G'})\overline{\overline{\boldsymbol{D}}}^{-1}(\boldsymbol{k},\boldsymbol{G'},\boldsymbol{G''}) = \overline{\overline{\boldsymbol{I}}}\delta_{\boldsymbol{G},\boldsymbol{G''}}. \tag{2.3.79}$$

Let us use (2.3.79) and the dynamic matrix in the form (2.3.68). One obtains

$$\sum_{\boldsymbol{G'}}\left(\overline{\overline{\boldsymbol{K}}}_{15\times 15}(\boldsymbol{k}+\boldsymbol{G})\delta_{\boldsymbol{G},\boldsymbol{G'}} - \frac{\overline{\overline{\boldsymbol{\Omega}}}}{i}\overline{\overline{\boldsymbol{A}}}(\boldsymbol{G}-\boldsymbol{G'})\right)\overline{\overline{\boldsymbol{D}}}^{-1}(\boldsymbol{k},\boldsymbol{G'},\boldsymbol{G''}) = \overline{\overline{\boldsymbol{I}}}\delta_{\boldsymbol{G},\boldsymbol{G''}}. \tag{2.3.80}$$

Hence,

$$\overline{\overline{\boldsymbol{K}}}_{15\times 15}(\boldsymbol{k}+\boldsymbol{G})\overline{\overline{\boldsymbol{D}}}^{-1}(\boldsymbol{k},\boldsymbol{G},\boldsymbol{G''}) - \sum_{\boldsymbol{G'}}\frac{\overline{\overline{\boldsymbol{\Omega}}}}{i}\overline{\overline{\boldsymbol{A}}}(\boldsymbol{G}-\boldsymbol{G'})\overline{\overline{\boldsymbol{D}}}^{-1}(\boldsymbol{k},\boldsymbol{G'},\boldsymbol{G''}) = \overline{\overline{\boldsymbol{I}}}\delta_{\boldsymbol{G},\boldsymbol{G''}}. \tag{2.3.81}$$

The proposed approach is concerned about reaching an effective matrix expression that is dependent only on the central block ($\boldsymbol{G} = 0$, $\boldsymbol{G''} = 0$) of the dynamic matrix.

Justification of taking only *one* block from the theoretically infinite dynamic matrix is that central block is *already* expressed in terms of non-zero reciprocal lattice vectors $\boldsymbol{G} \neq 0$. In other words, spatial dispersion modes inside the medium are already expressed in terms of slow-oscillating part with $(\boldsymbol{G} = 0, \boldsymbol{G'} = 0)$. This feature is a very important property of the theory and it allows to provide feasible calculation of the effective parameters even beyond the long wavelength limit. Considering $\boldsymbol{G} = 0$ and $\boldsymbol{G''} = 0$ gives

$$\overline{\overline{\boldsymbol{K}}}_{15\times15}(\boldsymbol{k})\overline{\overline{\boldsymbol{D}}}^{-1}(\boldsymbol{k},0,0) - \sum_{\boldsymbol{G'}} \frac{\overline{\overline{\boldsymbol{\Omega}}}}{i}\overline{\overline{\boldsymbol{A}}}(-\boldsymbol{G'})\overline{\overline{\boldsymbol{D}}}^{-1}(\boldsymbol{k},\boldsymbol{G'},0) = \overline{\overline{\boldsymbol{I}}}. \tag{2.3.82}$$

Moving summation to the other side and changing index $\boldsymbol{G'} \to \boldsymbol{G}$, one gets

$$\sum_{\boldsymbol{G}} \frac{\overline{\overline{\boldsymbol{\Omega}}}}{i}\overline{\overline{\boldsymbol{A}}}(-\boldsymbol{G})\overline{\overline{\boldsymbol{D}}}^{-1}(\boldsymbol{k},\boldsymbol{G},0) = \overline{\overline{\boldsymbol{K}}}_{15\times15}(\boldsymbol{k})\overline{\overline{\boldsymbol{D}}}^{-1}(\boldsymbol{k},0,0) - \overline{\overline{\boldsymbol{I}}}, \tag{2.3.83}$$

and finally,

$$\sum_{\boldsymbol{G}} \overline{\overline{\boldsymbol{A}}}(-\boldsymbol{G})\overline{\overline{\boldsymbol{D}}}^{-1}(\boldsymbol{k},\boldsymbol{G},0) = i\overline{\overline{\boldsymbol{\Omega}}}^{-1}\overline{\overline{\boldsymbol{K}}}_{15\times15}(\boldsymbol{k})\overline{\overline{\boldsymbol{D}}}^{-1}(\boldsymbol{k},0,0) - i\overline{\overline{\boldsymbol{\Omega}}}^{-1}. \tag{2.3.84}$$

2.3.7 Effective nonlocal response matrix

Looking back to the expression for $\boldsymbol{W_0}$ (2.3.78) it is noticeable that equation (2.3.84) is just a part of it:

$$\boldsymbol{W_0} = \left(i\overline{\overline{\boldsymbol{\Omega}}}^{-1}\overline{\overline{\boldsymbol{K}}}_{15\times15}(\boldsymbol{k})\overline{\overline{\boldsymbol{D}}}^{-1}(\boldsymbol{k},0,0) - i\overline{\overline{\boldsymbol{\Omega}}}^{-1}\right)\left(\overline{\overline{\boldsymbol{D}}}^{-1}(\boldsymbol{k},0,0)\right)^{-1}\boldsymbol{V_0}. \tag{2.3.85}$$

Grouping and simplifying terms gives:

$$\boldsymbol{W_0} = \left(i\overline{\overline{\boldsymbol{\Omega}}}^{-1}\overline{\overline{\boldsymbol{K}}}_{15\times15}(\boldsymbol{k}) - i\overline{\overline{\boldsymbol{\Omega}}}^{-1}\left(\overline{\overline{\boldsymbol{D}}}^{-1}(\boldsymbol{k},0,0)\right)^{-1}\right)\boldsymbol{V_0}. \tag{2.3.86}$$

On the other side, the relation between macroscopic fields turns out to be determined by an effective nonlocal matrix:

$$\boldsymbol{W}_0 = \overline{\overline{\boldsymbol{A}}}_{\text{eff}}(\boldsymbol{k})\boldsymbol{V}_0. \tag{2.3.87}$$

The effective piezoelectromagnetic response matrix $\overline{\overline{\boldsymbol{A}}}_{\text{eff}}(\boldsymbol{k})$ links the macroscopic fields $\boldsymbol{W_0}$ and $\boldsymbol{V_0}$ and is given by:

$$\overline{\overline{\boldsymbol{A}}}_{\text{eff}}(\boldsymbol{k}) = i\overline{\overline{\boldsymbol{\Omega}}}^{-1}\overline{\overline{\boldsymbol{K}}}_{15\times15}(\boldsymbol{k}) - i\overline{\overline{\boldsymbol{\Omega}}}^{-1}\left(\overline{\overline{\boldsymbol{D}}}^{-1}(\boldsymbol{k},0,0)\right)^{-1}. \tag{2.3.88}$$

The final expression for the effective response matrix $\overline{\overline{\boldsymbol{A}}}_{\text{eff}}(\boldsymbol{k},\omega)$ in the case of a homogenized piezoelectromagnetic crystal is:

$$\overline{\overline{\boldsymbol{A}}}_{\text{eff}}(\boldsymbol{k},\omega) = i\overline{\overline{\boldsymbol{\Omega}}}^{-1}\left\{-\left[\overline{\overline{\boldsymbol{D}}}^{-1}(\boldsymbol{k},0,0)\right]^{-1} + \begin{pmatrix} 0_{3\times3} & \overline{\overline{\overline{\boldsymbol{K}}}}_{3\times6} & 0_{3\times3} & 0_{3\times3} \\ (\overline{\overline{\overline{\boldsymbol{K}}}}_{3\times6})^T & 0_{6\times6} & 0_{6\times3} & 0_{6\times3} \\ 0_{3\times3} & 0_{3\times6} & 0_{3\times3} & \overline{\overline{\boldsymbol{K}}}^{rot}_{3\times3} \\ 0_{3\times3} & 0_{3\times6} & -\overline{\overline{\boldsymbol{K}}}^{rot}_{3\times3} & 0_{3\times3} \end{pmatrix}\right\} \tag{2.3.89}$$

For a given $\boldsymbol{k}$ and frequency ω the effective nonlocal piezoelectromagnetic matrix $\overline{\overline{\boldsymbol{A}}}^{\text{PEM}}_{\text{eff,NL}}(\boldsymbol{k},\omega)$ contains all coefficients of the homogenized nonlocal electromagnetoelastic crystal in the next form:

$$\overline{\overline{\boldsymbol{A}}}^{\text{PEM}}_{\text{eff,NL}}(\boldsymbol{k},\omega) = \begin{pmatrix} \overset{\leftrightarrow}{\boldsymbol{\rho}}(\boldsymbol{k},\omega) & 0_{3\times6} & 0_{3\times3} & 0_{3\times3} \\ 0_{6\times3} & \overset{\leftrightarrow}{\boldsymbol{S}}(\boldsymbol{k},\omega) & \overset{\leftrightarrow}{\boldsymbol{S}}(\boldsymbol{k},\omega)\cdot\overset{\leftrightarrow}{\boldsymbol{e}}^T(\boldsymbol{k},\omega) & \overset{\leftrightarrow}{\boldsymbol{S}}(\boldsymbol{k},\omega)\cdot\overset{\leftrightarrow}{\boldsymbol{d}}^T(\boldsymbol{k},\omega) \\ 0_{3\times3} & \overset{\leftrightarrow}{\boldsymbol{e}}(\boldsymbol{k},\omega)\cdot\overset{\leftrightarrow}{\boldsymbol{S}}(\boldsymbol{k},\omega) & \overset{\leftrightarrow}{\boldsymbol{\epsilon}'}(\boldsymbol{k},\omega) & \overset{\leftrightarrow}{\boldsymbol{\gamma}'}(\boldsymbol{k},\omega) \\ 0_{3\times3} & \overset{\leftrightarrow}{\boldsymbol{d}}(\boldsymbol{k},\omega)\cdot\overset{\leftrightarrow}{\boldsymbol{S}}(\boldsymbol{k},\omega) & \overset{\leftrightarrow}{\boldsymbol{\delta}'}(\boldsymbol{k},\omega) & \overset{\leftrightarrow}{\boldsymbol{\mu}'}(\boldsymbol{k},\omega) \end{pmatrix} \tag{2.3.90}$$

In fact, the obtained matrix of 15 × 15 size describes the relation between macroscopic fields inside the homogenized crystal in terms of the nonlocal response.

2.3.8 Form factor division approach and average field approximation

The effective nonlocal response tensor $\overline{\overline{\boldsymbol{A}}}_{\text{eff}}(\boldsymbol{k}(\omega),\omega)$ is explicitly given by the expression (2.3.89) and $\overline{\overline{\boldsymbol{D}}}^{-1}(\boldsymbol{k};0,0)$ is a 15×15 block, obtained from the inverse $\overline{\overline{\boldsymbol{D}}}^{-1}(\boldsymbol{k};\boldsymbol{G},\boldsymbol{G}')$ of the infinite-size matrix,

$$\overline{\overline{\boldsymbol{D}}}(\boldsymbol{k},\boldsymbol{G},\boldsymbol{G}') = (\overline{\overline{\overline{\boldsymbol{K}}}}_{15\times15}(\boldsymbol{k}+\boldsymbol{G}) + i\overline{\overline{\overline{\boldsymbol{\Omega}\boldsymbol{A}_{\boldsymbol{b}}}}})\delta_{\boldsymbol{G},\boldsymbol{G'}} + i\overline{\overline{\boldsymbol{\Omega}}}\Delta\overline{\overline{\boldsymbol{A}}}F(\boldsymbol{G}-\boldsymbol{G'}), \tag{2.3.91}$$

where $\boldsymbol{G}$ and $\boldsymbol{G}'$ are vectors of the reciprocal lattice, $\delta_{\boldsymbol{G},\boldsymbol{G}'}$ stands for the Kronecker delta, and $\overline{\overline{\boldsymbol{A}}}(\boldsymbol{G}-\boldsymbol{G}')$ is the Fourier coefficient for 15×15 matrix $\overline{\overline{\boldsymbol{A}}}(\boldsymbol{r})$ (2.3.45) which is a periodic function of the coordinate $\boldsymbol{r}$:

$$\overline{\overline{\boldsymbol{A}}}(\boldsymbol{G}-\boldsymbol{G}') = \frac{1}{V_c}\int\limits_{V_c}\overline{\overline{\boldsymbol{A}}}(\boldsymbol{r})e^{-i(\boldsymbol{G}-\boldsymbol{G}')\cdot\boldsymbol{r}}d\boldsymbol{r}, \tag{2.3.92}$$

where V_c is the volume of the piezoelectromagnetic crystal unit cell.

It should be noted that in obtaining the matrix block $\overline{\overline{\boldsymbol{D}}}^{-1}(\boldsymbol{k};0,0)$ appearing in Eq. (2.3.89) for the effective nonlocal response tensor $\overline{\overline{\boldsymbol{A}}}_{\text{eff}}(\boldsymbol{k}(\omega),\omega)$, it is not necessary to calculate the complete inverse matrix $\overline{\overline{\boldsymbol{D}}}^{-1}(\boldsymbol{k};\boldsymbol{G},\boldsymbol{G}')$, but the block column $\overline{\overline{\boldsymbol{D}}}^{-1}(\boldsymbol{k};\boldsymbol{G},0)$, which corresponds to the linear system of algebraic equations:

$$\sum_{\boldsymbol{G}'}\overline{\overline{\boldsymbol{D}}}(\boldsymbol{k},\boldsymbol{G},\boldsymbol{G}')\overline{\overline{\boldsymbol{D}}}^{-1}(\boldsymbol{k},\boldsymbol{G}',0)=\overline{\overline{\boldsymbol{I}}}\delta_{\boldsymbol{G},0}, \tag{2.3.93}$$

where $\overline{\overline{\boldsymbol{I}}}$ is 15×15 unity matrix.

For a homogenized piezoelectromagnetic crystal, the Fourier coefficients (2.3.92) appearing in Eq. (2.3.91) can be written as

$$\overline{\overline{\boldsymbol{A}}}(\boldsymbol{G}-\boldsymbol{G}')=\overline{\overline{\boldsymbol{A}}}_b\delta_{\boldsymbol{G},\boldsymbol{G}'}+\Delta\overline{\overline{\boldsymbol{A}}}F(\boldsymbol{G}-\boldsymbol{G}'), \tag{2.3.94}$$

where $\Delta\overline{\overline{\boldsymbol{A}}}=\overline{\overline{\boldsymbol{A}}}_a-\overline{\overline{\boldsymbol{A}}}_b$, $\overline{\overline{\boldsymbol{A}}}_a$ and $\overline{\overline{\boldsymbol{A}}}_b$ are respectively the piezoelectromagnetic response matrices of the inclusion and host materials inside the unit cell, and $F(\boldsymbol{G})$ is the form factor of the inclusion:

$$F(\boldsymbol{G})=\frac{1}{V_c}\int\limits_{V_{\text{inc}}}\exp[-i\boldsymbol{G}\cdot\boldsymbol{r}]d\boldsymbol{r}, \tag{2.3.95}$$

where V_{inc} is the volume of the inclusion.

Substituting (2.3.91) and (2.3.94) into (2.3.93), one gets

$$\overline{\overline{\boldsymbol{T}}}(\boldsymbol{G})\overline{\overline{\boldsymbol{D}}}^{-1}(\boldsymbol{k},\boldsymbol{G},0)+i\overline{\overline{\boldsymbol{\Omega}}}\Delta\overline{\overline{\boldsymbol{A}}}\sum_{\boldsymbol{G}'}F(\boldsymbol{G}-\boldsymbol{G}')\overline{\overline{\boldsymbol{D}}}^{-1}(\boldsymbol{k},\boldsymbol{G}',0)=\overline{\overline{\boldsymbol{I}}}\delta_{\boldsymbol{G},0}, \tag{2.3.96}$$

where, $\overline{\overline{\boldsymbol{T}}}(\boldsymbol{G})$ is:

$$\overline{\overline{\boldsymbol{T}}}(\boldsymbol{G})=\overline{\overline{\boldsymbol{K}}}_{15\times 15}(\boldsymbol{k}+\boldsymbol{G})+i\overline{\overline{\boldsymbol{\Omega}\boldsymbol{A_b}}}. \tag{2.3.97}$$

Multiplying equation (2.3.96) by $\overline{\overline{\boldsymbol{T}}}^{-1}(\boldsymbol{G})$, it follows

$$\overline{\overline{\boldsymbol{D}}}^{-1}(\boldsymbol{k},\boldsymbol{G},0)+i\overline{\overline{\boldsymbol{T}}}^{-1}(\boldsymbol{G})\overline{\overline{\boldsymbol{\Omega}}}\Delta\overline{\overline{\boldsymbol{A}}}\sum_{\boldsymbol{G}'}F(\boldsymbol{G}-\boldsymbol{G}')\overline{\overline{\boldsymbol{D}}}^{-1}(\boldsymbol{k},\boldsymbol{G}',0)=\overline{\overline{\boldsymbol{T}}}^{-1}(\boldsymbol{G})\delta_{\boldsymbol{G},0}. \tag{2.3.98}$$

In order to simplify the numerical calculation process, the so called form-factor division approach (FFDA) shall be applied. According to the FFDA, the inclusion is being divided into a finite number n of small volumes V_j $(j=1,2,...,n)$, compared with V_c, and expand the form factor $F(\boldsymbol{G})$ (2.3.95) as:

$$F(\boldsymbol{G})=\sum_{j=1}^{n}e^{-i\boldsymbol{G}\cdot\boldsymbol{r}_j}F_j(\boldsymbol{G}), \tag{2.3.99}$$

where $F_j(\boldsymbol{G})$ denotes the form factor of the j-th small volume, and the vector $\boldsymbol{r}_j$ indicates the position of its centroid. Assuming that all the small volumes are identical ($F_j(\boldsymbol{G}) = F_v(\boldsymbol{G})$, $j = 1, ..., n$), it is possible to write $F(\boldsymbol{G})$ as

$$F(\boldsymbol{G}) = F_v(\boldsymbol{G})\sum_{j=1}^{n} e^{-i\boldsymbol{G}\cdot\boldsymbol{r}_j}, \tag{2.3.100}$$

where

$$F_v(\boldsymbol{G}) = \frac{1}{V_c}\int\limits_{v} \exp[-i\boldsymbol{G}\cdot\boldsymbol{r}]d\boldsymbol{r}, \tag{2.3.101}$$

and v is a small volume, which is here assumed to have the form of a cube ($v = V_{cube}$). The accuracy in calculating the effective parameters strongly depends on the cubes number and volume ratio $V_{cube} \ll V_c$. Making cubes smaller results into the more accurate calculation. On the other hand, in the case of many cubes involved, the calculations are being carried out slowly, but still faster than a direct inversion of a huge matrix.

Now, Eq. (2.3.98) can be rewritten in the form

$$\overline{\overline{\boldsymbol{D}}}^{-1}(\boldsymbol{k},\boldsymbol{G},0) + i\overline{\overline{\boldsymbol{T}}}^{-1}(\boldsymbol{G})\overline{\overline{\boldsymbol{\Omega}}}\Delta\overline{\overline{\boldsymbol{A}}}\sum_{j=1}^{n}\sum_{\boldsymbol{G}'} F_v(\boldsymbol{G}-\boldsymbol{G}')e^{-i(\boldsymbol{G}-\boldsymbol{G}')\cdot\boldsymbol{r}_j}\overline{\overline{\boldsymbol{D}}}^{-1}(\boldsymbol{k},\boldsymbol{G}',0) = \overline{\overline{\boldsymbol{T}}}^{-1}(\boldsymbol{G})\delta_{\boldsymbol{G},0}. \tag{2.3.102}$$

Using Eq. (2.3.101) to express $F_v(\boldsymbol{G}-\boldsymbol{G}')$ of (2.3.102) as an integral over the small volume v and introducing the tensor

$$\overline{\overline{\boldsymbol{P}}}_j(\boldsymbol{r}) = \sum_{\boldsymbol{G}'} e^{i\boldsymbol{G}'\cdot\boldsymbol{r}_j}e^{i\boldsymbol{G}'\cdot\boldsymbol{r}}\overline{\overline{\boldsymbol{D}}}^{-1}(\boldsymbol{k},\boldsymbol{G}',0), \tag{2.3.103}$$

Eq. (2.3.102) can be expressed in the form

$$\overline{\overline{\boldsymbol{D}}}^{-1}(\boldsymbol{k},\boldsymbol{G},0) + i\frac{1}{V_c}\overline{\overline{\boldsymbol{T}}}^{-1}(\boldsymbol{G})\overline{\overline{\boldsymbol{\Omega}}}\Delta\overline{\overline{\boldsymbol{A}}}\sum_{j=1}^{n}\int\limits_{V_{cube}} e^{-i\boldsymbol{G}\cdot\boldsymbol{r}_j}e^{-i\boldsymbol{G}\cdot\boldsymbol{r}'}\overline{\overline{\boldsymbol{P}}}_j(\boldsymbol{r}')d\boldsymbol{r}' = \overline{\overline{\boldsymbol{T}}}^{-1}(\boldsymbol{G})\delta_{\boldsymbol{G},0}. \tag{2.3.104}$$

Multiplying both sides of Eq. (2.3.104) by $e^{i\boldsymbol{G}\cdot\boldsymbol{r}_i+i\boldsymbol{G}\cdot\boldsymbol{r}}$ and then summing over the vectors $\boldsymbol{G}$, a system of integral equations for the tensors $\overline{\overline{\boldsymbol{P}}}_i(\boldsymbol{r})$ ($i = 1, \ldots, n$) is obtained:

$$\overline{\overline{\boldsymbol{P}}}_i(\boldsymbol{r}) + i\frac{1}{V_c}\sum_{\boldsymbol{G}} e^{i\boldsymbol{G}\cdot\boldsymbol{r}_i+i\boldsymbol{G}\cdot\boldsymbol{r}}\overline{\overline{\boldsymbol{T}}}^{-1}(\boldsymbol{G})\overline{\overline{\boldsymbol{\Omega}}}\Delta\overline{\overline{\boldsymbol{A}}}\sum_{j=1}^{n}\int\limits_{V_{cube}} e^{-i\boldsymbol{G}\cdot\boldsymbol{r}_j-i\boldsymbol{G}\cdot\boldsymbol{r}'}\overline{\overline{\boldsymbol{P}}}_j(\boldsymbol{r}')d\boldsymbol{r}' = \overline{\overline{\boldsymbol{T}}}^{-1}(0). \tag{2.3.105}$$

Averaging both sides of Eq. (2.3.105) over the i-th cube volume, one gets

$$< \overline{\overline{\boldsymbol{P}}}_i > + \sum_{j=1}^{n}\int\limits_{V_{cube}}\int\limits_{V_{cube}} \overline{\overline{\boldsymbol{K}}}_{ij}(\boldsymbol{r}-\boldsymbol{r}')\overline{\overline{\boldsymbol{P}}}_j(\boldsymbol{r}')d\boldsymbol{r}d\boldsymbol{r}' = \overline{\overline{\boldsymbol{T}}}^{-1}(0), \tag{2.3.106}$$

where

$$< \overline{\overline{\boldsymbol{P}}}_i >= \frac{1}{V_{cube}} \int\limits_{V_{cube}} \overline{\overline{\boldsymbol{P}}}_i(\boldsymbol{r}) d\boldsymbol{r}, \tag{2.3.107}$$

and

$$\overline{\overline{\boldsymbol{K}}}_{ij}(\boldsymbol{r}-\boldsymbol{r}') = \frac{i}{V_c V_{cube}} \sum_{\boldsymbol{G}} e^{i\boldsymbol{G}\cdot(\boldsymbol{r}_i-\boldsymbol{r}_j)+i\boldsymbol{G}\cdot(\boldsymbol{r}-\boldsymbol{r}')} \overline{\overline{\boldsymbol{T}}}^{-1}(\boldsymbol{G}) \overline{\overline{\boldsymbol{\Omega}}} \Delta \overline{\overline{\boldsymbol{A}}}. \tag{2.3.108}$$

In the case of sufficiently-small volumes ($V_{cube} \ll V_c$), $\overline{\overline{\boldsymbol{P}}}_j(\boldsymbol{r}')$ in (2.3.106) can be approximated by its average, namely $< \overline{\overline{\boldsymbol{P}}}_j >$. Consequently, the coupled integral equations in (2.3.106) become an algebraic system of n equations for the average tensors $< \overline{\overline{\boldsymbol{P}}}_i >$:

$$\sum_{j=1}^{n} \left(\int\limits_{V_{cube}} \int\limits_{V_{cube}} \overline{\overline{\boldsymbol{K}}}_{ij}(\boldsymbol{r}-\boldsymbol{r}') \right) d\boldsymbol{r} d\boldsymbol{r}' < \overline{\overline{\boldsymbol{P}}}_j > + < \overline{\overline{\boldsymbol{P}}}_i >= \overline{\overline{\boldsymbol{T}}}^{-1}(0). \tag{2.3.109}$$

Finally, using Eq. (2.3.108), the system of equations for the tensors $< \overline{\overline{\boldsymbol{P}}}_i >$ can be written as

$$< \overline{\overline{\boldsymbol{P}}}_i > + i\frac{V_c}{V_{cube}} \sum_{j=1}^{n} \sum_{\boldsymbol{G}} e^{i\boldsymbol{G}\cdot(\boldsymbol{r}_i-\boldsymbol{r}_j)} F_v(-\boldsymbol{G}) F_v(\boldsymbol{G}) \overline{\overline{\boldsymbol{T}}}^{-1}(\boldsymbol{G}) \overline{\overline{\boldsymbol{\Omega}}} \Delta \overline{\overline{\boldsymbol{A}}} < \overline{\overline{\boldsymbol{P}}}_j >= \overline{\overline{\boldsymbol{T}}}^{-1}(0). \tag{2.3.110}$$

The solution of this system is directly related to the tensor $\overline{\overline{\boldsymbol{D}}}^{-1}(\boldsymbol{k}; 0, 0)$. Indeed, evaluating Eq. (2.3.104) at $\boldsymbol{G} = 0$, the following expression is obtained:

$$\overline{\overline{\boldsymbol{D}}}^{-1}(\boldsymbol{k}; 0, 0) = \overline{\overline{\boldsymbol{T}}}^{-1}(0) \left[\overline{\overline{\boldsymbol{I}}} - \frac{iV_{cube}}{V_c} \overline{\overline{\boldsymbol{\Omega}}} \Delta \overline{\overline{\boldsymbol{A}}} \sum_{j=1}^{n} < \overline{\overline{\boldsymbol{P}}}_j > \right]. \tag{2.3.111}$$

After solving the system of equations (2.3.110) and using Eq. (2.3.111), it is possible to obtain the matrix block $\overline{\overline{\boldsymbol{D}}}^{-1}(\boldsymbol{k}; 0, 0)$ which determines the effective nonlocal response tensor $\overline{\overline{\boldsymbol{A}}}_{\text{eff}}(\boldsymbol{k}(\omega), \omega)$ (Eq. (2.3.89)).

The effective nonlocal response tensor allows us to calculate not only the photonic-phononic dispersion relation but also the total electric, magnetic, stress and displacement fields at any point $\boldsymbol{r}$ in terms of their macroscopic components (with $\boldsymbol{G} = 0$). Indeed, using Eqs. (2.3.73) and (2.3.74), it is possible to express the microscopic field as

$$\boldsymbol{V}(\boldsymbol{r}) = e^{i\boldsymbol{k}\cdot\boldsymbol{r}} \left(\sum_{\boldsymbol{G}} \overline{\overline{\boldsymbol{D}}}^{-1}(\boldsymbol{k}, \boldsymbol{G}, 0) e^{i\boldsymbol{G}\cdot\boldsymbol{r}} \right) \left(\overline{\overline{\boldsymbol{D}}}^{-1}(\boldsymbol{k}, 0, 0) \right)^{-1} \boldsymbol{V}_0. \tag{2.3.112}$$

2.4 Metamaterial transformation of the nonlocal piezoelectromagnetic response

In previous section a method to calculate the effective nonlocal parameters of a homogenized piezoelectromagnetic crystal has been developed. However, such parameters are commonly used for a limited number of cases. For example, consider an electromagnetic metamaterial with non-magnetic constituents, possessing a negative refractive index in a certain frequency range. The spatial dispersion of the homogenized crystal can be described by a nonlocal dielectric function $\epsilon(\omega, \boldsymbol{k})$ with effective permeability μ being constant. Despite the fact that the nonlocal dielectric response contains all the information about dynamic effects inside the crystal ([69], [112]), the origin of the negative refraction is explained as the result of a magnetic-dipole moment appearance in a structure of non-magnetic constituents. Obviously, only using the effective nonlocal dielectric function, it is not possible to achieve a dynamic effective structure-dependent permeability. Nevertheless, metamaterials made from non-magnetic materials are found to exhibit a negative refractive index [113]. Hence, it would be very useful to obtain effective metamaterial parameters, depending on the crystal structure, in order to predict and explain the negative refractive index appearance.

Since the nonlocal response describes spatial dispersion effects, it is possible to redefine the obtained nonlocal response in terms of new re-calibrated fields and effective parameters. This kind of nonlocal response transformation will be called a *metamaterial transformation*. There are many ways to introduce the effective parameters, however, it is strongly recommended to ensure that newly redefined parameters still describe the medium with same photonic-phononic dispersion. As it is shown below, the obtained nonlocal response can be transformed into a metamaterial one far beyond the local limit, which provides an instrument to design and fabricate metamaterials with desired properties.

To proceed to the transformation of effective parameters, it is convenient to write down the dynamic matrix of the homogenized piezoelectromagnetic crystal as:

$$\overline{\overline{\boldsymbol{D}}}(\boldsymbol{k},\boldsymbol{G},\boldsymbol{G'}) = \overline{\overline{\boldsymbol{K}}}_{15\times15}(\boldsymbol{k}+\boldsymbol{G})\delta_{\boldsymbol{G},\boldsymbol{G'}} + i\overline{\overline{\boldsymbol{\Omega A}}}(\boldsymbol{G}-\boldsymbol{G'}), \tag{2.4.1}$$

where $\overline{\overline{\boldsymbol{K}}}_{15\times15}(\boldsymbol{k}+\boldsymbol{G})$ is:

$$\overline{\overline{\boldsymbol{K}}}_{15\times15}(\boldsymbol{k}+\boldsymbol{G}) = \begin{pmatrix} 0_{3\times3} & \overline{\overline{\boldsymbol{K}}}_{3\times6}(\boldsymbol{k}+\boldsymbol{G}) & 0_{3\times3} & 0_{3\times3} \\ (\overline{\overline{\boldsymbol{K}}}_{3\times6})(\boldsymbol{k}+\boldsymbol{G})^T & 0_{6\times6} & 0_{6\times3} & 0_{6\times3} \\ 0_{3\times3} & 0_{3\times6} & 0_{3\times3} & \overline{\overline{\boldsymbol{K}}}^{rot}_{3\times3}(\boldsymbol{k}+\boldsymbol{G}) \\ 0_{3\times3} & 0_{3\times6} & -\overline{\overline{\boldsymbol{K}}}^{rot}_{3\times3}(\boldsymbol{k}+\boldsymbol{G}) & 0_{3\times3} \end{pmatrix} \tag{2.4.2}$$

The components of matrix $\overline{\overline{\boldsymbol{K}}}_{15\times15}(\boldsymbol{k}+\boldsymbol{G})$ depend on the wave-vector as it is specified below:

$$\overline{\overline{\boldsymbol{K}}}_{3\times6}(\boldsymbol{k}) = \begin{pmatrix} k_x & 0 & 0 & 0 & k_z & k_y \\ 0 & k_y & 0 & k_z & 0 & k_x \\ 0 & 0 & k_z & k_y & k_x & 0 \end{pmatrix}, \quad \overline{\overline{\boldsymbol{K}}}^{rot}_{3\times3}(\boldsymbol{k}) = \begin{pmatrix} 0 & -k_z & k_y \\ k_z & 0 & -k_x \\ -k_y & k_z & 0 \end{pmatrix} \tag{2.4.3}$$

The macroscopic equations system, namely the equation for $\boldsymbol{V}_0$ can be written in terms of the effective nonlocal response matrix (2.3.88) as

$$\left[\overline{\overline{\boldsymbol{K}}}_{15\times15}(\boldsymbol{k}+\boldsymbol{G}) + i\overline{\overline{\boldsymbol{\Omega A}}}_{\text{eff}}(\boldsymbol{k})\right]\boldsymbol{V_0} = 0. \tag{2.4.4}$$

In compact form, the macroscopic equations set (2.4.4) can be rewritten as:

$$k\overline{\overline{\boldsymbol{K}}}\boldsymbol{V_0} = -i\overline{\overline{\boldsymbol{\Omega A}}}^{\text{PEM}}_{\text{eff,NL}}(\boldsymbol{k})\boldsymbol{V_0}, \tag{2.4.5}$$

with $\overline{\overline{\boldsymbol{K}}}$ equal to:

$$\overline{\overline{\boldsymbol{K}}} = \frac{1}{k}\overline{\overline{\boldsymbol{K}}}_{15\times15}(\boldsymbol{k}). \tag{2.4.6}$$

Metamaterial transformation procedure is a redistribution of the effective nonlocal response in terms of the local response, and nonlocal anti-symmetric and symmetric tensors:

$$\overline{\overline{\boldsymbol{A}}}^{\text{PEM}}_{\text{eff,NL}}(\boldsymbol{k}) = \overline{\overline{\boldsymbol{A}}}_{\text{eff},0} + k\overline{\overline{\boldsymbol{A}}}_{\text{eff},1} + k^2\overline{\overline{\boldsymbol{A}}}_{\text{eff},2}, \tag{2.4.7}$$

where the local response in obtained in the limit $\boldsymbol{k} \to 0$:

$$\overline{\overline{\boldsymbol{A}}}_{\text{eff},0} = \overline{\overline{\boldsymbol{A}}}^{\text{PEM}}_{\text{eff,NL}}(\boldsymbol{k} \to 0). \tag{2.4.8}$$

Nonlocal tensors are determined by the difference matrices $\overline{\overline{\boldsymbol{A}}}_{\text{diff}}(\boldsymbol{k})$ and $\overline{\overline{\boldsymbol{A}}}_{\text{diff}}(-\boldsymbol{k})$:

$$\begin{aligned}\overline{\overline{\boldsymbol{A}}}_{\text{diff}}(\boldsymbol{k}) &= \overline{\overline{\boldsymbol{A}}}^{\text{PEM}}_{\text{eff,NL}}(\boldsymbol{k}) - \overline{\overline{\boldsymbol{A}}}_{\text{eff},0},\\ \overline{\overline{\boldsymbol{A}}}_{\text{diff}}(-\boldsymbol{k}) &= \overline{\overline{\boldsymbol{A}}}^{\text{PEM}}_{\text{eff,NL}}(-\boldsymbol{k}) - \overline{\overline{\boldsymbol{A}}}_{\text{eff},0}.\end{aligned} \tag{2.4.9}$$

Finally, the explicit expressions for the anti-symmetric and symmetric matrices are listed below:

$$\begin{aligned}\overline{\overline{\boldsymbol{A}}}_{\text{eff},1} &= \frac{1}{2k}\left(\overline{\overline{\boldsymbol{A}}}_{\text{diff}}(\boldsymbol{k}) - \overline{\overline{\boldsymbol{A}}}_{\text{diff}}(-\boldsymbol{k})\right) = \frac{1}{2k}\left(\overline{\overline{\boldsymbol{A}}}^{\text{PEM}}_{\text{eff,NL}}(\boldsymbol{k}) - \overline{\overline{\boldsymbol{A}}}^{\text{PEM}}_{\text{eff,NL}}(-\boldsymbol{k})\right),\\ \overline{\overline{\boldsymbol{A}}}_{\text{eff},2} &= \frac{1}{2k^2}\left(\overline{\overline{\boldsymbol{A}}}_{\text{diff}}(\boldsymbol{k}) + \overline{\overline{\boldsymbol{A}}}_{\text{diff}}(-\boldsymbol{k})\right) = \frac{1}{2k^2}\left(\overline{\overline{\boldsymbol{A}}}^{\text{PEM}}_{\text{eff,NL}}(\boldsymbol{k}) + \overline{\overline{\boldsymbol{A}}}^{\text{PEM}}_{\text{eff,NL}}(-\boldsymbol{k}) - 2\overline{\overline{\boldsymbol{A}}}_{\text{eff},0}\right).\end{aligned} \tag{2.4.10}$$

For systems with central symmetry the matrix $\overline{\overline{\boldsymbol{A}}}_{\text{eff},1}$ vanishes. Indeed, such a system has the same nonlocal response for $\boldsymbol{k}$ and $-\boldsymbol{k}$. However, the contribution of anti-symmetric tensor $\overline{\overline{\boldsymbol{A}}}_{\text{eff},1}$ is significant and should be taken into account for systems without inversion symmetry.

The next step is to introduce the quadratic operator $\overline{\overline{\overline{\boldsymbol{K}}}}_2$:

$$\overline{\overline{\overline{\boldsymbol{K}}}}_2 = \frac{1}{k^2}\begin{pmatrix} \boldsymbol{K}_{3\times6}\cdot(\boldsymbol{K}_{3\times6})^T & 0_{3\times6} & 0_{3\times3} & 0_{3\times3}\\ 0_{6\times3} & 0_{6\times6} & 0_{6\times3} & 0_{6\times3}\\ 0_{3\times3} & 0_{3\times6} & (\boldsymbol{k}\times\overline{\overline{\boldsymbol{I}}})\cdot(-\boldsymbol{k}\times\overline{\overline{\boldsymbol{I}}}) & 0_{3\times3}\\ 0_{3\times3} & 0_{3\times6} & 0_{3\times3} & 0_{3\times3}\end{pmatrix} \tag{2.4.11}$$

Here, the product of $\boldsymbol{K}_{3\times6}\cdot(\boldsymbol{K}_{3\times6})^T$ and $(\boldsymbol{k}\times\overline{\overline{\boldsymbol{I}}})\cdot(-\boldsymbol{k}\times\overline{\overline{\boldsymbol{I}}})$ are matrices having the form:

$$\begin{aligned}\boldsymbol{K}_{3\times6}\cdot(\boldsymbol{K}_{3\times6})^T &= \begin{pmatrix} k_x^2+k_y^2+k_z^2 & k_xk_y & k_xk_z\\ k_xk_y & k_x^2+k_y^2+k_z^2 & k_yk_z\\ k_xk_z & k_yk_z & k_x^2+k_y^2+k_z^2\end{pmatrix},\\ (\boldsymbol{k}\times\overline{\overline{\boldsymbol{I}}})\cdot(-\boldsymbol{k}\times\overline{\overline{\boldsymbol{I}}}) &= \begin{pmatrix} k_y^2+k_z^2 & -k_xk_y & -k_xk_z\\ -k_xk_y & k_x^2+k_z^2 & -k_yk_z\\ -k_xk_z & -k_yk_z & k_x^2+k_y^2\end{pmatrix}\end{aligned} \tag{2.4.12}$$

It should be commented that the quadratic operator $\overline{\overline{\overline{\boldsymbol{K}}}}_2$ allows us to redistribute the nonlocal response between different effective parameters. For the particular case of a homogenized metal-dielectric crystal, the applied operator $\overline{\overline{\overline{\boldsymbol{K}}}}_2$ redistributes the nonlocal dielectric response between the effective tensors of the bianisotropic response. In a more general case of a homogenized piezoelectromagnetic system, the quadratic operator $\overline{\overline{\boldsymbol{K}}}_2$ is responsible for the redistribution of nonlocal response between effective tensors.

In order to proceed, let us multiply both sides of equation (2.4.7) by the frequency matrix $\overline{\overline{\boldsymbol{\Omega}}}$ from the left:

$$\begin{aligned}\overline{\overline{\boldsymbol{\Omega A}}}^{\mathrm{PEM}}_{\mathrm{eff,NL}}(\boldsymbol{k}) = \overline{\overline{\boldsymbol{\Omega A}}}_{\mathrm{eff},0} \quad &+ \quad k\left[\overline{\overline{\boldsymbol{I}}}-\overline{\overline{\boldsymbol{K_2}}}+\overline{\overline{\boldsymbol{K_2}}}\right]\overline{\overline{\boldsymbol{\Omega A}}}_{\mathrm{eff},1}+\\ &+ \quad k^2\left[\overline{\overline{\boldsymbol{I}}}-\overline{\overline{\boldsymbol{K_2}}}+\overline{\overline{\boldsymbol{K_2}}}\right]\overline{\overline{\boldsymbol{\Omega A}}}_{\mathrm{eff},2}\left[\overline{\overline{\boldsymbol{I}}}-\overline{\overline{\boldsymbol{K_2}}}+\overline{\overline{\boldsymbol{K_2}}}\right].\end{aligned} \tag{2.4.13}$$

The antisymmetric term with $\overline{\overline{\boldsymbol{A}}}_{\mathrm{eff},1}$ can be split into two terms:

$$\begin{aligned}\overline{\overline{\boldsymbol{\Omega A}}}^{\mathrm{PEM}}_{\mathrm{eff,NL}}(\boldsymbol{k}) = \overline{\overline{\boldsymbol{\Omega A}}}_{\mathrm{eff},0} \quad &+ \quad \frac{k}{2}\left[\overline{\overline{\boldsymbol{I}}}-\overline{\overline{\boldsymbol{K_2}}}+\overline{\overline{\boldsymbol{K_2}}}\right]\overline{\overline{\boldsymbol{\Omega A}}}_{\mathrm{eff},1}+\frac{k}{2}\overline{\overline{\boldsymbol{\Omega A}}}_{\mathrm{eff},1}\left[\overline{\overline{\boldsymbol{I}}}-\overline{\overline{\boldsymbol{K_2}}}+\overline{\overline{\boldsymbol{K_2}}}\right]+\\ &+ \quad k^2\left[\overline{\overline{\boldsymbol{I}}}-\overline{\overline{\boldsymbol{K_2}}}+\overline{\overline{\boldsymbol{K_2}}}\right]\overline{\overline{\boldsymbol{\Omega A}}}_{\mathrm{eff},2}\left[\overline{\overline{\boldsymbol{I}}}-\overline{\overline{\boldsymbol{K_2}}}+\overline{\overline{\boldsymbol{K_2}}}\right].\end{aligned} \tag{2.4.14}$$

Now, the terms with $\overline{\overline{\boldsymbol{A}}}_{\mathrm{eff},2}$ is expanded as:

$$\begin{aligned}&k^2\left[\overline{\overline{\boldsymbol{I}}}-\overline{\overline{\boldsymbol{K_2}}}+\overline{\overline{\boldsymbol{K_2}}}\right]\overline{\overline{\boldsymbol{\Omega A}}}_{\mathrm{eff},2}\left[\overline{\overline{\boldsymbol{I}}}-\overline{\overline{\boldsymbol{K_2}}}+\overline{\overline{\boldsymbol{K_2}}}\right] = k^2\left[\overline{\overline{\boldsymbol{I}}}-\overline{\overline{\boldsymbol{K_2}}}\right]\overline{\overline{\boldsymbol{\Omega A}}}_{\mathrm{eff},2}\left[\overline{\overline{\boldsymbol{I}}}-\overline{\overline{\boldsymbol{K_2}}}\right]+\\ &+k^2\left[\overline{\overline{\boldsymbol{I}}}-\overline{\overline{\boldsymbol{K_2}}}\right]\overline{\overline{\boldsymbol{\Omega A}}}_{\mathrm{eff},2}\overline{\overline{\boldsymbol{K_2}}}+k^2\overline{\overline{\boldsymbol{K_2\Omega A}}}_{\mathrm{eff},2}\left[\overline{\overline{\boldsymbol{I}}}-\overline{\overline{\boldsymbol{K_2}}}\right]+k^2\overline{\overline{\boldsymbol{K_2\Omega A}}}_{\mathrm{eff},2}\overline{\overline{\boldsymbol{K_2}}}.\end{aligned} \tag{2.4.15}$$

It is convenient to introduce the terms $\overline{\overline{\boldsymbol{\Omega}}}\overline{\overline{\boldsymbol{A'}}}_{\mathrm{eff}}(\boldsymbol{k})$:

$$\begin{aligned}\overline{\overline{\boldsymbol{\Omega}}}\overline{\overline{\boldsymbol{A'}}}_{\mathrm{eff}}(\boldsymbol{k}) = \overline{\overline{\boldsymbol{\Omega A}}}_{\mathrm{eff},0} \quad &+ \quad \frac{k}{2}\left[\overline{\overline{\boldsymbol{I}}}-\overline{\overline{\boldsymbol{K_2}}}\right]\overline{\overline{\boldsymbol{\Omega A}}}_{\mathrm{eff},1}+\frac{k}{2}\overline{\overline{\boldsymbol{\Omega A}}}_{\mathrm{eff},1}\left[\overline{\overline{\boldsymbol{I}}}-\overline{\overline{\boldsymbol{K_2}}}\right]+\\ &+ \quad k^2\left[\overline{\overline{\boldsymbol{I}}}-\overline{\overline{\boldsymbol{K_2}}}\right]\overline{\overline{\boldsymbol{\Omega A}}}_{\mathrm{eff},2}\left[\overline{\overline{\boldsymbol{I}}}-\overline{\overline{\boldsymbol{K_2}}}\right].\end{aligned} \tag{2.4.16}$$

Hence,

$$\begin{aligned}\overline{\overline{\boldsymbol{A'}}}_{\mathrm{eff}}(\boldsymbol{k}) = \overline{\overline{\boldsymbol{A}}}_{\mathrm{eff},0} \quad &+ \quad \frac{k}{2}\overline{\overline{\boldsymbol{\Omega}}}^{-1}\left[\overline{\overline{\boldsymbol{I}}}-\overline{\overline{\boldsymbol{K_2}}}\right]\overline{\overline{\boldsymbol{\Omega A}}}_{\mathrm{eff},1}+\frac{k}{2}\overline{\overline{\boldsymbol{A}}}_{\mathrm{eff},1}\left[\overline{\overline{\boldsymbol{I}}}-\overline{\overline{\boldsymbol{K_2}}}\right]+\\ &+ \quad k^2\overline{\overline{\boldsymbol{\Omega}}}^{-1}\left[\overline{\overline{\boldsymbol{I}}}-\overline{\overline{\boldsymbol{K_2}}}\right]\overline{\overline{\boldsymbol{\Omega A}}}_{\mathrm{eff},2}\left[\overline{\overline{\boldsymbol{I}}}-\overline{\overline{\boldsymbol{K_2}}}\right].\end{aligned} \tag{2.4.17}$$

Now, the tensor $\overline{\overline{\boldsymbol{\Omega A}}}^{\mathrm{PEM}}_{\mathrm{eff,NL}}(\boldsymbol{k})$ is expressed as:

$$\begin{aligned}\overline{\overline{\boldsymbol{\Omega A}}}^{\mathrm{PEM}}_{\mathrm{eff,NL}}(\boldsymbol{k}) = \overline{\overline{\boldsymbol{\Omega}}}\overline{\overline{\boldsymbol{A'}}}_{\mathrm{eff}}(\boldsymbol{k}) \quad &+ \quad \frac{k}{2}\overline{\overline{\boldsymbol{K_2\Omega A}}}_{\mathrm{eff},1}+\frac{k}{2}\overline{\overline{\boldsymbol{\Omega A}}}_{\mathrm{eff},1}\overline{\overline{\boldsymbol{K_2}}}+\\ &+ \quad k^2\left[\overline{\overline{\boldsymbol{I}}}-\overline{\overline{\boldsymbol{K_2}}}\right]\overline{\overline{\boldsymbol{\Omega A}}}_{\mathrm{eff},2}\overline{\overline{\boldsymbol{K_2}}}+k^2\overline{\overline{\boldsymbol{K_2\Omega A}}}_{\mathrm{eff},2}\left[\overline{\overline{\boldsymbol{I}}}-\overline{\overline{\boldsymbol{K_2}}}\right]\\ &+ \quad k^2\overline{\overline{\boldsymbol{K_2\Omega A}}}_{\mathrm{eff},2}\overline{\overline{\boldsymbol{K_2}}}.\end{aligned} \tag{2.4.18}$$

Substituting (2.4.18) into (2.4.5) to get

$$\begin{aligned}k\overline{\overline{\boldsymbol{K}}}\vec{V_0} \quad &= \quad -i\left[\overline{\overline{\boldsymbol{\Omega}}}\overline{\overline{\boldsymbol{A'}}}_{\mathrm{eff}}(\boldsymbol{k})+\frac{k}{2}\overline{\overline{\boldsymbol{K_2\Omega A}}}_{\mathrm{eff},1}+\frac{k}{2}\overline{\overline{\boldsymbol{\Omega A}}}_{\mathrm{eff},1}\overline{\overline{\boldsymbol{K_2}}}+k^2\left[\overline{\overline{\boldsymbol{I}}}-\overline{\overline{\boldsymbol{K_2}}}\right]\overline{\overline{\boldsymbol{\Omega A}}}_{\mathrm{eff},2}\overline{\overline{\boldsymbol{K_2}}}+\right.\\ &+ \quad \left.k^2\overline{\overline{\boldsymbol{K_2\Omega A}}}_{\mathrm{eff},2}\left[\overline{\overline{\boldsymbol{I}}}-\overline{\overline{\boldsymbol{K_2}}}\right]+k^2\overline{\overline{\boldsymbol{K_2\Omega A}}}_{\mathrm{eff},2}\overline{\overline{\boldsymbol{K_2}}}\right]\vec{V_0}.\end{aligned} \tag{2.4.19}$$

The terms, being multiplied by tensor $\overline{\overline{\boldsymbol{K_2}}}$ from the left, are moved to the left side of the equation, others will remain on the right side:

$$\begin{aligned}&\left[k\overline{\overline{\boldsymbol{K}}} + \frac{k}{2}\overline{\overline{\boldsymbol{K_2}\boldsymbol{\Omega}\boldsymbol{A}}}_{\mathrm{eff},1} + k^2\overline{\overline{\boldsymbol{K_2}\boldsymbol{\Omega}\boldsymbol{A}}}_{\mathrm{eff},2}\left[\overline{\overline{\boldsymbol{I}}} - \overline{\overline{\boldsymbol{K_2}}}\right] + k^2\overline{\overline{\boldsymbol{K_2}\boldsymbol{\Omega}\boldsymbol{A}}}_{\mathrm{eff},2}\overline{\overline{\boldsymbol{K_2}}}\right]\vec{V_0} = \\ &-i\left[\overline{\overline{\boldsymbol{\Omega}}}\,\overline{\overline{\boldsymbol{A}'}}_{\mathrm{eff}}(\boldsymbol{k}) + \frac{k}{2}\overline{\overline{\boldsymbol{\Omega}\boldsymbol{A}}}_{\mathrm{eff},1}\overline{\overline{\boldsymbol{K_2}}} + k^2\left[\overline{\overline{\boldsymbol{I}}} - \overline{\overline{\boldsymbol{K_2}}}\right]\overline{\overline{\boldsymbol{\Omega}\boldsymbol{A}}}_{\mathrm{eff},2}\overline{\overline{\boldsymbol{K_2}}}\right]\vec{V_0}.\end{aligned} \tag{2.4.20}$$

Now, $\overline{\overline{\boldsymbol{K_2}}}$ is expressed in terms of $\overline{\overline{\boldsymbol{K}}}$:

$$\begin{aligned}(a)\quad \overline{\overline{\boldsymbol{K_2}}} &= \frac{1}{k}\begin{pmatrix} 0_{3\times3} & \overline{\overline{\boldsymbol{K}}}_{3\times6}(\boldsymbol{k}) & 0_{3\times3} & 0_{3\times3} \\ (\overline{\overline{\boldsymbol{K}}}_{3\times6})^T(\boldsymbol{k}) & 0_{6\times6} & 0_{6\times3} & 0_{6\times3} \\ 0_{3\times3} & 0_{3\times6} & 0_{3\times3} & \overline{\overline{\boldsymbol{K}}}^{rot}_{3\times3}(\boldsymbol{k}) \\ 0_{3\times3} & 0_{3\times6} & -\overline{\overline{\boldsymbol{K}}}^{rot}_{3\times3}(\boldsymbol{k}) & 0_{3\times3} \end{pmatrix} \cdot \frac{1}{k}\underbrace{\begin{pmatrix} 0_{3\times3} & 0_{3\times6} & 0_{3\times3} & 0_{3\times3} \\ (\overline{\overline{\boldsymbol{K}}}_{3\times6})^T(\boldsymbol{k}) & 0_{6\times6} & 0_{6\times3} & 0_{6\times3} \\ 0_{3\times3} & 0_{3\times6} & 0_{3\times3} & 0_{3\times3} \\ 0_{3\times3} & 0_{3\times6} & -\overline{\overline{\boldsymbol{K}}}^{rot}_{3\times3}(\boldsymbol{k}) & 0_{3\times3} \end{pmatrix}}_{\overline{\overline{\boldsymbol{K}}}_-} = \frac{1}{k}\overline{\overline{\boldsymbol{K}}}\,\overline{\overline{\boldsymbol{K}}}_- \\ (b)\quad \overline{\overline{\boldsymbol{K_2}}} &= \frac{1}{k}\underbrace{\begin{pmatrix} 0_{3\times3} & \overline{\overline{\boldsymbol{K}}}_{3\times6}(\boldsymbol{k}) & 0_{3\times3} & 0_{3\times3} \\ 0_{6\times3} & 0_{6\times6} & 0_{6\times3} & 0_{6\times3} \\ 0_{3\times3} & 0_{3\times6} & 0_{3\times3} & \overline{\overline{\boldsymbol{K}}}^{rot}_{3\times3}(\boldsymbol{k}) \\ 0_{3\times3} & 0_{3\times6} & 0_{3\times3} & 0_{3\times3} \end{pmatrix}}_{\overline{\overline{\boldsymbol{K}}}_+} \cdot \frac{1}{k}\begin{pmatrix} 0_{3\times3} & \overline{\overline{\boldsymbol{K}}}_{3\times6}(\boldsymbol{k}) & 0_{3\times3} & 0_{3\times3} \\ (\overline{\overline{\boldsymbol{K}}}_{3\times6})^T(\boldsymbol{k}) & 0_{6\times6} & 0_{6\times3} & 0_{6\times3} \\ 0_{3\times3} & 0_{3\times6} & 0_{3\times3} & \overline{\overline{\boldsymbol{K}}}^{rot}_{3\times3}(\boldsymbol{k}) \\ 0_{3\times3} & 0_{3\times6} & -\overline{\overline{\boldsymbol{K}}}^{rot}_{3\times3}(\boldsymbol{k}) & 0_{3\times3} \end{pmatrix} = \frac{1}{k}\overline{\overline{\boldsymbol{K}}}_+\,\overline{\overline{\boldsymbol{K}}}\end{aligned} \tag{2.4.21}$$

Both forms (a) and (b) of the quadratic operator $\overline{\overline{\boldsymbol{K}}}_2$ will be used to write down the macroscopic equation systems:

$$\begin{aligned}&\left[k\overline{\overline{\boldsymbol{K}}} + \frac{k}{2}\cdot\frac{1}{k}\overline{\overline{\boldsymbol{K}}}\,\overline{\overline{\boldsymbol{K}}}_-\overline{\overline{\boldsymbol{\Omega}\boldsymbol{A}}}_{\mathrm{eff},1} + \frac{k^2}{k}\overline{\overline{\boldsymbol{K}}}\,\overline{\overline{\boldsymbol{K}}}_-\overline{\overline{\boldsymbol{\Omega}\boldsymbol{A}}}_{\mathrm{eff},2}\left[\overline{\overline{\boldsymbol{I}}} - \overline{\overline{\boldsymbol{K_2}}}\right] + \frac{k^2}{k}\overline{\overline{\boldsymbol{K}}}\,\overline{\overline{\boldsymbol{K}}}_-\overline{\overline{\boldsymbol{\Omega}\boldsymbol{A}}}_{\mathrm{eff},2}\cdot\frac{1}{k}\overline{\overline{\boldsymbol{K}}}_+\,\overline{\overline{\boldsymbol{K}}}\right]\vec{V_0} = \\ &-i\left[\overline{\overline{\boldsymbol{\Omega}}}\,\overline{\overline{\boldsymbol{A}'}}_{\mathrm{eff}}(\boldsymbol{k}) + \frac{k}{2}\overline{\overline{\boldsymbol{\Omega}\boldsymbol{A}}}_{\mathrm{eff},1}\cdot\frac{1}{k}\overline{\overline{\boldsymbol{K}}}_+\,\overline{\overline{\boldsymbol{K}}} + k^2\left[\overline{\overline{\boldsymbol{I}}} - \overline{\overline{\boldsymbol{K_2}}}\right]\overline{\overline{\boldsymbol{\Omega}\boldsymbol{A}}}_{\mathrm{eff},2}\cdot\frac{1}{k}\overline{\overline{\boldsymbol{K}}}_+\,\overline{\overline{\boldsymbol{K}}}\right]\vec{V_0}.\end{aligned} \tag{2.4.22}$$

The tensor $k\overline{\overline{\boldsymbol{K}}}$ can be factorized out from the left:

$$\begin{aligned}&k\overline{\overline{\boldsymbol{K}}}\left[\overline{\overline{\boldsymbol{I}}} + \frac{1}{2k}\overline{\overline{\boldsymbol{K}}}_-\overline{\overline{\boldsymbol{\Omega}\boldsymbol{A}}}_{\mathrm{eff},1} + \overline{\overline{\boldsymbol{K}}}_-\overline{\overline{\boldsymbol{\Omega}\boldsymbol{A}}}_{\mathrm{eff},2}\left[\overline{\overline{\boldsymbol{I}}} - \overline{\overline{\boldsymbol{K_2}}}\right] + \frac{1}{k}\overline{\overline{\boldsymbol{K}}}_-\overline{\overline{\boldsymbol{\Omega}\boldsymbol{A}}}_{\mathrm{eff},2}\overline{\overline{\boldsymbol{K}}}_+\,\overline{\overline{\boldsymbol{K}}}\right]\vec{V_0} = \\ &\qquad -i\left[\overline{\overline{\boldsymbol{\Omega}}}\,\overline{\overline{\boldsymbol{A}'}}_{\mathrm{eff}}(\boldsymbol{k}) + \frac{1}{2}\overline{\overline{\boldsymbol{\Omega}\boldsymbol{A}}}_{\mathrm{eff},1}\overline{\overline{\boldsymbol{K}}}_+\,\overline{\overline{\boldsymbol{K}}} + k\left[\overline{\overline{\boldsymbol{I}}} - \overline{\overline{\boldsymbol{K_2}}}\right]\overline{\overline{\boldsymbol{\Omega}\boldsymbol{A}}}_{\mathrm{eff},2}\overline{\overline{\boldsymbol{K}}}_+\,\overline{\overline{\boldsymbol{K}}}\right]\vec{V_0},\end{aligned} \tag{2.4.23}$$

and, according to expression (2.4.5), $k\overline{\overline{\boldsymbol{K}}}$ can be replaced by $-i\overline{\overline{\boldsymbol{\Omega}\boldsymbol{A}}}^{\mathrm{PEM}}_{\mathrm{eff,NL}}(\boldsymbol{k})$:

$$\begin{aligned}&k\overline{\overline{\boldsymbol{K}}}\left[\overline{\overline{\boldsymbol{I}}} + \frac{1}{2k}\overline{\overline{\boldsymbol{K}}}_-\overline{\overline{\boldsymbol{\Omega}\boldsymbol{A}}}_{\mathrm{eff},1} + \overline{\overline{\boldsymbol{K}}}_-\overline{\overline{\boldsymbol{\Omega}\boldsymbol{A}}}_{\mathrm{eff},2}\left[\overline{\overline{\boldsymbol{I}}} - \overline{\overline{\boldsymbol{K_2}}}\right] + \frac{1}{k^2}\overline{\overline{\boldsymbol{K}}}_-\overline{\overline{\boldsymbol{\Omega}\boldsymbol{A}}}_{\mathrm{eff},2}\overline{\overline{\boldsymbol{K}}}_+\Big(-i\overline{\overline{\boldsymbol{\Omega}\boldsymbol{A}}}^{\mathrm{PEM}}_{\mathrm{eff,NL}}(\boldsymbol{k})\Big)\right]\vec{V_0} = \\ &-i\left[\overline{\overline{\boldsymbol{\Omega}}}\,\overline{\overline{\boldsymbol{A}'}}_{\mathrm{eff}}(\boldsymbol{k}) + \frac{1}{2k}\overline{\overline{\boldsymbol{\Omega}\boldsymbol{A}}}_{\mathrm{eff},1}\overline{\overline{\boldsymbol{K}}}_+\Big(-i\overline{\overline{\boldsymbol{\Omega}\boldsymbol{A}}}^{\mathrm{PEM}}_{\mathrm{eff,NL}}(\boldsymbol{k})\Big) + \left[\overline{\overline{\boldsymbol{I}}} - \overline{\overline{\boldsymbol{K_2}}}\right]\overline{\overline{\boldsymbol{\Omega}\boldsymbol{A}}}_{\mathrm{eff},2}\overline{\overline{\boldsymbol{K}}}_+\Big(-i\overline{\overline{\boldsymbol{\Omega}\boldsymbol{A}}}^{\mathrm{PEM}}_{\mathrm{eff,NL}}(\boldsymbol{k})\Big)\right]\vec{V_0}.\end{aligned} \tag{2.4.24}$$

Terms simplification inside the parenthesis gives:

$$\begin{aligned}
&k\overline{\overline{\boldsymbol{K}}}\left[\overline{\overline{\boldsymbol{I}}}+\frac{1}{2k}\overline{\overline{\boldsymbol{K}}}_{-}\overline{\overline{\boldsymbol{\Omega A}}}_{\mathrm{eff},1}+\overline{\overline{\boldsymbol{K}}}_{-}\overline{\overline{\boldsymbol{\Omega A}}}_{\mathrm{eff},2}\left[\overline{\overline{\boldsymbol{I}}}-\overline{\overline{\boldsymbol{K_2}}}\right]-\frac{i}{k^2}\overline{\overline{\boldsymbol{K}}}_{-}\overline{\overline{\boldsymbol{\Omega A}}}_{\mathrm{eff},2}\overline{\overline{\boldsymbol{K}}}_{+}\overline{\overline{\boldsymbol{\Omega A}}}^{\mathrm{PEM}}_{\mathrm{eff,NL}}(\boldsymbol{k})\right]\vec{V}_0=\\
&-i\left[\overline{\overline{\boldsymbol{\Omega}}}\overline{\overline{\boldsymbol{A'}}}_{\mathrm{eff}}(\boldsymbol{k})-\frac{i}{2k}\overline{\overline{\boldsymbol{\Omega A}}}_{\mathrm{eff},1}\overline{\overline{\boldsymbol{K}}}_{+}\overline{\overline{\boldsymbol{\Omega A}}}^{\mathrm{PEM}}_{\mathrm{eff,NL}}(\boldsymbol{k})-i\left[\overline{\overline{\boldsymbol{I}}}-\overline{\overline{\boldsymbol{K_2}}}\right]\overline{\overline{\boldsymbol{\Omega A}}}_{\mathrm{eff},2}\overline{\overline{\boldsymbol{K}}}_{+}\overline{\overline{\boldsymbol{\Omega A}}}^{\mathrm{PEM}}_{\mathrm{eff,NL}}(\boldsymbol{k})\right]\vec{V}_0.
\end{aligned}\tag{2.4.25}$$

The frequency tensor $\overline{\overline{\boldsymbol{\Omega}}}$ is being factorized out from the right side:

$$\begin{aligned}
&k\overline{\overline{\boldsymbol{K}}}\left[\overline{\overline{\boldsymbol{I}}}+\frac{1}{2k}\overline{\overline{\boldsymbol{K}}}_{-}\overline{\overline{\boldsymbol{\Omega A}}}_{\mathrm{eff},1}+\overline{\overline{\boldsymbol{K}}}_{-}\overline{\overline{\boldsymbol{\Omega A}}}_{\mathrm{eff},2}\left[\overline{\overline{\boldsymbol{I}}}-\overline{\overline{\boldsymbol{K_2}}}\right]-\frac{i}{k^2}\overline{\overline{\boldsymbol{K}}}_{-}\overline{\overline{\boldsymbol{\Omega A}}}_{\mathrm{eff},2}\overline{\overline{\boldsymbol{K}}}_{+}\overline{\overline{\boldsymbol{\Omega A}}}^{\mathrm{PEM}}_{\mathrm{eff,NL}}(\boldsymbol{k})\right]\vec{V}_0=\\
&-i\overline{\overline{\boldsymbol{\Omega}}}\left[\overline{\overline{\boldsymbol{A'}}}_{\mathrm{eff}}(\boldsymbol{k})-\frac{i}{2k}\overline{\overline{\boldsymbol{A}}}_{\mathrm{eff},1}\overline{\overline{\boldsymbol{K}}}_{+}\overline{\overline{\boldsymbol{\Omega A}}}^{\mathrm{PEM}}_{\mathrm{eff,NL}}(\boldsymbol{k})-i\overline{\overline{\boldsymbol{\Omega}}}^{-1}\left[\overline{\overline{\boldsymbol{I}}}-\overline{\overline{\boldsymbol{K_2}}}\right]\overline{\overline{\boldsymbol{\Omega A}}}_{\mathrm{eff},2}\overline{\overline{\boldsymbol{K}}}_{+}\overline{\overline{\boldsymbol{\Omega A}}}^{\mathrm{PEM}}_{\mathrm{eff,NL}}(\boldsymbol{k})\right]\vec{V}_0.
\end{aligned}\tag{2.4.26}$$

Finally, the expression for the piezoelectromagnetic metamaterial response tensor $\overline{\overline{\boldsymbol{A}}}^{\mathrm{PEM}}_{\mathrm{eff,MM}}$ is:

$$\begin{aligned}
\overline{\overline{\boldsymbol{A}}}^{\mathrm{PEM}}_{\mathrm{eff,MM}}(\boldsymbol{k})=&\left(\overline{\overline{\boldsymbol{A'}}}_{\mathrm{eff}}(\boldsymbol{k})-\frac{i}{2k}\overline{\overline{\boldsymbol{A}}}_{\mathrm{eff},1}\overline{\overline{\boldsymbol{K}}}_{+}\overline{\overline{\boldsymbol{\Omega A}}}^{\mathrm{PEM}}_{\mathrm{eff,NL}}(\boldsymbol{k})-i\overline{\overline{\boldsymbol{\Omega}}}^{-1}\left[\overline{\overline{\boldsymbol{I}}}-\overline{\overline{\boldsymbol{K_2}}}\right]\overline{\overline{\boldsymbol{\Omega A}}}_{\mathrm{eff},2}\overline{\overline{\boldsymbol{K}}}_{+}\overline{\overline{\boldsymbol{\Omega A}}}^{\mathrm{PEM}}_{\mathrm{eff,NL}}(\boldsymbol{k})\right)\times\\
&\left(\overline{\overline{\boldsymbol{I}}}+\frac{1}{2k}\overline{\overline{\boldsymbol{K}}}_{-}\overline{\overline{\boldsymbol{\Omega A}}}_{\mathrm{eff},1}+\overline{\overline{\boldsymbol{K}}}_{-}\overline{\overline{\boldsymbol{\Omega A}}}_{\mathrm{eff},2}\left[\overline{\overline{\boldsymbol{I}}}-\overline{\overline{\boldsymbol{K_2}}}\right]-\frac{i}{k^2}\overline{\overline{\boldsymbol{K}}}_{-}\overline{\overline{\boldsymbol{\Omega A}}}_{\mathrm{eff},2}\overline{\overline{\boldsymbol{K}}}_{+}\overline{\overline{\boldsymbol{\Omega A}}}^{\mathrm{PEM}}_{\mathrm{eff,NL}}(\boldsymbol{k})\right)^{-1}.
\end{aligned}\tag{2.4.27}$$

Chapter 3

Case of electromagnetic metamaterials

3.1 Nonlocal dielectric response of a homogenized 3D photonic crystal

A consistent formalism for homogenizing an electromagnetic crystal directly can be described by employing the approach developed in Chapter II for piezoelectromagnetic crystals. Indeed, in the case when piezoelectric $\overset{\leftrightarrow}{e}_{3\times 6}\,(\boldsymbol{r})$ and piezomagnetic $\overset{\leftrightarrow}{d}_{3\times 6}\,(\boldsymbol{r})$ tensors in Eq. (2.3.45) are zero matrices,

$$\begin{aligned} \overset{\leftrightarrow}{e}\,(\boldsymbol{r}) &= 0_{3\times 6}, \\ \overset{\leftrightarrow}{d}\,(\boldsymbol{r}) &= 0_{3\times 6}, \end{aligned} \tag{3.1.1}$$

the elastic and electromagnetic responses of a piezoelectromagnetic medium can be treated separately. In fact, the piezoelectromagnetic periodic matrix $\overline{\overline{\boldsymbol{A}}}(\boldsymbol{r})$ with the condition (3.1.1) has the following form:

$$\overline{\overline{\boldsymbol{A}}}(\boldsymbol{r}) = \begin{pmatrix} \overset{\leftrightarrow}{\rho}\,(\boldsymbol{r}) & 0_{3\times 6} & 0_{3\times 3} & 0_{3\times 3} \\ 0_{6\times 3} & \overset{\leftrightarrow}{S}\,(\boldsymbol{r}) & 0_{6\times 3} & 0_{6\times 3} \\ 0_{3\times 3} & 0_{3\times 6} & \overset{\leftrightarrow}{\epsilon}\,(\boldsymbol{r}) & \overset{\leftrightarrow}{\gamma}\,(\boldsymbol{r}) \\ 0_{3\times 3} & 0_{3\times 6} & \overset{\leftrightarrow}{\delta}\,(\boldsymbol{r}) & \overset{\leftrightarrow}{\mu}\,(\boldsymbol{r}) \end{pmatrix} \tag{3.1.2}$$

As a result, tensors $\overset{\leftrightarrow}{\epsilon'}\,(\boldsymbol{r})$, $\overset{\leftrightarrow}{\gamma'}\,(\boldsymbol{r})$, $\overset{\leftrightarrow}{\delta'}\,(\boldsymbol{r})$ and $\overset{\leftrightarrow}{\mu'}\,(\boldsymbol{r})$ coincide with those of the photonic bianisotropic response (2.3.34). The piezoelectric and piezomagnetic effects have real physical origin. According to (3.1.1), if one theoretically removes tensors $\overset{\leftrightarrow}{e}(\boldsymbol{r})$ and $\overset{\leftrightarrow}{d}(\boldsymbol{r})$, the elastic and electromagnetic wave independently propagate inside the same crystal. Besides, in many cases this approximation is viable since the piezoelectric response of metamaterials is rather weak, particularly, in the microwave range.

As long as tensors $\overset{\leftrightarrow}{e}(\boldsymbol{r})$, $\overset{\leftrightarrow}{d}(\boldsymbol{r})$ are absent, the elastic and electromagnetic parts of the periodic matrix $\overline{\overline{\boldsymbol{A}}}(\boldsymbol{r})$ can be treated separately. Therefore, the macroscopic equations of the piezoelectromagnetic system (2.3.42) can be reduced to those of a homogenized electromagnetic crystal as follows:

$$\overline{\overline{\overline{\boldsymbol{\nabla}}}}\boldsymbol{v}(\boldsymbol{r}) = \overline{\overline{\boldsymbol{\Omega}\boldsymbol{A}}}(\boldsymbol{r})\boldsymbol{v}(\boldsymbol{r}), \tag{3.1.3}$$

where column-vector $\boldsymbol{v}(\boldsymbol{r})$ contains the components of electric and magnetic fields only:

$$[\boldsymbol{v}(\boldsymbol{r})]^T = (E_x, E_y, E_z, H_x, H_y, H_z). \tag{3.1.4}$$

Here, $\overline{\overline{\boldsymbol{\Omega}}}$ is a matrix including the frequency ω:

$$\overline{\overline{\boldsymbol{\Omega}}} = \begin{bmatrix} -i\omega \overset{\leftrightarrow}{I}_3 & 0_{3\times3} \\ 0_{3\times3} & -i\omega \overset{\leftrightarrow}{I}_3 \end{bmatrix} \tag{3.1.5}$$

The matrix $\overline{\overline{\overline{\boldsymbol{\nabla}}}}$ has the form:

$$\overline{\overline{\overline{\boldsymbol{\nabla}}}} = \begin{bmatrix} 0_{3\times3} & \nabla^{rot}_{3\times3} \\ -\nabla^{rot}_{3\times3} & 0_{3\times3} \end{bmatrix} = \begin{bmatrix} 0 & 0 & 0 & 0 & -\nabla_z & \nabla_y \\ 0 & 0 & 0 & \nabla_z & 0 & -\nabla_x \\ 0 & 0 & 0 & -\nabla_y & \nabla_z & 0 \\ 0 & \nabla_z & -\nabla_y & 0 & 0 & 0 \\ -\nabla_z & 0 & \nabla_x & 0 & 0 & 0 \\ \nabla_y & -\nabla_z & 0 & 0 & 0 & 0 \end{bmatrix}. \tag{3.1.6}$$

The 6×6 matrix $\overline{\overline{\boldsymbol{A}}}(\boldsymbol{r})$ in (3.1.3) is defined in terms of 3×3 matrices: the permittivity $\overset{\leftrightarrow}{\boldsymbol{\epsilon}}(\boldsymbol{r})$, permeability $\overset{\leftrightarrow}{\boldsymbol{\mu}}(\boldsymbol{r})$ and crossed magneto-electric dyadics - $\overset{\leftrightarrow}{\boldsymbol{\gamma}}(\boldsymbol{r})$ and $\overset{\leftrightarrow}{\boldsymbol{\delta}}(\boldsymbol{r})$:

$$\overline{\overline{\boldsymbol{A}}}(\boldsymbol{r}) \equiv \begin{bmatrix} \overset{\leftrightarrow}{\boldsymbol{\epsilon}}(\boldsymbol{r}) & \overset{\leftrightarrow}{\boldsymbol{\gamma}}(\boldsymbol{r}) \\ \overset{\leftrightarrow}{\boldsymbol{\delta}}(\boldsymbol{r}) & \overset{\leftrightarrow}{\boldsymbol{\mu}}(\boldsymbol{r}) \end{bmatrix}, \tag{3.1.7}$$

where the above described tensors are periodic functions of the coordinate $\boldsymbol{r}$.

The effective dynamic parameters of the photonic crystal will be calculated by applying the explicit formulas for all the components of the effective nonlocal-response tensor:

$$\overline{\overline{\boldsymbol{A}}}_{\text{eff}}(\boldsymbol{k}(\omega), \omega) \equiv \begin{bmatrix} \overset{\leftrightarrow}{\boldsymbol{\epsilon}}_{\text{eff}}(\boldsymbol{k}, \omega) & \overset{\leftrightarrow}{\boldsymbol{\gamma}}_{\text{eff}}(\boldsymbol{k}, \omega) \\ \overset{\leftrightarrow}{\boldsymbol{\delta}}_{\text{eff}}(\boldsymbol{k}, \omega) & \overset{\leftrightarrow}{\boldsymbol{\mu}}_{\text{eff}}(\boldsymbol{k}, \omega) \end{bmatrix}, \tag{3.1.8}$$

where $\overleftrightarrow{\boldsymbol{\epsilon}}_{\text{eff}}\,(\boldsymbol{k},\omega)$, $\overleftrightarrow{\boldsymbol{\mu}}_{\text{eff}}\,(\boldsymbol{k},\omega)$, $\overleftrightarrow{\boldsymbol{\gamma}}_{\text{eff}}\,(\boldsymbol{k},\omega)$, $\overleftrightarrow{\boldsymbol{\delta}}_{\text{eff}}\,(\boldsymbol{k},\omega)$ are the effective bianisotropic response tensors, which depend on both the Bloch wave vector $\boldsymbol{k}$ and frequency ω. In principle, applying the expression (3.1.1) within the nonlocal piezoelectromagnetic formalism, it is straightforward to obtain the effective parameters for homogenized electromagnetic and elastic crystals. In particular, the obtained here expressions for the effective tensors of a homogenized electromagnetic crystal are fully consistent with those presented in [52].

The direct calculation of the effective nonlocal response matrix $\overline{\overline{\boldsymbol{A}}}_{\text{eff}}(\boldsymbol{k}(\omega),\omega)$ requires the solution of very large algebraic systems of equations. In order to reduce the computing time of the numerical simulations, an FFDA will be used that is rather accurate in comparison with that proposed in [52].

Another novelty is that the iterative procedure, used to obtain the effective nonlocal parameters, allows the calculation of the exact photonic dispersion relation for an arbitrary magnitude and direction of the wave vector $\boldsymbol{k}$. On the first step, the *local* response tensor $\overline{\overline{\boldsymbol{A}}}_{\text{eff}}(\boldsymbol{k}\to 0,\omega)$ is being calculated and the resulting effective parameters are used to calculate in the first (local) approximation the photonic dispersion relation $\boldsymbol{k}(\omega)$. Afterwards, the nonlocal effective response tensor $\overline{\overline{\boldsymbol{A}}}_{\text{eff}}(\boldsymbol{k}(\omega),\omega)$ (3.1.8) is calculated by using previous $\boldsymbol{k}(\omega)$ to obtain a new set of effective bianisotropic parameters, which are then used to obtain a more accurate photonic dispersion relation $\boldsymbol{k}(\omega)$, and so on.

3.2 Metamaterial transformation of the nonlocal dielectric response

To carry out the metamaterial transformation of the nonlocal dielectric response, the corresponding formulas of the more general piezoelectromagnetic case, given in Section 2.4, will be used. For a homogenized electromagnetic crystal without piezoelectric and piezomagnetic effects (3.1.1) the nonlocal dielectric response $\overline{\overline{\boldsymbol{A}}}^{\text{EM}}_{\text{eff,NL}}(\boldsymbol{k})$ calculated by the iterative procedure, can be represented in the already known form:

$$\overline{\overline{\boldsymbol{A}}}^{\text{EM}}_{\text{eff,NL}}(\boldsymbol{k}) = \overline{\overline{\boldsymbol{A}}}_{\text{eff},0} + k\overline{\overline{\boldsymbol{A}}}_{\text{eff},1} + k^2\overline{\overline{\boldsymbol{A}}}_{\text{eff},2}. \tag{3.2.1}$$

The electromagnetic quadratic operator $\overline{\overline{\boldsymbol{K_2}}}$ in this case is:

$$\overline{\overline{\boldsymbol{K_2}}} = \frac{1}{k}\begin{bmatrix} 0_{3\times3} & \boldsymbol{k}\times\overline{\overline{\boldsymbol{I}}} \\ 0_{3\times3} & 0_{3\times3} \end{bmatrix} \cdot \frac{1}{k}\begin{bmatrix} 0_{3\times3} & 0_{3\times3} \\ -\boldsymbol{k}\times\overline{\overline{\boldsymbol{I}}} & 0_{3\times3} \end{bmatrix} = \frac{1}{k^2}\begin{bmatrix} (\boldsymbol{k}\times\overline{\overline{\boldsymbol{I}}})\cdot(-\boldsymbol{k}\times\overline{\overline{\boldsymbol{I}}}) & 0_{3\times3} \\ 0_{3\times3} & 0_{3\times3} \end{bmatrix}. \tag{3.2.2}$$

In full matrix form, the expression for $\overline{\overline{\boldsymbol{K}}}_2$ is:

$$\overline{\overline{\boldsymbol{K_2}}} = \frac{1}{k^2} \begin{bmatrix} k_y^2 + k_z^2 & -k_x k_y & -k_x k_z & 0 & 0 & 0 \\ -k_x k_y & k_x^2 + k_z^2 & -k_y k_z & 0 & 0 & 0 \\ -k_x k_z & -k_y k_z & k_x^2 + k_y^2 & 0 & 0 & 0 \\ 0 & 0 & 0 & 0 & 0 & 0 \\ 0 & 0 & 0 & 0 & 0 & 0 \\ 0 & 0 & 0 & 0 & 0 & 0 \end{bmatrix} \tag{3.2.3}$$

Finally, the metamaterial transformation for the nonlocal dielectric response is given by the next expression:

$$\begin{aligned} \overline{\overline{\boldsymbol{A}}}^{\mathrm{EM}}_{\mathrm{eff,MM}}(\boldsymbol{k}) = &\left(\overline{\overline{\boldsymbol{A}'}}_{\mathrm{eff}}(\boldsymbol{k}) - \frac{\omega}{2k} \overline{\overline{\boldsymbol{A}}}_{\mathrm{eff},1} \overline{\overline{\boldsymbol{K}}}_{+} \overline{\overline{\boldsymbol{A}}}^{\mathrm{EM}}_{\mathrm{eff,NL}}(\boldsymbol{k}) - \omega \left[\overline{\overline{\boldsymbol{I}}} - \overline{\overline{\boldsymbol{K_2}}} \right] \overline{\overline{\boldsymbol{A}}}_{\mathrm{eff},2} \overline{\overline{\boldsymbol{K}}}_{+} \overline{\overline{\boldsymbol{A}}}^{\mathrm{EM}}_{\mathrm{eff,NL}}(\boldsymbol{k}) \right) \times \\ &\left(\overline{\overline{\boldsymbol{I}}} + \frac{\omega}{2k} \overline{\overline{\boldsymbol{K}}}_{-} \overline{\overline{\boldsymbol{A}}}_{\mathrm{eff},1} + \overline{\overline{\boldsymbol{K}}}_{-} \omega \overline{\overline{\boldsymbol{A}}}_{\mathrm{eff},2} \left[\overline{\overline{\boldsymbol{I}}} - \overline{\overline{\boldsymbol{K_2}}} \right] - \frac{\omega^2}{k^2} \overline{\overline{\boldsymbol{K}}}_{-} \overline{\overline{\boldsymbol{A}}}_{\mathrm{eff},2} \overline{\overline{\boldsymbol{K}}}_{+} \overline{\overline{\boldsymbol{A}}}^{\mathrm{EM}}_{\mathrm{eff,NL}}(\boldsymbol{k}) \right)^{-1} \end{aligned} \tag{3.2.4}$$

Here, $\overline{\overline{\boldsymbol{I}}}$ is a 6 × 6 unit matrix, ω is frequency, tensors $\overline{\overline{\boldsymbol{K}}}_{-}$ and $\overline{\overline{\boldsymbol{K}}}_{+}$ correspondingly are:

$$\overline{\overline{\boldsymbol{K}}}_{-} = \begin{bmatrix} 0_{3\times3} & 0_{3\times3} \\ -\boldsymbol{k} \times \overline{\overline{\boldsymbol{I}}} & 0_{3\times3} \end{bmatrix}, \qquad \overline{\overline{\boldsymbol{K}}}_{+} = \begin{bmatrix} 0_{3\times3} & \boldsymbol{k} \times \overline{\overline{\boldsymbol{I}}} \\ 0_{3\times3} & 0_{3\times3} \end{bmatrix} \tag{3.2.5}$$

The tensor $\overline{\overline{\boldsymbol{A}'}}_{\mathrm{eff}}(\boldsymbol{k})$ is explicitly expressed as:

$$\overline{\overline{\boldsymbol{A}'}}_{\mathrm{eff}}(\boldsymbol{k}) = \overline{\overline{\boldsymbol{A}}}_{\mathrm{eff},0} + k \left[\overline{\overline{\boldsymbol{I}}} - \overline{\overline{\boldsymbol{K_2}}} \right] \overline{\overline{\boldsymbol{A}}}_{\mathrm{eff},1} + k^2 \left[\overline{\overline{\boldsymbol{I}}} - \overline{\overline{\boldsymbol{K_2}}} \right] \overline{\overline{\boldsymbol{A}}}_{\mathrm{eff},2} \left[\overline{\overline{\boldsymbol{I}}} - \overline{\overline{\boldsymbol{K_2}}} \right]. \tag{3.2.6}$$

3.3 Specific results

3.3.1 Nonlocal response of 3D semiconductor-dielectric photonic crystal in the far-infrared range

Photonic crystals (PC) with tunable photonic band gaps (PBG) have been an object of intensive study in the previous decade [114], [115]. Several ways are available to tune PBG of PC: by applying an electrical field to liquid-crystal inclusions [116], [117]; as well as a magnetic field to control the frequency position and width of PBG [118], [119]. An outstanding idea to fabricate a tunable PC is the use of a semiconductor component [114] with a sufficiently large number of free charge carriers. Evidently, the plasma frequency of such constituents will strongly depend on temperature leading to a thermal shift of the PBG structure.

The temperature-dependent effective parameters for two types of homogenized photonic crystals will be calculated below. The first one is a square two-dimensional (2D) lattice of infinitely-long InSb square bars embedded in a silica glass (SiO_2) matrix. The second system to be considered here is a cubic three-dimensional (3D) PC composed of cut square bars of InSb in the dielectric glass matrix.

3.3.1.1 Semiconductor-dielectric photonic crystals description

The formalism described in Sec. 3.1 will be applied to calculate the effective parameters of a homogenized semiconductor-dielectric photonic crystal (SDPC). To obtain the effective nonlocal response matrix $\overline{\overline{\boldsymbol{A}}}_{\text{eff}}(\boldsymbol{k}(\omega),\omega)$, it is necessary to specify the components of the tensor $\overline{\overline{\boldsymbol{A}}}(\boldsymbol{r})$ (3.1.7), which here has the form

$$\overline{\overline{\boldsymbol{A}}}(\boldsymbol{r}) = \begin{bmatrix} \overset{\leftrightarrow}{\boldsymbol{\epsilon}}\ (\boldsymbol{r}) & 0 \\ 0 & \mu_0\ \overset{\leftrightarrow}{\boldsymbol{I}} \end{bmatrix}, \tag{3.3.1}$$

because the materials of the SDPC are assumed to have dielectric non-magnetic response with zero magneto-electric tensors (μ_0 is the vacuum permeability). The inclusion (semiconductor) and host material (dielectric) in the unit cell are isotropic having, respectively, permittivities ϵ_a and ϵ_b. In this case, the effective nonlocal-response matrix $\overline{\overline{\boldsymbol{A}}}_{\text{eff}}(\boldsymbol{k}(\omega),\omega)$ (3.1.8) is completely determined by the nonlocal effective permittivity tensor:

$$\overline{\overline{\boldsymbol{A}}}_{\text{eff}}(\boldsymbol{k}(\omega),\omega) = \begin{bmatrix} \overset{\leftrightarrow}{\boldsymbol{\epsilon}}_{\text{eff}}\ (\boldsymbol{k},\omega) & 0 \\ 0 & \mu_0\ \overset{\leftrightarrow}{\boldsymbol{I}} \end{bmatrix}. \tag{3.3.2}$$

We shall consider an inclusion of intrinsic indium antimonide whose frequency-dependent permittivity $\epsilon_a(\omega)$ in the THz range (below the phonon resonance) can be described by the Drude model as

$$\frac{\epsilon_a}{\epsilon_0} = \epsilon_r(0)\left(1 - \frac{\omega_p^2}{\omega^2 + i\nu\omega}\right), \tag{3.3.3}$$

where ϵ_0 is the vacuum permittivity, ω_p is a temperature-dependent plasma frequency, $\epsilon_r(0)$ (=17.7 for InSb) is the static background relative permittivity, and ν is a damping constant.

The semiconductor plasma frequency ω_p is given by the expression

$$\omega_p = \sqrt{\frac{N_e e^2}{m^* \epsilon_r(0)}}, \tag{3.3.4}$$

where N_e is the electron density, e is the electron charge, m^* ($= 0.015m_e$ for InSb) is the electron effective mass, and m_e is the free electron mass.

As it is seen in Eq. (3.3.4), the semiconductor plasma frequency is mainly affected by the free carrier concentration N_e. For indium antimonide the temperature dependence $N_e(T)$ is given by [114]:

$$N_e = 5.76 \times 10^{20} T^{3/2} \exp(-0.13/k_B T), \quad (1/\mathrm{m}^3). \tag{3.3.5}$$

The host matrix material is assumed to be silica glass (SiO_2) with low losses in the THz frequency range [120]; thus, the permittivity of the background material is $\epsilon_b = 4.0$.

3.3.1.2 Calculated nonlocal effective parameters

Consider two systems: i) a two-dimensional square lattice of indium antimonide bars embedded in silica glass (Fig. 3.1(a)) and ii) a 3D cubic array of InSb square bars in a host SiO_2-glass matrix (Fig. 3.1(b)).

In applying the nonlocal homogenization approach, described in Sec. 3.1, together with the modified FFDA, the InSb inclusions have been divided into n small cubes of side $a/13$, where a is the lattice constant of the 2D (square) and 3D (cubic) photonic crystals, respectively (here $a = 40\mu$m). The area of the square bars section is equal to $(4a/13)^2$ in both cases. The height of the isolated InSb bars in the cubic array is $12a/13 < a$.

The effective parameters for the square 2D PC are calculated as for the cubic array of square semiconductor bars, but having a height equal to the lattice constant a. Thus, the InSb bars of neighboring unit cells touch each other along the z direction, forming a square 2D PC.

For each of these systems, the nonlocal effective permittivity tensor (3.3.2) has been calculated at temperatures $T = 200$K and $T = 300$K. The carrier concentration and plasma frequencies for intrinsic indium antimonide at the chosen temperatures are:

$$\begin{aligned} T = 200K: \quad & N_e = 8.63198 \cdot 10^{20} (1/\mathrm{m}^3), \\ & \omega_p = 3.21627 \cdot 10^{12} (\mathrm{rad/s}) = 0.511885(\mathrm{THz}), \\ T = 300K: \quad & N_e = 1.95975 \cdot 10^{22} (1/\mathrm{m}^3), \\ & \omega_p = 1.53249 \cdot 10^{13} (\mathrm{rad/s}) = 2.43903(\mathrm{THz}). \end{aligned} \tag{3.3.6}$$

The temperature-dependent damping constant $\nu(T)$ used in the calculations is equal to $0.01\omega_p(T)$.

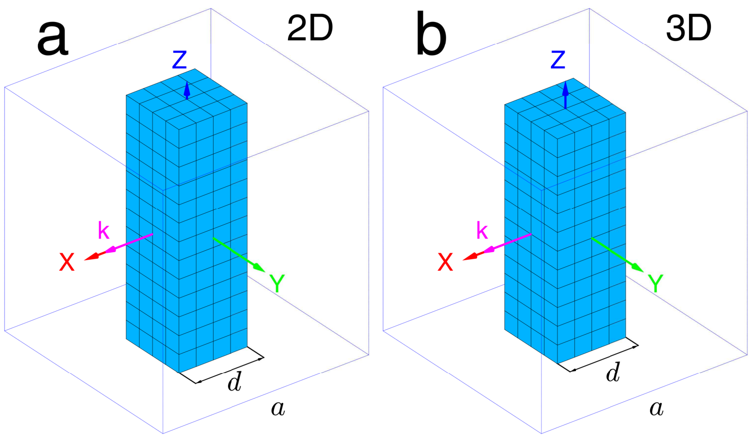

Figure 3.1: Square lattice of InSb bars (filling fraction $f_a = 9.5\%$) in silica glass background matrix (a); square bars of indium antimonide arranged in a cubic lattice (b) with filling fraction $f_a = 8.7\%$; in both cases the propagation wave vector is parallel to the x direction.

3.3.1.3 Square 2D array of InSb bars embedded in glass

We have considered electromagnetic modes, having electric field parallel to the z-axis and propagating along the x direction ($\boldsymbol{k} = k_x\hat{x}$) in the above-described InSb-glass square 2D PC. In this case, the nonlocal effective permittivity tensor $\overleftrightarrow{\boldsymbol{\epsilon}}_{\text{eff}}\,(\boldsymbol{k},\omega)$ (3.3.2) is diagonal with different principal values: $\epsilon_{xx} \neq \epsilon_{yy} \neq \epsilon_{zz}$ as for an orthorhombic PC.

Fig. 3.2 exhibits the numerically-calculated frequency dependences for the effective permittivity component ϵ_{zz} (Fig. 3.2(a)), the refractive index $n^{(z)} = \sqrt{\epsilon_{zz}/\epsilon_0}$ (Fig. 3.2(b)), as well as the dispersion relation $k_x(\omega)$ for the z-polarized photonic modes at $T = 200$K and $T = 300$K (Fig. 3.2(c)).

As it is seen in panel (a) of Fig. 3.2 the component ϵ_{zz} of the nonlocal effective permittivity tensor (Eq. (3.3.2)) turns out to be a complex number with $|\Re\epsilon_{zz}| \gg |\Im\epsilon_{zz}|$ because of the relatively-low losses of the semiconductor inclusion in the frequency range $\omega \gg \nu$ (see Eq. (3.3.3)).

At temperature $T = 200$K ($T = 300$K), $\Re\epsilon_{zz}(\omega)$ has a zero at the frequency $\omega = 1.8(7.4)$Trad/s, being negative below such a frequency and positive above it. Therefore, the effective refractive index $n^{(z)}$ is almost imaginary at the low-frequency range, but it is real above the zero of $\Re\epsilon_{zz}(\omega)$. The zero of $\Re\epsilon_{zz}(\omega)$ can be defined as an effective plasma frequency of the semiconductor-dielectric PC for photonic modes polarized along the axis of the infinite bars. It means that the InSb-glass square 2D array has, in fact, a “metallic” behavior with plasma frequency in the THz range.

Notice that the calculated effective parameter $\epsilon_{zz}(\omega)$ allows to obtain the exact phononic dispersion $k_x(\omega)$ (Fig.3.2(c)) within the whole first Brillouin zone (BZ) and even beyond it by using the formula:

$$k_x(\omega) = \omega\sqrt{\epsilon_{zz}(\omega)\mu_0}. \tag{3.3.7}$$

The band gaps for z-polarized photonic modes are characterized by a considerable imaginary part of their wave vector component k_x. In panel (c) of Fig. 3.2, two band gaps are observed. As the temperature is increased, the lowest photonic band gap becomes wider and the second band gap is shifted to higher frequencies. These results are due to the increase of the carrier concentration and plasma frequency of the InSb component with temperature (see Eq (3.3.6)) and totally agree with the photonic-band-structure calculations carried out in the work [114] for an InSb-dielectric 2D PC.

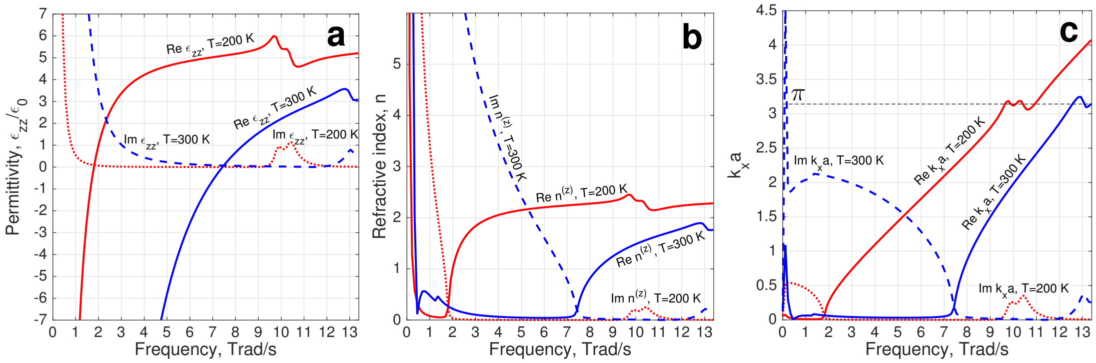

Figure 3.2: Effective permittivity (a), refractive index (b) and dispersion relation (c) for a square lattice of indium antimonide bars (filling fraction = 9.5 %).

3.3.1.4 Cubic array of InSb bars embedded in glass

Now consider the 3D PC with the unit cell as that shown in panel (b) of Fig. 3.1. As in the previous subsection, the nonlocal effective permittivity is calculated in the case of photonic modes, propagating along the x-axis and having electric field parallel to the z-direction (the axis of the InSb square bars). Again, the nonlocal effective permittivity tensor $\overleftrightarrow{\boldsymbol{\epsilon}}_{\text{eff}}\ (\boldsymbol{k}, \omega)$ (3.3.2) turns out to be diagonal and corresponds to the orthorhombic symmetry.

Comparing with the results, shown in Fig. 3.2, for the InSb-glass square 2D PC, the absence of a layer of small InSb cubes inside the unit cell, drastically modifies the relevant component (ϵ_{zz}) of the effective permittivity for such photonic modes.

Indeed, as it is observed in Fig. 3.2(a), the permittivity component $\epsilon_{zz}(\omega)$ and the effective refractive index $n^{(z)} = \sqrt{\epsilon_{zz}/\epsilon_0}$ are almost real numbers at the low-frequency range. Consequently, a low-frequency pass band emerges (see panel (c) of Fig. 3.2) and the InSb-glass cubic 3D PC behaves as a dielectric. The width of such a pass band increases with temperature.

Another interesting feature of the semiconductor-dielectric 3D PC is the presence of several band gaps. The lowest band gap (just above the first pass band) is very narrow, whereas the second one, turns out to be rather wide.

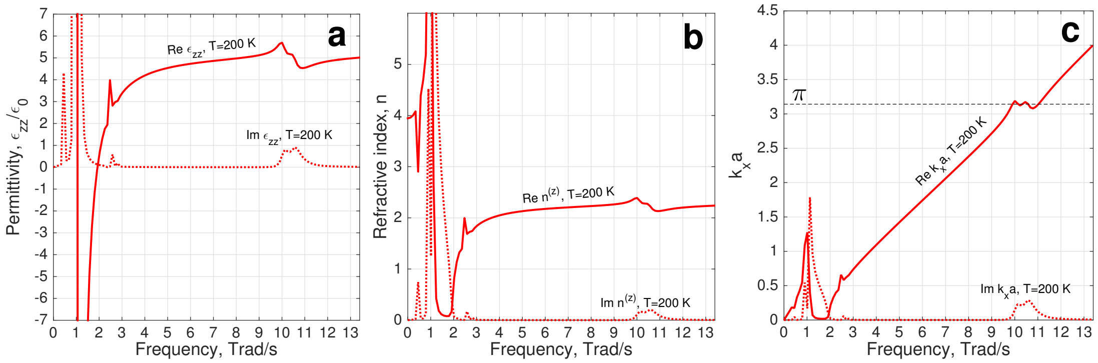

Figure 3.3: Effective permittivity (a), refractive index (b) and dispersion relation (c) for a 3D photonic crystal composed of indium antimonide (filling fraction = 8.7 %) in SiO_2-glass background, T = 200 K.

3.3.1.5 Optical spectra of a slab composed of InSb bars

Consider a slab of indium antimonide square bars in SiO_2 glass matrix at temperature T = 200 K (Fig. 3.5). The incident electromagnetic wave in vacuum ($x < 0$) is polarized along the semiconductor bars (z direction):

$$\boldsymbol{E}_i = (0, 0, E_i) e^{i\boldsymbol{q}_i \cdot \boldsymbol{r} - i\omega t} \tag{3.3.8}$$

The electric field of the reflected electromagnetic wave can be expressed as:

$$\boldsymbol{E}_r = (0, 0, E_r(x, y)), \tag{3.3.9}$$

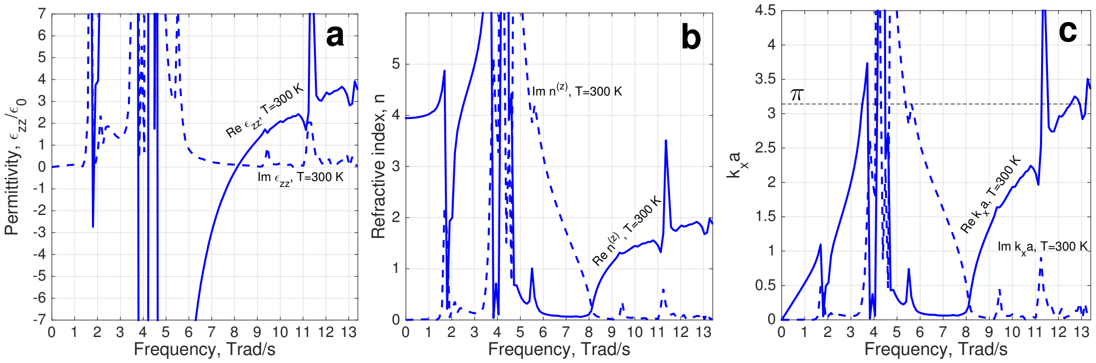

Figure 3.4: Effective permittivity (a), refractive index (b) and dispersion relation (c) for a 3D photonic crystal composed of indium antimonide (filling fraction = 8.7 %) in SiO_2-glass background, T = 300 K.

with $E_r(x, y)$ determined as following:

$$E_r(x, y) = e^{-i\omega t} \sum_{G_y} E_r(G_y) e^{iG_y y} e^{i\boldsymbol{q}_r(G_y)\cdot\boldsymbol{r}}, \tag{3.3.10}$$

where $\boldsymbol{q}_i$ and $\boldsymbol{q}_r$ correspondingly are:

$$\begin{aligned} \boldsymbol{q}_i =& (q_x(0), q_y, 0), \\ \boldsymbol{q}_r =& (-q_x(G_y), q_y, 0). \end{aligned} \tag{3.3.11}$$

Here, q_y and $q_x(G_y)$ are given by

$$\begin{aligned} q_y =& \frac{\omega}{c} \sin(\theta), \\ q_x(G_y) =& \sqrt{\frac{\omega^2}{c^2} - (q_y + G_y)^2}, \end{aligned} \tag{3.3.12}$$

where θ stands for the incidence angle, c is the speed of light in vacuum, $G_y = 2\pi n/a$ $(n = 0, \pm 1, \pm 2, ...)$, and $\Im(q_x(G_y)) > 0$.

The electric field of the transmitted electromagnetic wave in vacuum ($x > l$, where l is the slab thickness) can be written as:

$$\boldsymbol{E}_t = (0, 0, E_t(x, y)), \tag{3.3.13}$$

where $E_t(x, y)$ has the form:

$$E_t(x, y) = e^{-i\omega t} \sum_{G_y} E_t(G_y) e^{iG_y y} e^{i\boldsymbol{q}_t(G_y)\cdot\boldsymbol{r}}, \tag{3.3.14}$$

and $\boldsymbol{q}_t$ is:

$$\boldsymbol{q}_t = (q_x(G_y), q_y, 0). \tag{3.3.15}$$

We can describe the optical response of the composite system by using the nonlocal effective permittivity (3.3.2) when the wavelength λ in the external medium (vacuum) is sufficiently larger than the lattice constant a. In this case, the diffracted photonic modes ($G_y \neq 0$) are evanescent and the reflected and transmitted electric fields are well described by:

$$\begin{aligned} E_r(x,y) &\approx e^{-i\omega t} E_r(0) e^{i\boldsymbol{q}_r(0)\cdot\boldsymbol{r}}, \\ E_t(x,y) &\approx e^{-i\omega t} E_t(0) e^{i\boldsymbol{q}_t(0)\cdot\boldsymbol{r}}. \end{aligned} \tag{3.3.16}$$

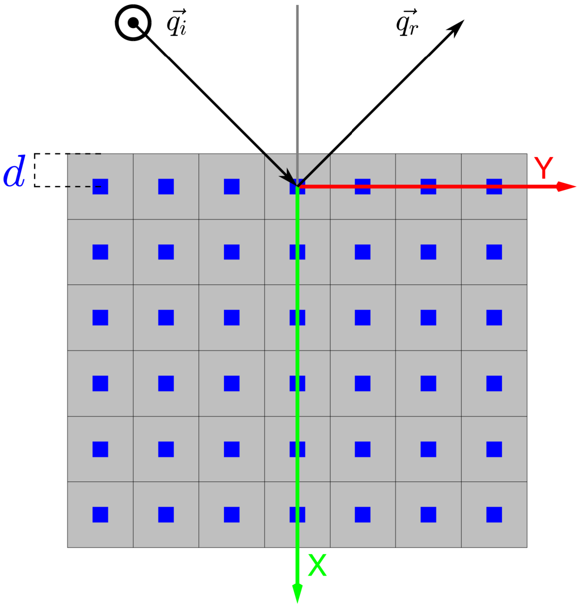

Figure 3.5: Scheme of a slab having a square periodic array of InSb bars embedded in silica-glass and six unit cells along the growth direction (x axis). The filling fraction of InSb is equal to 5.3 %, T = 200 K. The distance from the centroid of the bars to the vacuum-SDPC interface is given by parameter d.

For the system considered here, $\lambda > a$ (with $a = 40\mu$m) at frequencies below 47 Trad/s. In calculating the effective permittivity $\epsilon_{zz}(\boldsymbol{k}, \omega)$ for a homogenized medium, the component k_y should coincide with q_y (Eq. (3.3.12)) and the $k_x(\omega, q_y)$ component is calculated by using the above described iteration procedure and the expression:

$$k_x(\omega) = \sqrt{\epsilon_{zz}(q_y, \omega)\mu_0\omega^2 - q_y^2}. \tag{3.3.17}$$

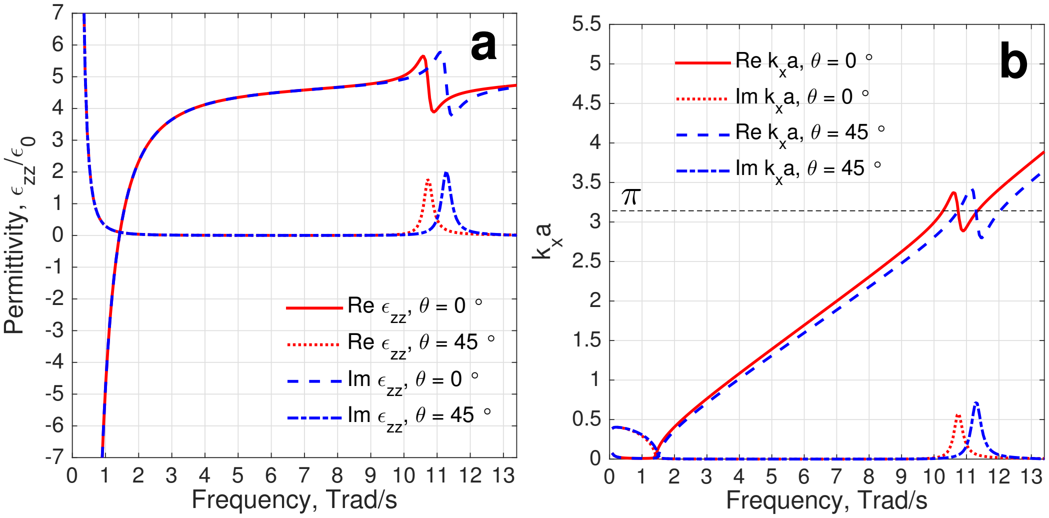

Figure 3.6: Effective permittivity (a) and dispersion relation (b) for a 2D photonic crystal composed of indium antimonide (filling fraction = 5.3 %) in SiO$_2$-glass background, T = 200 K.

In Fig. 3.6 the effective permittivity (panel (a)) and calculated dispersion relation $k_x(\omega)$ is presented (panel (b)) for a slab of indium antimonide square bars of side length $3a/13$ immersed into a glass matrix at the temperature T = 200 K with angles of incidence $\theta = 0°$ (red lines) and $\theta = 45°$ (blue lines).

The total (microscopic) electric $\boldsymbol{E}$ and magnetic $\boldsymbol{H}$ fields inside the homogenized slab can be expressed as:

$$\begin{aligned} \boldsymbol{E}(\boldsymbol{r}) &= e^{-i\omega t} \sum_{\boldsymbol{G}} e^{i\boldsymbol{G}\cdot\boldsymbol{r}} \left[\boldsymbol{E}_1(\boldsymbol{G}) e^{i\boldsymbol{k}_1\cdot\boldsymbol{r}} + \boldsymbol{E}_2(\boldsymbol{G}) e^{i\boldsymbol{k}_2\cdot\boldsymbol{r}}\right], \\ \boldsymbol{H}(\boldsymbol{r}) &= e^{-i\omega t} \sum_{\boldsymbol{G}} e^{i\boldsymbol{G}\cdot\boldsymbol{r}} \left[\boldsymbol{H}_1(\boldsymbol{G}) e^{i\boldsymbol{k}_1\cdot\boldsymbol{r}} + \boldsymbol{H}_2(\boldsymbol{G}) e^{i\boldsymbol{k}_2\cdot\boldsymbol{r}}\right], \end{aligned} \tag{3.3.18}$$

where $\boldsymbol{k}_1$ and $\boldsymbol{k}_2$ respectively are:

$$\begin{aligned} \boldsymbol{k}_1 &= (k_x, q_y, 0), \\ \boldsymbol{k}_2 &= (-k_x, q_y, 0). \end{aligned} \tag{3.3.19}$$

3.3.1.6 Boundary conditions for the finite-size slab

The effective nonlocal parameters of a homogenized photonic crystal can be used for determining reflectance and transmission optical spectra of finite-size periodical systems (slabs). In this case, it is well known that an effective nonlocal response is sensitive to the surface microstructure of the sample. Therefore, the application of the Maxwell boundary conditions for the macroscopic electric and magnetic fields may lead to discrepancies between the optical spectra of the homogenized PC and those of the real PC even at rather low frequencies. To overcome this problem, one of the possible solutions is to introduce additional surface parameters or transition layers [58], [59].

Here, the exact boundary conditions for the "macroscopic" component of the electromagnetic field without introducing any additional surface parameters (surface susceptibilities) or transition layers will be derived within the framework of the developed homogenization theory.

To describe the full electromagnetic field inside a slab, especially at high frequencies in the strong nonlocal regime, it is necessary to take into account all the information about the spatially-dispersive finite-size sample. Secondly, one needs to express the microscopic field inside the slab in terms of the slow-oscillating macroscopic field. Finally, the obtained microscopic field, having all the information about the microstructure, is used for linking electric and magnetic fields at the boundaries of the slab.

The microscopic field inside of the homogenized medium is described as a Fourier expansion it follows (Subsection 2.3.6):

$$\boldsymbol{v}(\boldsymbol{G}) = -\sum_{\boldsymbol{G'}\neq 0} \overline{\overline{\boldsymbol{D}}}_s^{-1}(\boldsymbol{k},\boldsymbol{G},\boldsymbol{G'})\overline{\overline{\boldsymbol{D}}}(\boldsymbol{k},\boldsymbol{G'},0)\boldsymbol{V_0}. \tag{3.3.20}$$

Then, using the relation between the inverse dynamic matrix $\overline{\overline{\boldsymbol{D}}}(\boldsymbol{k},\boldsymbol{G},\boldsymbol{G'})$ and the inverse sub-matrix $\overline{\overline{\boldsymbol{D}}}_s(\boldsymbol{k},\boldsymbol{G},\boldsymbol{G'})$ [111], the following expression is obtained:

$$\boldsymbol{v}(\boldsymbol{G}) = -\overline{\overline{\boldsymbol{I}}}\delta_{\boldsymbol{G},0}\boldsymbol{V_0} + \overline{\overline{\boldsymbol{D}}}^{-1}(\boldsymbol{k},\boldsymbol{G},0)\left(\overline{\overline{\boldsymbol{D}}}^{-1}(\boldsymbol{k},0,0)\right)^{-1}\boldsymbol{V_0}. \tag{3.3.21}$$

The Bloch function of the microscopic field $\boldsymbol{v}(\boldsymbol{r})$ can be expressed as:

$$\boldsymbol{v}(\boldsymbol{r}) = e^{i\boldsymbol{k}\cdot\boldsymbol{r}}\boldsymbol{V}_0 + e^{i\boldsymbol{k}\cdot\boldsymbol{r}}\sum_{\boldsymbol{G}\neq 0}\boldsymbol{v}(\boldsymbol{G})e^{i\boldsymbol{G}\cdot\boldsymbol{r}}. \tag{3.3.22}$$

Employing the relation (3.3.21), the microscopic field inside the slab in terms of the macroscopic field $\boldsymbol{V}_0$ is:

$$\boldsymbol{v}(\boldsymbol{r}) = e^{i\boldsymbol{k}\cdot\boldsymbol{r}} \left(\sum_{\boldsymbol{G}} \overline{\overline{\boldsymbol{D}}}^{-1}(\boldsymbol{k},\boldsymbol{G},0) e^{i\boldsymbol{G}\cdot\boldsymbol{r}} \right) \left(\overline{\overline{\boldsymbol{D}}}^{-1}(\boldsymbol{k},0,0) \right)^{-1} \boldsymbol{V}_0. \tag{3.3.23}$$

The important outcome of the derived above expression is that neglecting terms with $\boldsymbol{G} \neq 0$, the usual macroscopic Maxwell boundary conditions are obtained. The tensor $\left(\overline{\overline{\boldsymbol{D}}}^{-1}(\boldsymbol{k},0,0) \right)^{-1}$ is calculated within the developed homogenization approach, thus the component in the first parenthesis of Eq. (3.3.23) is responsible for describing the microscopic field. Using the form factor division approach together with the average field approximation (Subsection 2.3.8), one can find:

$$\sum_{\boldsymbol{G}} \overline{\overline{\boldsymbol{D}}}^{-1}(\boldsymbol{k},\boldsymbol{G},0) e^{i\boldsymbol{G}\cdot\boldsymbol{r}} = \overline{\overline{\boldsymbol{T}}}^{-1}(0) - \omega \sum_{\boldsymbol{G}} e^{i\boldsymbol{G}\cdot\boldsymbol{r}} \overline{\overline{\boldsymbol{T}}}^{-1}(\boldsymbol{G}) \Delta \overline{\overline{\boldsymbol{A}}} \sum_{j=1}^{n} e^{-i\boldsymbol{G}\cdot\boldsymbol{r}_j} F_v(\boldsymbol{G}) < \overline{\overline{\boldsymbol{P}}}_j > . \tag{3.3.24}$$

Here, ω is frequency in rad·s^{-1}, $F_v(\boldsymbol{G})$ is a form factor of a small inclusion cube, and $< \overline{\overline{\boldsymbol{P}}}_j >$ is an average field within the inclusion cube. It should be emphasized that Eq. (3.3.24) is sensitive to the position of the boundary inside the crystal (given by radius-vector $\boldsymbol{r}$).

Hence, knowing the parameters of an infinite homogeneous medium, it is possible to determine reflectance and transmission coefficients for a finite-size sample. The Maxwell boundary conditions for the tangential components of the total electric and magnetic fields at the vacuum/slab interface $x^{(1)} = -d$ (see Fig. 3.5) should be applied:

$$\begin{cases} E_z^{(1)}|_{x=x^{(1)}} = E_z^{(2)}|_{x=x^{(1)}}, \\ H_y^{(1)}|_{x=x^{(1)}} = H_y^{(2)}|_{x=x^{(1)}}. \end{cases} \tag{3.3.25}$$

At the second slab/vacuum boundary $x^{(2)} = 6a - d$:

$$\begin{cases} E_z^{(2)}|_{x=x^{(2)}} = E_z^{(3)}|_{x=x^{(2)}}, \\ H_y^{(2)}|_{x=x^{(2)}} = H_y^{(3)}|_{x=x^{(2)}}. \end{cases} \tag{3.3.26}$$

Equations (3.3.25) can be written as:

$$\begin{aligned} E_i\alpha_1 + E_r\alpha_2 &= \beta_1 V_E^{(1)} + \beta_2 V_E^{(2)}, \\ E_i\alpha_1^{'} + E_r\alpha_2^{'} &= \beta_1^{'} V_E^{(1)} + \beta_2^{'} V_E^{(2)}, \end{aligned} \tag{3.3.27}$$

where E_i is the amplitude of the incident wave (3.3.8), E_r is the amplitude of the reflected wave (3.3.10). The $V_E^{(1)}$ and $V_E^{(2)}$ is the z-components of the amplitude of the macroscopic electric field, respectively, $\boldsymbol{E}(\boldsymbol{G}=0,\boldsymbol{k}_x)$ and $\boldsymbol{E}(\boldsymbol{G}=0,-\boldsymbol{k}_x)$ inside the slab. Magnetic fields are expressed in terms of electric field using Ampere law.

Equations (3.3.26) can be rewritten in the form:

$$\begin{aligned} E_t\gamma_1 &= \xi_1 V_E^{(1)} + \xi_2 V_E^{(2)}, \\ E_t\gamma_1^{'} &= \xi_1^{'} V_E^{(1)} + \xi_2^{'} V_E^{(2)}. \end{aligned} \tag{3.3.28}$$

The corresponding coefficients are given below:

$$\begin{array}{lcllcl} \alpha_1 &=& e^{iq_x^{(0)}x^{(1)}} & \alpha_2 &=& e^{-iq_x^{(0)}x^{(1)}} \\ \alpha_1^{'} &=& -q_x^{(0)}\alpha_1 & \alpha_2^{'} &=& q_x^{(0)}\alpha_2 \\ && && & \\ \beta_1 &=& M_{33}^{(+)}e^{ik_x^{(2)}x^{(1)}} & \beta_2 &=& M_{33}^{(-)}e^{-ik_x^{(2)}x^{(1)}} \\ \beta_1^{'} &=& -k_x^{(2)}M_{55}^{(+)}e^{ik_x^{(2)}x^{(1)}} & \beta_2^{'} &=& k_x^{(2)}M_{55}^{(-)}e^{-ik_x^{(2)}x^{(1)}} \\ && && & \\ \xi_1 &=& \beta_1 e^{ik_x^{(2)}(x^{(2)}+d)} & \xi_2 &=& \beta_2 e^{-ik_x^{(2)}(x^{(2)}+d)} \\ \xi_1^{'} &=& \beta_1^{'} e^{ik_x^{(2)}(x^{(2)}+d)} & \xi_2^{'} &=& \beta_2^{'} e^{-ik_x^{(2)}(x^{(2)}+d)} \\ && && & \\ \gamma_1 &=& e^{iq_x^{(0)}x^{(2)}} & \gamma_1^{'} &=& -q_x^{(0)}e^{iq_x^{(0)}x^{(2)}} \end{array} \tag{3.3.29}$$

The coefficients of $\overline{\overline{\boldsymbol{\beta}}}$ matrix are described by 6 x 6 matrices $\overline{\overline{\boldsymbol{M}}}^{(+)}$ and $\overline{\overline{\boldsymbol{M}}}^{(-)}$ are:

$$\begin{aligned} \overline{\overline{\boldsymbol{M}}}^{(+)} &= \left(\sum_{G_x}\overline{\overline{\boldsymbol{D}}}^{-1}(k_x^{(2)},G_x,0)e^{iG_xx^{(1)}}\right)\left(\overline{\overline{\boldsymbol{D}}}^{-1}(k_x^{(2)},0,0)\right)^{-1} \\ \overline{\overline{\boldsymbol{M}}}^{(-)} &= \left(\sum_{G_x}\overline{\overline{\boldsymbol{D}}}^{-1}(-k_x^{(2)},G_x,0)e^{iG_xx^{(1)}}\right)\left(\overline{\overline{\boldsymbol{D}}}^{-1}(-k_x^{(2)},0,0)\right)^{-1} \end{aligned} \tag{3.3.30}$$

In the matrix form, equations (3.3.27) and (3.3.28) are expressed as follows:

$$\begin{aligned} \begin{pmatrix}\alpha_1 & \alpha_2 \\ \alpha_1^{'} & \alpha_2^{'}\end{pmatrix}\begin{pmatrix}E_i \\ E_r\end{pmatrix} &= \begin{pmatrix}\beta_1 & \beta_2 \\ \beta_1^{'} & \beta_2^{'}\end{pmatrix}\begin{pmatrix}V_E^{(1)} \\ V_E^{(2)}\end{pmatrix}, \\ \begin{pmatrix}\xi_1 & \xi_2 \\ \xi_1^{'} & \xi_2^{'}\end{pmatrix}\begin{pmatrix}V_E^{(1)} \\ V_E^{(2)}\end{pmatrix} &= \begin{pmatrix}\gamma_1 & 0 \\ 0 & \gamma_1^{'}\end{pmatrix}\begin{pmatrix}E_t \\ E_t\end{pmatrix} \end{aligned} \tag{3.3.31}$$

The relation between the amplitudes of the incident, reflected, and transmitted waves is given by the following matrix equation:

$$\begin{pmatrix}E_i \\ E_r\end{pmatrix} = \overline{\overline{\boldsymbol{X}}}_{2\times 2}\begin{pmatrix}E_t \\ E_t\end{pmatrix}, \tag{3.3.32}$$

where $\overline{\overline{\boldsymbol{X}}}_{2\times 2} = \overline{\overline{\boldsymbol{\alpha}}}^{-1} \cdot \overline{\overline{\boldsymbol{\beta}}} \cdot \overline{\overline{\boldsymbol{\xi}}}^{-1} \cdot \overline{\overline{\boldsymbol{\gamma}}}$, and the matrices $\overline{\overline{\boldsymbol{\alpha}}}, \overline{\overline{\boldsymbol{\beta}}}, \overline{\overline{\boldsymbol{\xi}}}, \overline{\overline{\boldsymbol{\gamma}}}$ are correspondingly defined by Eq. (3.3.31).

The reflectivity R and transmittance T are directly found by using the components of matrix $\overline{\overline{\boldsymbol{X}}}$:

$$\begin{aligned} t &= X_{11} + X_{12}, \\ r &= (X_{21} + X_{22})/t, \\ T &= \left|\frac{1}{t}\right|^2, \\ R &= |r|^2 . \end{aligned} \tag{3.3.33}$$

The reflectivity and transmittance spectra are presented in Fig. 3.7(a) for the angles of incidence $\theta = 0°$ and $\theta = 45°$ a slab thickness equal to $6a$. Note that the pass bands and stop bands have a good correspondence with the dispersion relations shown in Fig. 3.6. The pass bands exhibit Fabry-Perot resonances because of the finite size of the slab. Panels (b) and (c) show the influence of the surface microstructure, specifically, the effect of the parameter d on the optical spectra. Such an effect is well manifested in the nonlocal regime.

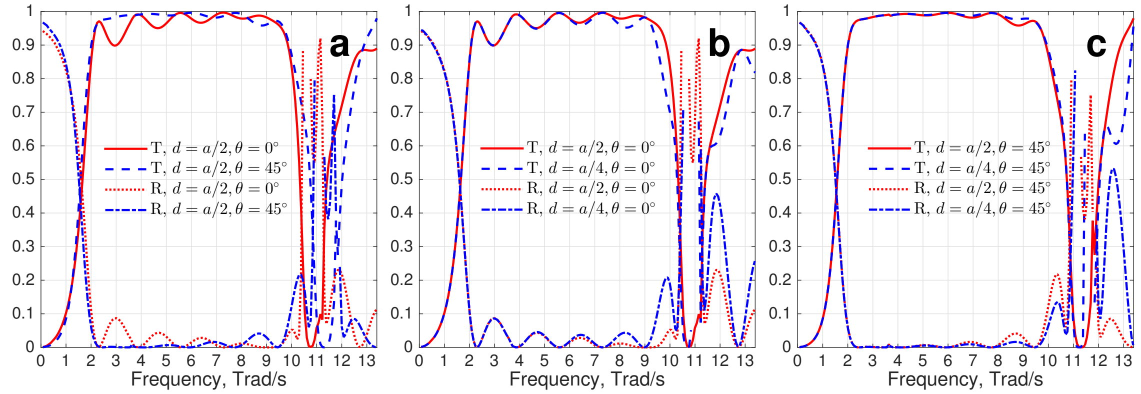

Figure 3.7: Transmission and reflection for 6-layered structure of InSb in glass for different values of the parameters d and θ and a filling fraction equal to 5.3 % at T = 200 K.

3.3.1.7 Discussion

The results presented here (Figs. 3.2 to 3.4) demonstrate the usefulness of the applied nonlocal homogenization approach, based on the Fourier formalism and the FFDA. Nevertheless, our approach still requires the calculation of sums over a large number of reciprocal lattice vectors for a good accuracy of the results.

In applying the nonlocal homogenization approach, an iterative procedure to determine the photonic dispersion relation $\boldsymbol{k}(\omega)$, which provides only one solution depending on the chosen initial value for the wave vector was used. The presented calculations, an initial value close to zero ($\boldsymbol{k} \rightarrow 0$) of the wave vector has been used. In addition, in each step of the iterative procedure, the complex wave vector (i.e. the root of Eq. (3.3.7)) with positive imaginary part ($\Im k_x > 0$) is chosen. At sufficiently large frequencies, the obtained solution for $\boldsymbol{k} = k_x(\omega)\hat{x}$ can lie in the second Brillouin zone in the extended scheme (see panels (c) of Figs. 3.2-3.4). The latter predictions agree with those of the work [86], where it was found that the nonlocal effective dielectric response for metal-dielectric photonic crystals can lead to wave vectors beyond the first BZ. Although the photonic band structure can be calculated by using other methods (for example, one of them is given by [114] for the 2D case), the applied-here homogenization method allows to analyze the complex nonlocal effective parameters and, consequently, physically describe the metamaterial behavior of the homogenized photonic crystals. Indeed, the exhibited results in Fig. 3.2 (Figs. 3.3 and 3.4) for a 2D (3D) semiconductor-dielectric photonic crystal have permitted to demonstrate the plasma-like (dielectric) behavior of such homogenized systems.

The presented here results were obtained for photonic modes propagating along one of the principal axes of the homogenized photonic crystal. Nevertheless, the nonlocal effective permittivity tensor depends on both magnitude and direction of the wave vector $\boldsymbol{k}$. For an arbitrary direction of $\boldsymbol{k}$, the permittivity tensor $\overset{\leftrightarrow}{\epsilon}$ can contain non-diagonal terms and, therefore, its form should be analyzed at every step of the iteration procedure.

In studying the propagation of electromagnetic waves in an infinite photonic crystal, the wave-vector depends on frequency. In this case, the spatial dispersion cannot be distinguished from the frequency dependence [112]. Within the proposed formalism, the formulas for the effective parameters (permittivity) provide the explicit dependence on the wave vector $\boldsymbol{k}$. Here it was shown that such formulas can be applied not only for calculating the dispersion relation of the photonic eigenmodes, but also for the excitation of photonic modes in finite-size samples.

Despite having considered here the simplest geometries, the described homogenization method itself does not impose any restriction on the inclusion structural complexity. This outcome opens a very wide field of possible systems to be studied - semiconductor-dielectric 3D photonic crystals with more sophisticated inclusions in the unit cell. Besides, the output effective matrix $\overline{\overline{\boldsymbol{A}}}_{\text{eff}}$ components are fully complex, which can be useful to estimate energy losses in the homogenized PC. Moreover, it should be commented that the applied nonlocal homogenization approach cannot lead to a magnetic or chiral response if the constituents are nonmagnetic or nonchiral materials in contrast to other homogenizations methods [60], [61]. The reason is that the magnetic and chiral effects are hidden in the wave vector dependence of the effective matrix $\overline{\overline{\boldsymbol{A}}}_{\text{eff}}(\boldsymbol{k}(\omega), \omega)$ (3.3.2) [75], [121].

The homogenization approach applied here provides the effective dielectric permittivity tensor of a periodic conductor-dielectric medium within the Fourier formalism not only in the long wavelength limit [79], [122], but also beyond it. In this kind of nonlocal approach, the artificial magnetism or chirality are hidden in the nonlocal dielectric response. There exist other homogenization methods which are based on averaging the fields over the unit cell of the periodic medium [61], [68], [69], [123]. The predictions of homogenization theories in the nonlocal regime may be different, particularly, for finite-size periodic systems. One of the reasons for such a difference is the sensitivity of the nonlocal average dielectric response to the surface structure of the sample [58].

Relying on the presented results, infra-red shutters and detectors may be fabricated with a cut-off frequency depending not only on the metamaterial structure but also on temperature. Complex inclusions typically will lead to changes in the photonic band structure, namely to the appearance of new band gaps. Therefore, our results can be useful for designing effective temperature-controlled filters for the THz range. In general, a whole new class of optical devices can be designed by including semiconductor constituents in metamaterial structures. An example of such an idea is the use of the well-known split-ring resonators [7] made of semiconductor immersed into a glass matrix for fabricating metamaterials with negative refractive index in a certain frequency range, which might be tuned by varying the temperature.

3.3.2 2D periodic array of metallic wires in air: nonlocal and metamaterial response

Consider a system of aluminium wires, which are arranged in a 2D square lattice in an air background. This is a relatively simple structure with well known physical properties [3], [4] to start with.

The unit cell is shown in Figure 3.8. The most interesting case of wave propagation

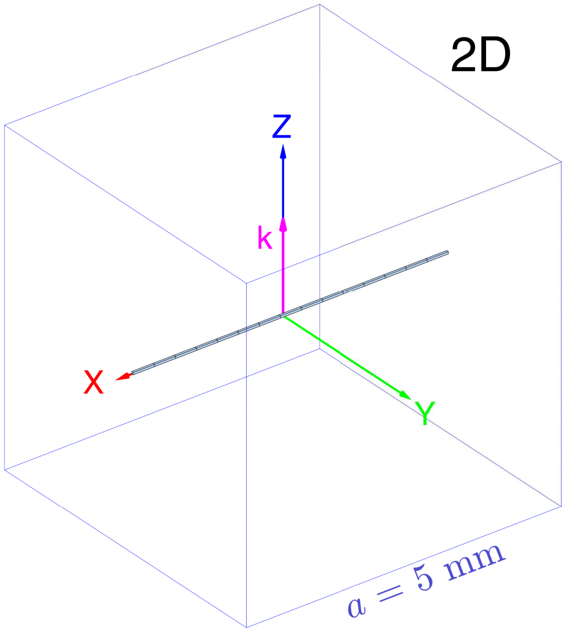

Figure 3.8: Aluminium wires in 2D square lattice, a = 5 mm, filling fraction of inclusion is 0.0016 %.

Lattice type	Square
Period, a	5 mm
Inclusion material	Aluminium
Background	Air
Aluminium plasma frequency, ω_p	15 eV
Aluminium damping constant, γ	0.1 eV
Wire side length l	20 μm
Inclusion filling fraction	0.0016 %
Analytical formula result for ω_p^{eff}	10.1797 GHz
Modeling result for ω_p^{eff}	10.67 GHz

Table 3.1: Main parameters of 2D metal-dielectric periodic structure.

is that when the wave vector $\boldsymbol{k}$ is parallel to z-axis and the electric field $\boldsymbol{E}||x$. In this case, the propagating TM modes will excite plasma oscillations along the $\hat{x}$ direction.

Aluminium square-profiled wires are used with the wire side length l equal to 20 μm. The effective plasma frequency for the square aluminium wires can be calculated by using the formula derived in the work [121]:

$$\omega_p^2 = \frac{2\pi c^2}{a^2 \ln(a/l)}, \tag{3.3.34}$$

where a is the structure period, l is the square wire side length. Varying the wire side length l, one can alter the effective plasma frequency ω_p^{eff} for a fixed period $a = 5$ mm (see Figure 3.9).

In our model, a frequency dependent permittivity of aluminium will be described by the Drude model:

$$\epsilon_r(\omega) = 1 - \frac{\omega_p^2}{\omega^2 + i\gamma\omega}, \tag{3.3.35}$$

with the parameters ω_p and γ given in Table 3.1.

Figure 3.10 shows the nonlocal dielectric response (NL) for $\boldsymbol{E}$-modes polarized

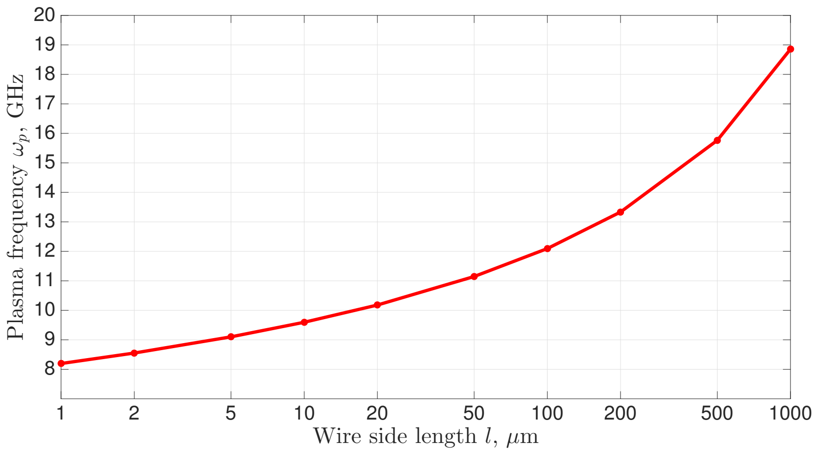

Figure 3.9: Dependence of the effective plasma frequency ω_p^{eff} on the square aluminium side length l for a simple cubic lattice, with period $a = 5$ mm.

along $\hat{x}$ direction. The filling fraction of metallic wires plays the main role in changing the electron density. At low frequencies the electron shielding against an incident wave is very effective, hence only evanescent modes can excited. At frequencies $\omega/\omega_p > 1$ electrons no longer provide a shielding against the incident electromagnetic wave allowing the propagation of electromagnetic modes in the homogenized crystal. Hereby, a typical metal behavior is observed because of the appearance of a low-frequency band gap. Increasing the metal volume fraction inside the unit cell, the effective plasma frequency rises to that of a pure metal; if the wire volume is too small then the low-frequency band gap vanishes. Hence, changing the section of metallic wires, one can control the width of the negative permittivity region from infrared to microwave range.

In addition, the calculated metamaterial transformation (MM) for a nonlocal dielectric response using (3.2.4) is presented in Figure 3.10. Initially, for each frequency, a nonlocal dielectric solution (NL) is found by using the FFDA with the iteration procedure to obtain the dispersion relation. Comparing the nonlocal dielectric response with the metamaterial, one should note that the resulting effective magnetic permeability is constant and equal to 1 (red line); indeed, there is no magnetic contrast between air and aluminium. However, as it is seen in the case of the metamaterial response, the effective permeability $\overset{\leftrightarrow}{\boldsymbol{\mu}}$ depends on both the frequency and the wave vector, whereas the effective permittivity tensor $\overset{\leftrightarrow}{\boldsymbol{\epsilon}}$ became partially local. The resulting dispersion relations of nonlocal dielectric response and of the metamaterial one are practically identical. It allows to state that the metamaterial transformation can be used to describe a photonic crystal in terms of nonlocal magnetic permeability function $\overset{\leftrightarrow}{\mu}(\boldsymbol{k},\omega)$ with the same dispersion that is described in terms of nonlocal dielectric function. The physical explanation of this fact is that electric and magnetic fields are not independent in the dynamic case, so the nonlocality can also be associated with the magnetic response [124].

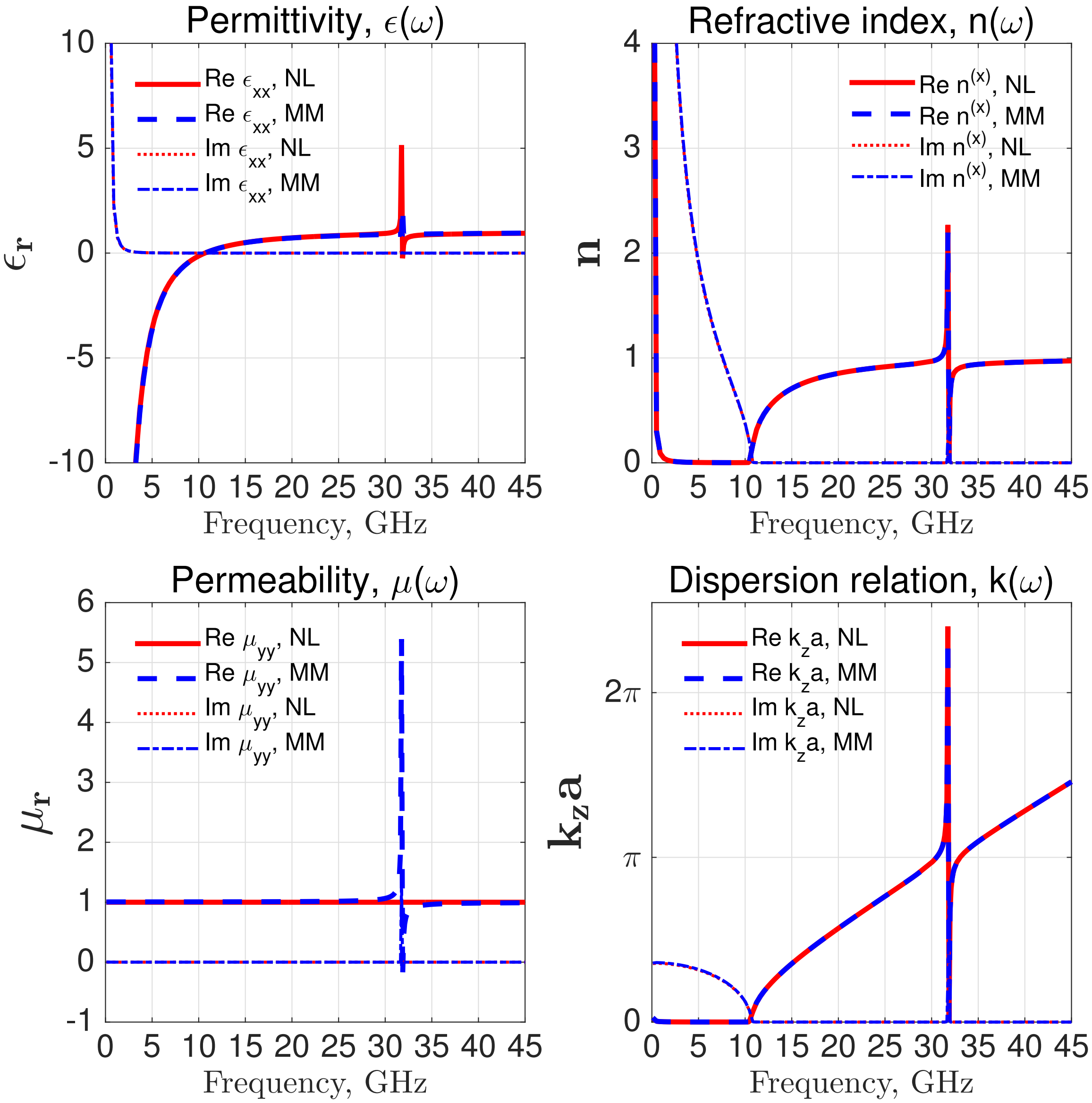

Figure 3.10: Comparison of the effective nonlocal dielectric (NL) and metamaterial (MM) response for 2D square lattice of Al wires, the lattice parameter $a = 5$ mm, and the aluminium wire square side $l = 20$ μm.

3.3.3 Metamaterial microwave response of 3D periodic structures

The microwave range is a part of the electromagnetic radiation spectrum, with the photon energies laying between the infra-red region and radio waves. The most important applications for the microwave range are radio-communications, wireless networks, medical treatment, space satellite communications, sensing, metals heating and much more.

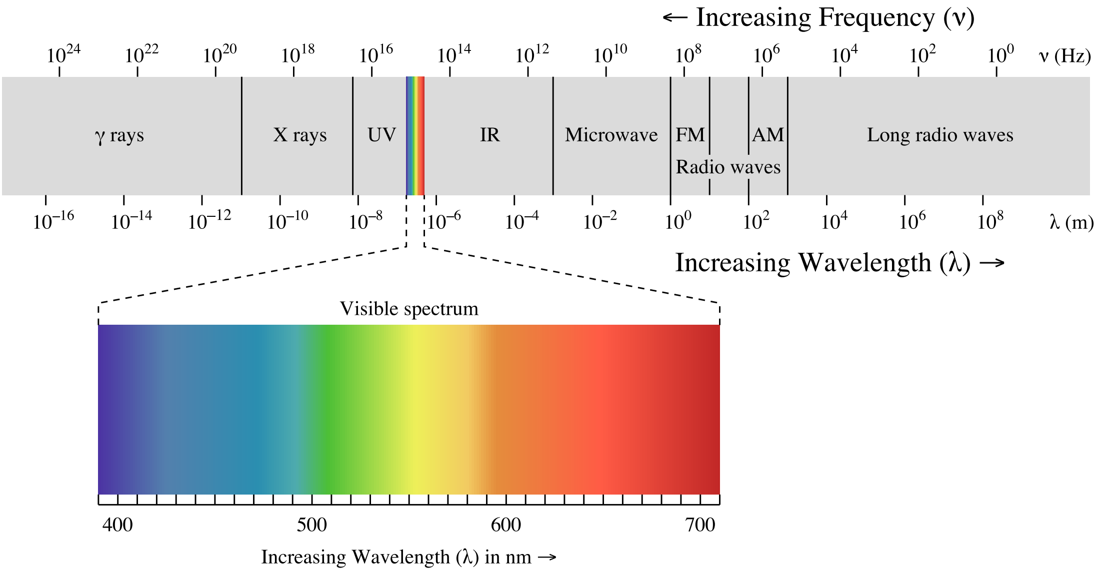

Figure 3.11: Electromagnetic spectrum diagram. Frequencies/wavelengths/photon energies corresponding to microwave range are situated between 300 MHz/ 100 cm/1.24 μeV and 300 GHz/ 0.1 cm/1.24 meV.

Wireless information transport is using microwave frequencies, whose range is being divided into bands. A short list of main bands is presented below in Table 3.2.

First experimental demonstration of metamaterials with negative refraction index was demonstrated at microwave frequencies [113] for the X-band and the reason is quite simple: macroscopic samples are easier to build, the equipment for the X-band (widely used radar band, see Appendix C) is accessible. Besides, a variety of prototyping methods is available to make a photonic crystal with very good unit cells repeatability: micro-lithography, 3D printing of metal-dielectric structures, mechanical milling etc. The other advantage of working in microwave is that a metamaterial can be easily characterized using modern spectrum analyzers.

Band	Frequency, GHz	Wavelength, cm	Purpose
L	1 — 2	30 — 15	Radio, mobile phones GSM
S	2 — 4	15 — 7.5	Wifi, mobile networks
C	4 — 8	7.5 — 3.75	Long-distance radio-communications
X	8 — 12	3.75 — 2.5	Radar, microwave microscopy
Ku	12 — 18	2.5 — 1.675	Satellite communications
K	18 — 26.5	1.675 — 1.13	Radars, astronomy observations
Ka	26.5 — 40	1.13 — 0.5	Satellite communications

Table 3.2: Commonly used microwave bands defined by IEEE standard [125].

3.3.3.1 Common substrates for GHz range

A typical microwave metamaterial is a metal-dielectric periodic structure; metamaterial effects are mainly determined by the metallic inclusion filling fraction and geometry; the dielectric part serves as a host matrix.

In the microwave, a copper-clad printed circuit fiberglass board is frequently used because of moderate losses, fabrication simplicity and relatively low cost. Furthermore, a high variety of methods (chemical etching, laser and mechanical engraving, lithography, direct printing) are available to print the desired matrix of resonators into the surface of copper. The whole class of such materials is called FR ("Flame resistant"), which is composed of the fiberglass cloth with an epoxy resin binder to achieve flame resistant properties. The standard itself determines certain groups of materials, however, one of the most used among them is FR4-class. A certain degree of manufacturer-production parameters fluctuation is always present [126]; materials from different manufacturers are often differing in the main physical parameters - dielectric permittivity, density etc. In frequency-critical applications, a difference in relative permittivity can shift the negative refraction zone of designed metamaterial. In particular, an increase of the real part of the dielectric permittivity results in a shift of the structure resonances to low frequencies.

Average parameters of common substrates potentially suitable for using in metamaterials fabrications are given in Table 3.3. Certain types of applications require ceramic based substrates made from alumina Al_2O_3 or aluminium nitride AlN with dopant elements (beryllium oxide). The main advantage of ceramic based substrates is a high thermal conductivity of the substrate, so the device can operate at higher work temperatures; thermal expansion coefficient close to that of silicon, which helps to integrate in micro-circuits. The typical alumina-based ceramic substrate board has a relative permittivity ϵ_r in the range between $9.0 - 9.5$.

	FR4	G10	RT Duroid 6035HTC
Type of dielectric	Flame-retardant brominated epoxy	Glass epoxy	Ceramic filled PTFE
Mass density, kg/m^3	1850	1810	2200
Relative permittivity, ϵ_r	4.5 + 0.018i	5.0 + 0.025i	3.50 + 0.0013i

Table 3.3: Average parameters of commonly used printed boards materials.

The results of measuring FR4 substrates in microwave and RF presented in [126] show a dissipation factor equal to 0.025 at 15 GHz. The given value for the dissipation factor is considered acceptable for metamaterials prototyping, and the presented results in this thesis are obtained using FR4 substrates.

3.3.3.2 Modeling of split-ring resonators structure

Above an electromagnetic metamaterial transformation has been developed and results for a square lattice of metallic wires in air were presented. It is interesting to demonstrate the metamaterial response for a structure possessing a verified negative refractive index. An example of such a system is the split-ring resonators structure [113].

A typical split-ring resonator is a structure consisting of two principal parts (Figure 3.12) - metallic wires, forming a 2D lattice on the plane whose normal is the z direction, and cut (or split) metallic rings. As it was demonstrated before [3], [4], a two-dimensional square lattice of thin wires can exhibit a negative permittivity at microwave frequencies. Controlling the wire thickness one can shift the plasma resonance frequency to desired values.

Assuming that the $\boldsymbol{k}$ vector is parallel to $y-$axis, the refractive index is defined as:

$$n = \sqrt{\epsilon_r^{zz} \mu_r^{xx}} \tag{3.3.36}$$

The split-ring resonators design has certain degree of the bianisotropic response [8], however, the results of the calculated dispersion relation will be presented considering the bianisotropic effects negligible.

The instrument to control effective permittivity was known, however, in order to form a left-handed medium it is strongly required to achieve a negative magnetic permeability in the same frequency range as permittivity does. This goal was achieved by adding concentric split-ring conducting wires, that act as a resonator at microwave frequencies. Splitting the metallic ring gives a capacitor, that brings a magnetic resonance to lower frequencies. First metamaterial samples provided only a narrow negative refractive index region, nevertheless, the experimental demonstration of the negative dispersion was a huge advance in modern physics.

Figure 3.12: Split-ring resonators sample demonstrating a negative refraction within X-band [113].

Applying the general homogenization approach, the effective metamaterial response parameters for the structure studied in [113] will be presented. Before proceeding to the results, it is necessary to mention a few points. Firstly, the used method of homogenization requires a cube discretization of the unit cell; as every discretization does, certain degree of geometry mismatch is introduced. The second one, the results for a homogenized infinite crystal are very different from the measurement on a real sample with a finite number of unit cells. Besides, in order to locate the negative refracted beam, a prismatic configuration of a metamaterial slab was applied in [113]. In this case, surface effects play an important role, especially at high frequencies [58]. Nevertheless, the metamaterial response results should reproduce a negative refraction index behavior of split-ring resonators structure, even if the qualitative results experience a shift due to the above described factors. The main system parameters used in the present modeling of a split-ring resonator structure are listed in Table 3.4.

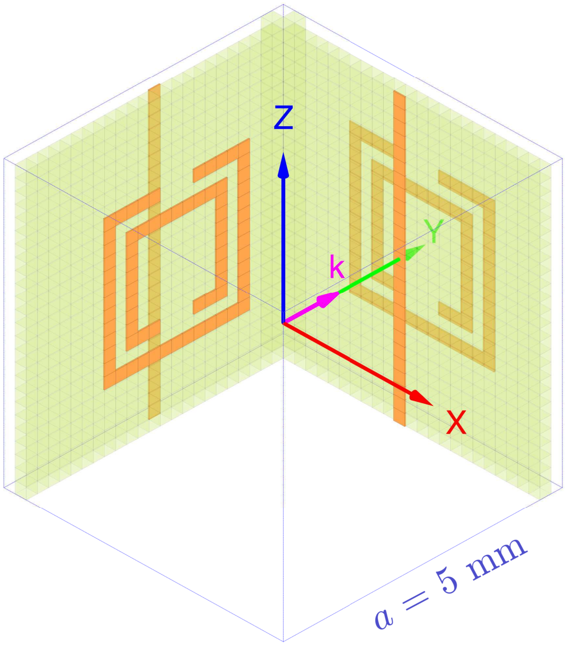

Lattice type	Simple cubic
Period, a	5 mm
Inclusion material	Copper
Copper thickness	16 μm
Background	G10 substrate in Air
Dielectric G10 thickness	0.25 mm
G10 plate permittivity ϵ_r	$3.4 + 0.003i$
Average background permittivity ϵ_b	$1.227 + 0.0003i$
Copper plasma frequency, ω_p	7.3891 eV
Copper damping constant, γ	0.009 eV

Figure 3.13: The unit cell of SRR in a simple cubic lattice with $a = 5$ mm.

Table 3.4: SRR system modeling parameters.

The calculated effective parameters of a split-ring resonators structure having metamaterial response are shown in Figure 3.14. Obtained band of negative refraction (from 10.24 to 10.5 GHz) is rather small, nevertheless, it was confirmed by the experiment described in the work [113]. It can be explained in such a way that a split-ring resonators structure basically depends on the magnetic resonance of the isolated circuits - external and internal one. In practice, permeability turns out to be negative in a very narrow frequency range; at same time the modeling shows, that the dielectric function is negative up to 17.92 GHz. The resulting negative refractive index appears only at the magnetic antiresonance, which appears in a limited frequency range.

Furthermore, within the framework of the used homogenization theory, it is possible to provide the dynamic effective parameters corresponding to the bianisotropic response. The main diagonal elements of the bianisotropic response tensors (2.3.32) $\overset{\leftrightarrow}{\delta}$ and $\overset{\leftrightarrow}{\gamma}$ are shown in Figs. 3.15 and 3.16, correspondingly.

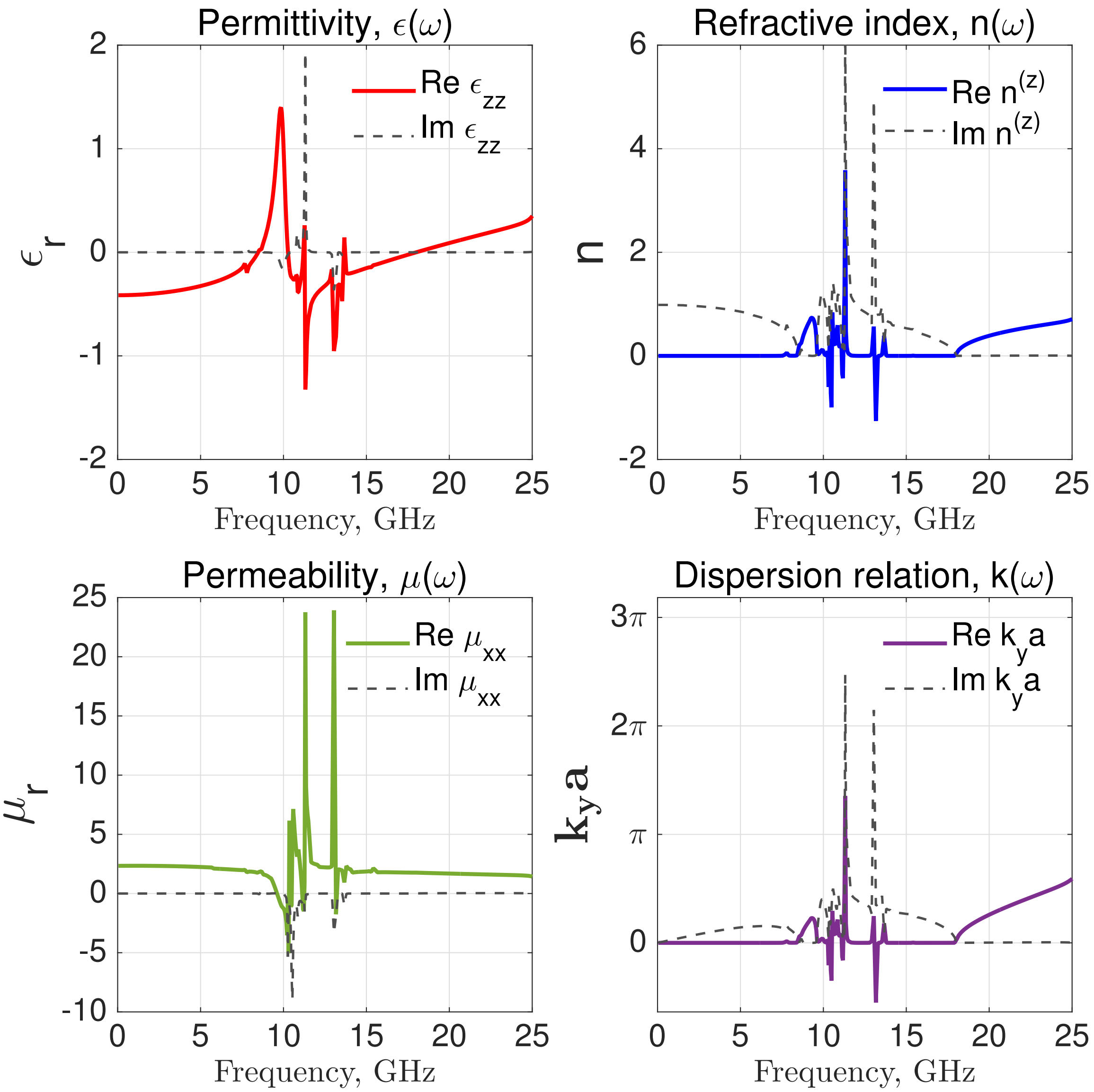

Figure 3.14: Effective parameters of a split-ring resonators structure being a simple cubic lattice with $a = 5$ mm. The wave-vector $\boldsymbol{k}$ is along y-direction, the electric field direction is parallel to the z-axis, and the magnetic field is oriented along the x-axis.

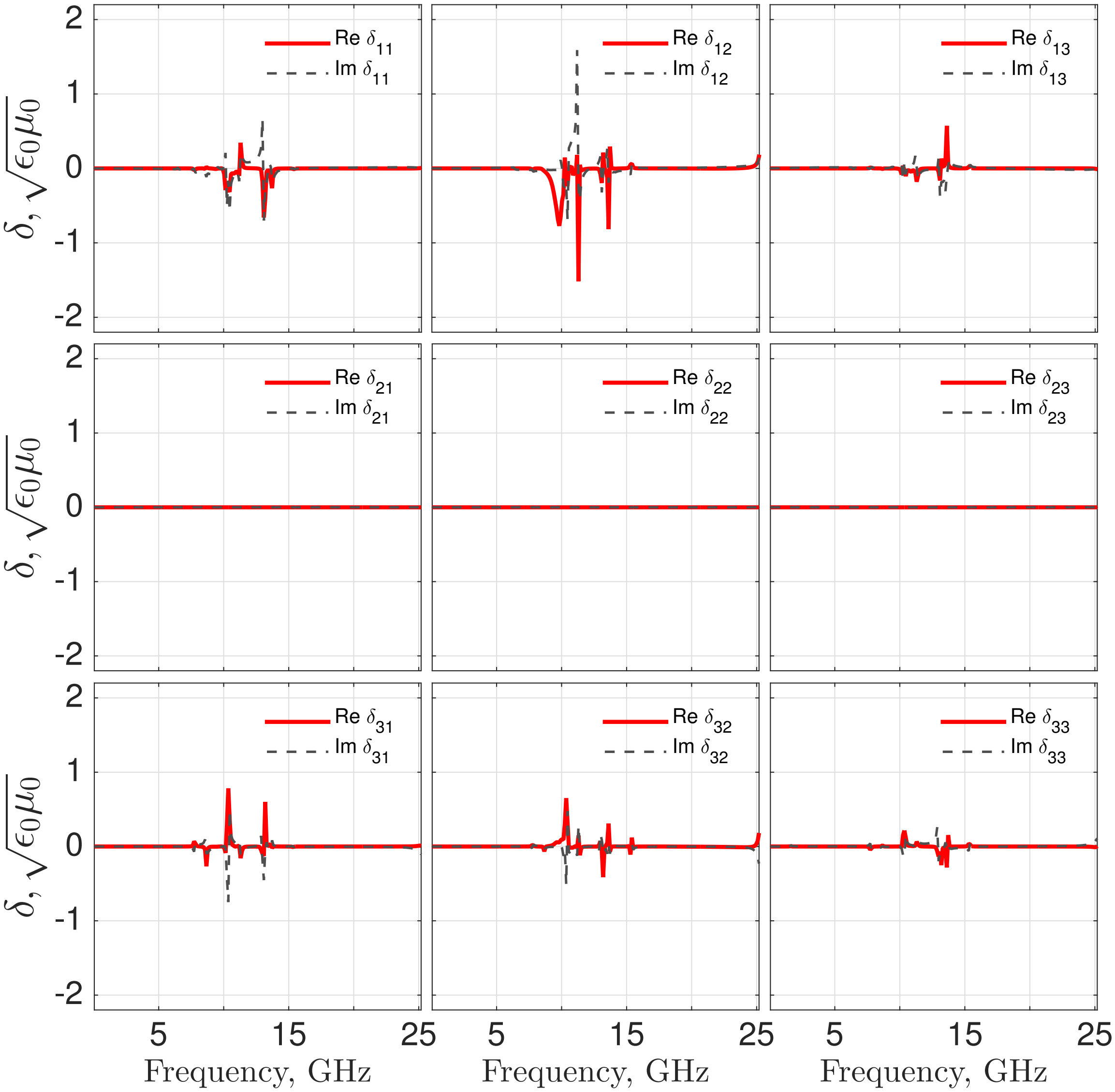

Figure 3.15: Components of the $\overset{\leftrightarrow}{\delta}$ bianisotropic response tensor (obtained by using the metamaterial transformation) for a split-ring resonators structure, being a simple cubic lattice with $a = 5$ mm. The wave-vector $\boldsymbol{k}$ is along the y-direction, the electric field direction is parallel to the z-axis, the magnetic field is oriented along the x-axis.

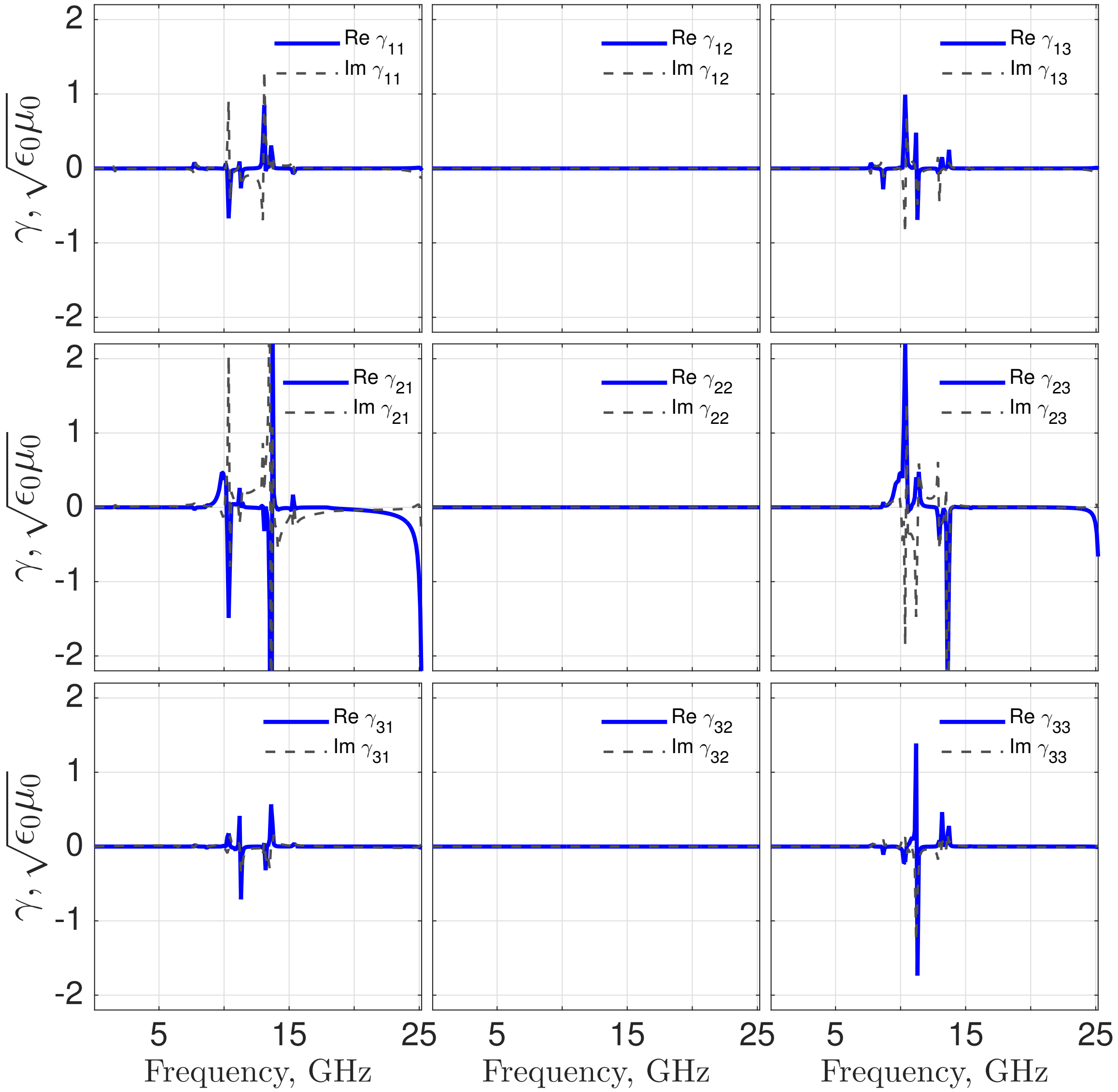

Figure 3.16: Components of the $\overset{\leftrightarrow}{\gamma}$ bianisotropic response tensor (obtained by using the metamaterial transformation) for a split-ring resonators structure, being a simple cubic lattice with $a = 5$ mm. The wave-vector $\boldsymbol{k}$ is along the y-direction, the electric field direction is parallel to the z-axis, the magnetic field is directed along the x-axis.

3.3.3.3 Design, fabrication and characterization of a window resonators structure

During the last decade, a variety of planar and volumetric structures were developed in order to demonstrate the negative refraction. From the introductory part of the present work, it is known that LHM can be realized using resonance-based structures (for example, split-ring resonators) or chiral ones. Resonance-based designs are seeking to achieve the magnetic moment appearance due to an electric circuit resonance, whereas chiral inclusions produce a significant change of fields polarization due to the symmetry properties of the structure.

A simple an symmetric design of a microwave metamaterial is here proposed - window resonators (WR) or framed crosses structure [127]. The schematic unit cell of a typical WR system is shown in Figure 3.17. Although the proposed design is fully central-symmetric (so the crossed magnetoelectric response vanishes), it can provide a negative refractive index region as a result of non-local effects. Furthermore, it is possible to expect a wider negative refraction zone from non-resonance based structures. Besides, normal incidence of electromagnetic waves with the wave vector $\boldsymbol{k}$ parallel to the z-axis is considered.

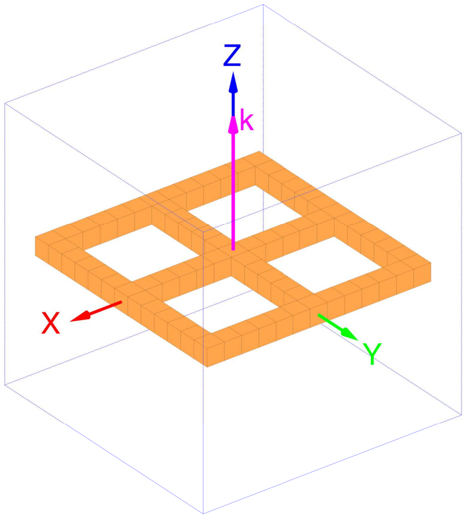

Figure 3.17: Window resonator design.

A window resonator element is a conductor-made square profile contour divided by two intersecting conductors forming four windows inside. The other name, framed crosses, is coming from the physical and visual analogy of symmetric cross resonators confined by a metallic frame. The metal inclusion can be fully immersed into a dielectric matrix or fixed at the surface of a substrate. Each resonator is separated from neighbors, there is no electric contact between them. Generally speaking, it means that physical behavior and band structure of framed crosses resonators are expected to be similar to that of cut wires system resulting into the appearance of a low-frequency pass band. Additionally, window resonators design is easily replicated, which is another advantage of WR structure.

3.3.3.3.1 Tetragonal lattice, a=[4;4;1.6] mm, 2-20 GHz

The first experimental sample of WR was designed with period $a = [4;\ 4;\ 1.6]$ mm in a tetragonal lattice. The unit cell is shown in Figure 3.18. The substrate is an FR4 dielectric, 1.55 mm thick with a copper layer of 35 μm. Each layer is a square of 20 cm x 20 cm size. In the xy-plane there are 50 periods of a structure, but only 4 layers will be assembled in the z-direction. The specified number of layers is used because of the relatively large losses of FR4 [126].

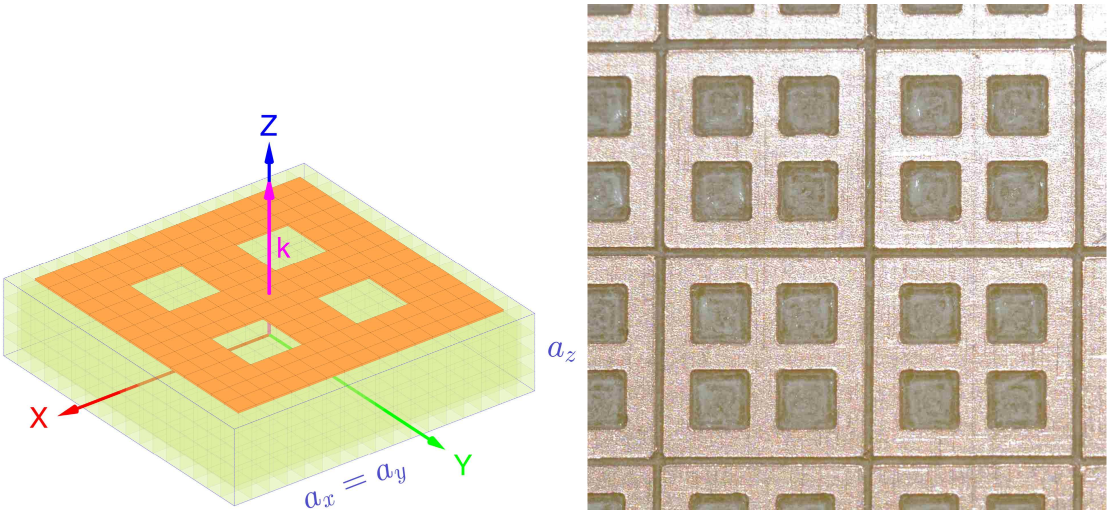

Figure 3.18: Unit cell of window resonators structure with $a_x = a_y = 4$ mm, $a_z = 1.6$ mm; right panel shows the real sample surface.

Metamaterial sample consists of 4 layers fixed by the 4 plastic bolts. At the right panel of Figure 3.18 the surface of a real metamaterial fabricated by micro-machinery engraving method (B.1) is shown.

The experimental setup is shown in Figure 3.21. The result of transmission mea-

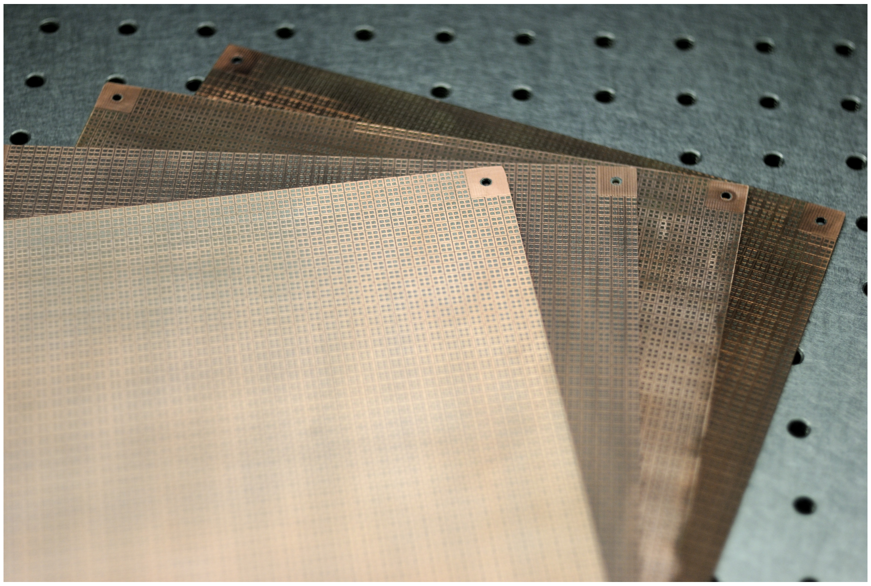

Figure 3.19: Fabricated sample of window resonators with $a_x = a_y = 4$ mm, $a_z = 1.6$ mm.

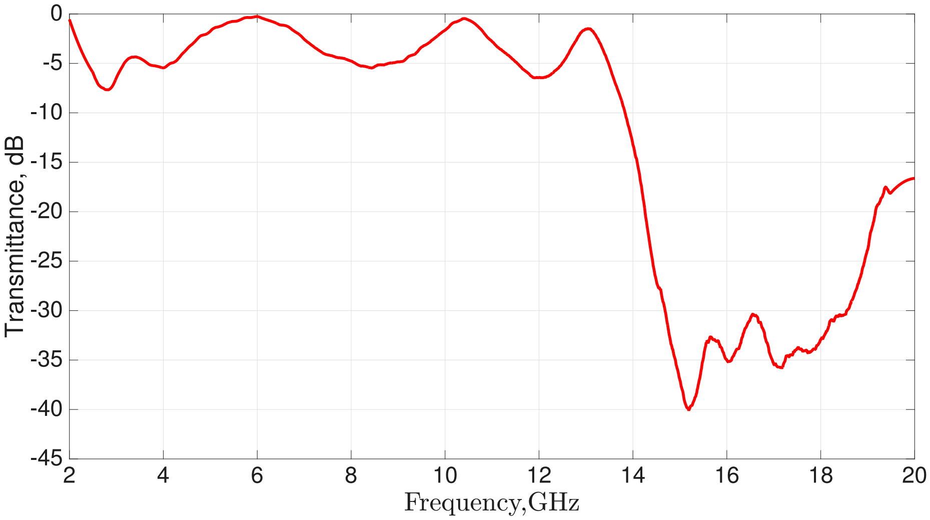

Figure 3.20: Measurement of transmittance for a window resonators sample for normal incidence; the metamaterial consists of 4 layers forming a tetragonal lattice with $a_x = a_y = 4$ mm, $a_z = 1.6$ mm. The experimental tool-chain is: VNA Port 1 → Emitter Antenna → 60 cm distance → Sample → 25 cm distance → Detector Antenna → VNA Port 2.

surement is shown in Figure 3.20. With 4 layers of the WR structure, the transmission results show a low-frequency pass band with 3 resonances of Fabry-Pérot type. However, in order to see the second pass-band, it was necessary to fabricate new samples to be measured with the existing equipment (see Appendix B.2).

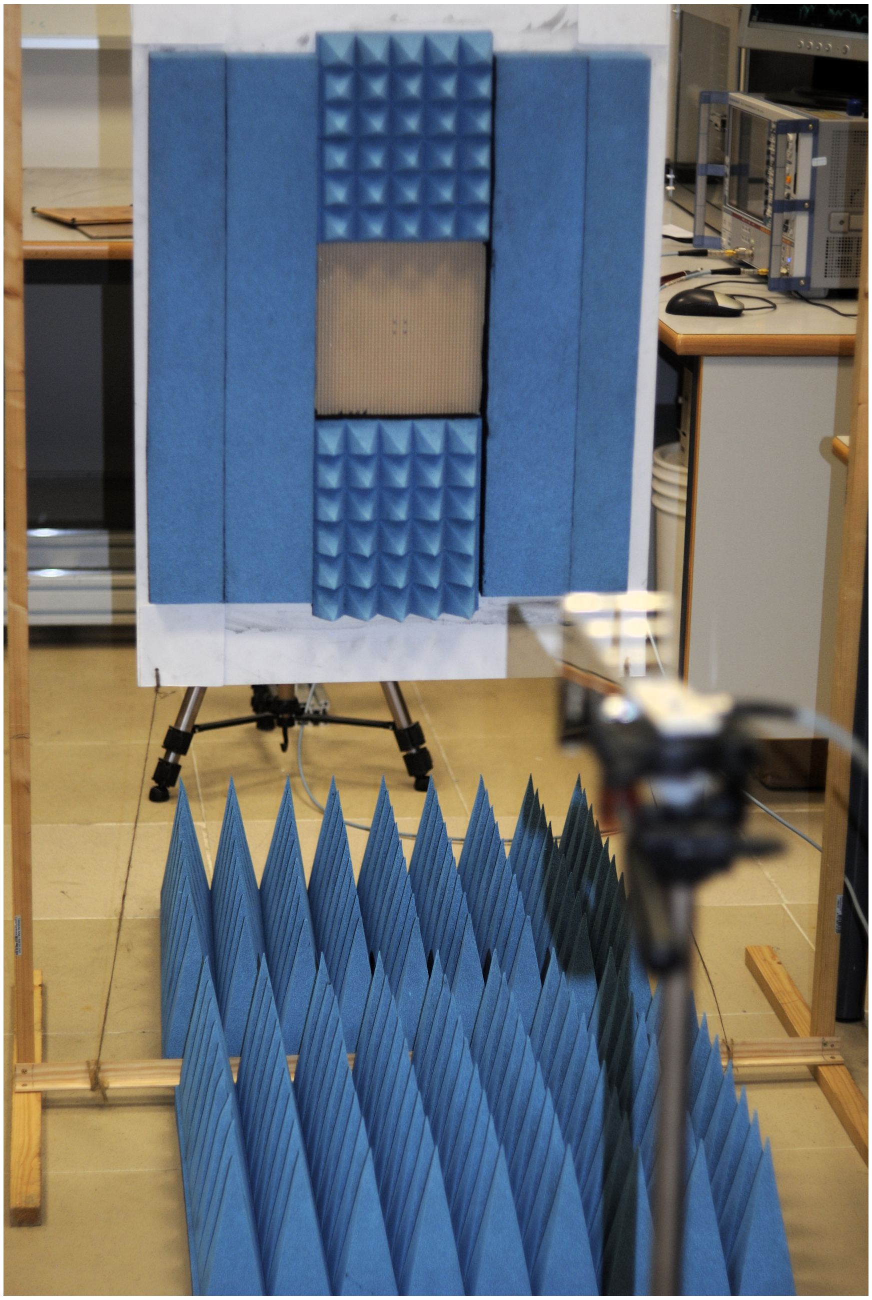

Figure 3.21: Experimental setup to measure microwave transmission for a window resonators sample for normal incidence of electromagnetic wave. Used equipment: vector network analyzer Rohde&Schwarz ZVA24, DRH-20 Standard Linear Horn Antennas 2-20 GHz.

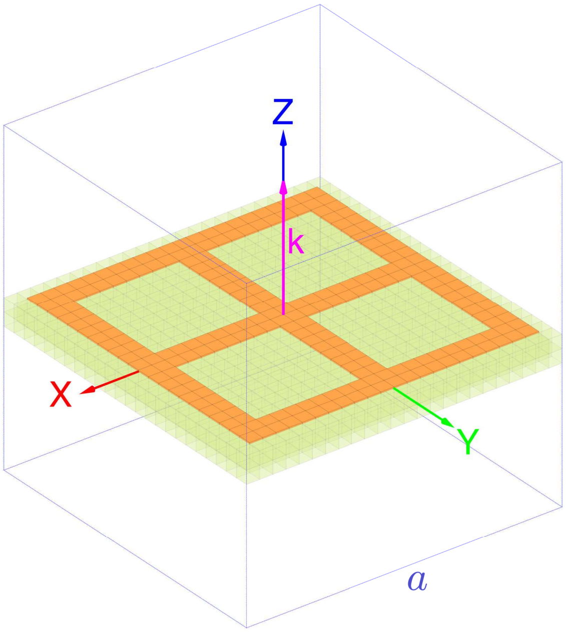

Lattice type	Simple cubic
Period, a	30 mm
Structure layers quantity	4
Layer dimensions	21 cm x 21 cm
Inclusion material	Copper
Copper thickness	35 μm
Background	FR4 plate in Air
Dielectric FR4 thickness	0.8 mm
FR4 permittivity, ϵ_r	4.5 + 0.018i
Average background permittivity ϵ_b	$1.087 + 0.02i$
Copper plasma frequency, ω_p	7.3891 eV
Copper damping constant, γ	0.009 eV

Figure 3.22: Unit cell with a window resonators system in a simple cubic lattice with $a = 30$ mm.

Table 3.5: The main parameters of the WR structure.

3.3.3.3.2 Cubic lattice, a=30 mm, 2-20 GHz

To overcome the physical restrictions of the existing equipment, a metamaterial with a larger period ($a = 30$ mm) was fabricated at IFUAP to be further measured in Universitat Politecnica de Valencia (UPV). The second metamaterial sample of WR structure was fabricated with larger lattice parameter $a = 30$ mm, producing a low-frequency shift of material resonances. The unit cell of the described material is shown in Figure 3.22.

Modeling parameters that were used to calculate the effective parameters of WR structure are listed in Table 3.5. The results of the effective parameters calculation are shown in Figure 3.23.

The result of photonic dispersion calculation using the metamaterial response predict a negative refractive index at 4.3 - 5.0 GHz range (Figure 3.23) having significant losses. An iterative method was used in order to refine the dispersion relation with a number of iterations equal to 10. Inside pass bands, the solution rapidly converged using only 2-3

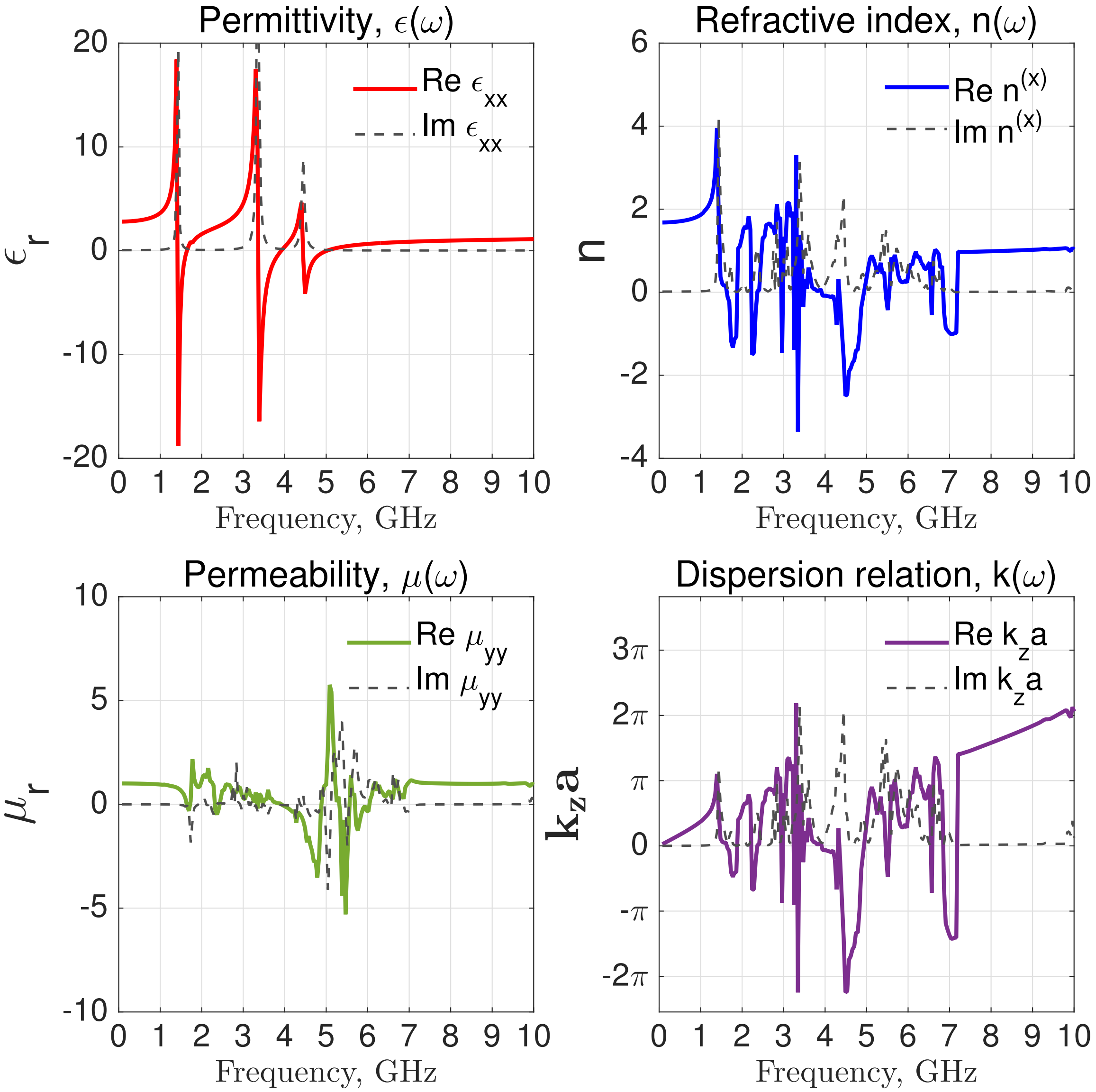

Figure 3.23: Effective parameters for a WR metamaterial being a cubic lattice with $a = 30$ mm. The modeling parameters are listed in Table 3.5.

iterations; however, within band gaps, the solution is iterating with the appearance of a significant imaginary part of the wave vector.

The influence of the dielectric properties of the background material on the solution is important. Firstly, the imaginary part of an effective dielectric background (in this case, air with a FR4 slab) plays a significant role in the nonlocal effective parameters calculation. A high imaginary part of background permittivity ϵ_b makes resonances smoother; in the same time, it increases the energy losses inside the material, practically vanishing the negative refraction effect. However, an increase of the imaginary part of the background matrix permittivity can be useful to distinguish between the pass band and the band gap, and it is directly related to the iteration method features. A metamaterial is assumed to be a passive medium and the used equations consider the absence of free charges/currents inside the structure, hence the wave vector with a positive imaginary part is only considered physical. With a very small imaginary part of the wave vector $\boldsymbol{k}$, a common problem of the determining the sign arises. The iteration method can not determine the correct sign of the solution, without good convergence of the procedure. With a higher value of the resulting imaginary part of the wave vector $\boldsymbol{k}$ (that depends on ϵ_b) the solution converges faster and has the correct sign.

The transmission measurement in the microwave was accomplished at the Polytechnic University of Valencia with the setup shown in Figure 3.24. It is necessary to make a description of the experimental setup and methodology before passing to the microwave transmission results and discussion. The vector network analyzer (VNA) Rohde&Schwarz ZVA 24 (10 MHz - 24 GHz) was used together with standard microwave horn antennas DRH-20 (2-18 GHz) (B.2); VNA has input and output ports, which are used to connect detector and emitter antennas correspondingly. The transmission measurement is realized using the radio-frequency output power equal to 1 mW (0 dBm), which is sufficient to pass through the sample and safe for short operational use.

Measurement preparation starts from VNA cables calibration; despite the fact that antennas are being connected to VNA using a high-quality RF cable, the existing capacitance together with non-ideal cables interconnections results in transmission signal losses and back reflections. Connecting the port 1 (input) of VNA to the port 2 (output) through the cables by the direct adapter connection gives the possibility to run a whole range (10 MHz - 24 GHz) calibration sweep. The results of such a calibration are applied to VNA settings, practically resulting in full compensation of cables transmission losses and reflections. When the cable calibration is finished, it is necessary to prepare a simple microwave setup, that consists of fixed antennas with a sample placeholder (Figure 3.24). Presented below results were measured at the normal beam incidence, the emitter antenna is mounted in the front of the sample at 80 cm distance. Certain distance is required to assure that measurements will be done in far-field, without a strong influence of the nonlinear electromagnetic field effects caused by a closely located emitter antenna. The sample is being fixed in the center of the placeholder, which is surrounded by an absorber material. The main reason for using a microwave absorber is to reduce the intensity of reflected waves at the detector. Finally, the antenna-detector is placed closer to the sample (25 cm) because of a less signal power transmitted after the sample output and features of standard microwave horns (specifically, directivity and gain) that should be taken into account to get better measurement results.

The capacitance of cables is compensated and antennas (detector and emitter) are now connected to the corresponding ports of VNA. Particular conditions of an experimental setup organization have a significant impact on the S-parameters measurement, mainly, giving certain noise level. To improve signal-to-noise ratio (SNR) it is possible to compensate the influence of an experimental setup using the next method. Let VNA, connected with antennas, do the full frequency sweep in a setup *without* sample in the placeholder; the obtained curve should be stored in the memory of the instrument as a reference signal. Then, the second frequency sweep should be done placing the metamaterial into the placeholder. Finally, the resulting signal is obtained as the difference of these two signals with an enhanced SNR obtained under the same conditions. A typical VNA has a high input sensitivity, hence a real signal measured by antenna-detector come with noise. In order to make a signal more readable and clean, it is possible to make it smoother employing a sample averaging functionality of VNA. Practically it means that resulting signal will be given averaged from a number of attempts specified by the user. The increase of averaging number results into a more smooth signal, but makes measurement process longer. Presented further results were obtained using 64 measurements averaging procedure.

Result of the experimental microwave transmission measurement is presented in Figure 3.25. Resonators are isolated from their neighboring elements, therefore the first pass band appears in the low frequencies. The standard microwave horn antennas B.2 have a lower frequency limit of 2 GHz, consequently it is not possible to show the whole low-frequency pass band. Nevertheless, resonances in the first pass band are expected to

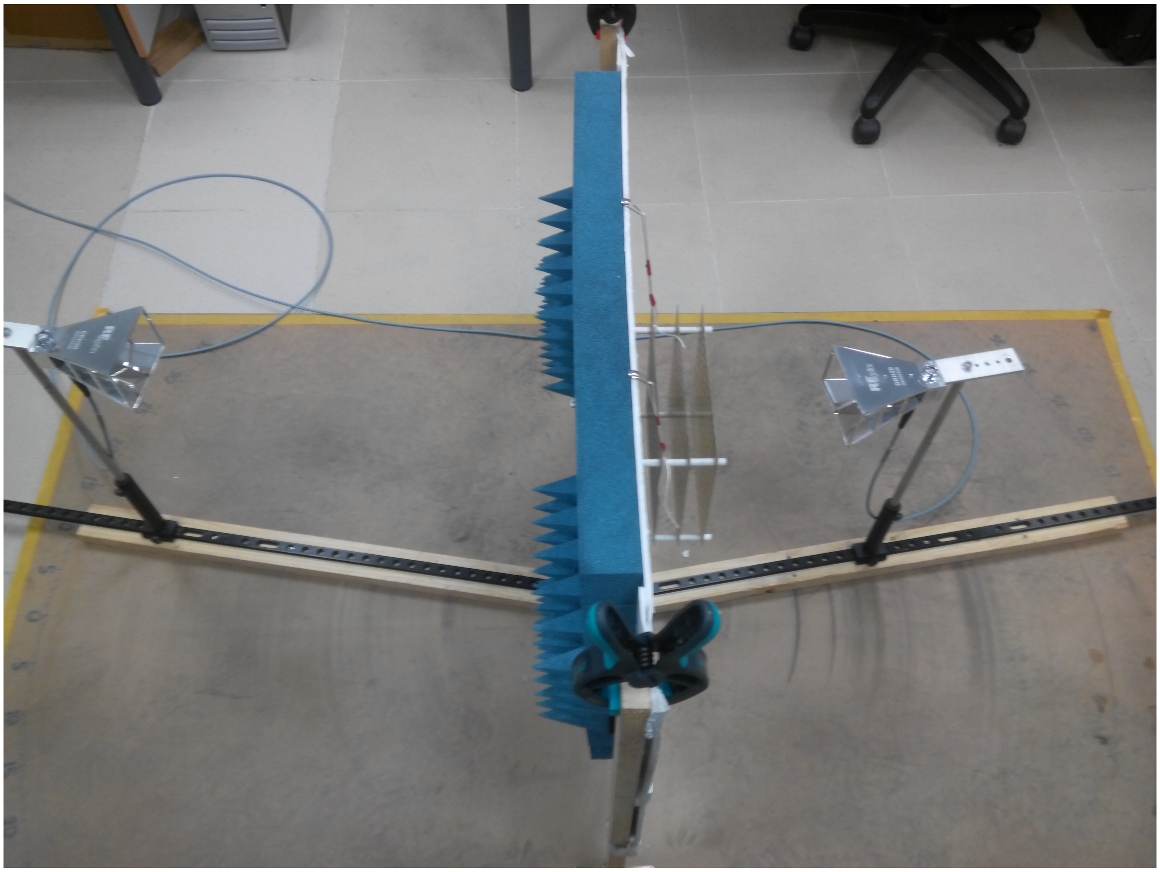

Figure 3.24: Experimental layout for microwave transmission measurement at UPV; the left antenna is emitting a signal, the right one is the antenna-detector. The irradiated area is a sample placeholder, and diffracted beams are being effectively absorbed by the absorbent material (blue color). Although the setup has the ability to change angles of incidence for both antennas, it should be emphasized that the following results of the microwave transmission are for normal incidence of the electromagnetic wave.

be similar to the structure with $a = 4$ mm measured earlier (Subsection 3.3.3.3.1). The second pass band (4.3 - 5.0 GHz) has 3 resonances and this band is potentially has a negative refraction behavior, according to the homogenization theory results (Figure 3.23). Besides, experimental curve shows that second pass band has a significant loss level (-12 dB). Finally, the third pass band (8 - 10 GHz) contains 3 well-defined resonances corresponding to interplanar 4-layered structure interference behavior.

The calculation of the microwave transmission coefficient is very important for any

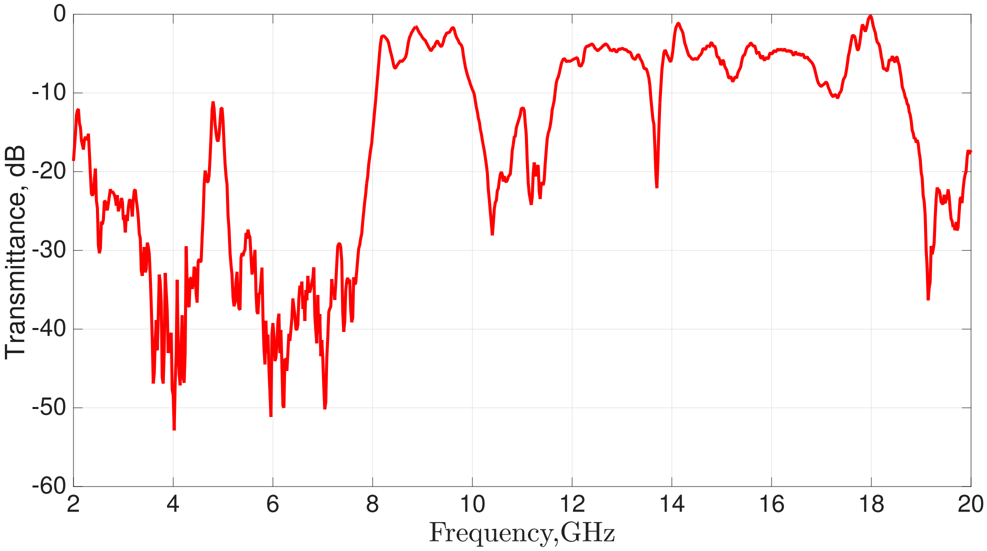

Figure 3.25: Transmission measurement result for window resonators at normal incidence, $a = 30$ mm. Experimental tool-chain is: VNA Port 1 → Emitter Antenna → 80 cm distance → Sample → 25 cm distance → Detector Antenna → VNA Port 2.

practical use, and the corresponding transformation can be done by employing the refined boundary conditions method (refer to 3.3.1.6) with two principal restrictions (Subsection 3.3.1.5):

- A metamaterial sample has an integer number of unit cells.
- Transmittance and reflectance can be calculated only within diffraction-less region.

Here, the results of the microwave transmittance measurement, COMSOL modeling, and transmission coefficient calculations using refined boundary conditions are presented in Figure 3.26.

Both COMSOL and homogenization approach give similar qualitative results, however, the experiment shows a certain degree of difference. Indeed, a metamaterial sample fabrication accuracy and assembly affecting the results of the measurement; model parameters and used numerical methods are equally important for the theoretical modeling of metamaterials. The most important result is that the transmittance calculated by a homogenization theory with refined boundary conditions presented in Figure 3.23 gives a good correspondence with the experimental data for a real fabricated metamaterial. Hence, the result predicted for an *infinite* homogenized medium can be used to predict measurement

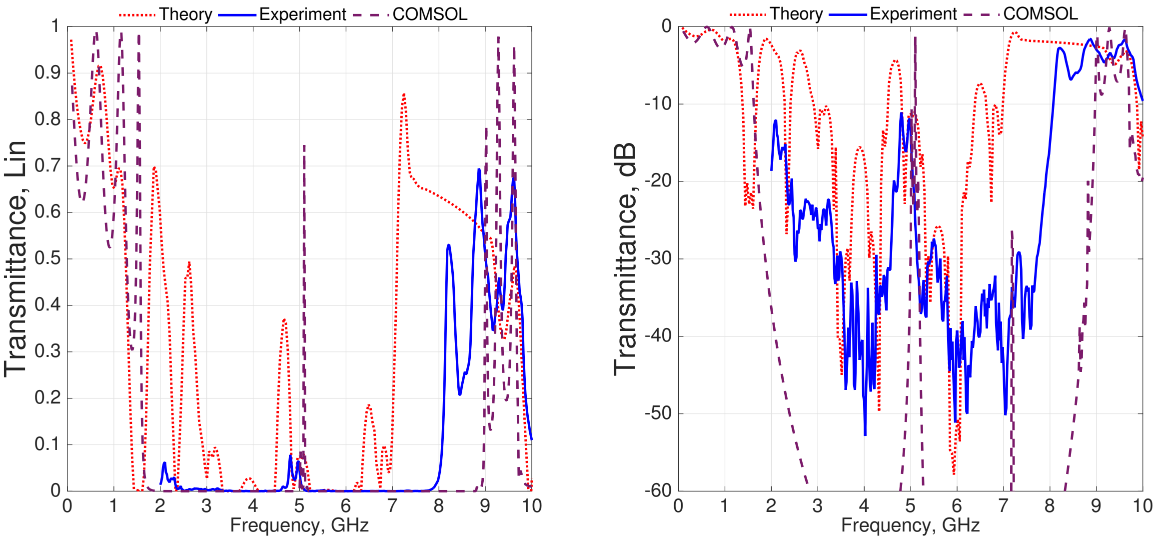

Figure 3.26: Results of measurement (solid line), homogenization theory for 4 layers (dotted line) and COMSOL modeling (dashed line) for the 4 layers WR structure in a simple cubic lattice, $a = 30$ mm. Linear transmittance is converted to logarithmic units using expression $P_{dB} = 10\log_{10} P_{Lin}$.

results with an integer number of the metamaterial unit cells. Finally, to prove that the structure with inversion symmetry (such as WR) has no chiral response, the results of $\overset{\leftrightarrow}{\delta}$ and $\overset{\leftrightarrow}{\gamma}$ tensors calculation are shown in Figure 3.27.

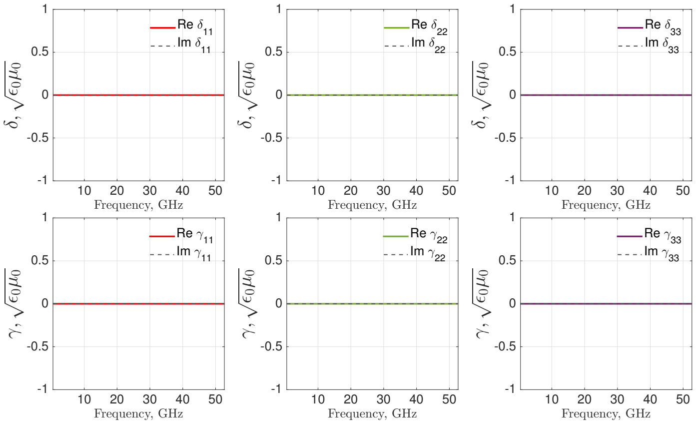

Figure 3.27: The main diagonal components of $\overset{\leftrightarrow}{\delta}$ and $\overset{\leftrightarrow}{\gamma}$ tensors for the WR structure being a simple cubic lattice with $a = 30$ mm.

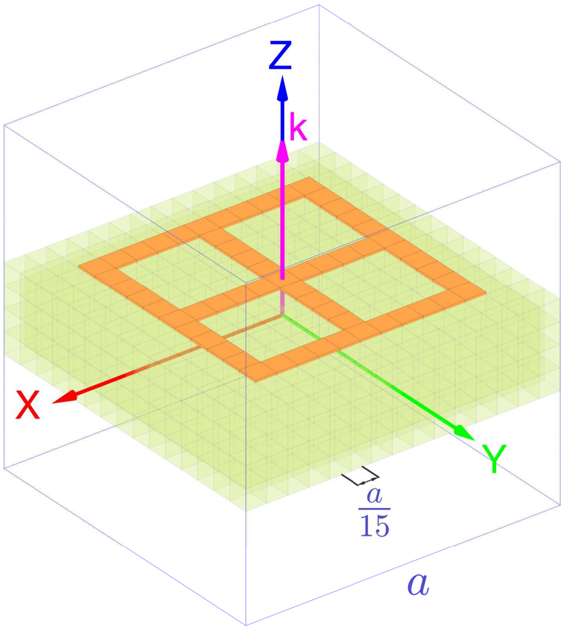

Figure 3.28: WR unit cell in a simple cubic lattice with period $a = 5$ mm.

Lattice type	Simple cubic
Period, a	5 mm
Structure layers quantity	4
Layer dimensions	10 cm x 10 cm
Inclusion material	Copper
Conductor thickness	35 μm
Background	FR4 plate in Air
Dielectric thickness	1.5 mm
FR4 permittivity, ϵ_r	4.5 + 0.018i
Average background ϵ_r	2.2 + 0.09i
Copper plasma frequency, ω_p	7.3891 eV
Copper damping constant, γ	0.009 eV

Table 3.6: The main parameters of the structure modeling.

3.3.3.3.3 Cubic lattice, a=5 mm, 2-50 GHz

To demonstrate the microwave transmission results up to third pass band, a new sample of WR was constructed to be measured further in a range of 2-50 GHz with plane lattice constant $a_x = a_y = 5$ mm. The unit cell of the constructed material is shown in Figure 3.28. The metamaterial sample was assembled from 4 layers (10 cm x 10 cm) either in a cubic or tetragonal lattice using plastic bolts that practically does not affect the microwave transmission results. Each layer is based on a FR4 substrate of thickness d = 1.5 mm with the copper thickness of 35 μm.

Modeling of the WR structure was carried out by using the data given in Table 3.6. Results for the metamaterial response obtained by using homogenization theory are shown below in Figure 3.29. It should be commented, that due to the combination of the effective parameters, it is possible to obtain a negative refractive index within the range 23.0 - 24.76 GHz with significant losses. The number of iterations used (10 in this case) is sufficient to determine the band gaps, at the same time, the obtained result of negative refraction practically does not change with the number of iterations. It means that solution obtained inside the pass bands is already converged and stable, whereas the band gaps are characterized by an unstable iterative procedure in the complex plane.

In order to prove the results of homogenization theory calculations, a measurement of microwave transmission was done at the University of California, San Diego (UCSD) in the range 2-50 GHz using a 2-18 GHz standard microwave horn together with 18-50 GHz high-frequency linear horn with a frequency doubler. The experimental setup is shown in Figures 3.30 and 3.31.

The signal generator HP 8673B (10 MHz - 26.5 GHz) and HP 8565E spectrum analyzer (9 kHz - 50 GHz) were used to generate and receive signal respectively. Both the signal generator and spectrum analyzer were included into a controlled-by-computer network using a GPIB interface. The measurement flow is:

- Set fixed frequency at the signal generator using GPIB.
- Wait a few seconds to refine signal using power averaging procedure (256 samples was used for each frequency).
- Read averaged amplitude from spectrum analyzer by GPIB bus.
- Move onto the next frequency.

The standard microwave horns are designed to operate within certain bands, therefore the two-step measurement process took place. Firstly, the microwave antennas (emitter and detector) with the frequency response in range 2-18 GHz were used; consequently, the two traces were written - with and without the sample, a difference between those traces gives a resulting signal with a high level of reproducibility. The second step is to mount horn antennas with frequency response 18-50 GHz, calibrate them during an empty run and finally obtain results of transmission by the two traces subtraction. The upper frequency of HP 8673B signal generator is limited to 26.5 GHz, to reach higher frequencies a frequency doubler with radio-frequency amplifier was connected to the output of the signal generator to enhance operating frequency of emitter antenna up to the 52 GHz. The final result of a microwave transmission measurement for WR structure is obtained combining results of the 2-18 GHz and 18-50 GHz measurements (Figure 3.32).

In the same experimental setup, a very interesting result was obtained changing a number of WR structure layers in a simple cubic lattice with period $a = 5$ mm. The result

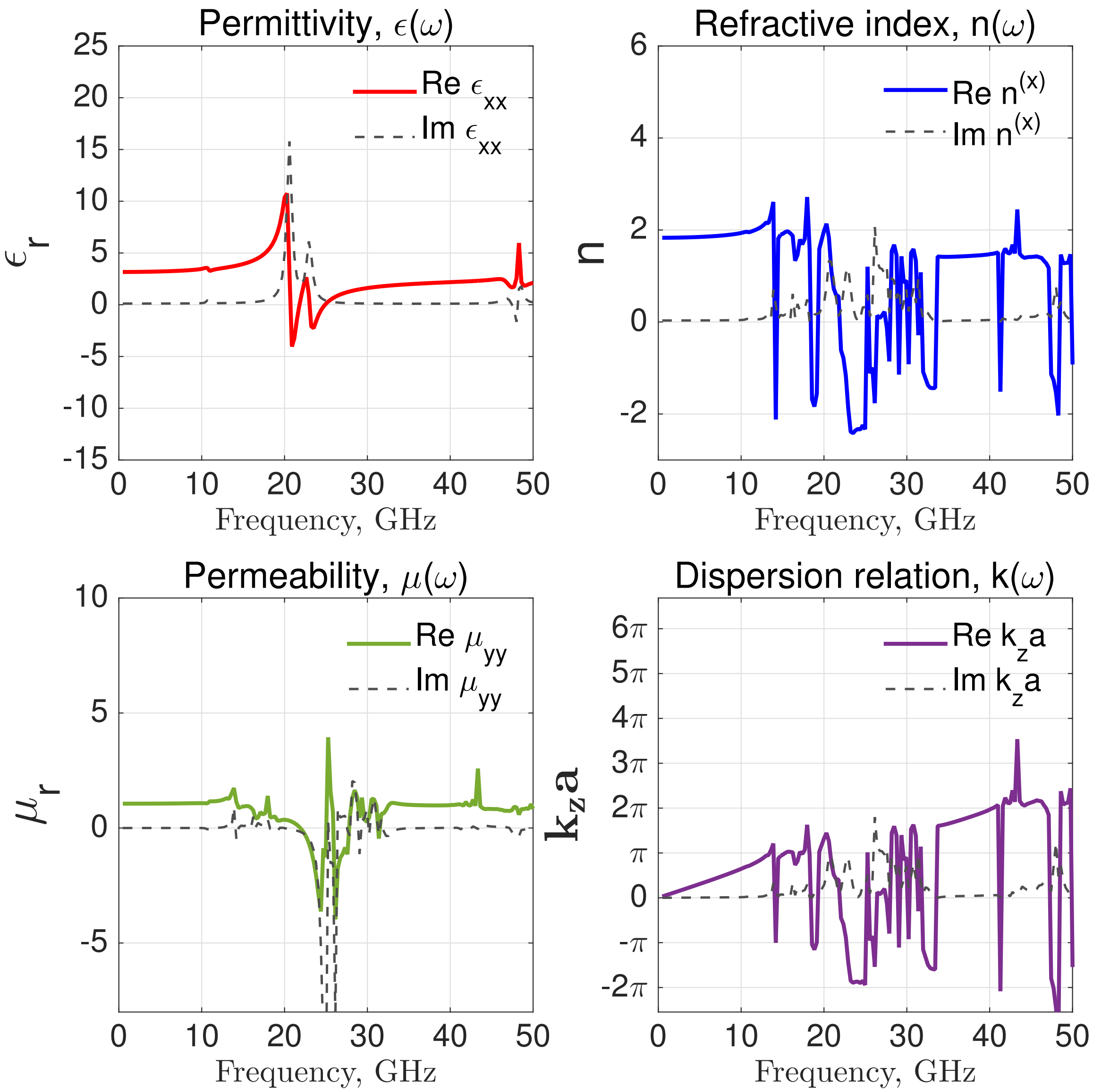

Figure 3.29: Results obtained by homogenization theory - effective permittivity $\epsilon(\omega, \boldsymbol{k})$, permeability $\mu(\omega, \boldsymbol{k})$, refractive index and dispersion relation for the WR structure (Fig. 3.28) with parameters listed in Table 3.6.

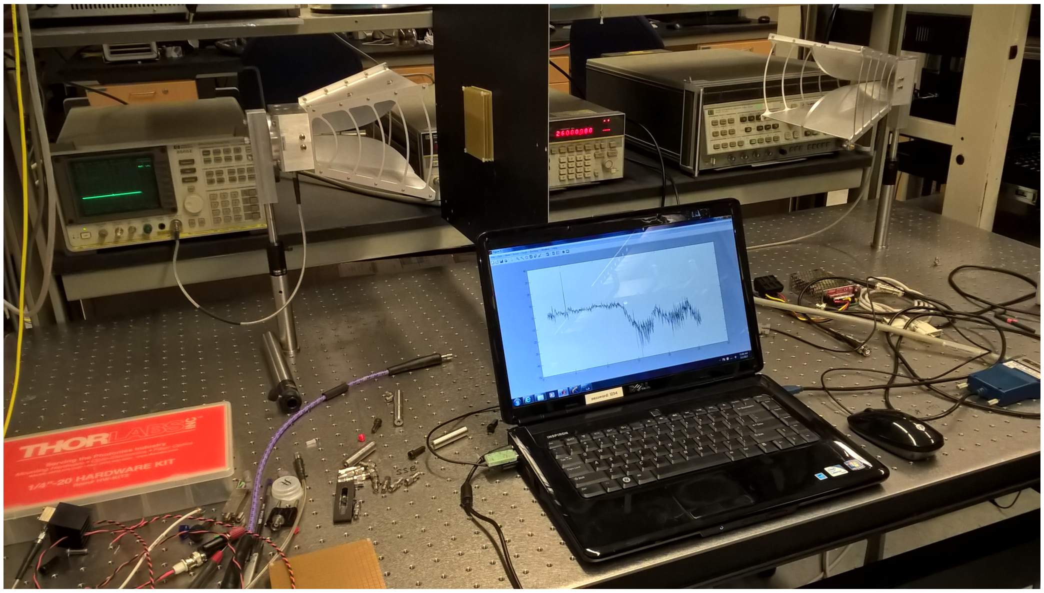

Figure 3.30: Experimental setup for microwave measurement at UCSD, low frequency measurement. Toolchain: HP 8673B Signal Generator → 2-18 GHz Emitter Antenna → Sample → 2-18 GHz Detector Antenna → HP 8565E Spectrum Analyzer.

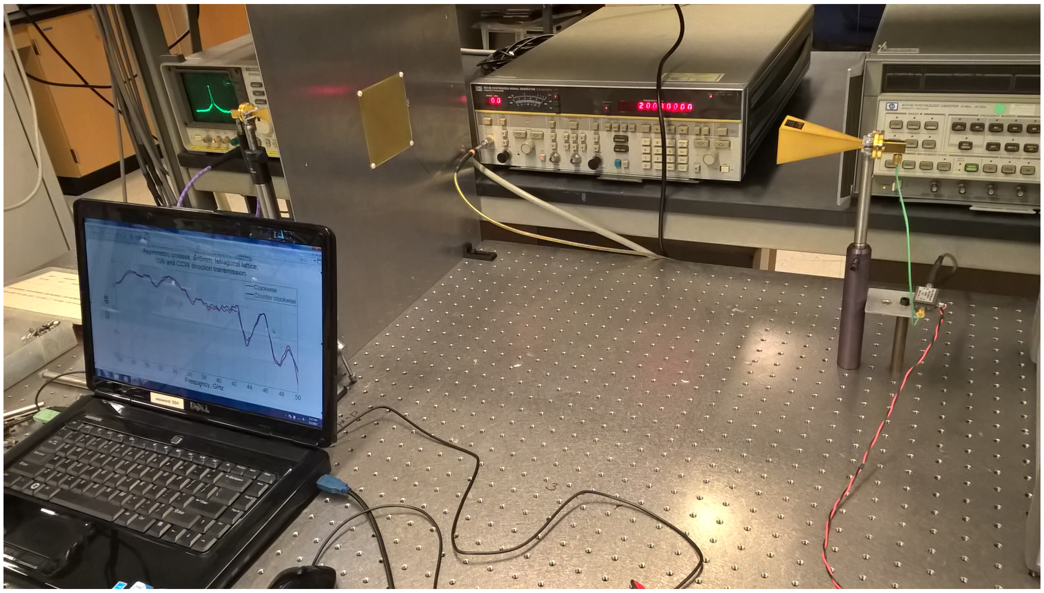

Figure 3.31: Experimental setup for microwave measurement at UCSD, high frequency measurement. Toolchain: HP 8673B Signal Generator → Frequency doubler + RF Amplifier → Sample → 18-50 GHz Emitter Antenna → - HP 8565E Spectrum Analyzer.

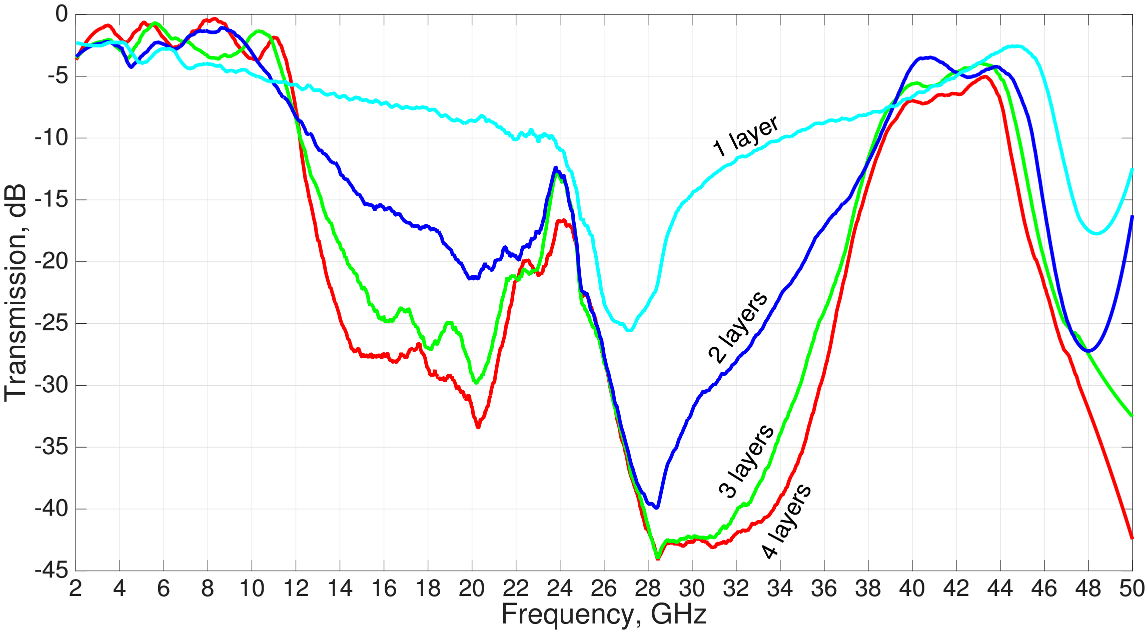

Figure 3.32: Transmission measurement experimental result for variable number of WR layers in a cubic lattice $a = 5$ mm.

presented in Figure 3.32 gives an idea about how many layers of the specified structure are necessary to give a well-defined band structure. Indeed, the each additional layer makes the effect more explicit, however, a large number of layers is being characterized by the increased transmission losses that are undesirable for real applications.

If WR-based metamaterial is required to work in narrower band width, then it is sufficient to have only two layers to exhibit negative refraction index. Adding more layers results in a second pass band enhancement with certain transmission losses. At 24 GHz, the difference in transmission power between 2 and 4 layers is equal to 4.5 dB. If the desired properties of the metamaterial include better filtering of side frequencies, then third and even fourth layers can be added to increase selectivity.

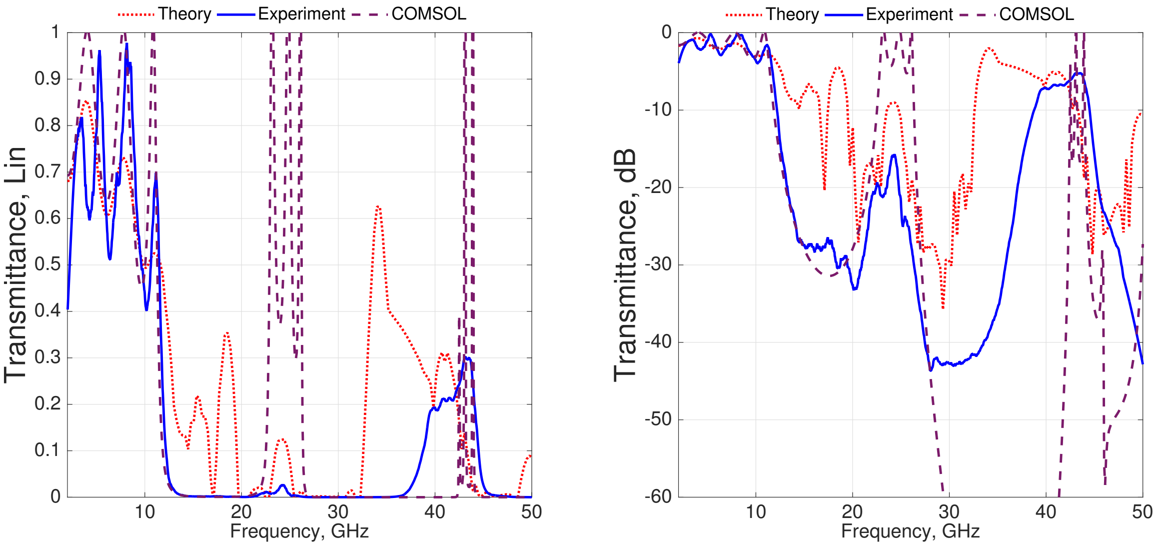

Figure 3.33: Results of experiment (solid line), homogenization theory application with refined boundary conditions for 4 layers (dotted line) and COMSOL modeling (dashed line) for the 4 layers WR structure in a simple cubic lattice, $a = 5$ mm. The left panel represents the linear transmittance, the right panel corresponds to the converted into a logarithmic scale result.

3.3.3.3.4 Tetragonal lattice, a=[5;5;1.55] mm, 2-50 GHz

Finally, mentioned above WR structure with the xy-plane lattice constant equal to 5 mm was assembled into a tetragonal lattice to achieve the $a_z = 1.55$ mm period in z-direction (Figure 3.34). Layers of the window resonators structure are assembled by using plastic bolts in the corner of each board to form a rigid construction.

The surface of the sample is demonstrated in Figure 3.35.

Modeling and experimental measurement procedures are similar to the previous samples. The full-frequency sweep is presented in Figure 3.37. It should be noticed that first pass-band resonances (of Fabry-Pérot type) are shifted to higher frequencies. At the same time, the second pass band (which potentially possesses a negative refractive index) does not shift so much. Such observation gives the possibility to state that the second pass band resonances weakly depend on the structure in z-direction.

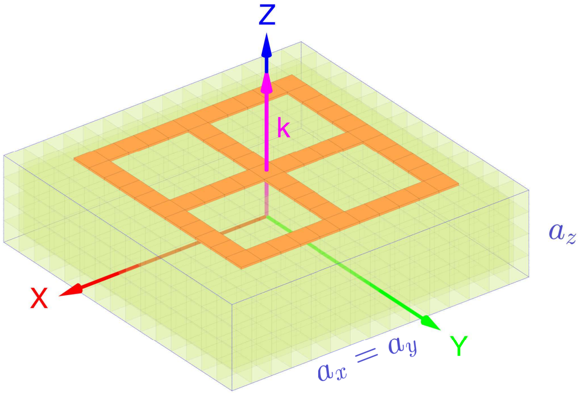

Figure 3.34: Window resonators in tetragonal lattice with $a_x = a_y = 5$ mm, $a_z = 1.55$ mm.

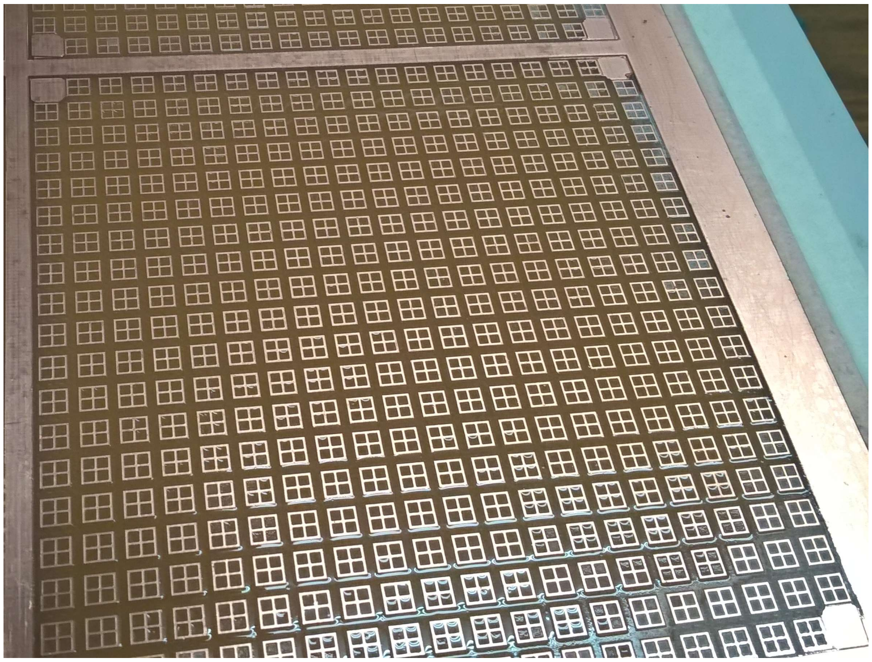

Figure 3.35: The fabricated plate with window resonators structure with lattice constant in xy-plane equal to 5 mm and FR4 board thickness of 1.5 mm. The size of a single layer (10 x 10 cm) can give a discrepancy between the theory and experiment at low frequencies, to avoid sample border effects it is desirable to increase the linear dimensions of each WR plane.

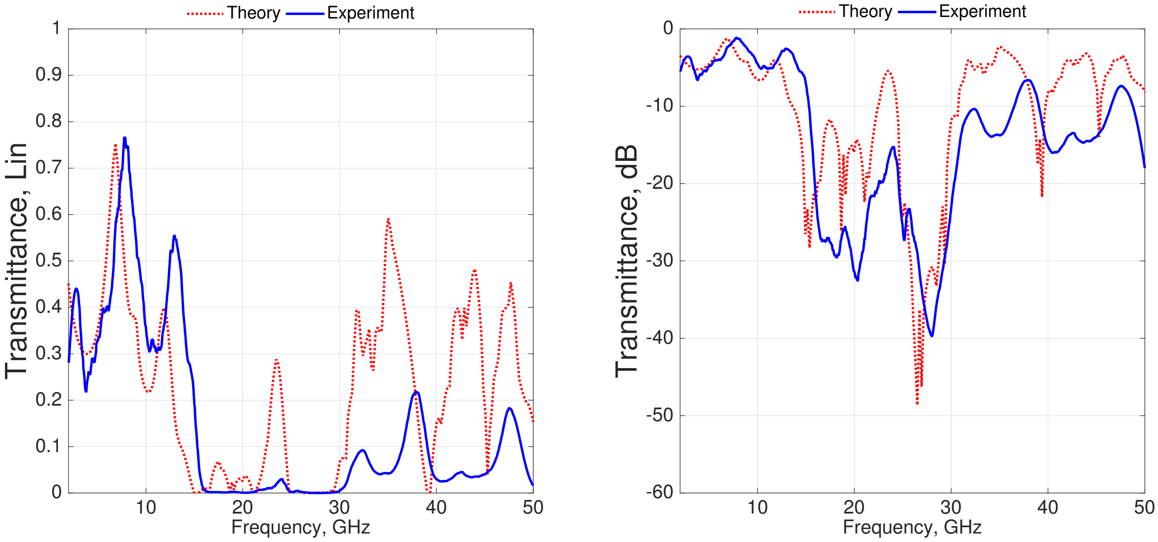

Figure 3.36: Results of experiment (solid line) and homogenization theory application for 4 layers (dotted line) in a tetragonal lattice with $a_x = a_y = 5$ mm, $a_z = 1.55$ mm. The left panel represents the linear transmittance, the right panel shows results in logarithmic scale of the linear transmission transformation.

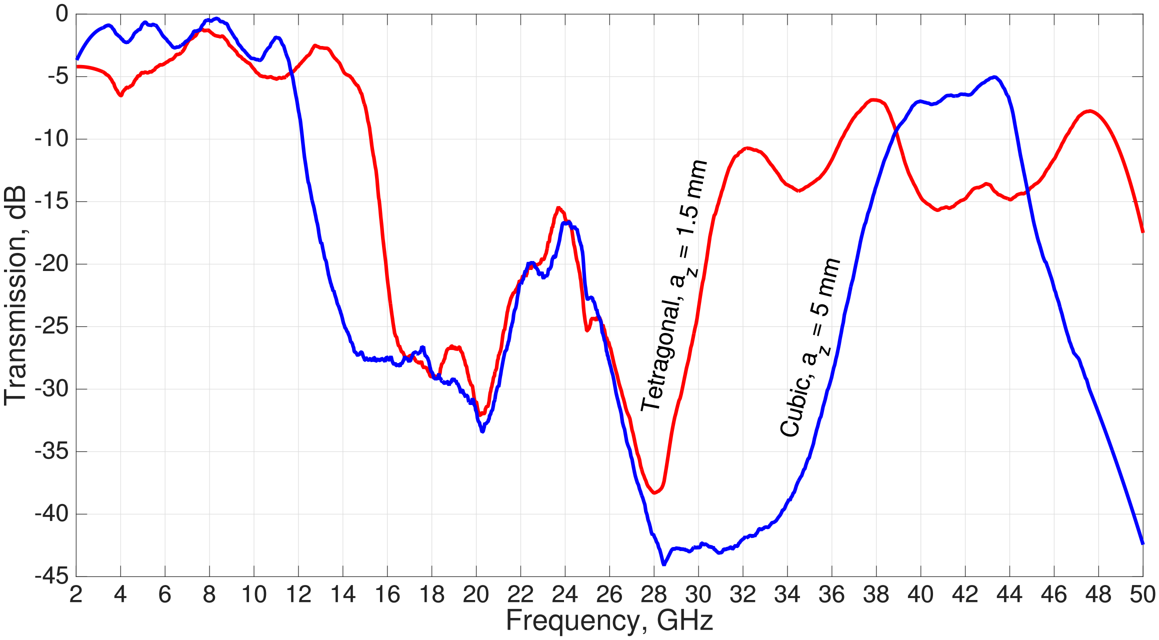

Figure 3.37: Comparison microwave transmission for WR ($a_x = a_y = 5$ mm) in cubic $a_z = 5$ mm and tetragonal $a_z = 1.5$ mm lattices.

Chapter 4

Case of phononic metamaterials

4.1 Nonlocal elastic response of a homogenized phononic crystal

Having a piezoelectromagnetic homogenization formalism, it is easy to describe the elastic properties of a 3D periodic structure. In Section 3.1, it was demonstrated that neglecting the acoustic-electromagnetic coupling and using (3.1.1), the formalism can be split into independent elastic and electromagnetic parts. The vibrational properties of the elastic medium are then expressed by the following relation

$$\overline{\overline{\boldsymbol{\nabla}}}\boldsymbol{v}(\boldsymbol{r}) = \overline{\overline{\boldsymbol{\Omega}\boldsymbol{A}}}(\boldsymbol{r})\boldsymbol{v}(\boldsymbol{r}), \tag{4.1.1}$$

where $\overline{\overline{\boldsymbol{\nabla}}}$ is 9×9 matrix:

$$\overline{\overline{\boldsymbol{\nabla}}} = \begin{bmatrix} 0_3 & \nabla_{3\times6} \\ (\nabla_{3\times6})^T & 0_3 \end{bmatrix}, \tag{4.1.2}$$

$\boldsymbol{v}(\boldsymbol{r})$ is a nine-dimensional column vector, having the components of the displacement and stress vectors:

$$(\boldsymbol{v}(\boldsymbol{r}))^T = (u_x, u_y, u_z, \sigma_1, \sigma_2, \sigma_3, \sigma_4, \sigma_5, \sigma_6), \tag{4.1.3}$$

and $\overline{\overline{\boldsymbol{\Omega}}}$ is:

$$\overline{\overline{\boldsymbol{\Omega}}} \equiv \begin{bmatrix} -\omega^2 I_3 & 0_{3\times6} \\ 0_{6\times3} & I_6 \end{bmatrix}. \tag{4.1.4}$$

Here, ω is the frequency, I_3 and I_6 are unity matrices of order 3 and 6; 0_3, 0_6, $0_{3\times6}$, and $0_{6\times3}$ are zero matrices of order 3, 6, 3×6, and 6×3, respectively. The 9×9 matrix $\overline{\overline{\boldsymbol{A}}}(\boldsymbol{r})$

in Eq. (4.1.1) is defined in terms of the mass density $\rho(\boldsymbol{r})$ and the 6×6 compliance matrix $\overset{\leftrightarrow}{S}(\boldsymbol{r})$:

$$\overline{\overline{\boldsymbol{A}}}(\boldsymbol{r}) \equiv \begin{bmatrix} \rho(\boldsymbol{r}) I_3 & 0_{3\times 6} \\ 0_{6\times 3} & \overset{\leftrightarrow}{S}(\boldsymbol{r}) \end{bmatrix}, \tag{4.1.5}$$

where $\rho(\boldsymbol{r})$ and the elements of $\overset{\leftrightarrow}{S}(\boldsymbol{r})$ are periodic functions of the coordinate $\boldsymbol{r}$.

The effective nonlocal parameters of the phononic crystal will be calculated by applying the explicit formulas of the effective nonlocal-response tensor $\overline{\overline{\boldsymbol{A}}}_{\text{eff}}(\boldsymbol{k}(\omega), \omega)$ obtained directly from the more general piezoelectromagnetic case:

$$\overline{\overline{\boldsymbol{A}}}_{\text{eff}}(\boldsymbol{k}(\omega), \omega) \equiv \begin{bmatrix} \overset{\leftrightarrow}{\rho}_{\text{eff}}(\boldsymbol{k}, \omega) & 0_{3\times 6} \\ 0_{6\times 3} & \overset{\leftrightarrow}{S}_{\text{eff}}(\boldsymbol{k}, \omega) \end{bmatrix}, \tag{4.1.6}$$

where $\overset{\leftrightarrow}{\rho}_{\text{eff}}(\boldsymbol{k}, \omega)$ and $\overset{\leftrightarrow}{S}_{\text{eff}}(\boldsymbol{k}, \omega)$ are the effective dynamic mass density and compliance tensors, which depend on both the Bloch wave vector $\boldsymbol{k}$ and frequency ω. The obtained formulas are coincide with those derived in Ref. [51].

The direct calculation of the effective nonlocal-response matrix $\overline{\overline{\boldsymbol{A}}}_{\text{eff}}(\boldsymbol{k}(\omega), \omega)$ requires the solution of very large algebraic systems of equations including large number of reciprocal lattice vectors (see Eq. (16) in Ref. [51]). The novelty of the presented calculations is the form-factor division approach usage together with the iteration procedure applied (see Section 3.1) to a 3D phononic crystal. Besides, the results obtained with employing a large number of plane waves, the calculations using an integral approach method will be presented here. In the latter case, an infinite number of plane waves in the expansion of the displacement and stress fields inside the phononic crystal is considered.

4.2 Integral approach method

According to the FFDA, to calculate the effective parameters of the nonlocal elastic response, it is necessary to carry out large summations over the reciprocal lattice vectors $\boldsymbol{G}$ (see l.h.s. of Eq. (2.3.110)). A method for approximating the summations in Eq. (2.3.110) by improper integrals will be presented below.

Let us split the sums over $\boldsymbol{G}$ on the l.h.s. of Eq. (2.3.110) into two parts as:

$$\sum_{\boldsymbol{G}} e^{i\boldsymbol{G}\cdot(\boldsymbol{r}_i - \boldsymbol{r}_j)} F_v(-\boldsymbol{G}) F_v(\boldsymbol{G}) \overline{\overline{\boldsymbol{T}}}^{-1}(\boldsymbol{G}) = \overline{\overline{\boldsymbol{S}}}_D(i,j) + \overline{\overline{\boldsymbol{S}}}_I(i,j), \tag{4.2.1}$$

where the first part, $\overline{\overline{\boldsymbol{S}}}_D(i,j)$, of the sums is carried out over the reciprocal lattice vectors $\boldsymbol{G}$, whose magnitude $|\boldsymbol{G}|$ is smaller than or equal to a relatively-large value G_0: $|\boldsymbol{G}| \leq G_0$, $G_0 \gg 2\pi/a$. The second (remaining) part, $S_I(i,j)$, of the series contains summands with $|\boldsymbol{G}| > G_0 \gg 2\pi/a$ and can be approximated by integrals, in the reciprocal space, outside a sphere of radius G_0:

$$\overline{\overline{\boldsymbol{S}}}_I(i,j) = \frac{V_c}{(2\pi)^3} \int\limits_{|\boldsymbol{G}|>G_0} e^{i\boldsymbol{G}\cdot(\boldsymbol{r}_i-\boldsymbol{r}_j)} F_v(-\boldsymbol{G}) F_v(\boldsymbol{G}) \overline{\overline{\boldsymbol{T}}}^{-1}(\boldsymbol{G}) d\boldsymbol{G}. \tag{4.2.2}$$

Using spherical coordinates, $\overline{\overline{\boldsymbol{S}}}_I(i,j)$ can be written in the form

$$\overline{\overline{\boldsymbol{S}}}_I(i,j) = \frac{V_c}{(2\pi)^3} \int\limits_0^{2\pi} \int\limits_0^{\pi} \int\limits_{G_0}^{\infty} e^{i\boldsymbol{G}\cdot(\boldsymbol{r}_i-\boldsymbol{r}_j)} F_v^2(\boldsymbol{G}) \overline{\overline{\boldsymbol{T}}}^{-1}(\boldsymbol{G}) G^2\, dG\, \sin\theta d\theta d\phi. \tag{4.2.3}$$

In writing Eq. (4.2.4), the equality $F_v(-\boldsymbol{G}) = F_v(\boldsymbol{G})$ which is valid for the form factor of a cube has been employed. Now, the variable $\tilde{\boldsymbol{G}} = \boldsymbol{G}/G_0$ is introduced:

$$\overline{\overline{\boldsymbol{S}}}_I(i,j) = \frac{V_c G_0^3}{(2\pi)^3} \int\limits_0^{2\pi} \int\limits_0^{\pi} \int\limits_{1}^{\infty} e^{iG_0\tilde{\boldsymbol{G}}\cdot(\boldsymbol{r}_i-\boldsymbol{r}_j)} F_v^2(G_0\tilde{\boldsymbol{G}}) \overline{\overline{\boldsymbol{T}}}^{-1}(G_0\tilde{\boldsymbol{G}}) \tilde{G}^2\, d\tilde{G}\, \sin\theta d\theta d\phi. \tag{4.2.4}$$

The improper integral with respect to the magnitude $\tilde{G}$ in Eq. (4.2.4) can be straightforwardly calculated by variable replacement $\tilde{G} = 1/\tau$ with $0 < \tau \leq 1$. It should be noted that the contribution of $\overline{\overline{\boldsymbol{S}}}_I(i,j)$ to the series (4.2.1) is significant for the case $i = j$ only. Another approximation can be carried out by noticing that the matrix $\overline{\overline{\boldsymbol{T}}}^{-1}(\boldsymbol{G})$ practically does not depend on the magnitude of $\boldsymbol{G}$ if $|\boldsymbol{G}| > G_0 \gg 2\pi/a$.

4.3 Results for 2D and 3D Au-Si phononic crystals

4.3.1 Quasi-static limit

In Figs. 4.1 and 4.2, the results for a square 2D lattice and cubic 3D periodic arrays of metallic (Au) inclusions are presented, having the form of square bars and cubes, respectively, which are embedded in a solid host matrix (Si). The principal axes of the Au and Si cubic crystals are assumed to be parallel to the axes of the coordinate system. Using the FFDA, all the metallic (Au) inclusions were divided into n small cubes of side $a/10$ (Fig. 4.1) and $l/5$ (Fig. 4.2), where a is the lattice constant of both 2D and 3D phononic crystals. For the 2D PC, l is the side of the square section of the infinite Au bars ($l = pa$,

$p = 0, 1, ..., 10$). For the 3D PC, l is the side of the cubic inclusion. The quasi-static *local* response tensor $\overline{\overline{\boldsymbol{A}}}_{\text{eff}}(\boldsymbol{k} \to 0, \omega \to 0)$ is calculated with the Au (Si) parameters [128]–[130]: mass density $\rho_{\text{Au(Si)}} = 19300$ (2330) kg/m^3, $C_{11} = 192.5$ (166.2) GPa, $C_{12} = 163.0$ (64.4) GPa, $C_{44} = 42.4$ (79.8) GPa. The chosen lattice constant a is equal to 50μm.

In Fig. 4.1, the calculated dependences of the nonzero components of the effective mass density ($\overset{\leftrightarrow}{\rho}_{\text{eff}}$), compliance ($\overset{\leftrightarrow}{S}_{\text{eff}}$) and stiffness ($\overset{\leftrightarrow}{C}_{\text{eff}}=\overset{\leftrightarrow}{S}{}^{-1}_{\text{eff}}$) tensors vs Au filling fraction $f = (l/a)^2$ are exhibited. According to our numerical results, the quasi-static (qs) effective mass density is isotropic:

$$\overset{\leftrightarrow}{\rho}_{\text{eff}} = \rho_{qs} I_3, \tag{4.3.1}$$

where the scalar ρ_{qs} linearly depends on f:

$$\rho_{qs} = \rho_{\text{Au}} f + \rho_{\text{Si}}(1 - f). \tag{4.3.2}$$

The system evidently has cubic symmetry at $f = 0$ and $f = 1$. However, for f values in the open interval (0,1) the homogenized elastic composite behaves as a tetragonal crystal with 6 independent stiffness constants: $C_{11} = C_{22}$, C_{33}, C_{12}, $C_{13} = C_{23}$, $C_{44} = C_{55}$ and C_{66} (see panel (d)). These results agree with the predictions of the works [51], [53] for solid 2D phononic crystals.

In panels (b), (c) and (d) of Fig. 4.2, the dependences of the effective quasi-static parameters vs filling fraction $f = (l/a)^3$ of Au cubes are shown. As in the case of the 2D PC (Fig. 4.1,(b)) the effective mass density is isotropic (Eq. 4.3.1) and linearly depends on f. In addition, for any value of f, the stiffness tensor $\overset{\leftrightarrow}{C}_{\text{eff}}$ has only three independent elements (C_{11}, C_{12}, and C_{44}) and, therefore, the symmetry of the homogenized phononic crystal is cubic as that of their Au and Si components.

4.3.2 Nonlocal elastic response

Applying the FFDA, the calculation of the effective nonlocal-response tensor $\overline{\overline{\boldsymbol{A}}}_{\text{eff}}$ for a given frequency ω and wave vector $\boldsymbol{k}$ is reduced to the solution of a linear system of algebraic equations, with $9n$ unknown variables, where n is the number of small cubes occupying the inclusion volume. Besides, an iterative procedure is used, which allows to describe the exact phononic dispersion relation for an arbitrary magnitude and direction of the wave vector $\boldsymbol{k}$. At the first step, the *local* response tensor $\overline{\overline{\boldsymbol{A}}}_{\text{eff}}(\boldsymbol{k} \to 0, \omega)$ is calculated and the resulting effective parameters (mass density and compliance constants) are used

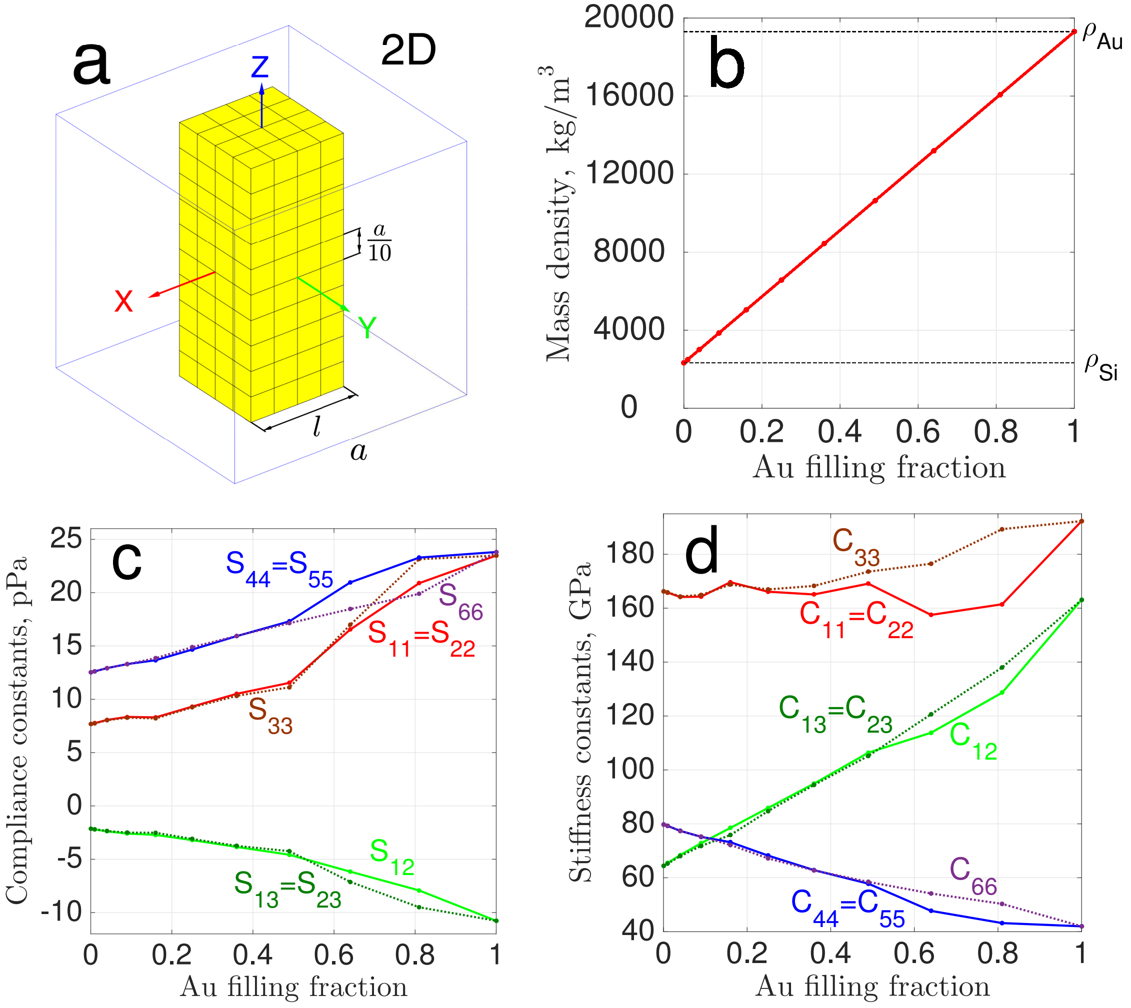

Figure 4.1: Scheme of unit cell for a square 2D lattice of Au bars embedded in Si (a) and graphs of the calculated elements of the effective mass density (b), compliance (c) and stiffness (d) tensors vs the Au filling fraction in the quasi-static limit.

to calculate in the first (local) approximation the phononic dispersion relation $\boldsymbol{k}(\omega)$. With the obtained results the nonlocal response tensor $\overline{\overline{\boldsymbol{A}}}_{\text{eff}}(\boldsymbol{k}(\omega),\omega)$ is calculate (Eq. (4.1.6)) to find a new set of effective dynamic parameters, which are then used to determine a more accurate phononic dispersion relation $\boldsymbol{k}(\omega)$, and so on.

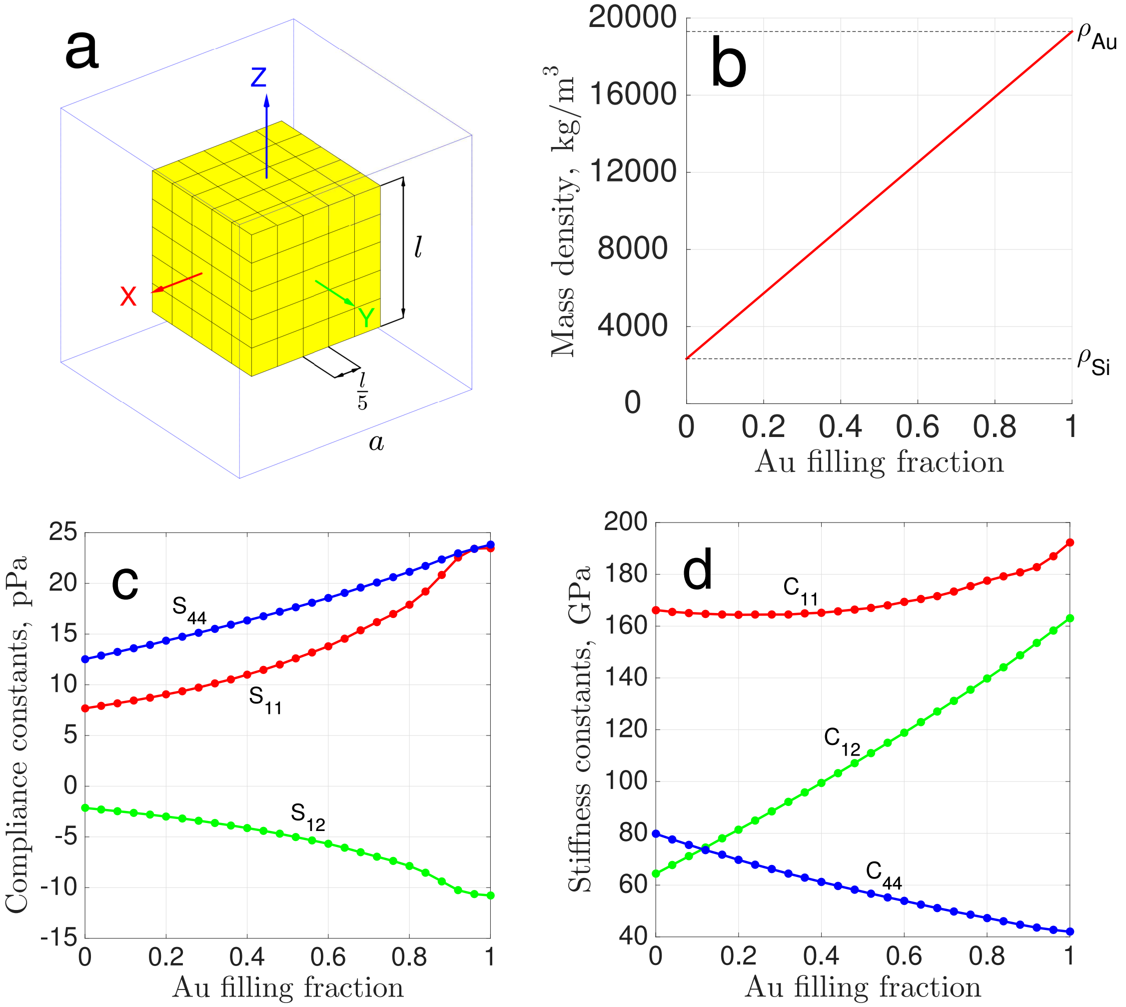

Figure 4.2: Scheme of unit cell for a cubic 3D lattice of Au cubes embedded in Si (a) and graphs of the calculated elements of the effective mass density (b), compliance (c) and stiffness (d) tensors vs the Au filling fraction in the quasistatic limit.

4.3.3 Cubic array of Au cubes embedded in Si

Fig. 4.3 exhibits the frequency dependence of the relevant elements of the effective mass density ($\overleftrightarrow{\rho}_{\text{eff}}$) and stiffness ($\overleftrightarrow{C}_{\text{eff}}=\overleftrightarrow{S}_{\text{eff}}^{-1}$) tensors, as well as the phononic dispersion for transverse (T) and longitudinal (L) phononic modes propagating along the x-axis (i.e. $\boldsymbol{k} = k_x\hat{x}$) at $f = (3/10)^3 = 0.027$. It should be noted that the obtained effective parameters permit to calculate the exact phononic dispersion $k_x(\omega)$ within the whole first Brillouin

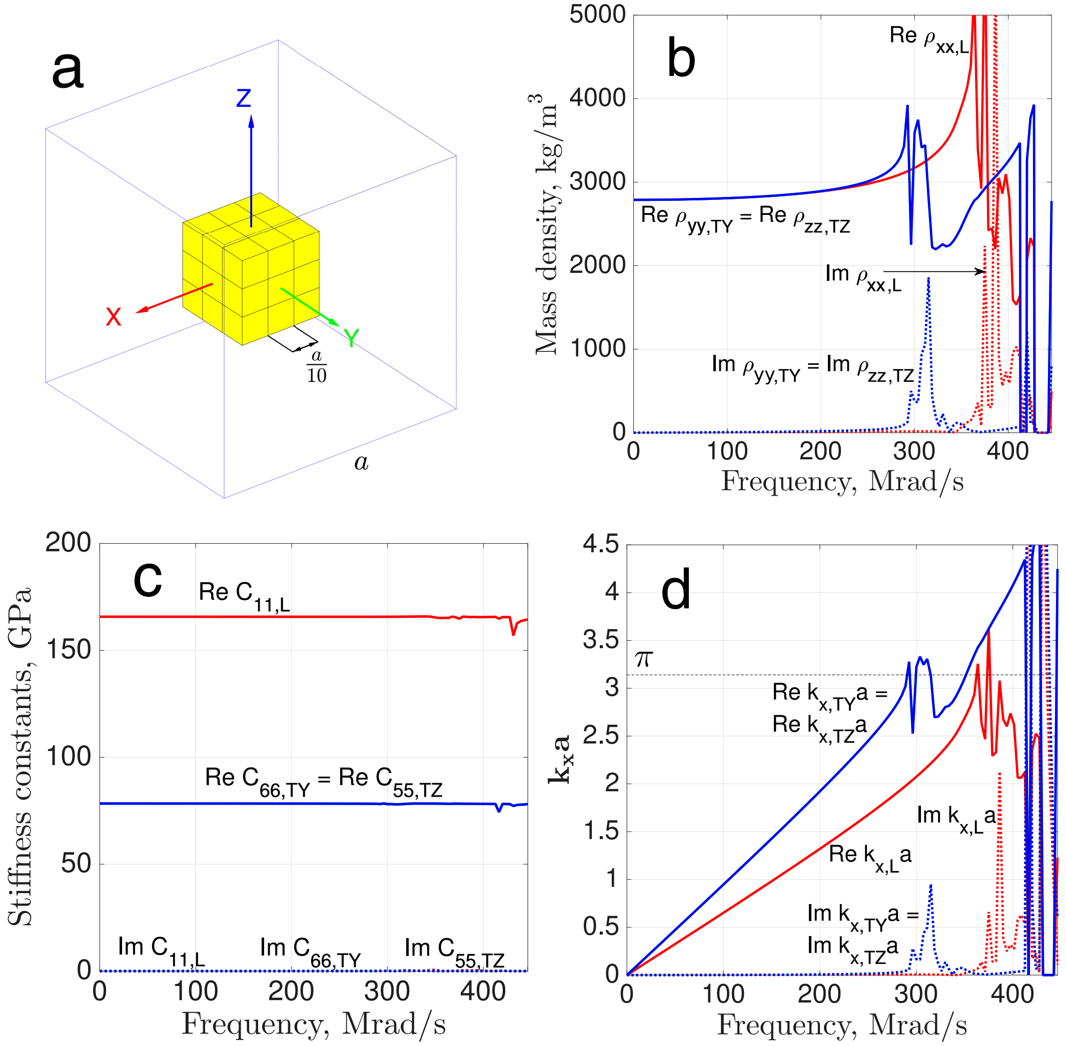

Figure 4.3: (a) Scheme of a unit cell for a cubic lattice of Au cubes embedded in Si. Panels (b) and (c): Graphs of the calculated frequency dependence for elements of the effective mass density and stiffness tensors. (d) Dispersion relations for transverse (TY and TZ) and longitudinal (L) phononic modes.

zone (BZ) by using the formulas:

$$\begin{aligned} k_x &= \omega\sqrt{\rho_{xx}/C_{11}}, && \text{for L modes,} \\ k_x &= \omega\sqrt{\rho_{yy}/C_{66}}, && \text{for TY modes,} \\ k_x &= \omega\sqrt{\rho_{zz}/C_{55}}, && \text{for TZ modes,} \end{aligned} \tag{4.3.3}$$

that correspond to a homogeneous elastic medium with tetragonal symmetry. The phononic dispersions $k_x(\omega)$ for transverse (TY and TZ) and longitudinal (L) modes were separately calculated by employing only the relevant elements of the effective matrix $\overline{\overline{\boldsymbol{A}}}_{\text{eff}}(\boldsymbol{k}(\omega),\omega)$ in each step of the iteration procedure. In fact, only one element (C_{11} or $C_{66} = C_{55}$) from the six independent ones of the stiffness tensor $\overset{\leftrightarrow}{C}_{\text{eff}}\ (\boldsymbol{k}(\omega),\omega)$ is used in calculating the dispersion relation for each polarization (L, TY, or TZ).

The phononic band gaps for transverse (longitudinal) modes are characterized by a complex dynamic mass density $\rho_{yy} = \rho_{zz}$ (ρ_{xx}) (see panel (b) in Fig. 4.3) and, consequently, a wave number k_x with nonzero imaginary part ($\Im[k_x] > 0$). Interestingly, the calculation of the phononic dispersion relation $k_x(\omega)$ with the effective parameters (Eq. (4.1.6)) at frequencies above the first band gap leads to values of the wave vector beyond the first BZ (see panel (d) of Fig. 4.3). In total agreement with conventional theories, the three principal values of the mass density tensor coincide in the quasi-static limit: $\rho_{xx} = \rho_{yy} = \rho_{zz} = \rho_{qs}$ when $\omega \to 0$. However, at sufficiently high frequencies, such values turn out to be different. In particular, $\rho_{xx}(\omega)$ is noticeably different from the other two components because the first phononic band gap for transverse modes appears at lower frequencies in comparison with the gap of longitudinal modes. On the other hand, the stiffness components turned out to be almost constant in the pass bands, where k_x is a real number.

4.3.4 Cubic array of Au square bars embedded in Si

In Fig. 4.4, the calculated frequency dependences of the effective elastic parameters (panels (b) and (c)) and dispersion relations $k_x(\omega)$ for transverse and longitudinal modes (panel (d)) propagating along the x-axis in a cubic periodic array of Au square bars embedded in Si (see panel (a)) are presented. Each bar has a height equal to $7a/10$ and its square cross-sectional area is $(2a/10)^2 = 0.04a^2$ (i.e. the Au filling fraction $f = 0.028$). The used f value to calculate the curves shown in Fig. 4.4 is close to that of the filling fraction for Au cubes considered in Fig. 4.3. Therefore, the results in Figs. 4.3 and 4.4 illustrate the effect of the inclusion shape upon both nonlocal effective elastic parameters and dispersion relations for phononic modes. At very low frequencies ($\omega \to 0$), the principal values of the mass density are equal to ρ_{qs} (Eq. (4.3.2)) (see. Fig. 4.4(b)). As the frequency ω is increased, the nonzero (diagonal) elements of the dynamic mass-density tensor become different ($\rho_{xx} \neq \rho_{yy} \neq \rho_{zz}$) and the homogenized SPC possesses orthorhombic symmetry

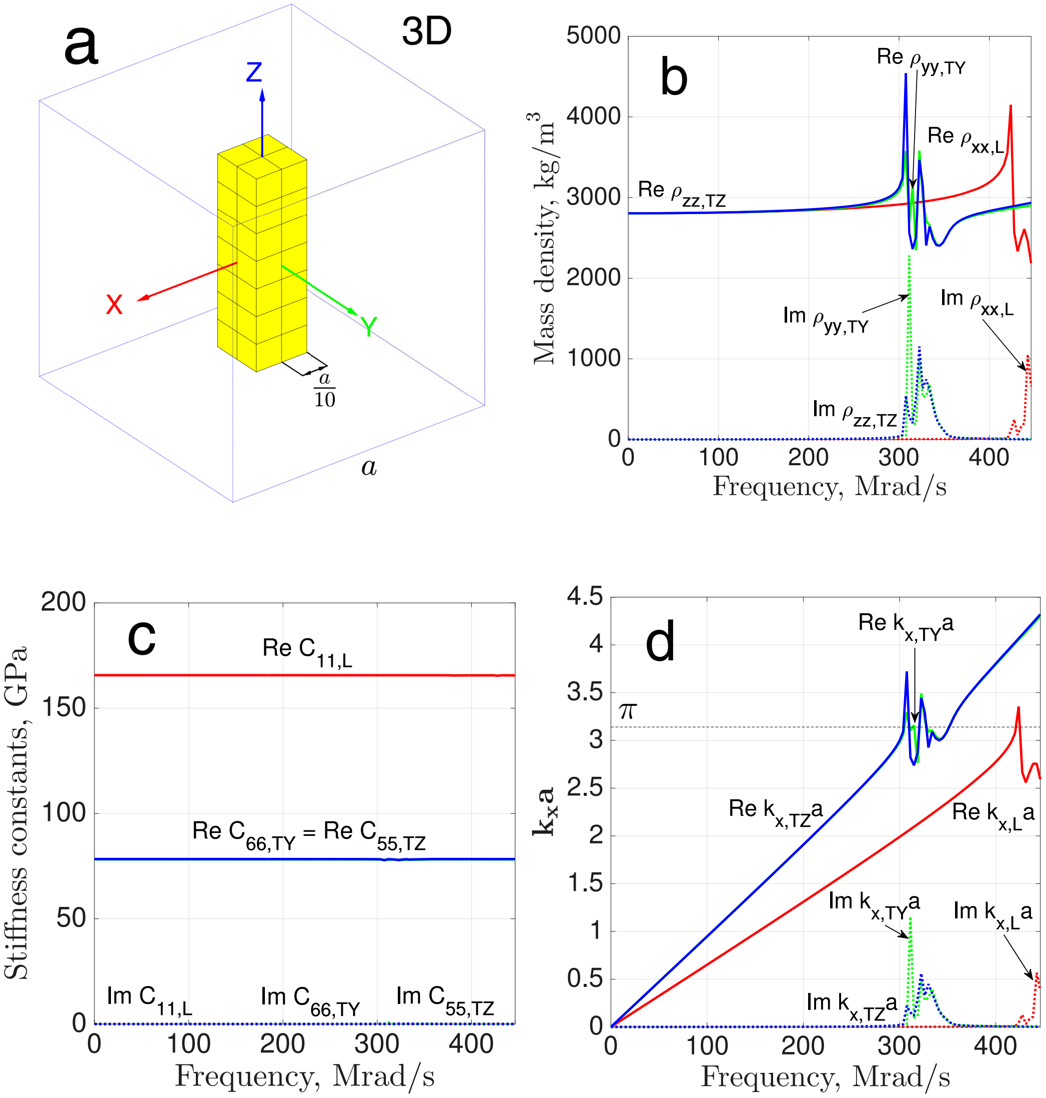

Figure 4.4: (a) Scheme of a unit cell for a cubic lattice of Au square bars embedded in Si. Panels (b) and (c): Graphs of the calculated frequency dependence for elements of the effective mass density and stiffness tensors. (d) Dispersion relations for transverse (TY and TZ) and longitudinal (L) phononic modes.

with nine independent elements of the stiffness tensor $\overleftrightarrow{C}_{\text{eff}}\,(\boldsymbol{k}(\omega),\omega)$. Nevertheless, the dispersion relations for L, TY, and TZ modes can be separately calculated by employing only one element (C_{11}, C_{55}, or C_{66}) in the expressions (4.3.3), which are also valid for phononic modes propagating along the [100] direction of an orthorhombic crystal. Using the effective parameters shown in panels (b) and (c) of Fig. 4.4 and Eq. (4.3.3), the exact

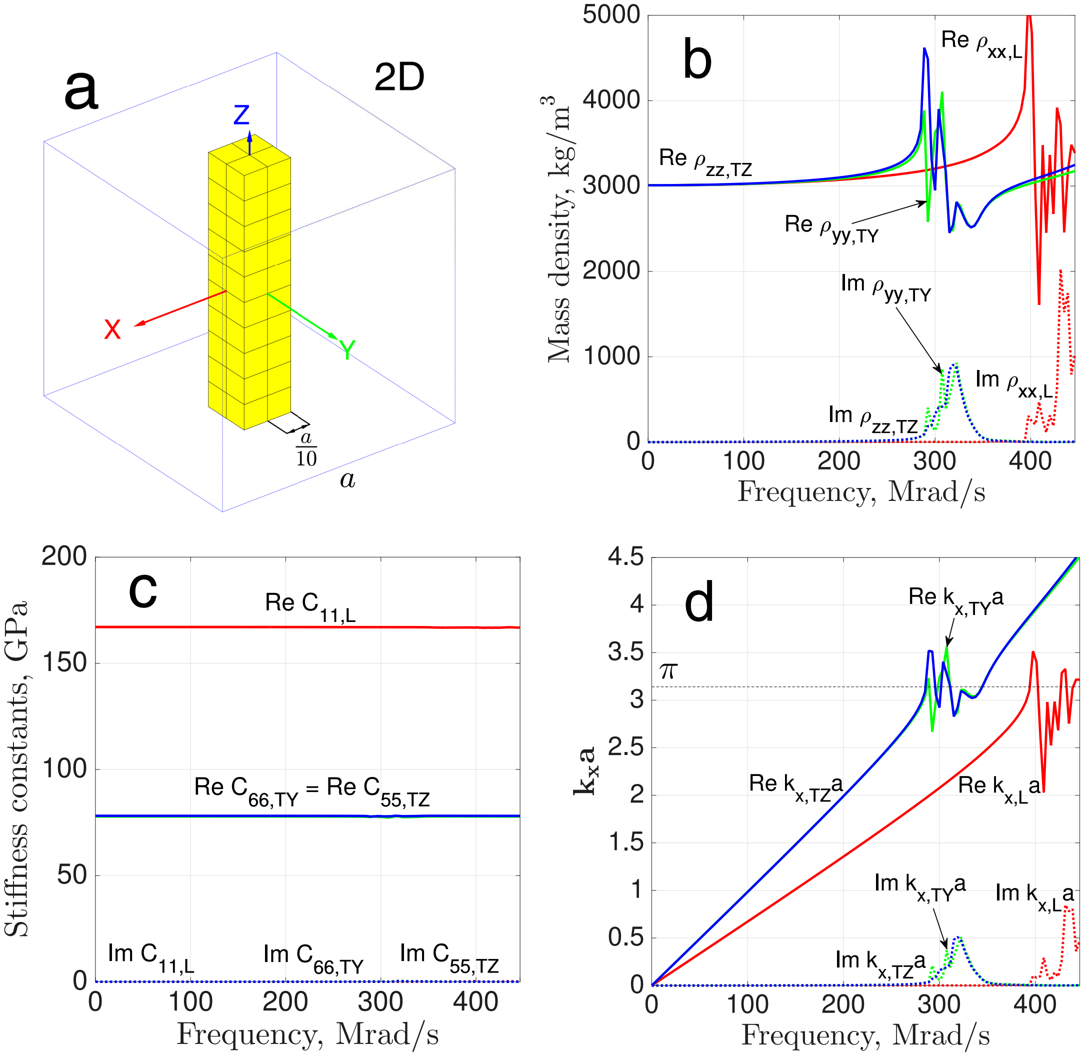

Figure 4.5: (a) Scheme of a unit cell for a 2D square lattice of Au square bars embedded in Si. Panels (b) and (c): Graphs of the calculated frequency dependence for elements of the effective mass density and stiffness tensors. (d) Dispersion relations for transverse (TY and TZ) and longitudinal (L) phononic modes.

phononic dispersion $k_x(\omega)$ for the SPC is obtained even beyond the local low-frequency limit. The phononic gaps for transverse and longitudinal modes in the SPC with square bars (Fig. 4.4(d)) appear at higher frequencies in comparison with the band gaps of the corresponding modes in the SPC with cubic inclusions (Fig. 4.3(d)).

In the case, when the height of the Au square bar is equal to the lattice constant

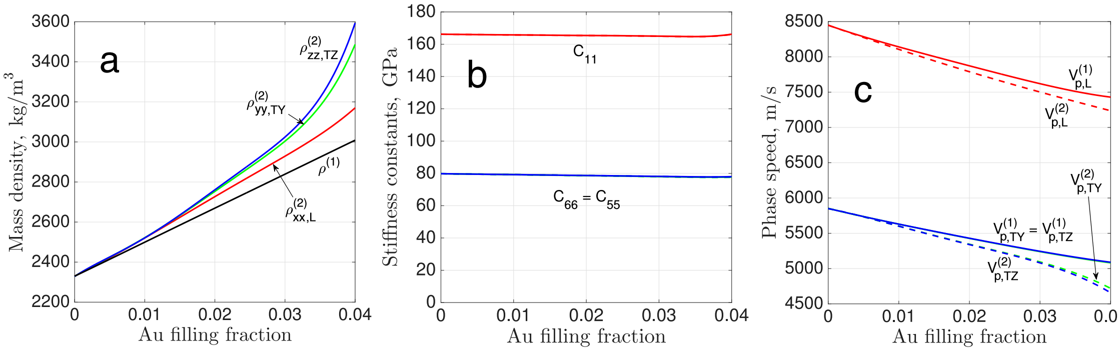

Figure 4.6: Elements of the effective mass density (a) and stiffness (b) tensors for a cubic array of Au square bars embedded in Si vs the Au filling fraction f at two different frequencies [$\omega = 30$ krad/s (label 1) and $\omega = 280$ Mrad/s (label 2)]. Phase speeds v_p for the transverse and longitudinal phononic modes vs f calculated with the effective parameters shown in panels (a) and (b).

a, the phononic crystal becomes a two-dimensional one (2D SPC, see panel (a) of Fig. 4.5). After comparing Figs. 4.4(b) and 4.5(b), one can see that both anisotropy and nonlocality of the dynamic mass density, observed at sufficiently high frequencies, are stronger than those observed for the three-dimensional SPC (panel (a) of Fig. 4.4). Besides, the band gaps for both transverse and longitudinal phononic modes in the 2D SPC appear at lower frequencies in comparison with the respective gaps for the 3D SPC.

The panels (a) and (b) of Fig. 4.6 present the dependences of the components of the effective mass density and stiffness tensors for the TY, TZ, and L phononic modes vs the Au filling fraction f (in fact, the height of the Au square bar), which was calculated at two different frequencies. At the lower frequency, namely $\omega = 30$ krad/s, there is no manifestation of the mass-density anisotropy because the conditions for the local long-wavelength limit are still satisfied, i.e. $k_x a \ll 1$ for the three phononic modes. Moreover, the effective mass density $\rho^{(1)} = \rho_{xx} = \rho_{yy} = \rho_{zz}$ at $\omega = 30$ krad/s linearly depends on the Au filling fraction as in Eq. (4.3.2). At the frequency, $\omega = 280$ Mrad/s, just below the first band gap for the transverse phononic modes, the anisotropy of the dynamic mass density becomes stronger as the Au filling fraction f is increased. The components of the stiffness tensor practically do not change within the interval $0 < f < 0.04$ at the two chosen frequencies (see panel (b) of Fig. 4.6). In the panel (c) of the figure, the dependence of the phase speed $v_p = \omega/k_x$ on the Au filling fraction f is shown at the same two frequencies as in panels (a) and (b). As it is seen, the phase speeds for the transverse (TY, TZ) and longitudinal (L) modes decrease with f. Moreover, such a decrease is faster at the higher frequency ($\omega = 280$ Mrad/s) where the wave vector $k_x > 1/a$ for the three polarizations of phononic modes. These results allow to explain the shift to lower frequencies of the first phononic gaps for both transverse and longitudinal modes, which was observed in Figs. 4.4 and 4.5, as a direct consequence of the increase of the effective dynamic mass density. Indeed, according to Eq. (4.3.3), the phase velocity ω/k_x at the bottom of the first phononic gap (at $k_x a = \pi$) decreases with the mass density.

4.3.5 Tetragonal array of Au cubes embedded in Si

Now, consider a noncubic (namely, tetragonal) lattice of Au cubes in a Si host matrix as in panel (a) of Fig. 4.7. The calculated frequency dependences of the effective elastic parameters and the dispersion relations for phononic modes, propagating along [100] direction of the SPC are also displayed in Fig. 4.7. The homogenized SPC has an orthorhombic symmetry, characterized by nine independent elements in the effective stiffness tensor. However, as in the previous subsections, the phononic dispersion curves $k_x(\omega)$ for transverse (TY and TZ) and longitudinal (L) modes can be separately calculated by using the equations (4.3.3) with the corresponding stiffness element (C_{11}, C_{55}, or C_{66}). As it is seen in Fig. 4.7(b), in the low-frequency limit ($\omega \to 0$), the principal values of the effective dynamic mass-density tensor are identical ($\rho_{xx} = \rho_{yy} = \rho_{zz}$), but at sufficiently large frequencies the anisotropy in the dynamic mass-density is well manifest despite the relatively small Au filling fraction $f = 0.0135$. A striking result is connected with the appearance of a phononic gap for longitudinal modes partially overlapping the phononic gap for transverse modes (see panel (d) in Fig. 4.7). This result suggests a strong coupling of transverse and longitudinal modes in comparison with the cases of Au cubes and bars arranged in cubic lattices (compare with all the dispersion relations above presented).

In Fig. 4.8, there is a comparison of the obtained numerical results for the frequency-dependent mass density and dispersion relation of longitudinal phononic modes in a cubic (panels (a), (b)) and tetragonal (panels (c), (d)) lattices of cubic Au inclusions calculated by using FFDA with direct summations over a very large number of reciprocal wave vectors ($N_{max} = 41^3 = 68921$) and with the integral approach (Sec. 4.2). The calculation of sum $\overline{\overline{\boldsymbol{S}}}_D(i,j)$ in Eq. (4.2.1) was carried out over reciprocal lattice vectors having

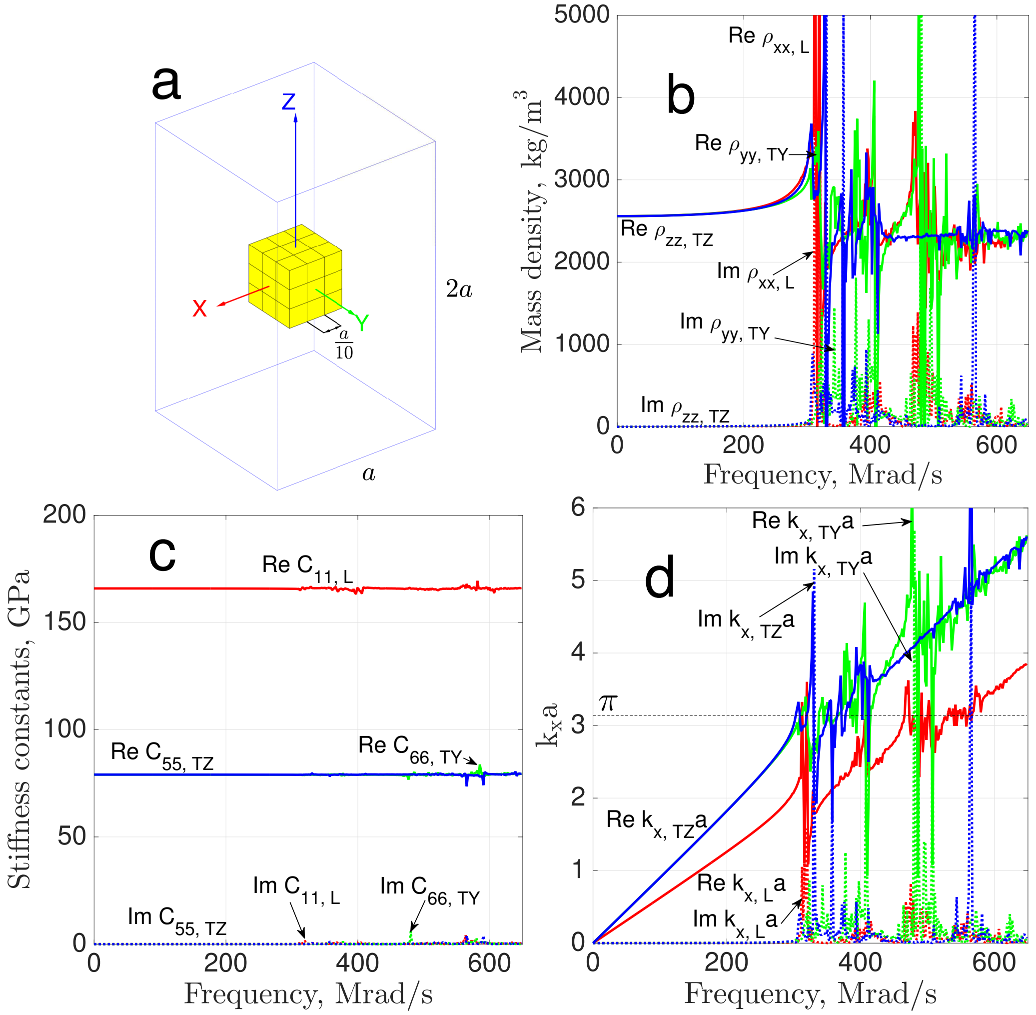

Figure 4.7: (a) Scheme of a unit cell of a tetragonal lattice of Au cubes embedded in Si. Panels (b) and (c): Graphs of the calculated frequency dependence for elements of the effective mass density and stiffness tensors. (d) Dispersion relations for transverse (TY and TZ) and longitudinal (L) phononic modes.

the magnitude $|\boldsymbol{G}| \leq G_0$, where $G_0 = 10(2\pi/a)$. The number of reciprocal wave vectors inside the sphere of radius G_0 is, respectively, 4169 and 9261 for cubic and tetragonal lattices. Both methods predict almost identical results in the pass bands. However, the IAM is faster than the direct summation method. Indeed, the calculations of the results, shown in Fig. 4.8, for the cubic lattice with using the direct summation method, required 1079 minutes, whereas the IAM needed only 154 minutes of computing time. Hence, the IAM could be very useful when the direct summation method cannot be applied because of the excessive computing time.

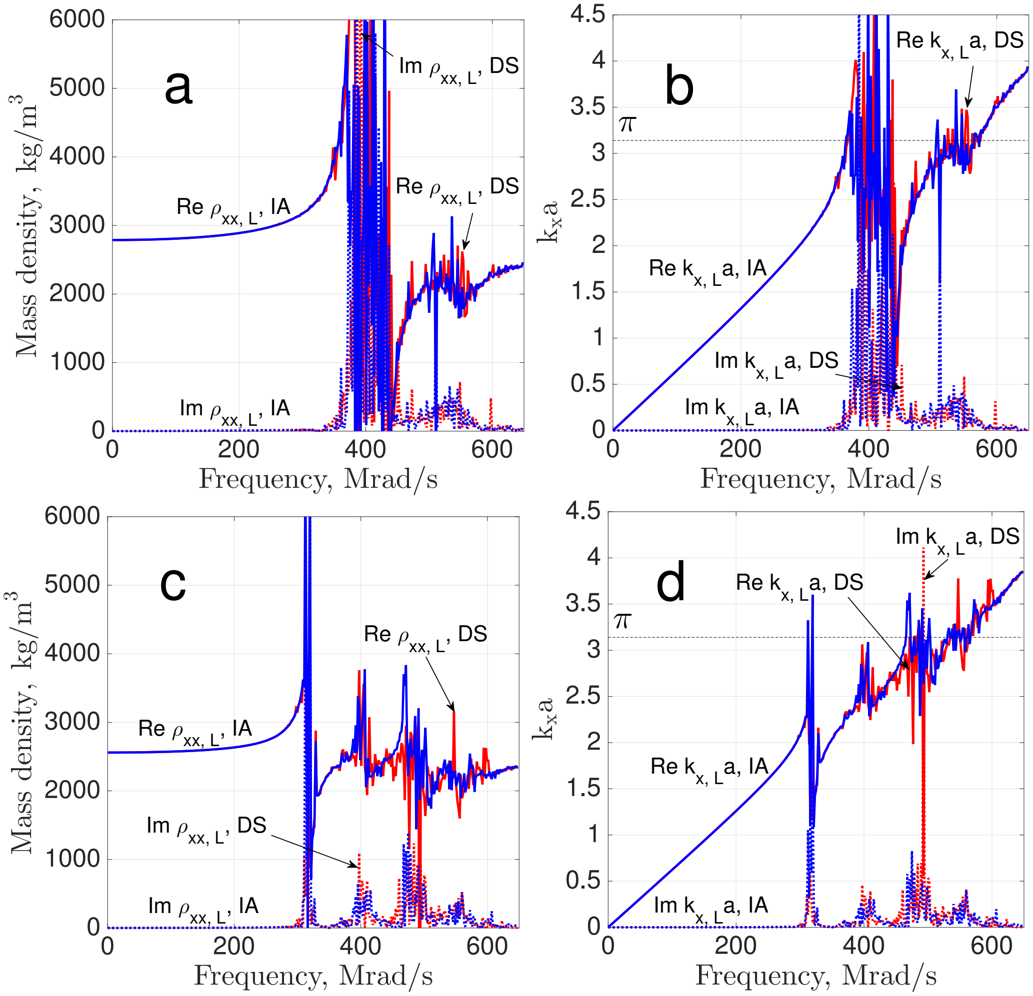

Figure 4.8: Graphs for the frequency-dependent ρ_{xx} and dispersion relation for longitudinal phononic modes in a cubic ((a), (b)) and tetragonal ((c), (d)) lattices of cubic Au inclusions calculated by using FFDA with direct summations (DS) over a very large number of reciprocal wave vectors (red lines) and with the integral approach (IA, blue lines).

4.3.6 Discussion and conclusions

Our results (Figs. 4.1 to 4.8) illustrate the usefulness of the applied nonlocal homogenization approach, based on the Fourier formalism. The FFDA allows to reduce the size of the system of equations, which should be solved to calculate the effective elastic parameters (see Sec. 2.3.8). However, such an approach still requires the calculation of sums over a large number of reciprocal lattice vectors for a good accuracy of the results, especially when there is a high contrast of the mass density and elastic moduli of the materials in the unit cell of the phononic crystal. In the case of Au inclusions in a Si host matrix, the mass density contrast is noticeable ($\rho_{\mathrm{Si}} \ll \rho_{\mathrm{Au}}$), whereas their stiffness components (C_{11}, C_{12} and C_{44}) are comparable (see panels (b) and (d) of Figs. 4.1 and 4.2). The numerical difficulties for the calculation of the effective nonlocal metasolid response could be managed within the FFDA by calculating both sums with a very large number of reciprocal vectors (Sec. 2.3.8), and approximating series by improper integrals (as it is shown in Sec. 4.2). The later approach might be helpful, particularly, in calculating the nonlocal effective parameters for phononic crystals with large elastic contrast and inclusions of very small size. Indeed, in the latter case, the convergence of the series in the expressions for the elements of the effective nonlocal-response matrix $\overline{\overline{\boldsymbol{A}}}_{\mathrm{eff}}(\boldsymbol{k}(\omega), \omega)$ is achieved with using an extremely-large number of reciprocal lattice vectors.

It should be noted that the iterative procedure, applied here to determine the phononic dispersion relation $\boldsymbol{k}(\omega)$, provides only one solution which depends on the chosen initial value for the wave vector. The initial value of wave vector is close to zero ($\boldsymbol{k} \to 0$). At sufficiently large frequencies (above the first band gap) the obtained solution for $\boldsymbol{k} = k_x(w)\hat{x}$ can lie in the second Brillouin zone in the extended scheme (see panels (d) of Figs. 4.3-4.5, 4.7 and 4.8). Interestingly, this result is similar to that found in Ref. [86], where it was shown that the effective parameters of the effective nonlocal dielectric response for photonic crystals can lead to wave vectors beyond the first BZ.

Our results were obtained for phononic modes propagating along one of the principal axes of the homogenized SPC and demonstrate that the homogenized SPC behaves as a metasolid with anisotropic dynamic mass density in the nonlocal regime. However, the nonlocal effective elastic response depends not only on the magnitude of the wave vector $\boldsymbol{k}$, but also on its direction. For arbitrary direction of $\boldsymbol{k}$, the phononic dispersion relation can also be calculated by iteratively solving Christoffel equations with the corresponding effective nonlocal-response matrix $\overline{\overline{\boldsymbol{A}}}_{\mathrm{eff}}(\boldsymbol{k}(\omega), \omega)$.

Using a general homogenization theory, which coincides with the developed one in [51], the nonlocal effective parameters were calculated, namely mass density and stiffness tensor, for a 3D solid phononic crystal composed of Au cubes or square bars, embedded in a Si host matrix. In order for the calculation to be feasible, the form-factor division approach has been applied in two versions: i) with expressions for the effective parameters having sums over a very large number of reciprocal lattice vectors, and ii) with expressions having series which are approximated by improper integrals.

The calculated effective parameters allow to describe the phononic band structure of the phononic crystal not only in the local low-frequency limit, $k_x a \ll 1$ but also beyond it. Besides, it was shown that the anisotropy in the effective dynamic mass-density, appearing at sufficiently large frequencies, is associated with the dependence of the nonlocal metasolid response on the phononic-mode polarization, the form of the inclusions, and type of the periodic array. On the other hand, the stiffness components turned out to be almost independent of frequency. The latter result is specific for Au-Si periodic composites, which have relatively-large mass-density contrast, but the stiffness elements of both materials are comparable. In addition, for the case of Au cubes arranged in a tetragonal lattice, the first gap for longitudinal modes partially overlaps the gap of transverse modes.

Chapter 5

Conclusions

Metamaterials are one of the most developed topics of materials science with new physics involved. The significant contribution of the present work is a derivation of a nonlocal homogenization theory of a electromagnetoelastic crystal which is able to calculate accurately the effective material tensors even far beyond the local limit. The piezoelectric and piezomagnetic effects are the origin of the acoustic-electromagnetic waves coupling inside real structures. Particular cases of homogenized electromagnetic and phononic media can be derived directly from the presented theory by considering piezoelectric and piezomagnetic effects negligible.

The nonlocal effects are responsible for the metamaterial behavior - the appearance of the negative refractive index with non-magnetic materials or the electromagnetoelastic coupling inside the non-piezoelectric/non-piezomagnetic constituents. In order to extract the metamaterial effects from the nonlocal response, making them more understandable, a method of nonlocal parameters transformation is proposed. The metamaterial response is fully equivalent to the original nonlocal description. During the design, fabrication, and characterization of the metamaterials, the extreme usefulness of the introduced metamaterial response was verified experimentally. Furthermore, new metamaterials were designed and fabricated using the developed piezoelectromagnetic homogenization theory as an instrument.

Within the developed piezoelectromagnetic formalism, the microscopic field inside a electromagnetoelastic crystal has been expressed in terms of the macroscopic field. This advance gives the possibility of calculating reflectance and transmission of both acoustic and electromagnetic metamaterials having the form of finite-size samples.

The obtained results for both electromagnetic and elastic structures encourage to design metamaterials possessing, in principle, a simultaneously quadruple-negative behavior of a foxonic crystal - negative bulk modulus, negative dynamic density, negative permittivity, and permeability. As a consequence, simultaneous control of acoustic and electromagnetic waves propagation could give a variety of real-world applications.

Chapter 6

Publications

Articles in international refereed journals

1. A. Konovalenko, E. Gutiérrez-Reyes, A. L. González, J. Flores-Méndez and F. Pérez-Rodríguez, "Nonlocal metasolid response of homogenized phononic crystals", *Journal of Applied Physics*, vol. 121, no. 15, pp. 155102, 2017.
2. A. Konovalenko and F. Pérez-Rodríguez, "Nonlocal response of tunable photonic metamaterials with semiconductor inclusions", *Journal of Optical Society of America B*, vol. 34, no. 9, 2017.

Articles in Proceedings

1. A. Konovalenko, J. A. Reyes-Avendaño, and F. Pérez-Rodríguez, "Chiral metamaterials based on twisted U-shaped inclusions," in Latin America Optics and Photonics Conference, OSA Technical Digest (online) (Optical Society of America, 2014), LM4A.33. ISBN: 978-1-55752-825-4, http://dx.doi.org/10.1364/LAOP.2014.LM4A.33
2. A. Konovalenko, J. A. Reyes-Avendaño, and F. Pérez-Rodríguez, "Influence of metal conductivity on the chirality of metamaterials with twisted U-shaped resonators", in VI Taller sobre Metamateriales, Cristales Fotónicos, Cristales Fonónicos y Estructuras Plasmónicas, San Miguel de Allende, 11-14 de Enero, 2015, pp. 111-113.
3. A. Konovalenko, J. A. Reyes-Avendaño, and F. Pérez-Rodríguez, "A Wideband Double-Negative Metamaterial Based on Framed Crosses", META'15 New York - USA, The

6th International Conference on Metamaterials, Photonic Crystals and Plasmonics, Proceedings, pp. 1468-1469. ISBN 978-2-9545460-7-0.

Participation in Congresses

1. Félipe Pérez-Rodríguez, Anatolii Konovalenko, and Jorge A. Reyes-Avendaño, "Chiral metamaterials based on twisted U-shaped inclusions". In Latin America Optics and Photonics Conference (pp. LM4A-33), Cancun, México, 17–21 November 2014.

2. Anatolii Konovalenko, Jorge A. Reyes-Avendaño, and Felipe Pérez-Rodríguez, "Influence of metal conductivity on the chirality of metamaterials with twisted U-shaped resonators", VI Taller sobre Metamateriales, Cristales Fotónicos, Cristales Fonónicos y Estructuras Plasmónicas, San Miguel de Allende, Guanajuato, México, 11-14 January 2015.

3. Anatolii Konovalenko, Jorge A. Reyes-Avendaño and Felipe Pérez-Rodríguez, "A Wideband Double-Negative Metamaterial Based on Framed Crosses", META, New York, Session 1P1, 4-7 August 2015.

4. Anatolii Konovalenko, E. Gutiérrez-Reyes, A. L. González, J. Flores-Méndez and Felipe Pérez-Rodríguez, "Nonlocal Metasolid Response Of Homogenized Phononic Crystals", EMN Meeting Metamaterials, Dubrovnik, Croatia, 8-12 May 2016.

5. Anatolii Konovalenko, Jorge A. Reyes-Avendaño, and Felipe Pérez-Rodríguez, "Double-negative metamaterial in optical range based on nanoscaled gold framed crosses", The 6th Mexican Workshop on Nanostructured Materials, Session P2-20, Benemérita Universidad Autónoma de Puebla, México, 12-14 October 2016.

6. Anatolii Konovalenko and Felipe Pérez-Rodríguez, "Nonlocal Bianisotropic Response of Homogenized 3D Photonic Crystals", The 38th PIERS, Session 3P10, St. Petersburg, Russia, 22-25 May 2017.

Bibliography

[1] V. Veselago, “Electrodynamics of materials both permittivity and permeability being negative”, *Uspekhi Fizicheskikh Nauk (in Russian)*, vol. 92, no. 7, pp. 517–526, 1967.

[2] R. M. Walser, “Electromagnetic metamaterials”, vol. 4467, 2001, pp. 1–15.

[3] J. B. Pendry, A. J. Holden, W. J. Stewart, and I. Youngs, “Extremely low frequency plasmons in metallic mesostructures”, *Phys. Rev. Lett.*, vol. 76, pp. 4773–4776, 25 Jun. 1996.

[4] J. B. Pendry, A. J. Holden, D. J. Robbins, and W. J. Stewart, “Low frequency plasmons in thin-wire structures”, *Journal of Physics-Condensed Matter*, vol. 10, pp. 4785–4809, 1998.

[5] J. B. Pendry, A. J. Holden, D. Robbins, and W. Stewart, “Magnetism from conductors and enhanced nonlinear phenomena”, *IEEE transactions on microwave theory and techniques*, vol. 47, no. 11, pp. 2075–2084, 1999.

[6] F. Capolino, *Theory and phenomena of metamaterials.* CRC Press, 2009.

[7] D. R. Smith, W. J. Padilla, D. C. Vier, S. C. Nemat-Nasser, and S. Schultz, “Composite medium with simultaneously negative permeability and permittivity”, *Phys. Rev. Lett.*, vol. 84, pp. 4184–4187, 18 May 2000.

[8] R. Marqués, F. Medina, and R. Rafii-El-Idrissi, “Role of bianisotropy in negative permeability and left-handed metamaterials”, *Phys. Rev. B*, vol. 65, p. 144 440, 14 Apr. 2002.

[9] N. Katsarakis, M. Kafesaki, I. Tsiapa, E. Economou, and C. Soukoulis, “High transmittance left-handed materials involving symmetric split-ring resonators”, *Photonics and Nanostructures-Fundamentals and Applications*, vol. 5, no. 4, pp. 149–155, 2007.

[10] T. Koschny, L. Zhang, and C. M. Soukoulis, “Isotropic three-dimensional left-handed metamaterials”, *Phys. Rev. B*, vol. 71, p. 121 103, 12 Mar. 2005.

[11] V. M. Shalaev, W. Cai, U. K. Chettiar, H.-K. Yuan, A. K. Sarychev, V. P. Drachev, and A. V. Kildishev, “Negative index of refraction in optical metamaterials”, *Opt. Lett.*, vol. 30, no. 24, pp. 3356–3358, Dec. 2005.

[12] S. Zhang, W. Fan, B. K. Minhas, A. Frauenglass, K. J. Malloy, and S. R. J. Brueck, “Midinfrared resonant magnetic nanostructures exhibiting a negative permeability”, *Phys. Rev. Lett.*, vol. 94, p. 037 402, 3 Jan. 2005.

[13] S. Zhang, W. Fan, N. C. Panoiu, K. J. Malloy, R. M. Osgood, and S. R. J. Brueck, “Experimental demonstration of near-infrared negative-index metamaterials”, *Phys. Rev. Lett.*, vol. 95, p. 137 404, 13 Sep. 2005.

[14] G. Dolling, C. Enkrich, M. Wegener, C. M. Soukoulis, and S. Linden, “Simultaneous negative phase and group velocity of light in a metamaterial”, *Science*, vol. 312, no. 5775, pp. 892–894, 2006, ISSN: 0036-8075.

[15] I. Bergmair, B. Dastmalchi, M. Bergmair, A. Saeed, W. Hilber, G. Hesser, C. Helgert, E. Pshenay-Severin, T. Pertsch, E. B. Kley, U. Hübner, N. H. Shen, R. Penciu, M. Kafesaki, C. M. Soukoulis, K. Hingerl, M. Muehlberger, and R. Schoeftner, “Single and multilayer metamaterials fabricated by nanoimprint lithography”, *Nanotechnology*, vol. 22, no. 32, p. 325 301, 2011.

[16] C. Imhof and R. Zengerle, “Pairs of metallic crosses as a left-handed metamaterial with improved polarization properties”, *Opt. Express*, vol. 14, no. 18, pp. 8257–8262, Sep. 2006.

[17] O. Paul, C. Imhof, B. Reinhard, R. Zengerle, and R. Beigang, “Negative index bulk metamaterial at terahertz frequencies”, *Opt. Express*, vol. 16, no. 9, pp. 6736–6744, Apr. 2008.

[18] Z. Wei-Ren and Z. Xiao-Peng, “Numerical study of low-loss cross left-handed metamaterials at visible frequency”, *Chinese Physics Letters*, vol. 26, no. 7, p. 074 212, 2009.

[19] A. Vallecchi, F. Capolino, and A. G. Schuchinsky, “2D isotropic effective negative refractive index metamaterial in planar technology”, *IEEE Microwave and Wireless Components Letters*, vol. 19, no. 5, pp. 269–271, May 2009, ISSN: 1531-1309.

[20] J. Wang, S. Qu, H. Ma, S. Xia, Y. Yang, L. Lu, X. Wu, Z. Xu, and Q. Wang, “Experimental verification of anisotropic three-dimensional left-handed metamaterial composed of jerusalem crosses”, *Piers Online*, vol. 6, no. 1, pp. 31–35, 2010.

[21] C. M. Soukoulis and M. Wegener, “Past achievements and future challenges in the development of three-dimensional photonic metamaterials”, *Nat Photon*, vol. 5, no. 9, pp. 523–530, Sep. 2011, ISSN: 1749-4885.

[22] Z. Li, M. Mutlu, and E. Ozbay, “Chiral metamaterials: From optical activity and negative refractive index to asymmetric transmission”, *Journal of Optics*, vol. 15, no. 2, p. 023 001, 2013.

[23] T. G. Mackay and A. Lakhtakia, “Negatively refracting chiral metamaterials: A review”, *Journal of Photonics for Energy*, pp. 018003-018003-29, 2010.

[24] M. Wegener and N. Zheludev, “Artificial chiral materials”, *J. Opt. A: Pure Appl. Opt*, vol. 11, no. 070201, p. 2, 2009.

[25] A. V. Rogacheva, V. A. Fedotov, A. S. Schwanecke, and N. I. Zheludev, “Giant gyrotropy due to electromagnetic-field coupling in a bilayered chiral structure”, *Phys. Rev. Lett.*, vol. 97, p. 177 401, 17 Oct. 2006.

[26] E. Plum, J. Zhou, J. Dong, V. A. Fedotov, T. Koschny, C. M. Soukoulis, and N. I. Zheludev, "Metamaterial with negative index due to chirality", *Phys. Rev. B*, vol. 79, p. 035 407, 3 Jan. 2009.

[27] J. Zhou, J. Dong, B. Wang, T. Koschny, M. Kafesaki, and C. M. Soukoulis, "Negative refractive index due to chirality", *Physical Review B*, vol. 79, no. 12, p. 121 104, 2009.

[28] J. Dong, J. Zhou, T. Koschny, and C. Soukoulis, "Bi-layer cross chiral structure with strong optical activity and negative refractive index", *Opt. Express*, vol. 17, no. 16, pp. 14 172–14 179, Aug. 2009.

[29] Z. Li, H. Caglayan, E. Colak, J. Zhou, C. M. Soukoulis, and E. Ozbay, "Coupling effect between two adjacent chiral structure layers", *Optics express*, vol. 18, no. 6, pp. 5375–5383, 2010.

[30] Z. Li, R. Zhao, T. Koschny, M. Kafesaki, K. B. Alici, E. Colak, H. Caglayan, E. Ozbay, and C. Soukoulis, "Chiral metamaterials with negative refractive index based on four "U" split ring resonators", *Applied Physics Letters*, vol. 97, no. 8, p. 081 901, 2010.

[31] M. Mutlu, A. E. Akosman, A. E. Serebryannikov, and E. Ozbay, "Asymmetric transmission of linearly polarized waves and polarization angle dependent wave rotation using a chiral metamaterial", *Opt. Express*, vol. 19, no. 15, pp. 14 290–14 299, Jul. 2011.

[32] R. Zhao, L. Zhang, J. Zhou, T. Koschny, and C. M. Soukoulis, "Conjugated gammadion chiral metamaterial with uniaxial optical activity and negative refractive index", *Phys. Rev. B*, vol. 83, p. 035 105, 3 Jan. 2011.

[33] W. Panpradit, A. Sonsilphong, C. Soemphol, and N. Wongkasem, "High negative refractive index in chiral metamaterials", *Journal of Optics*, vol. 14, no. 7, p. 075 101, 2012.

[34] J. K. Gansel, M. Thiel, M. S. Rill, M. Decker, K. Bade, V. Saile, G. von Freymann, S. Linden, and M. Wegener, "Gold helix photonic metamaterial as broadband circular polarizer", *Science*, vol. 325, no. 5947, pp. 1513–1515, 2009.

[35] B. Wang, J. Zhou, T. Koschny, and C. M. Soukoulis, "Nonplanar chiral metamaterials with negative index", *Applied Physics Letters*, vol. 94, no. 15, p. 151 112, 2009.

[36] Z. Li, K. B. Alici, E. Colak, and E. Ozbay, "Complementary chiral metamaterials with giant optical activity and negative refractive index", *Applied Physics Letters*, vol. 98, no. 16, p. 161 907, 2011.

[37] M. Giloan and S. Astilean, "Negative index optical chiral metamaterial based on asymmetric hexagonal arrays of metallic triangular nanoprisms", *Optics Communications*, vol. 315, pp. 122–129, 2014, ISSN: 0030-4018.

[38] S. Zhang, Y.-S. Park, J. Li, X. Lu, W. Zhang, and X. Zhang, "Negative refractive index in chiral metamaterials", *Phys. Rev. Lett.*, vol. 102, p. 023 901, 2 Jan. 2009.

[39] J. Li and C. Chan, "Double-negative acoustic metamaterial", *Physical Review E*, vol. 70, no. 5, p. 055 602, 2004.

[40] N. Fang, D. Xi, J. Xu, M. Ambati, W. Srituravanich, C. Sun, and X. Zhang, "Ultrasonic metamaterials with negative modulus", *Nature materials*, vol. 5, no. 6, pp. 452–456, 2006.

[41] M. Ambati, N. Fang, C. Sun, and X. Zhang, "Surface resonant states and superlensing in acoustic metamaterials", *Physical Review B*, vol. 75, no. 19, p. 195 447, 2007.

[42] D. Torrent and J. Sánchez-Dehesa, "Sound scattering by anisotropic metafluids based on two-dimensional sonic crystals", *Physical Review B*, vol. 79, no. 17, p. 174 104, 2009.

[43] M. J. Seitel, J. W. Shan, and D. T. Stephen, "Controllable acoustic media having anisotropic mass density and tunable speed of sound", *Applied Physics Letters*, vol. 101, no. 6, p. 061 916, 2012.

[44] R. Graciá-Salgado, D. Torrent, and J. Sánchez-Dehesa, "Double-negative acoustic metamaterials based on quasi-two-dimensional fluid-like shells", *New Journal of Physics*, vol. 14, no. 10, p. 103 052, 2012.

[45] X. Zhou and G. Hu, "Analytic model of elastic metamaterials with local resonances", *Physical Review B*, vol. 79, no. 19, p. 195 109, 2009.

[46] Y. Wu, Y. Lai, and Z.-Q. Zhang, "Elastic metamaterials with simultaneously negative effective shear modulus and mass density", *Physical review letters*, vol. 107, no. 10, p. 105 506, 2011.

[47] S. Nemat-Nasser, J. R. Willis, A. Srivastava, and A. V. Amirkhizi, "Homogenization of periodic elastic composites and locally resonant sonic materials", *Physical Review B*, vol. 83, no. 10, p. 104 103, 2011.

[48] I. Solís-Mora, M. Palomino-Ovando, and F. Pérez-Rodríguez, "Elastic superlattices with simultaneously negative effective mass density and shear modulus", *Journal of Applied Physics*, vol. 113, no. 9, p. 093 508, 2013.

[49] Y. Lai, Y. Wu, P. Sheng, and Z.-Q. Zhang, "Hybrid elastic solids", *Nature materials*, vol. 10, no. 8, pp. 620–624, 2011.

[50] R. Zhu, X. Liu, G. Huang, H.-H. Huang, and C. Sun, "Microstructural design and experimental validation of elastic metamaterial plates with anisotropic mass density", *Physical Review B*, vol. 86, no. 14, p. 144 307, 2012.

[51] J. Flores-Méndez and F. Perez-Rodriguez, "Metasolid with anisotropic mass density", *EPL (Europhysics Letters)*, vol. 103, no. 5, p. 54 001, 2013.

[52] V. Cerdán-Ramírez, B. Zenteno-Mateo, M. P. Sampedro, M. A. Palomino-Ovando, B. Flores-Desirena, and F. Pérez-Rodríguez, "Anisotropy effects in homogenized magnetodielectric photonic crystals", *J. Appl. Phys.*, vol. 106, no. 10, p. 103 520, 2009.

[53] A. A. Krokhin, J. Arriaga, and L. Gumen, "Speed of sound in periodic elastic composites", *Physical review letters*, vol. 91, no. 26, p. 264 302, 2003.

[54] X.-W. Zhou, X.-Y. Zou, T.-H. Wang, and J.-C. Cheng, "Effective velocity of 2D phononic crystals with rectangular lattice", *Ultrasonics*, vol. 50, no. 6, pp. 577–582, 2010.

[55] Y. Wu, Y. Lai, and Z.-Q. Zhang, "Effective medium theory for elastic metamaterials in two dimensions", *Physical Review B*, vol. 76, no. 20, p. 205 313, 2007.

[56] Z. Liu, X. Zhang, Y. Mao, Y. Zhu, Z. Yang, C. Chan, and P. Sheng, "Locally resonant sonic materials", *Science*, vol. 289, no. 5485, pp. 1734–1736, 2000.

[57] X. Liu, G. Hu, G. Huang, and C. Sun, "An elastic metamaterial with simultaneously negative mass density and bulk modulus", *Applied physics letters*, vol. 98, no. 25, p. 251 907, 2011.

[58] U. C. Hasar, J. J. Barroso, M. Bute, A. Muratoglu, and M. Ertugrul, "Boundary effects on the determination of electromagnetic properties of bianisotropic metamaterials from scattering parameters", *IEEE Transactions on Antennas and Propagation*, vol. 64, no. 8, pp. 3459–3469, 2016.

[59] A. Vinogradov, A. Ignatov, A. Merzlikin, S. Tretyakov, and C. Simovski, "Additional effective medium parameters for composite materials (excess surface currents)", *Optics express*, vol. 19, no. 7, pp. 6699–6704, 2011.

[60] D. R. Smith, D. C. Vier, T. Koschny, and C. M. Soukoulis, "Electromagnetic parameter retrieval from inhomogeneous metamaterials", *Phys. Rev. E*, vol. 71, p. 036 617, 3 Mar. 2005.

[61] D. R. Smith and J. B. Pendry, "Homogenization of metamaterials by field averaging (invited paper)", *J. Opt. Soc. Am. B*, vol. 23, no. 3, pp. 391–403, Mar. 2006.

[62] J. Jin, S. Liu, Z. Lin, and S. T. Chui, "Effective-medium theory for anisotropic magnetic metamaterials", *Phys. Rev. B*, vol. 80, p. 115 101, 11 Sep. 2009.

[63] R. Zhao, T. Koschny, and C. M. Soukoulis, "Chiral metamaterials: retrieval of the effective parameters with and without substrate", *Opt. Express*, vol. 18, no. 14, pp. 14 553–14 567, Jul. 2010.

[64] A. Andryieuski, C. Menzel, C. Rockstuhl, R. Malureanu, F. Lederer, and A. Lavrinenko, "Homogenization of resonant chiral metamaterials", *Physical Review B*, vol. 82, no. 23, p. 235 107, 2010.

[65] L. Peng and N. A. Mortensen, "Equal-potential interpretation of electrically induced resonances in metamaterials", *New Journal of Physics*, vol. 13, no. 5, p. 053 012, 2011.

[66] D. Zarifi, M. Soleimani, and A. Abdolali, "Parameter retrieval of chiral metamaterials based on the state-space approach", *Phys. Rev. E*, vol. 88, p. 023 204, 2 Aug. 2013.

[67] A. Demetriadou and O. Hess, "Analytic theory of optical nanoplasmonic metamaterials", *Phys. Rev. B*, vol. 87, p. 161 101, 16 Apr. 2013.

[68] A. Alu, "First-principles homogenization theory for periodic metamaterials", *Physical Review B*, vol. 84, no. 7, p. 075 153, 2011.

[69] M. G. Silveirinha, "Nonlocal homogenization model for a periodic array of ϵ-negative rods", *Physical Review E*, vol. 73, no. 4, p. 046 612, 2006.

[70] J. Zhou, T. Koschny, M. Kafesaki, and C. M. Soukoulis, "Size dependence and convergence of the retrieval parameters of metamaterials", *Photonics and Nanostructures - Fundamentals and Applications*, vol. 6, no. 1, pp. 96–101, 2008, The Seventh International Symposium on Photonic and Electromagnetic Crystal StructuresPECS-VII, ISSN: 1569-4410.

[71] D. Song, Z. Tang, L. Zhao, Z. Sui, S. Wen, and D. Fan, "Thickness Conditions for Characterizing the Periodic Nanostructures with the Retrieved Electromagnetic Parameters", *Journal of the European Optical Society*, vol. 8, Apr. 2013.

[72] A. Chipouline, C. Simovski, and S. Tretyakov, "Basics of averaging of the maxwell equations for bulk materials", *Metamaterials*, vol. 6, no. 3, pp. 77–120, 2012.

[73] A. P. Vinogradov and A. M. Merzlikin, "Comment on "Basics of averaging of the maxwell equations for bulk materials"", *Metamaterials*, vol. 6, no. 3, pp. 121–125, 2012.

[74] A. Vinogradov and A. Merzlikin, "On the problem of homogenizing one-dimensional systems", *Journal of Experimental and Theoretical Physics*, vol. 94, no. 3, pp. 482–488, 2002.

[75] J. Reyes-Avendaño, U. Algredo-Badillo, P. Halevi, and F. Pérez-Rodríguez, "From photonic crystals to metamaterials: the bianisotropic response", *New Journal of Physics*, vol. 13, no. 7, p. 073 041, 2011.

[76] R. Tao, Z. Chen, and P. Sheng, "First-principles Fourier approach for the calculation of the effective dielectric constant of periodic composites", *Physical Review B*, vol. 41, no. 4, p. 2417, 1990.

[77] L. C. Shen, C. Liu, J. Korringa, and K. J. Dunn, "Computation of conductivity and dielectric constant of periodic porous media", *Journal of Applied Physics*, vol. 67, no. 11, pp. 7071–7081, 1990.

[78] D. J. Bergman and K.-J. Dunn, "Bulk effective dielectric constant of a composite with a periodic microgeometry", *Physical Review B*, vol. 45, no. 23, p. 13 262, 1992.

[79] S. Datta, C. Chan, K. Ho, and C. Soukoulis, "Effective dielectric constant of periodic composite structures", *Physical Review B*, vol. 48, no. 20, p. 14 936, 1993.

[80] P. Halevi, A. Krokhin, and J. Arriaga, "Photonic crystal optics and homogenization of 2D periodic composites", *Physical review letters*, vol. 82, no. 4, p. 719, 1999.

[81] A. A. Krokhin and E. Reyes, "Homogenization of magnetodielectric photonic crystals", *Physical review letters*, vol. 93, no. 2, p. 023 904, 2004.

[82] G. P. Ortiz, B. E. Martinez-Zerega, B. S. Mendoza, and W. L. Mochán, "Effective optical response of metamaterials", *Physical Review B*, vol. 79, no. 24, p. 245 132, 2009.

[83] B. Zenteno-Mateo, V. Cerdan-Ramirez, B. Flores-Desirena, M. P. Sampedro, E. Juarez-Ruiz, and F. Perez-Rodriguez, "Effective permittivity tensor for a metal-dielectric superlattice", *Progress In Electromagnetics Research Letters*, vol. 22, pp. 165–174, 2011.

[84] W. L. Mochán, G. P. Ortiz, and B. S. Mendoza, "Efficient homogenization procedure for the calculation of optical properties of 3D nanostructured composites", *Optics express*, vol. 18, no. 21, pp. 22 119–22 127, 2010.

[85] E. Cortes, L. Mochán, B. S. Mendoza, and G. P. Ortiz, "Optical properties of nanostructured metamaterials", *Physica status solidi (b)*, vol. 247, no. 8, pp. 2102–2107, 2010.

[86] J. S. Pérez-Huerta, G. P. Ortiz, B. S. Mendoza, and W. L. Mochán, "Macroscopic optical response and photonic bands", *New J. Phys.*, vol. 15, no. 4, p. 043 037, 2013.

[87] R. Haydock, "The recursive solution of the Schrödinger equation", *Computer Physics Communications*, vol. 20, no. 1, pp. 11–16, 1980.

[88] Q. Ni and J. Cheng, "Anisotropy of effective velocity for elastic wave propagation in two-dimensional phononic crystals at low frequencies", *Phys. Rev. B*, vol. 72, no. 1, p. 014 305, 2005.

[89] N. Qing and C. Jian-Chun, "Homogenization of two-dimensional phononic crystals at low frequencies", *Chin. Phys. Lett.*, vol. 22, no. 9, p. 2305, 2005.

[90] Q. Ni and J. Cheng, "Long wavelength propagation of elastic waves in three-dimensional periodic solid-solid media", *J. Appl. Phys.*, vol. 101, no. 7, p. 073 515, 2007.

[91] N. Qing and C. Jian-Chun, "Homogenization of three-dimensional periodic solid-solid elastic composites", *Chin. Phys. Lett.*, vol. 24, no. 3, p. 747, 2007.

[92] J. Liu, Y. Wu, F. Li, P. Zhang, Y. Liu, and J. Wu, "Anisotropy of homogenized phononic crystals with anisotropic material", *Europhys. Lett.*, vol. 98, no. 3, p. 36 001, 2012.

[93] J. Flores Mendez, M. Salazar Villanueva, R. C. Ambrosio Lazaro, B. Calixto Sirene, M. L. Mota Gonzalez, and F. Candia Garcia, "Plane wave-perturbative method for evaluating the effective speed of sound in 1D phononic crystals", *Adv. Mater. Sci. Eng.*, vol. 2016, 2016.

[94] A. P. Liu, R. Zhu, X. N. Liu, G. K. Hu, and G. L. Huang, "Multi-displacement microstructure continuum modeling of anisotropic elastic metamaterials", *Wave motion*, vol. 49, no. 3, p. 411, 2012.

[95] D. Torrent and J. Sánchez-Dehesa, "Acoustic cloaking in two dimensions: a feasible approach",

[96] B.-I. Popa and S. A. Cummer, "Design and characterization of broadband acoustic composite metamaterials", *Physical Review B*, vol. 80, no. 17, p. 174 303, 2009.

[97] L. Zigoneanu, B.-I. Popa, A. F. Starr, and S. A. Cummer, "Design and measurements of a broadband two-dimensional acoustic metamaterial with anisotropic effective mass density", *Journal of Applied Physics*, vol. 109, no. 5, p. 054 906, 2011.

[98] L. Gumen, J. Arriaga, and A. Krokhin, "Metafluid with anisotropic dynamic mass", *Low Temperature Physics*, vol. 37, no. 11, pp. 975–978, 2011.

[99] A. N. Norris, A. L. Shuvalov, and A. A. Kutsenko, "Analytical formulation of three-dimensional dynamic homogenization for periodic elastic systems", *Proceedings of the Royal Society of London A: Mathematical, Physical and Engineering Sciences*, vol. 468, p. 1629, 2012, ISSN: 1364-5021.

[100] V. Parton and B. Kudryavtsev, "Electromagnetoelasticity", *Gordon and Breach Science Publishers, New York*, vol. 2, pp. 90 059–, 1988.

[101] R. Bechmann, "Elastic and piezoelectric constants of Alpha-quartz", *Phys. Rev.*, vol. 110, pp. 1060–1061, 5 Jun. 1958.

[102] P. Chen, "Characterization of the three dimensional properties of poled PZT 65/35 in the absence of losses", *Acta Mechanica*, vol. 47, no. 1, pp. 95–106, 1983.

[103] D. Berlincourt, O. Mattiat, and Y. Kikuchi, *Ultrasonic transducer materials.* Plenum Pub Corp, 1971.

[104] "IEEE standard on magnetostrictive materials: Piezomagnetic nomenclature", *IEEE Std 319-1990*, pp. 1–, 1991.

[105] I. Dzyaloshinskii, "The problem of piezomagnetism", *Sov. Phys. JETP*, vol. 6, p. 621, 1958.

[106] A. Borovik-Romanov, "Piezomagnetism in the antiferromagnetic fluorides of cobalt and manganese", *Sov. Phys. JETP*, vol. 11, p. 786, 1960.

[107] T. Phillips, R. Townsend Jr, and R. White, "Piezomagnetism of $\mathrm{CoF_2}$ and α-$\mathrm{Fe_2O_3}$ from electron-paramagnetic-resonance pressure experiments", *Physical Review Letters*, vol. 18, no. 16, p. 646, 1967.

[108] I. J. Busch-Vishniac, *Electromechanical sensors and actuators.* Springer Science Business Media, 2012.

[109] Z. Wu, Y. Wen, P. Li, J. Yang, and X. Dai, "Effect of permeability and piezomagnetic coefficient on magnetostrictive/piezoelectric laminate composite", *Journal of Magnetics*, vol. 16, no. 2, pp. 157–160, 2011.

[110] C.-W. Nan, "Magnetoelectric effect in composites of piezoelectric and piezomagnetic phases", *Physical Review B*, vol. 50, no. 9, p. 6082, 1994.

[111] E. Juarez Ruiz, R. Cortes Maldonado, and F. Perez Rodriguez, "Relationship between the inverses of a matrix and a submatrix", *Computacion y Sistemas*, vol. 20, no. 2, 2016.

[112] V. M. Agranovich and V. Ginzburg, *Crystal optics with spatial dispersion, and excitons.* Springer, 1984.

[113] R. A. Shelby, D. R. Smith, and S. Schultz, "Experimental verification of a negative index of refraction", *Science*, vol. 292, no. 5514, pp. 77–79, 2001.

[114] P. Halevi and F. Ramos-Mendieta, "Tunable photonic crystals with semiconducting constituents", *Phys. Rev. Lett.*, vol. 85, pp. 1875–1878, 9 Aug. 2000.

[115] T.-W. Chang, J.-J. Wu, and C.-J. Wu, "Complex photonic band structures in a photonic crystal containing lossy semiconductor InSb", *Progress In Electromagnetics Research*, vol. 131, pp. 153–167, 2012.

[116] P. Halevi, J. Reyes-Avendano, and J. Reyes-Cervantes, "Electrically tuned phase transition and band structure in a liquid-crystal-infilled photonic crystal", *Physical Review E*, vol. 73, no. 4, p. 040 701, 2006.

[117] D. McPhail, M. Straub, and M. Gu, "Optical tuning of three-dimensional photonic crystals fabricated by femtosecond direct writing", *Applied Physics Letters*, vol. 87, no. 9, p. 091 117, 2005.

[118] I. L. Lyubchanskii, N. N. Dadoenkova, M. I. Lyubchanskii, E. A. Shapovalov, and T. Rasing, "Magnetic photonic crystals", *Journal of Physics D: Applied Physics*, vol. 36, no. 18, R277, 2003.

[119] H. Tian and J. Zi, "One-dimensional tunable photonic crystals by means of external magnetic fields", *Optics communications*, vol. 252, no. 4, pp. 321–328, 2005.

[120] R. Kitamura, L. Pilon, and M. Jonasz, "Optical constants of silica glass from extreme ultraviolet to far infrared at near room temperature", *Applied optics*, vol. 46, no. 33, pp. 8118–8133, 2007.

[121] J. Reyes-Avendaño, M. Sampedro, E. Juárez-Ruiz, and F. Pérez-Rodríguez, "Bianisotropic metamaterials based on twisted asymmetric crosses", *Journal of Optics*, vol. 16, no. 6, p. 065 102, 2014.

[122] A. Krokhin, P. Halevi, and J. Arriaga, "Long-wavelength limit (homogenization) for two-dimensional photonic crystals", *Physical Review B*, vol. 65, no. 11, p. 115 208, 2002.

[123] A. Alù, M. G. Silveirinha, A. Salandrino, and N. Engheta, "Epsilon-near-zero metamaterials and electromagnetic sources: Tailoring the radiation phase pattern", *Physical Review B*, vol. 75, no. 15, p. 155 410, 2007.

[124] L. D. Landau, E. M. Lifshitz, and L. P. Pitaevskii, *Electrodynamics of continuous media; 2nd ed.* Ser. Course of theoretical physics. Oxford: Butterworth, 1984.

[125] "IEEE standard letter designations for radar-frequency bands", *IEEE Std 521-2002 (Revision of IEEE Std 521-1984)*, pp. 1–3, 2003.

[126] J. Aguilar, M. Beadle, P. Thompson, and M. Shelley, "The microwave and RF characteristics of FR4 substrates", 1998.

[127] A. Konovalenko, J. Reyes-Avendano, and F. Pérez-Rodrıguez, "A wideband double-negative metamaterial based on framed crosses",

[128] Y. A. Chang and L. Himmel, "Temperature dependence of the elastic constants of Cu, Ag, and Au above room temperature", *J. Appl. Phys.*, vol. 37, no. 9, p. 3567, 1966.

[129] C. Kittel, *Introduction to Solid State Physics.* John Wiley & Sons, 2005.

[130] Y. Pang and R. Huang, "Effect of elastic anisotropy on surface pattern evolution of epitaxial thin films", *International Int. J. Solids Struct. of Solids and Structures*, vol. 46, no. 14, p. 2822, 2009.

[131] M. De Jong, W. Chen, H. Geerlings, M. Asta, and K. A. Persson, "A database to enable discovery and design of piezoelectric materials", *Scientific data*, vol. 2, 2015.

Appendix A

Symmetry of material tensors

A.1 Stiffness/compliance tensor

Crystallography helps to reduce the number of elements in stiffness/compliance tensor in the case of certain unit cell symmetry:

System	Constants	Symmetry point group	Tensor form
Isotropic	2		$\begin{pmatrix} C_{11} & C_{12} & C_{12} & 0 & 0 & 0 \\ C_{12} & C_{11} & C_{12} & 0 & 0 & 0 \\ C_{12} & C_{12} & C_{11} & 0 & 0 & 0 \\ 0 & 0 & 0 & C_{44} & 0 & 0 \\ 0 & 0 & 0 & 0 & C_{44} & 0 \\ 0 & 0 & 0 & 0 & 0 & C_{44} \end{pmatrix}$ $C_{44} = \frac{1}{2}(C_{11} - C_{12}), \quad S_{44} = 2(S_{11} - S_{12})$
Cubic	3	$23, m3, 432, \bar{4}3m, m3m$	$\begin{pmatrix} C_{11} & C_{12} & C_{12} & 0 & 0 & 0 \\ C_{12} & C_{11} & C_{12} & 0 & 0 & 0 \\ C_{12} & C_{12} & C_{11} & 0 & 0 & 0 \\ 0 & 0 & 0 & C_{44} & 0 & 0 \\ 0 & 0 & 0 & 0 & C_{44} & 0 \\ 0 & 0 & 0 & 0 & 0 & C_{44} \end{pmatrix}$

System	Constants	Symmetry point group	Tensor form
Hexagonal	5	$6, \overline{6}, \frac{6}{m}, 622, 6mm, \overline{6}2m, \frac{6}{m}mm$	$\begin{pmatrix} C_{11} & C_{12} & C_{13} & 0 & 0 & 0 \\ C_{12} & C_{11} & C_{13} & 0 & 0 & 0 \\ C_{13} & C_{13} & C_{33} & 0 & 0 & 0 \\ 0 & 0 & 0 & C_{44} & 0 & 0 \\ 0 & 0 & 0 & 0 & C_{44} & 0 \\ 0 & 0 & 0 & 0 & 0 & C_{66} \end{pmatrix}$ $C_{66} = \frac{1}{2}(C_{11} - C_{12}), \quad S_{66} = 2(S_{11} - S_{12})$
Tetragonal	6	$\frac{4}{m}mm, 422, \overline{4}2m, 4mm$	$\begin{pmatrix} C_{11} & C_{12} & C_{13} & 0 & 0 & 0 \\ C_{12} & C_{11} & C_{13} & 0 & 0 & 0 \\ C_{13} & C_{13} & C_{33} & 0 & 0 & 0 \\ 0 & 0 & 0 & C_{44} & 0 & 0 \\ 0 & 0 & 0 & 0 & C_{44} & 0 \\ 0 & 0 & 0 & 0 & 0 & C_{66} \end{pmatrix}$
Tetragonal	7	$4, \overline{4}, \frac{4}{m}$	$\begin{pmatrix} C_{11} & C_{12} & C_{13} & 0 & 0 & C_{16} \\ C_{12} & C_{11} & C_{13} & 0 & 0 & -C_{16} \\ C_{13} & C_{13} & C_{33} & 0 & 0 & 0 \\ 0 & 0 & 0 & C_{44} & 0 & 0 \\ 0 & -C_{16} & 0 & 0 & C_{44} & 0 \\ C_{16} & 0 & 0 & 0 & 0 & C_{66} \end{pmatrix}$
Trigonal	6	$32, 3m, \overline{3}m$	$\begin{pmatrix} C_{11} & C_{12} & C_{13} & C_{14} & 0 & 0 \\ C_{12} & C_{11} & C_{13} & -C_{14} & 0 & 0 \\ C_{13} & C_{13} & C_{33} & 0 & 0 & 0 \\ C_{14} & -C_{14} & 0 & C_{44} & 0 & 0 \\ 0 & 0 & 0 & 0 & C_{44} & C_{14} \\ 0 & 0 & 0 & 0 & C_{14} & C_{66} \end{pmatrix}$ $C_{66} = \frac{1}{2}(C_{11} - C_{12}), \quad S_{66} = 2(S_{11} - S_{12})$

System	Constants	Symmetry point group	Tensor form
Trigonal	7	$3, \overline{3}$	$\begin{pmatrix} C_{11} & C_{12} & C_{13} & C_{14} & C_{15} & 0 \\ C_{12} & C_{11} & C_{13} & -C_{14} & -C_{15} & 0 \\ C_{13} & C_{13} & C_{33} & 0 & 0 & 0 \\ C_{14} & -C_{14} & 0 & C_{44} & 0 & -C_{15} \\ C_{15} & -C_{15} & 0 & 0 & C_{44} & C_{14} \\ 0 & 0 & 0 & -C_{15} & C_{14} & C_{66} \end{pmatrix}$ $C_{66} = \frac{1}{2}(C_{11} - C_{12}), \quad S_{66} = 2(S_{11} - S_{12})$
Orthorhombic	9	$222, mmm, mm2$	$\begin{pmatrix} C_{11} & C_{12} & C_{13} & 0 & 0 & 0 \\ C_{12} & C_{22} & C_{23} & 0 & 0 & 0 \\ C_{13} & C_{23} & C_{33} & 0 & 0 & 0 \\ 0 & 0 & 0 & C_{44} & 0 & 0 \\ 0 & 0 & 0 & 0 & C_{55} & 0 \\ 0 & 0 & 0 & 0 & 0 & C_{66} \end{pmatrix}$
Monoclinic	13	$2, m, \frac{2}{m}$	$\begin{pmatrix} C_{11} & C_{12} & C_{13} & 0 & C_{15} & 0 \\ C_{12} & C_{22} & C_{23} & 0 & C_{25} & 0 \\ C_{13} & C_{23} & C_{33} & 0 & C_{35} & 0 \\ 0 & 0 & 0 & C_{44} & 0 & C_{46} \\ C_{15} & C_{25} & C_{35} & 0 & C_{55} & 0 \\ 0 & 0 & 0 & C_{46} & 0 & C_{66} \end{pmatrix}$
Triclinic	21	$1, \overline{1}$	$\begin{pmatrix} C_{11} & C_{12} & C_{13} & C_{14} & C_{15} & C_{16} \\ C_{12} & C_{22} & C_{23} & C_{24} & C_{25} & C_{26} \\ C_{13} & C_{23} & C_{33} & C_{34} & C_{35} & C_{36} \\ C_{14} & C_{24} & C_{34} & C_{44} & C_{45} & C_{46} \\ C_{15} & C_{25} & C_{35} & C_{45} & C_{55} & C_{56} \\ C_{16} & C_{26} & C_{36} & C_{46} & C_{56} & C_{66} \end{pmatrix}$

A.2 Piezoelectric tensor e_{ik}

The piezoelectric tensor can be described in matrix form (e_{ik} of 3×6 size) as below listed, depending on the symmetry of unit cell [131]:

System	Constants	Symmetry point group	Tensor form
Cubic	1	$23, \bar{4}3m$	$\begin{pmatrix} 0 & 0 & 0 & e_{14} & 0 & 0 \\ 0 & 0 & 0 & 0 & e_{14} & 0 \\ 0 & 0 & 0 & 0 & 0 & e_{14} \end{pmatrix}$
Hexagonal	1	$\bar{6}m2$	$\begin{pmatrix} 0 & 0 & 0 & 0 & 0 & -e_{22} \\ -e_{22} & e_{22} & 0 & 0 & 0 & 0 \\ 0 & 0 & 0 & 0 & 0 & 0 \end{pmatrix}$
	2	$\bar{6}$	$\begin{pmatrix} e_{11} & -e_{11} & 0 & 0 & 0 & -e_{22} \\ -e_{22} & e_{22} & 0 & 0 & 0 & -e_{11} \\ 0 & 0 & 0 & 0 & 0 & 0 \end{pmatrix}$
Tetragonal	2	$\bar{4}2m$	$\begin{pmatrix} 0 & 0 & 0 & e_{14} & 0 & 0 \\ 0 & 0 & 0 & 0 & e_{14} & 0 \\ 0 & 0 & 0 & 0 & 0 & e_{36} \end{pmatrix}$
	4	$\bar{4}$	$\begin{pmatrix} 0 & 0 & 0 & e_{14} & e_{15} & 0 \\ 0 & 0 & 0 & -e_{15} & e_{14} & 0 \\ e_{31} & -e_{31} & 0 & 0 & 0 & e_{36} \end{pmatrix}$
Hexagonal, tetragonal	4	$6mm, 4mm$	$\begin{pmatrix} 0 & 0 & 0 & 0 & e_{15} & 0 \\ 0 & 0 & 0 & e_{15} & 0 & 0 \\ e_{31} & e_{31} & e_{33} & 0 & 0 & 0 \end{pmatrix}$
	4	$6, 4$	$\begin{pmatrix} 0 & 0 & 0 & e_{14} & e_{15} & 0 \\ 0 & 0 & 0 & e_{15} & -e_{14} & 0 \\ e_{31} & e_{31} & e_{33} & 0 & 0 & 0 \end{pmatrix}$

System	Constants	Symmetry point group	Tensor form
Trigonal	2	32	$\begin{pmatrix} e_{11} & -e_{11} & 0 & e_{14} & 0 & 0 \\ 0 & 0 & 0 & 0 & -e_{14} & -e_{11} \\ 0 & 0 & 0 & 0 & 0 & 0 \end{pmatrix}$
	4	$3m$	$\begin{pmatrix} 0 & 0 & 0 & 0 & e_{15} & -e_{22} \\ -e_{22} & e_{22} & 0 & e_{15} & 0 & 0 \\ e_{31} & e_{31} & e_{33} & 0 & 0 & 0 \end{pmatrix}$
	6	3	$\begin{pmatrix} e_{11} & -e_{11} & 0 & e_{14} & e_{15} & -e_{22} \\ -e_{22} & e_{22} & 0 & e_{15} & -e_{14} & -e_{11} \\ e_{31} & e_{31} & e_{33} & 0 & 0 & 0 \end{pmatrix}$
Orthorhombic	3	222	$\begin{pmatrix} 0 & 0 & 0 & e_{14} & 0 & 0 \\ 0 & 0 & 0 & 0 & e_{25} & 0 \\ 0 & 0 & 0 & 0 & 0 & e_{36} \end{pmatrix}$
	5	$mm2$	$\begin{pmatrix} 0 & 0 & 0 & 0 & e_{15} & 0 \\ 0 & 0 & 0 & e_{24} & 0 & 0 \\ e_{31} & e_{32} & e_{33} & 0 & 0 & 0 \end{pmatrix}$
Monoclinic	8	2	$\begin{pmatrix} 0 & 0 & 0 & e_{14} & 0 & e_{16} \\ e_{21} & e_{22} & e_{23} & 0 & e_{25} & 0 \\ 0 & 0 & 0 & e_{34} & 0 & e_{36} \end{pmatrix}$
	10	m	$\begin{pmatrix} e_{11} & e_{12} & e_{13} & 0 & e_{15} & 0 \\ 0 & 0 & 0 & e_{24} & 0 & e_{26} \\ e_{31} & e_{32} & e_{33} & 0 & e_{35} & 0 \end{pmatrix}$
Triclinic	18	1	$\begin{pmatrix} e_{11} & e_{12} & e_{13} & e_{14} & e_{15} & e_{16} \\ e_{21} & e_{22} & e_{23} & e_{24} & e_{25} & e_{26} \\ e_{31} & e_{32} & e_{33} & e_{34} & e_{35} & e_{36} \end{pmatrix}$

Appendix B

Equipment list

B.1 LPKF E33 Rapid Prototyping CNC machine

For fabrication of metamaterials, there are exist various methods - chemical etching, mechanical punch pressing or milling, laser cutting etc. Within this work, a mechanical milling using LPKF E33 CNC machine on the FR4 circuit board will be used to fabricate metamaterials samples.

The LPKF ProtoMat E33 is a CNC machine for rapid printing board prototyping using a high-speed tungsten carbide end mills and cutters (Figure B.1). It uses a high RPM motor to operate which gives a very good accuracy and samples repeatability. The ProtoMat E33 needs a dust extraction unit, a set of bits with copper-clad board, and a PC with CircuitPro software installed to produce a printed circuit board. The maximum resolution of 1 μm, a high repeatability of +/-5 μm, and a precision inside the fitting hole system of +/-20 μm, the small mill/drill plotter typically meet the accuracy requirements for the production of single and double layer printed circuit boards with metamaterial resonators.

Specifications of E33 milling CNC machine is given in Table B.1.

The accuracy and precision of metamaterial sample under fabrication process strongly depend on substrate PCB roughness and types of end mills available.

The software included is CircuitPro, which can be used for drawing and machine controlling. To process a sample, it is necessary to glue an FR4 PCB to the main machine table, then import a technical draw in .DXF format using a CircuitPro. Another option is to use external CAD to design a structure, further procedure is to convert a technical draw

Maximum material size (X/ Y/ Z)	229 mm x 305 mm x 10 mm
Resolution (X/Y)	0.8 μm
Repeatability	± 0.005 mm
Precision of front/back alignment	± 0.02 mm
Milling spindle	Maximum 33000 RPM, software controlled
Tool change	Manual
Milling width adjustment	Manual
Tool holder	3.175 mm (1/8 inch)
Drilling speed	100 holes/min
Travel speed (X/Y)	Maximum 50 mm/sec
X/Y-drive	2-phase stepper motor
Z-drive	2-phase stepper motor
Dimensions (W x H x D)	370 mm x 300 mm x 450 mm
Weight	15 kg (33 lbs)
Power supply	90 – 240 V, 50 – 60 Hz, 150 W

Table B.1: Technical specification of LPKF ProtoMat E33 CNC machine

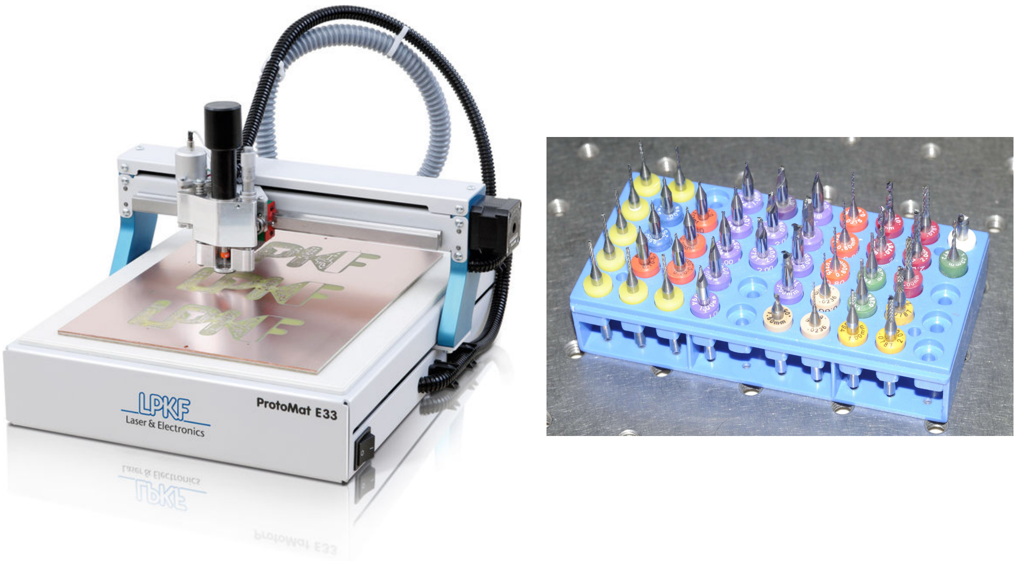

Figure B.1: LPKF ProtoMat E33 machine with universal cutters/end mills/drill bits.

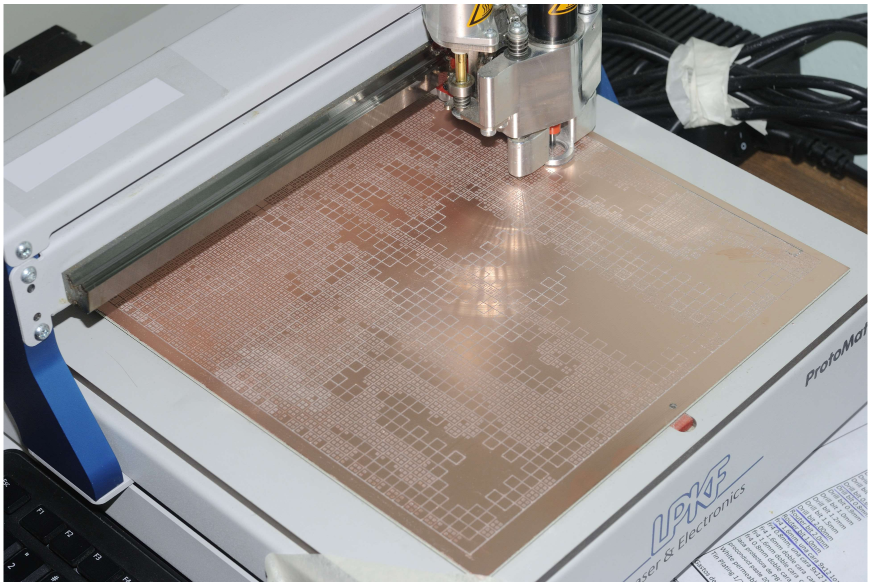

Figure B.2: LPKF ProtoMat E33 machine during window resonators structure fabrication at IFUAP.

into a native machine tool trajectories. Special routing algorithm calculates and designates parameters for sample prototyping - spindle speed for each of the types of cutters/end mills, routing path. The working flow of starts from finest cutters toolpath (usually 0.2 mm Universal Cutter), then going rub out procedure with end mills 0.5 - 3 mm, and finalizing the material production by drills and board contour cutting phase. Board time processing strongly depends on the complexity of metamaterial structure and can take up to 1 day. It is strongly recommended to follow machine manual safety manual and operating instructions! Figure B.2 shows the LPKF ProtoMat E33 CNC machine during the process of metamaterials milling. After each bit trajectory is finished, a machine will move head to home position for instrument change, this machine still requires manual operator bit changing.

B.2 Linear horn antenna, DRH-20, 2-20 GHz

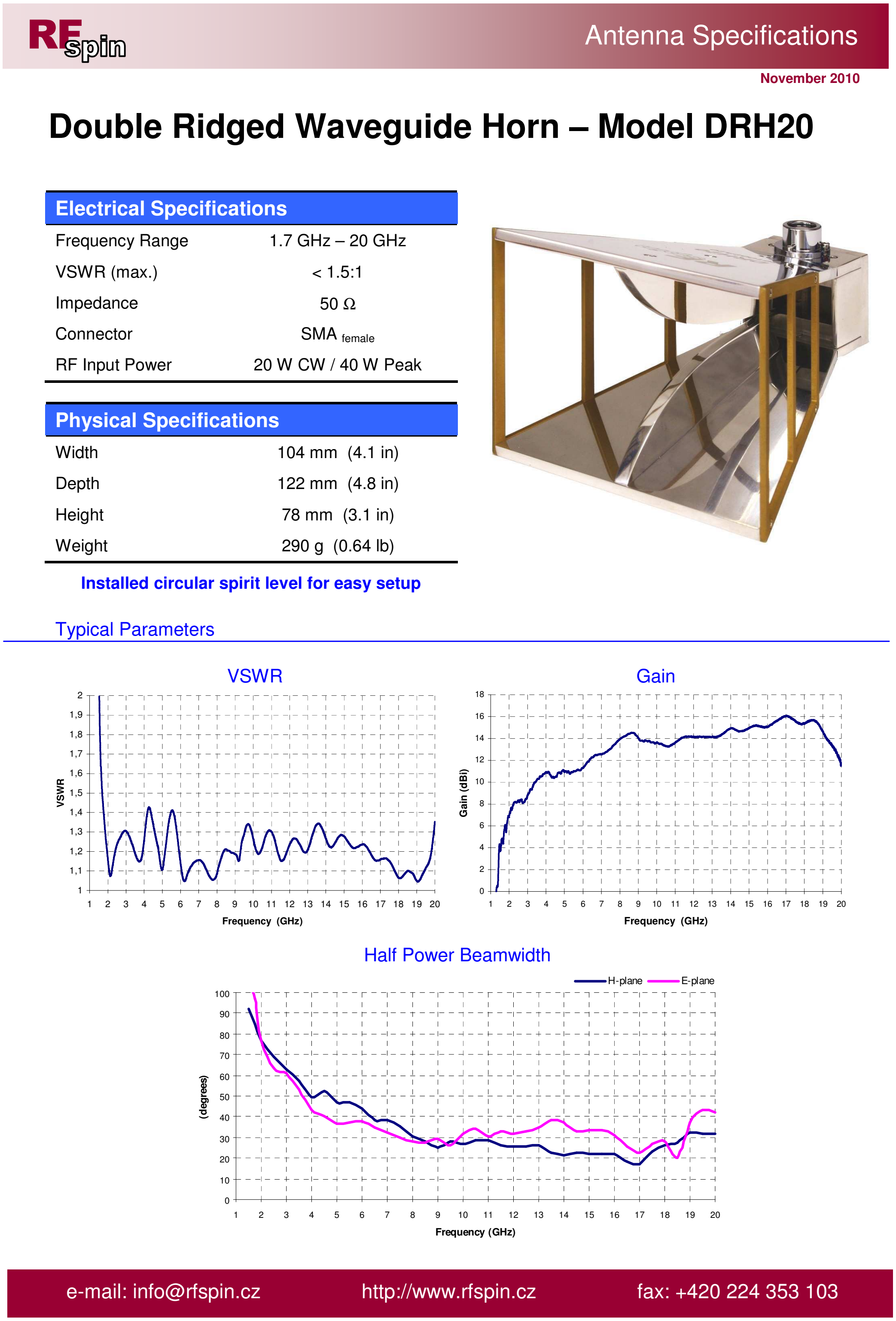

RFspin Antenna Specifications

November 2010

Double Ridged Waveguide Horn – Model DRH20

Electrical Specifications	
Frequency Range	1.7 GHz – 20 GHz
VSWR (max.)	< 1.5:1
Impedance	50 Ω
Connector	SMA female
RF Input Power	20 W CW / 40 W Peak

Physical Specifications	
Width	104 mm (4.1 in)
Depth	122 mm (4.8 in)
Height	78 mm (3.1 in)
Weight	290 g (0.64 lb)

Installed circular spirit level for easy setup

Typical Parameters

e-mail: info@rfspin.cz http://www.rfspin.cz fax: +420 224 353 103

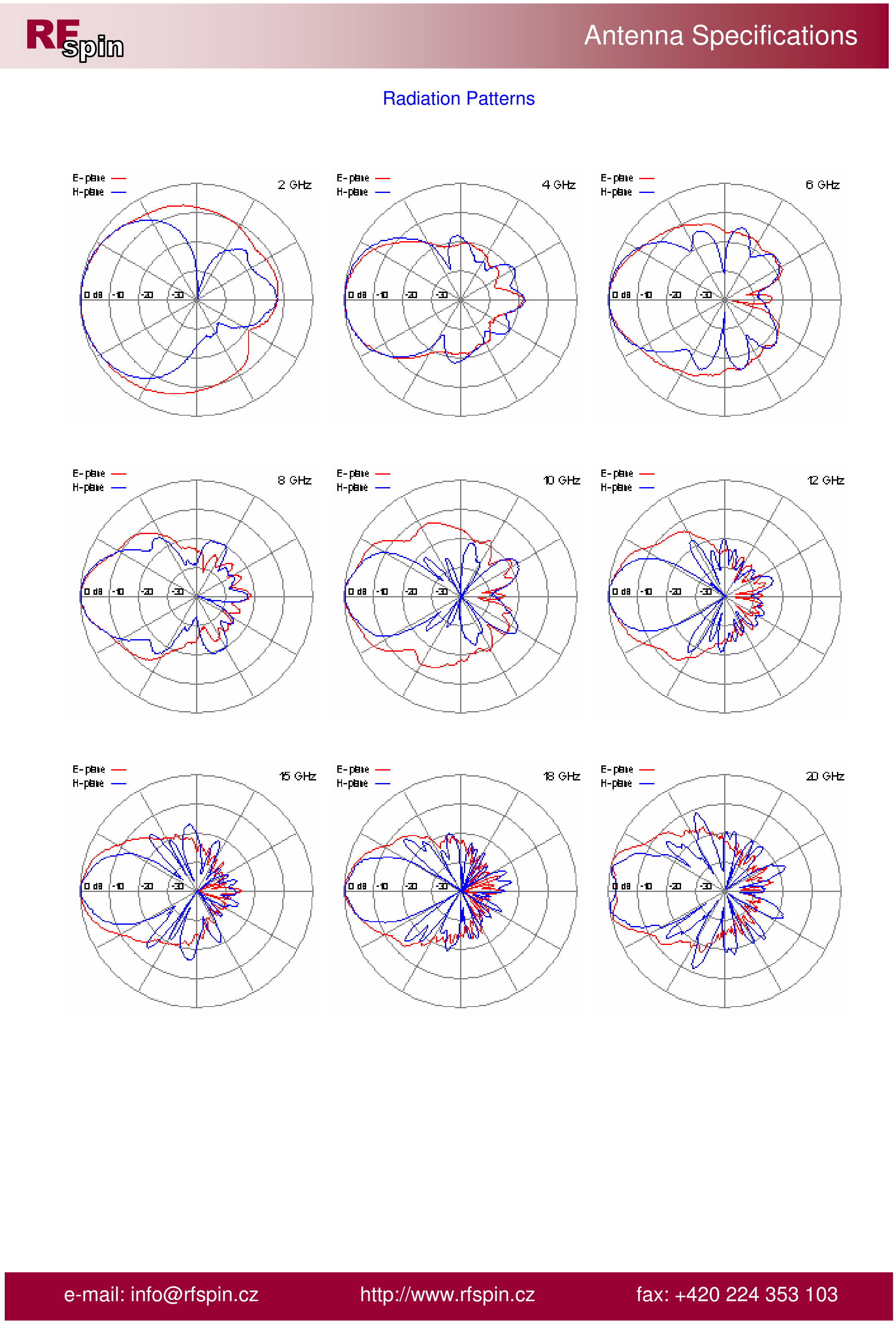

RFspin

Antenna Specifications

Radiation Patterns

e-mail: info@rfspin.cz http://www.rfspin.cz fax: +420 224 353 103

Appendix C

Microwave bands list

IEEE Standard for Letter Designations for Radar-Frequency Bands

1. Scope

Since World War II, radar systems engineers have used letter designations as a short notation for describing the frequency band of operation. This usage has continued throughout the years and is now an accepted practice of radar engineers. Radar-frequency letter designations are used for the following reasons:

1) They provide a convenient method for describing the band in which the radar operates without the need for awkwardly stating the limits of the frequency in numerical terms. For example, it is more convenient to say an L-band radar than a 1215–1400 MHz radar. This is especially important in titles of published papers on radar, in advertising of radar systems and components, or in any other situation where a short notation is desired.
2) In military radar systems, the exact frequency of operation cannot usually be disclosed, but it is permissible in many cases to describe the band in which it operates. The letter designations permit this.
3) Each radar-frequency band has its own particular characteristics. Thus an X-band radar will be different from an S-band radar. The letter designations are often used in this manner to indicate the particular nature of the radar as it is influenced by its frequency. There are vast differences in characteristics, applications, and environmental constraints that distinguish radars in the different bands. It is the need to communicate concisely the whole set of characteristics which are shared by S-band radar, as distinguished from L-band radar, C-band radar, and the others, which requires the established usage of letter designations.

2. Usage

The nomenclature of Table 1 shall be followed when letter designations are used to describe the frequency of radar operation. When appropriate, it is suggested that the specific International Telecommunications Union (ITU) radiolocation numerical band limits be inserted parenthetically; for example, VHF (216–225 MHz) or L-band (1.215–1.4 GHz).

3. Relation to other nomenclature

The radar letter designations are consistent with the recommended nomenclature of the ITU, as shown in Table 2. Note that the high frequency (HF) and the very high frequency (VHF) definitions are identical in the two systems. The essence of the radar nomenclature is to subdivide the existing ITU bands, in accordance with radar practice, without conflict or ambiguity.

The letter band designations should not be construed as being a substitute for the specific frequency limits of the frequency bands. The specific frequency limits should be used when appropriate, but when a letter designation of a radar-frequency band is called for, those of Table 1 shall be used.

The letter designations described in this standard are designed for radar usage and are used in current practice. They are not meant to be used for other radio or telecommunication purposes, unless they pertain to radar.

The letter designations for electronic countermeasure operations, as described in Air Force Regulation No. 55-44, Army Regulation No. 105-86, and Navy OPNAV Instruction 3430.9B, are not consistent with radar practice and shall not be used to describe radar-frequency bands.

Table 1—Standard radar-frequency letter band nomenclature

International table				
Band designation	**Nominal frequency range**	**Specific frequency ranges for radar based on ITU assignments** (see Notes 1, 2)		
		Region 1	**Region 2**	**Region 3**
HF	3–30 MHz	(Note 3)		
VHF	30–300MHz	None	138 –144 MHz 216– 225 MHz (See Note 4)	223-230 MHz
UHF	300–1000 MHz (Note 5)	420–450 MHz (Note 4) 890–942 MHz (Note 6)		
L	1–2 GHz	1215–1400 MHz		
S	2–4 GHz	2300–2500 MHz		
		2700–3600 MHz	2700–3700 MHz	
C	4–8 GHz	4200– 4400 MHz (Note 7)		
		5250–5850 MHz	5250–5925 MHz	
X	8–12 GHz	8.5–10.68 GHz		
Ku	12–18 GHz	13.4–14 GHz		
		15.7–17.7 GHz		
K	18–27 GHz	24.05–24.25 GHz	24.05–24.25 GHz 24.65–24.75 GHz (Note 8)	24.05–24.25 GHz
Ka	27–40 GHz	33.4–36 GHz		
V	40–75 GHz	59–64 GHz		
W	75–110 GHz	76–81 GHz		
		92–100 GHz		
mm (Note 9)	110–300 GHz	126–142 GHz		
		144–149 GHz		
		231–235 GHz 238–248 GHz (Note 10)		

NOTES

1—These international ITU frequency allocations are from the table contained in Article S5 of the *ITU Radio Regulations*, 1998 Edition. The ITU defines no specific service for radar, and the frequency assignments listed are derived from those radio services that use radiolocation. The frequency allocations listed include those for both *primary* and *secondary* service. The listings of frequency assignments are included for reference only and are subject to change.

2—The specific frequency ranges for radiolocation are listed in the *NTIA Manual of Regulations & Procedures for Federal Radio Frequency Management*, Chapter 4. The NTIA manual (known as the *Redbook*) can be downloaded from the website: http://www.ntia.doc.gov/osmhome/redbook/redbook.html.

3—There are no official ITU radiolocation bands at HF. So-called HF radars might operate anywhere from just above the broadcast band (1.605 MHz) to 40 MHz or higher.

4—Frequencies from 216–450 MHz were sometimes called *P-band*.

5—The official ITU designation for the ultra high frequency band extends to 3000 MHz. In radar practice, however, the upper limit is usually taken as 1000 MHz, L- and S-bands being used to describe the higher UHF region.

6—Sometimes included in L-band.

7—Designated for aeronautical navigation, this band is reserved (with few exceptions) exclusively for airborne radar altimeters.

8—The frequency range of 24.65–24.75 GHz includes satellite radiolocation (earth to space only).

9—The designation mm is derived from *millimeter* wave radar, and is also used to refer to V- and W-bands, and part of Ka-band, when general information relating to the region above 30 GHz is to be conveyed.

10—No ITU allocations are listed for frequencies above 275 GHz.

Table 2—Comparison of radar-frequency letter band nomenclature with ITU nomenclature

Radar nomenclature		**ITU nomenclature**			
Radar letter designation	**Frequency range**	**Frequency range**	**Band No.**	**Adjectival band designation**	**Corresponding metric designation**
HF	3–30 MHz	3–30 MHz	7	High frequency (HF)	Dekametric waves
VHF	30–300 MHz	30–300 MHz	8	Very high frequency (VHF)	Metric waves
UHF	300–1000 MHz	0.3–3 GHz	9	Ultra high frequency (UHF)	Decimetric waves
L	1–2 GHz				
S	2–4 GHz				
C	4–8 GHz	3–30 GHz	10	Super high frequency (SHF)	Centimetric waves
X	8–12 GHz				
Ku	12–18 GHz				
K	18–27 GHz				
Ka	27–40 GHz	30–300 GHz	11	Extremely high frequency (EHF)	Millimetric waves
V	40–75 GHz				
W	75–110 GHz				
mm	110 –300 GHz				

JOURNAL OF APPLIED PHYSICS **121**, 155102 (2017)

Nonlocal metasolid response of homogenized phononic crystals

A. Konovalenko,[1,a)] E. Gutiérrez-Reyes,[2,b)] A. L. González,[1] J. Flores-Méndez,[3,c)]
and F. Pérez-Rodríguez[1]
[1]*Instituto de Física, Benemérita Universidad Autónoma de Puebla, Apdo. Post. J-48, Puebla, Pue. 72570, Mexico*
[2]*CICESE, Unidad La Paz, Miraflores No. 334, La Paz, B.C.S., 23050, Mexico*
[3]*Facultad de Ciencias de la Electrónica, Benemérita Universidad Autónoma de Puebla, Puebla, Pue. 72570, Mexico*

(Received 18 January 2017; accepted 4 April 2017; published online 17 April 2017)

The nonlocal effective dynamic mass-density and stiffness tensors for a solid 3D phononic crystal having Au inclusions embedded in a Si host matrix have been calculated. The applied homogenization theory is based on the Fourier formalism and the form-factor division approach. Using the effective parameters, the phononic band structure of the homogenized elastic crystal can be described even beyond the long wavelength limit. It is found out that the effective dynamic mass-density becomes anisotropic as the frequency of the phononic modes is increased because the nonlocal metasolid response depends on the phononic-mode polarization, the shape of the inclusions, and the type of the periodic array. *Published by AIP Publishing.*
[http://dx.doi.org/10.1063/1.4981129]

I. INTRODUCTION

The description of sound propagation through a phononic crystal, composed of materials with different mass density, elastic parameters, arbitrary Bravais lattice, and any inclusion shape, could be a quite complex task. To simplify the calculations needed for such a description, nowadays a homogenization approach is commonly used. The main idea of a homogenization approximation is to consider a phononic crystal as a homogeneous medium with effective parameters, such as effective mass density and effective compliance tensor. In the quasi-static limit ($\omega \to 0$), where the phononic dispersion relation is linear and, therefore, phase and group velocities coincide, the effective sound velocity

$$v_{\text{eff}}(\hat{\boldsymbol{k}}) = \lim_{\omega,k\to 0}(\omega/k) \tag{1}$$

can be directly calculated by using the plane wave expansion (PWE) method (see, for example, Refs. 1–8). As it is shown there, v_{eff} depends not only on the type of periodic array and the geometry of the unit cell but also on the direction of propagation, i.e., on $\hat{\boldsymbol{k}} = \boldsymbol{k}/k$, where $\boldsymbol{k}$ is the wave vector and k its magnitude. According to the exact analytical formulas for the speed of transverse sound propagating in a two-dimensional arrangement of solids, derived in Ref. 1, the effective speed of transverse sound is determined by the average density $\overline{\rho}$ and an effective shear modulus depending on the details of the microstructure. On the basis of the homogenization method presented in Ref. 1, compact formulas of the effective velocities for the quasi-longitudinal, quasi-shear vertical, and shear horizontal modes were obtained in these works.[2,3] The fact that the effective mass density in the quasi-static limit is given by the average one, $\overline{\rho}$, implies that such an effective parameter depends only on the filling fraction of the components, but it is independent of their shape, as well as of their distribution inside the phononic crystal. As it has been shown in several works (see, for example, Refs. 9–11), at sufficiently high frequencies, the effective mass density for solid phononic crystals (SPCs) depends not only on the filling fraction of the components but also on the frequency ω of the phononic modes. Besides, the effective mass density turns out to be distinct for transverse and longitudinal phononic modes, and it may even be negative at certain frequency intervals.

Recently, a general homogenization theory,[12] based on the Fourier formalism, has been proposed to calculate the effective parameters for phononic crystals having solid inclusions embedded in a solid host matrix. The theory provides explicit formulas for determining all the components of the effective mass-density and compliance tensors for any Bravais lattice and shape of the inclusion not only in the long wavelength limit but also at high frequencies where the effective dynamic parameters depend on both frequency ω and wave vector $\boldsymbol{k}$ and, therefore, the effective elastic response is nonlocal. However, in Ref. 12, the proposed theory was only applied to two-dimensional (2D) solid phononic crystals at the quasi-static limit in order for the calculations, requiring the inversion of very large matrices, to be feasible. As it was demonstrated in Ref. 12, the theory can be extended to periodic systems with liquid components by introducing an infinitesimally small shear modulus for the liquid. In particular, applying the new approach in the low-frequency limit, the effective dynamic mass density and compliance tensors for square solid bars embedded in water were calculated. The homogenized rectangular 2D PC can be called *metafluid*[13–16] since it behaves as a liquid, having zero effective shear modulus, but possessing an anisotropic effective mass density tensor. Besides, it was found that rectangular two-dimensional

---

[a)] Electronic mail: anatolii@ifuap.buap.mx
[b)] Also at Instituto de Física, Benemérita Universidad Autónoma de Puebla, Apdo. Post. J-48, Puebla, Pue., 72570, Mexico.
[c)] Also at Instituto Tecnológico de Puebla—División de Estudios de Posgrado e Investigación, Puebla, Pue., 72220, Mexico.

Research Article Vol. 34, No. 9 / /Journal of the Optical Society of America B 1

Journal of the Optical Society of America B

OPTICAL PHYSICS

Nonlocal response of tunable photonic metamaterials with semiconductor inclusions

Anatolii Konovalenko* and Felipe Pérez Rodríguez

Instituto de Física, Benemérita Universidad Autónoma de Puebla, Apdo. Post. J-48, Puebla, Pue., 72570, Mexico
**Corresponding author: anatolii@ifuap.buap.mx*

Received 13 March 2017; revised 27 July 2017; accepted 10 August 2017; posted 15 August 2017 (Doc. ID 290659); published 0 MONTH 0000

Effective parameters of homogenized photonic crystals with a semiconductor bar in the unit cell are calculated and analyzed. The applied homogenization theory is based on the Fourier formalism within the form-factor division approach. The calculated effective parameters, namely, the components of the effective permittivity tensor, are nonlocal since they depend on not only frequency but also the wave vector. Using the nonlocal effective parameters, the complex dispersion relation for photonics modes propagating in a periodic semiconductor–dielectric array can be described even beyond the long-wavelength limit. We have analyzed the temperature dependence of the nonlocal effective parameters for photonic metamaterials composed of InSb square bars in a silica–glass host matrix. In the case of continuous (infinitely long) bars, the metamaterial shows plasma-like behavior with a temperature-dependent effective plasma frequency in the THz range. For the case of cut semiconductor bars, the metamaterial behaves as a dielectric in the lowest frequency band, whose width can also be tuned by varying the temperature. Using the nonlocal effective permittivity, the optical spectra (reflectivity and transmittance) for a slab of InSb square bars in a glass matrix were calculated and analyzed.

OCIS codes: (160.5293) Photonic bandgap materials; (160.5298) Photonic crystals; (160.6000) Semiconductor materials.

https://doi.org/10.1364/JOSAB.99.099999

1. INTRODUCTION

Photonic crystals (PCs) with tunable photonic band gaps (PBGs) have been an object of intensive study in the previous decade [1–3]. Several approaches are available to tune the PBGs of PCs: by applying an electrical field to liquid-crystal inclusions [4,5], as well as a magnetic field to control the frequency position and width of a PBG [6,7]. An outstanding idea to fabricate a tunable PC is to use a semiconductor component [1] with a sufficiently large number of free charge carriers. Evidently, the plasma frequency of such constituents will strongly depend on temperature, leading to a thermal shift of the PBG structure.

In the present work, we calculate the temperature-dependent effective parameters for two types of homogenized PCs. The first one is a square two-dimensional (2D) lattice of infinitely long InSb square bars embedded in a silica glass (SiO_2) matrix. The second system considered here is a cubic three-dimensional (3D) PC composed of cut square bars of InSb in a dielectric glass matrix. To obtain the effective parameters, we apply the general homogenization theory [8], which is based on the Fourier formalism.

The theory provides explicit formulas for determining all the components of bi-anisotropic response tensors, namely, effective permittivity, permeability, and crossed magnetoelectric tensors for arbitrary Bravais lattice and shape of inclusions. Interestingly, the homogenization theory can be applied in not only the long-wavelength limit, but also at high frequencies where the bi-anisotropic response becomes nonlocal, i.e., the effective parameters depend on both frequency ω and wave vector $\boldsymbol{k}$. Indeed, as was noted in Ref. [8], the complete photonic band structure of an *inherently inhomogeneous* PC can be calculated from either the system of equations for the Fourier components of the microscopic electromagnetic field (Eq. (15) in [8]) or the matrix equation for one of the components of the Fourier expansion [Eq. (A2) therein], which has the form of Maxwell equations for a *homogeneous* medium with a nonlocal effective bi-anisotropic response. However, in Ref. [8], the theory developed was only applied to periodic structures in the quasi-static limit.

The application of the homogenization theory developed in Ref. [8] requires the inversion of very large matrices and, consequently, a very long computing time. To make feasible the calculations of the effective parameters, an approach based on form-factor division was also proposed in Ref. [8]. Nevertheless, such an approach turns out to be sufficiently accurate for small inclusions only. Here, we modify the form-factor division approach (FFDA) to get highly accurate results at any filling fraction of the inclusions. The latter allows us to calculate the effective parameters for arbitrary forms of

0740-3224/17/090001-01 Journal © 2017 Optical Society of America

BUAP

MEMORANDUM

Para:	**Dr. Rafael Alberto Méndez Sánchez.**	**Presidente**
	Dr. J. Jesús Arriaga Rodríguez.	**Secretario**
	Dr. Gregorio Hernández Cocoletzi	**Vocal**
	Dr. Enrique Quiroga González.	**Vocal**
	Dr. Felipe Pérez Rodríguez.	**Vocal**
De:	**Dra. María Eugenia Mendoza Álvarez, Directora.**	
Asunto:	**Se cita al examen del M.C. Anatolii Konovalenko.**	
Fecha:	**Lunes 28 de agosto, 2017.**	

Me permito informarles que el Comité Académico del IFUAP, los ha designado integrantes del Comité para el EXAMEN DE GRADO de DOCTORADO EN CIENCIAS (EN LA ESPECIALIDAD DE CIENCIA DE MATERIALES) del M.C. Anatolii Konovalenko, con su tesis cuyo título es: "DISEÑO Y MODELADO DE METAMATERIALES PIEZOELECTROMAGNETICOS", que presentará el próximo día: **Lunes 04 de septiembre, 2017 a las 11:00hrs. en el Auditorio del IFUAP.**

Dra. María Eugenia Mendoza Álvarez
Directora

Instituto de Física
"Ing. Luis Rivera
Terrazas"

Av. San Claudio esq. 18 sur, edif 110 A, B y C.
Ciudad Universitaria, Col. San Manuel,
Puebla, Pue. C.P. 72570
01(222) 2295610, Fax: ext. 5611

/LAEmhr